NORTH ATLANTIC TREATY ORGANISATION

RESEARCH AND TECHNOLOGY ORGANISATION

AC/323(SET-064)TP/43

www.rta.nato.int

RTO EDUCATIONAL NOTES **EN-SET-064**

Advances in Navigation Sensors and Integration Technology

(Les avancées en matière de capteurs de navigation et de technologies d'intégration)

The material in this publication was assembled to support a Lecture Series under the sponsorship of the Sensors and Electronics Technology Panel (SET) presented on 20-21 October 2003 in London, UK; 23-24 October 2003 in Ankara, Turkey; and 27-28 October 2003 in Paris, France.

Published February 2004

Distribution and Availability on Back Cover



NORTH ATLANTIC TREATY ORGANISATION

RESEARCH AND TECHNOLOGY ORGANISATION

AC/323(SET-064)TP/43

www.rta.nato.int

RTO EDUCATIONAL NOTES **EN-SET-064**

Advances in Navigation Sensors and Integration Technology

(Les avancées en matière de capteurs de navigation et de technologies d'intégration)

The material in this publication was assembled to support a Lecture Series under the sponsorship of the Sensors and Electronics Technology Panel (SET) presented on 20-21 October 2003 in London, UK; 23-24 October 2003 in Ankara, Turkey; and 27-28 October 2003 in Paris, France.

The Research and Technology Organisation (RTO) of NATO

RTO is the single focus in NATO for Defence Research and Technology activities. Its mission is to conduct and promote co-operative research and information exchange. The objective is to support the development and effective use of national defence research and technology and to meet the military needs of the Alliance, to maintain a technological lead, and to provide advice to NATO and national decision makers. The RTO performs its mission with the support of an extensive network of national experts. It also ensures effective co-ordination with other NATO bodies involved in R&T activities.

RTO reports both to the Military Committee of NATO and to the Conference of National Armament Directors. It comprises a Research and Technology Board (RTB) as the highest level of national representation and the Research and Technology Agency (RTA), a dedicated staff with its headquarters in Neuilly, near Paris, France. In order to facilitate contacts with the military users and other NATO activities, a small part of the RTA staff is located in NATO Headquarters in Brussels. The Brussels staff also co-ordinates RTO's co-operation with nations in Middle and Eastern Europe, to which RTO attaches particular importance especially as working together in the field of research is one of the more promising areas of co-operation.

The total spectrum of R&T activities is covered by the following 7 bodies:

- AVT Applied Vehicle Technology Panel
- HFM Human Factors and Medicine Panel
- IST Information Systems Technology Panel
- NMSG NATO Modelling and Simulation Group
- SAS Studies, Analysis and Simulation Panel
- SCI Systems Concepts and Integration Panel
- SET Sensors and Electronics Technology Panel

These bodies are made up of national representatives as well as generally recognised 'world class' scientists. They also provide a communication link to military users and other NATO bodies. RTO's scientific and technological work is carried out by Technical Teams, created for specific activities and with a specific duration. Such Technical Teams can organise workshops, symposia, field trials, lecture series and training courses. An important function of these Technical Teams is to ensure the continuity of the expert networks.

RTO builds upon earlier co-operation in defence research and technology as set-up under the Advisory Group for Aerospace Research and Development (AGARD) and the Defence Research Group (DRG). AGARD and the DRG share common roots in that they were both established at the initiative of Dr Theodore von Kármán, a leading aerospace scientist, who early on recognised the importance of scientific support for the Allied Armed Forces. RTO is capitalising on these common roots in order to provide the Alliance and the NATO nations with a strong scientific and technological basis that will guarantee a solid base for the future.

The content of this publication has been reproduced
directly from material supplied by RTO or the authors.

Published February 2004

Copyright © RTO/NATO 2004
All Rights Reserved

ISBN 92-837-1114-9

Single copies of this publication or of a part of it may be made for individual use only. The approval of the RTA Information Management Systems Branch is required for more than one copy to be made or an extract included in another publication. Requests to do so should be sent to the address on the back cover.

Advances in Navigation Sensors and Integration Technology

(RTO-EN-SET-064)

Executive Summary

The objective of this two-day Lecture Series is to present the current state-of-the-art in inertial navigation sensors and system integration technology through the improved use of advanced, low-cost navigation sensor technologies. Lecturers will present material that provides an understanding of the issues faced by today's system designers. Through this Lecture Series, the technical community will be updated on sensors and current integration techniques as practiced by leading experts in the field. The first day of the Lecture Series is primarily a tutorial to bring the audience up-to-date with current practices. The second day focuses on sensors and applications.

The first day begins with an overview paper that focuses on accuracy and other technology trends for inertial sensors, Global Positioning Systems (GPS), and integrated Inertial Navigation System (INS/GPS) systems that will lead to better than 1-m accuracy navigation systems of the future. The paper provides the rationale for the remaining papers. The second paper starts with a brief overview of inertial sensing and the technology trends underway. Discussions are presented on gyro and accelerometer technology development, with specific emphasis on designs and performance of MEMS sensors. The third paper provides an overview of the major computational elements associated with strapdown inertial systems. The fourth paper provides an overview of assorted analysis techniques associated with strapdown inertial systems and computational elements. The fifth paper focuses on INS/GPS integration architectures including "loosely coupled", "tightly coupled", and "deeply integrated" configurations. The advantages and disadvantages of each level of integration are discussed. In the sixth and final paper of the first day, the three major INS/GPS systems architectures discussed in the previous paper will have their performance compared for various mission scenarios.

The second day of the Lecture Series focus on sensors and applications. The first paper discusses MEMS. The specific advantage of MEMS in ruggedness and size is demonstrated with reference to specific applications, such as guided munitions. The second paper provides details of a silicon vibrating structure gyro. Information is presented on the basic design of the silicon ring based structure and details of the gyro characteristics and performance are also provided. The third paper gives an overview of the French MEMS expertise from R&D to products within the European context. The fourth paper gives a systems application based on a silicon gyro based inertial measurement unit developed and tested for a number of munitions and missile programmes which all require operation under high dynamic range and high roll rate conditions. The fifth and final paper on the second day explains the main aspects of fiber optic gyros and of MEMS accelerometers. Examples for different inertial system architectures based upon these sensors are given and their special advantages are discussed.

Les avancées en matière de capteurs de navigation et de technologies d'intégration

(RTO-EN-SET-064)

Synthèse

Les deux journées de ce cycle de conférences ont pour objectif de présenter l'état actuel des connaissances dans le domaine des capteurs de navigation inertiels et des technologies de l'intégration des systèmes, en accordant une attention particulière à la mise en œuvre de technologies de capteurs de navigation avancées et de coût modique. Les conférenciers donneront un aperçu des défis qui sont à relever par les concepteurs de systèmes d'aujourd'hui. Ce cycle de conférences permettra d'informer les spécialistes techniques des pays membres de l'OTAN des derniers développements en ce qui concerne les capteurs et les techniques d'intégration, tels que réalisés par les meilleurs experts du domaine. La première journée prend la forme d'un cours destiné à informer les participants des dernières pratiques. La deuxième journée est axée sur les capteurs et les applications.

La première journée débute par une présentation de synthèse sur la précision, ainsi que sur d'autres tendances technologiques actuelles pour les capteurs inertiels, les systèmes de positionnement global (GPS) et les systèmes de navigation inertiels intégrés (INS/GPS), qui permettront d'obtenir une précision supérieure à 1m. Cette communication donne l'orientation pour les présentations qui suivent. La deuxième communication commence par un bref aperçu de la télédétection inertielle ainsi que des tendances technologiques actuelles. Des discussions sont présentées sur le développement des technologies des gyroscopes et des accéléromètres, l'accent étant mis en particulier sur les réalisations et les performances des capteurs MEMS. La troisième communication présente un tour d'horizon des principaux éléments informatiques associés aux centrales inertielles liées. La quatrième communication donne un aperçu de diverses techniques d'analyse associées aux centrales inertielles liées et aux éléments informatiques. La cinquième communication concerne les architectures d'intégration INS/GPS y compris les configurations « faiblement couplées », « fortement couplées » et « totalement intégrées ».Les avantages et les désavantages de chaque niveau d'intégration sont discutés. La sixième et dernière communication de la première journée fait la comparaison des trois principales architectures systèmes examinées lors de la présentation précédente, pour différents scénarios opérationnels.

La deuxième journée du Cycle de conférences porte sur les capteurs et les applications. La première communication examine les MEMS. Les avantages apportés par les MEMS du point de vue de leur robustesse et de leur faible encombrement La deuxième communication décrit un gyroscope à structure vibrante en silicone. Des informations sont présentées sur la conception de base de la structure à base d'anneau en silicone, ainsi que sur les caractéristiques et les performances du gyroscope. La troisième communication présente un aperçu des connaissances françaises en matière de MEMS, allant de la R&D jusqu'aux produits finis, dans le contexte de l'Europe. La quatrième communication décrit une application systèmes basée sur une centrale inertielle à gyroscope silicone développée et testée dans le cadre d'un certain nombre de programmes de munitions et de missiles, exploités dans des conditions de grande dynamique et de grande vitesse angulaire de roulis. La cinquième et dernière communication expose les principaux aspects des gyroscopes à fibres optiques et des accéléromètres MEMS. Des exemples sont donnés de différents architectures de systèmes inertiels basés sur ces capteurs et leurs avantages particuliers sont discutés.

Table of Contents

	Page
Executive Summary	**iii**
Synthèse	**iv**
Sensors and Electronics Technology Panel	**vi**

	Reference
INS/GPS Technology Trends by G.T. Schmidt	**1**
Inertial Navigation Sensors by N.M. Barbour	**2**
Strapdown System Computational Elements by P.G. Savage	**3**
Strapdown System Performance Analysis by P.G. Savage	**4**
INS/GPS Integration Architectures by G.T. Schmidt and R.E. Phillips	**5**
INS/GPS Integration Architecture Performance Comparisons by G.T. Schmidt and R.E. Phillips	**6**
Inertial MEMS System Applications by N.M. Barbour, R. Anderson, J. Connelly, D. Hanson, A. Kourepenis, J. Sitomer and P. Ward	**7**
Characteristics and Overview of a Silicon Vibrating Structure Gyroscope by J.R. Fountain	**8**
MEMS in FRANCE – An Overview of Trends and Products for Aeronautic and Defense Applications by G. Menozzi and E. Pleska	**9**
Silicon IMU for Missile and Munitions Applications by J.R. Fountain	**10**
Fiber Optic Gyro Systems and MEMS Accelerometer by G.E. Handrich	**11**

Sensors and Electronics Technology Panel

CHAIRMAN

Dr. D. FAUBERT
Director General
DRDC
Val Cartier, Quebec G3J 1X5
CANADA

DEPUTY CHAIRMAN

Professor M. TACKE
FGAN-FOM
Gutleuthausstr. 1
76275 Ettlingen
GERMANY

List of Authors/Lecturers

Lecture Series Director: Dr. George T. SCHMIDT
The Charles Stark Draper Laboratory, Inc.

SPEAKERS

Dr. Neil M. BARBOUR
The Charles Stark Draper Laboratory, Inc.

Dr J. Richard FOUNTAIN
BAE SYSTEMS

Dr. Gottfried Eberhard HANDRICH
LITEF GmbH

Mr Gaëtan MENOZZI
MEMSCAP S.A.

Mr. Paul G. SAVAGE
Strapdown Associates, Inc.

CO-AUTHORS

Mr. Richard E. PHILLIPS
The Charles Stark Draper Laboratory, Inc.

Mr. Eric PLESKA
DGA-STTC

PANEL EXECUTIVE

Lt. Colonel G. FIAMINGO (ITAF)
e-mail: fiamingog@rta.nato.int

From Europe:

RTA-OTAN
Attn: SET Executive
BP 25
F-92201 Neuilly-sur-Seine Cedex
FRANCE

From the USA or CANADA:

RTA-NATO
Attn: SET Executive
PSC 116
APO AE 09777

INS/GPS Technology Trends

George T. Schmidt
The Charles Stark Draper Laboratory, Inc.
555 Technology Square, MS 57
Cambridge, Massachusetts 02139-3563

Abstract
This paper focuses on accuracy and other technology trends for inertial sensors, Global Positioning Systems (GPS), and integrated Inertial Navigation System (INS)/GPS systems, including considerations of interference, that will lead to better than 1-m accuracy navigation systems of the future. For inertial sensors, trend-setting sensor technologies will be described. A vision of the inertial sensor instrument field and inertial systems for the future is given. Planned accuracy improvements for GPS are described. The trend toward deeply integrated INS/GPS is described, and the synergistic benefits are explored. Some examples of the effects of interference are described, and expected technology trends to improve system robustness are presented.

1.0 Introduction
During the last 60 years, INSs have progressed from the crude electromechanical devices that guided the early V-2 rockets to the current solid-state devices that are in many modern vehicles. The impetus for this significant progress came during the ballistic missile programs of the 1960s, in which the need for high accuracy at ranges of thousands of kilometers using autonomous navigation systems was apparent. By "autonomous" it is meant that no man-made signals from outside the vehicle are required to perform navigation. If no external man-made signals are required, then an enemy cannot jam them.

One of the early leaders in inertial navigation was the Massachusetts Institute of Technology (MIT) Instrumentation Laboratory (now Draper Laboratory), which was asked by the Air Force to develop inertial systems for the Thor and Titan missiles and by the Navy to develop an inertial system for the Polaris missile. This request was made after the Laboratory had demonstrated in 1953 the feasibility of autonomous all-inertial navigation for aircraft in a series of flight tests with a system called SPIRE (Space Inertial Reference Equipment), Figure 1. This system was 5 ft in diameter and weighed 2700 lb. The notable success of those early programs led to further application in aircraft, ships, missiles, and spacecraft such that inertial systems are now almost standard equipment in military and civilian navigation applications.



Figure 1. SPIRE system.

Inertial navigation systems do not indicate position perfectly because of errors in components (the gyroscopes and accelerometers) and errors in the model of the gravity field that the INS implements. Those errors cause the error in indicated position to grow with time. The best autonomous military aircraft INS have errors that grow at the rate of about 500 m/h. For vehicles with short flight times, such errors might be

acceptable. For longer-duration missions, it is usually necessary to provide periodic measurements to the navigation system such that the errors caused by the inertial system are reset as close to zero as possible. Because GPS offers world-wide, highly accurate navigation information at very low cost, it has rapidly become the primary aid to be used in updating inertial systems, at the penalty of using an aid that is vulnerable to interference. Clearly, the ideal situation would be low-cost but highly accurate INS that can do all, or almost all, of the mission without using GPS.

The military has access to a current specified accuracy of 21 m (95-percent probability) from the GPS Precise Positioning Service (PPS). This capability provides impressive worldwide navigation performance, especially when multiple GPS measurements are combined in a Kalman filter to update an INS on a military platform or a weapon. The Kalman filter provides an opportunity to calibrate some of the GPS errors, such as satellite clock and ephemeris errors, as well as several of the inertial system errors, and when properly implemented, Circular Error Probables (CEPs) better than 8 m have been observed. In the near term, accuracies in the integrated navigation solution will improve, first to the 3-m level, and then to the 1-m level or better. These accuracies will need to be available in the face of intentional interference of GPS, and the inertial system will provide autonomous navigation information during periods of GPS outage.

The following sections describe:

- The expected technology trends for inertial sensors and systems that can support autonomous operation at low cost. Expectations are for INS/GPS systems that are smaller than 3 in^3 and weigh less than a pound, and cost under $1000.
- Expected accuracy improvements and implementations for satellite navigation.
- Issues and benefits of INS/GPS integration, particularly in an environment with interference.

The combination of a robust, antijam GPS receiver and an accurate, low-cost inertial system will provide the global precision navigation system of the future. Figure 2 depicts the “roadmap” to meeting this objective.

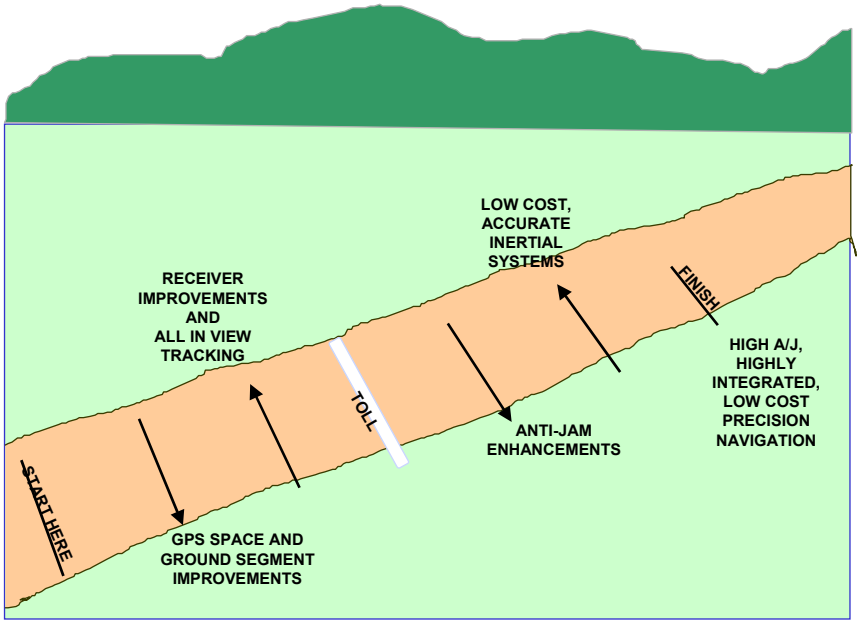


Figure 2. Roadmap to precision navigation for multiple applications.

2.0 Inertial Sensor Trends

The major error sources in the inertial navigation system are due to gyro and accelerometer inertial sensor imperfections, incorrect navigation system initialization, and imperfections in the gravity model used in the computations. But, in nearly all inertial navigation systems, the largest errors are due to the inertial sensors.

Whether the inertial sensor error is caused by internal mechanical imperfections, electronics errors, or other sources, the effect is to cause errors in the indicated outputs of these devices. For the gyros, the major errors are in measuring angular rates. For the accelerometers, the major errors are in measuring acceleration. For both instruments, the largest errors are usually a bias instability (measured in deg/h for gyro bias drift, or micro g (μg) for the accelerometer bias), and scale-factor stability (which is usually measured in parts per million (ppm) of the sensed inertial quantity). The smaller the inertial sensor errors, the better the quality of the instruments, the improved accuracy of the resulting navigation solution, and the higher the cost of the system. As a "rule-of-thumb," an inertial navigation system equipped with gyros whose bias stability is 0.01 deg/h will see its navigation error grow at a rate of 1 nmi/h of operation. The navigation performance requirements placed on the navigation system lead directly to the selection of specific inertial instruments in order to meet the mission requirements.

Figure 3, "Current Gyro Technology Applications," gives a comprehensive view of the gyro bias and scale-factor stability requirements for various mission applications and what type of gyro is likely to be used in current applications (see Ref. [1]).

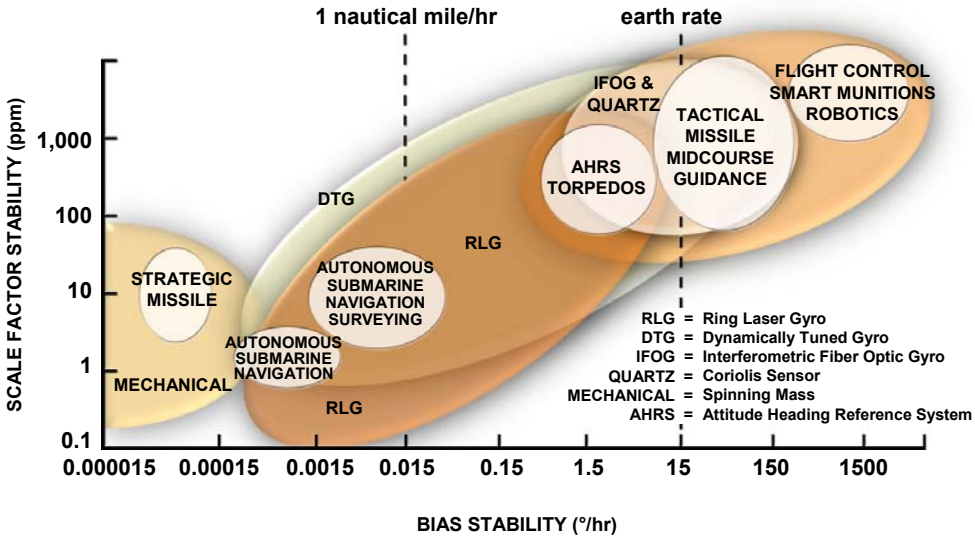


Figure 3. Current gyro technology applications.

Solid-state inertial sensors, such as Microelectromechanical System (MEMS) devices, have potentially significant cost, size, and weight advantages, which has resulted in a proliferation of the applications where such devices can be used in systems. While there are many conventional military applications, there are also many newer applications that will emerge with the low cost and very small size inherent in such sensors, particularly at the lower performance end of the spectrum. A vision of the gyro inertial instrument field for relevant military applications for the near-term (5 to 10 years) is shown in Figure 4.

The MEMS and Interferometric Fiber-Optic (IFOG) technologies are expected to replace many of the current systems using Ring Laser Gyros (RLGs) and mechanical instruments. However, one particular area where the RLG is expected to retain its superiority over the IFOG is in applications requiring extremely high scale-factor stability. The change to all-MEMS technology hinges primarily on MEMS gyro development. The performance of MEMS instruments is continually improving, and they are currently being developed for many applications. It is possible that by the year 2010, there will be a MEMS INS of 2 in^3 with navigation-grade performance of 0.01 deg/h. The cost could possibly be $1000, compared with an IFOG system of

$15,000 to $20,000. This low cost can only be attained by leveraging off the consumer industry, which will provide the infrastructure for supplying the MEMS sensors in extremely large quantities (millions). The use of these techniques will result in low-cost, high-reliability, small-size, and lightweight inertial sensors and the systems into which they are integrated.

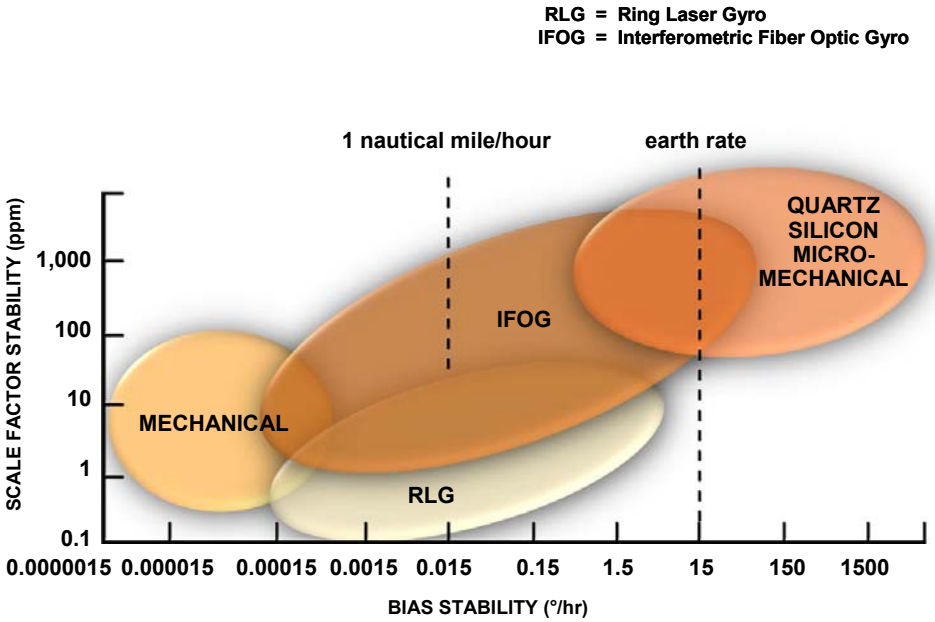


Figure 4. Near-term gyro technology applications.

The tactical (lower) performance end of the application spectrum will likely be dominated by micromechanical inertial sensors. The military market will push the development of these sensors for applications such as "competent" and "smart" munitions, aircraft and missile autopilots, short-time-of-flight tactical missile guidance, fire control systems, radar antenna motion compensation, "smart skins" using embedded inertial sensors, multiple intelligent small projectiles such as flechettes or even "bullets," and wafer-scale INS/GPS systems.

Figure 5 shows how the gyro technology may be applied to new applications in the far term, somewhere around 2020. The figure shows that the MEMS and micro-opto-electromechanical systems (MOEMS) technology will dominate the entire low- and medium-performance range. The rationale behind this projection is based on two premises. The first is that gains in performance in the MEMS devices will continue with similar progression to the dramatic 3 to 4 orders-of-magnitude improvement that has already been accomplished in the last decade. That further improvements are likely is not unreasonable since the designers are beginning to understand the effects of geometry, size, electronics, and packaging on performance and reliability. Second, efforts are already underway to put all six sensors on one (or two) chips, which is the only way to reach the desired cost goal of less than $1000 per INS/GPS system. In addition, since many of the MEMS devices are vibrating structures with a capacitive readout, this may restrict the performance gains. It is in this area that the MOEMS technology is most likely to be required to provide a true solid-state micromechanical gyro with optical readout. At this time, the technology to make a very small, accurate MOEMS gyro does not exist, but advances such as resonant microspheres are already under development in the communications industry. For the strategic application, the IFOG could become the dominant gyro. Work is underway now to develop radiation-hard IFOGs as well as super-high-performance IFOGs.

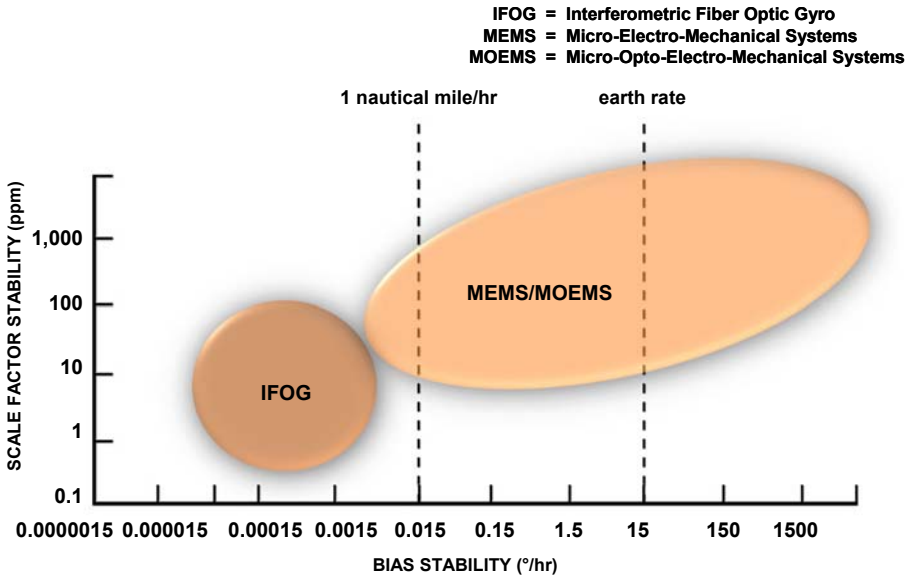


Figure 5. Far-term gyro technology applications.

Figure 6, "Current Accelerometer Technology Applications," gives a comprehensive view of the accelerometer bias and scale-factor stability requirements for various mission applications and what type of accelerometer is likely to be used in current applications. "Mechanical Instruments" refers to the use of a Pendulous Integrating Gyro Assembly (PIGA) which is a mass unbalanced spinning gyroscope used to measure specific force.

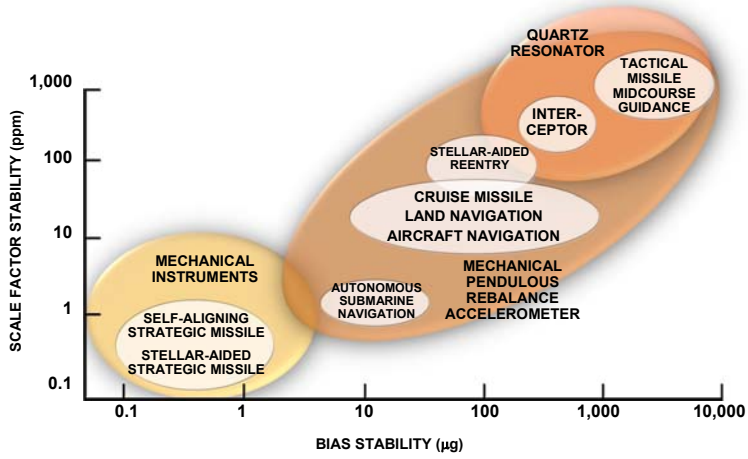


Figure 6. Current accelerometer technology applications.

Current applications are still dominated by electromechanical sensors, not only because they are generally low-cost for the performance required, but also because no challenging alternative technology has succeeded, except for quartz resonators, which are used in the lower-grade tactical and commercial applications. MEMS inertial sensors have not yet seriously broached the market, although they are on the verge of so doing, especially in consumer applications.

In the near-term (Figure 7), it is expected that the tactical (lower) performance end of the accelerometer application spectrum will be dominated by micromechanical accelerometers. As in the case for gyros, the military market will push the development of these sensors for applications such as "competent" and "smart"

munitions, aircraft and missile autopilots, short-time-of-flight tactical missile guidance, fire control systems, radar antenna motion compensation, "smart skins" using embedded inertial sensors, multiple intelligent small projectiles such as flechettes or even "bullets," and wafer-scale INS/GPS systems. Higher performance applications will continue to use mechanical accelerometers and possibly resonant accelerometers based on quartz or silicon. Quartz resonant accelerometers have proliferated widely into tactical and commercial (e.g., factory automation) applications. Silicon micromechanical resonator accelerometers are also being developed. Both of these technologies have possible performance improvements.

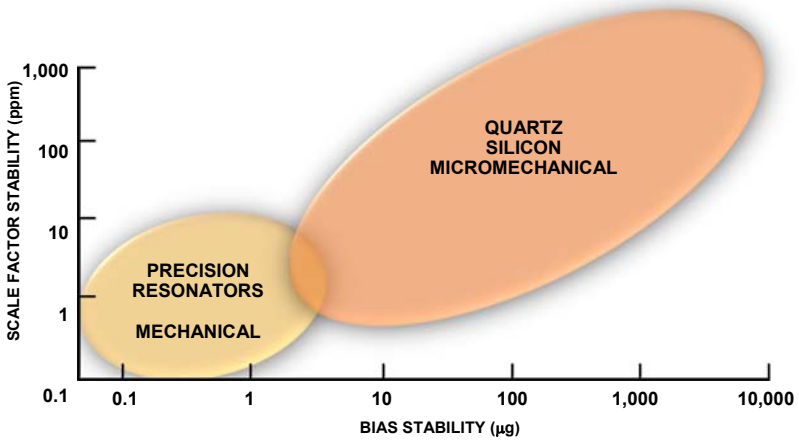


Figure 7. Near-term accelerometer technology applications.

Figure 8 shows how the accelerometer technology may be applied to new applications in the far term. As in the case of gyro projections for the future, the figure shows that the MEMS and MOEMS technology will dominate the entire low- and medium-performance range. The rationale behind this projection is based on exactly the same two premises as for the gyros. However, it is likely that the far-term accelerometer technology projections will be realized years sooner than the gyro.

Figure 9 shows INS or INS/GPS system cost as a function of inertial instrument technology and performance. The cost of a GPS receiver is likely to be so small that it will be insignificant. The systems are classified as: laser gyro or IFOG systems containing various types of accelerometer technologies; quartz systems with both quartz gyros and quartz accelerometers; and MEMS/ MOEMS systems, which are all silicon. The solid line indicates the range of approximate costs expected. Clearly, the quantity of systems produced affects the cost; large production quantities would be at the lower end of the cost range. The IFOG systems have the potential for lower cost than laser gyro systems because the IFOG should be well below the cost of an RLG. However, this has not happened to date, primarily because the RLG is in relatively large-volume production in well-facilitated factories and the IFOG is not yet manufactured in similar production quantities. Clearly, the MEMS/MOEMS INS/GPS systems offer the lowest cost. The ultimate low cost only becomes feasible in quantities of millions. This can be achieved only with multi-axis instrument clusters and on-chip or adjacent-chip electronics and batch packaging.

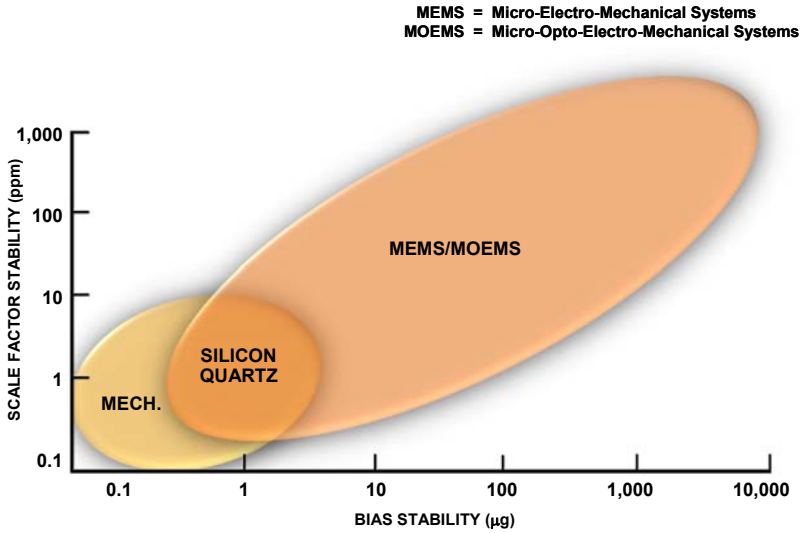


Figure 8. Far-term accelerometer technology applications.

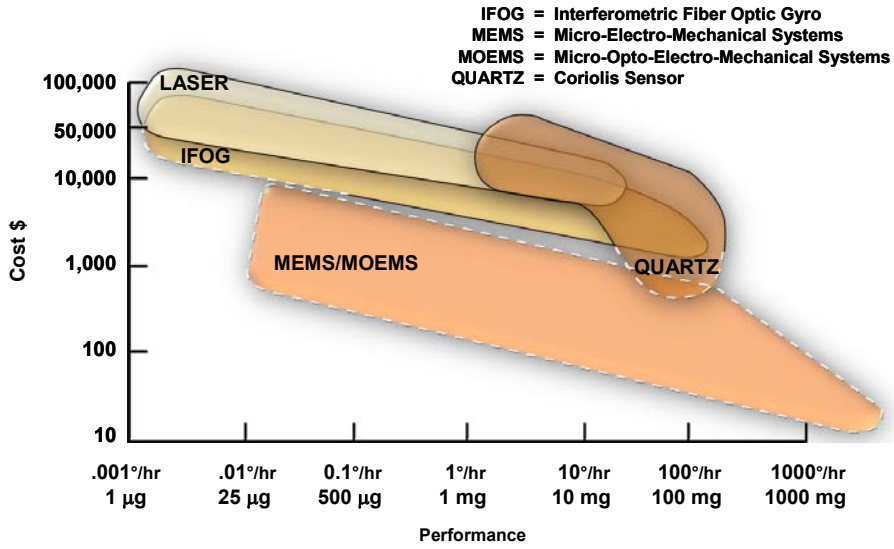


Figure 9. INS cost as a function of instrument technology.

The ability of silicon-based MEMS devices to withstand high "g" forces has been demonstrated recently in a series of firings in artillery shells where the g forces reached over 6500 g. These small MEMS-based systems, illustrated in Figure 10, have provided proof-of-principal that highly integrated INS/GPS systems can be developed and has led to further programs where the goal is a system on the order of 3 in^3, or 2 in^3 for the INS alone (Ref. [2]). This volume compares with current RLG systems of about 600 in^3 and IFOG systems with a volume of about 100 in^3. These systems also represent 4 orders of magnitude improvement in weight and volume over SPIRE. If micromechanical instrument performance improvements continue, they will come to dominate the entire inertial instrument application spectrum.

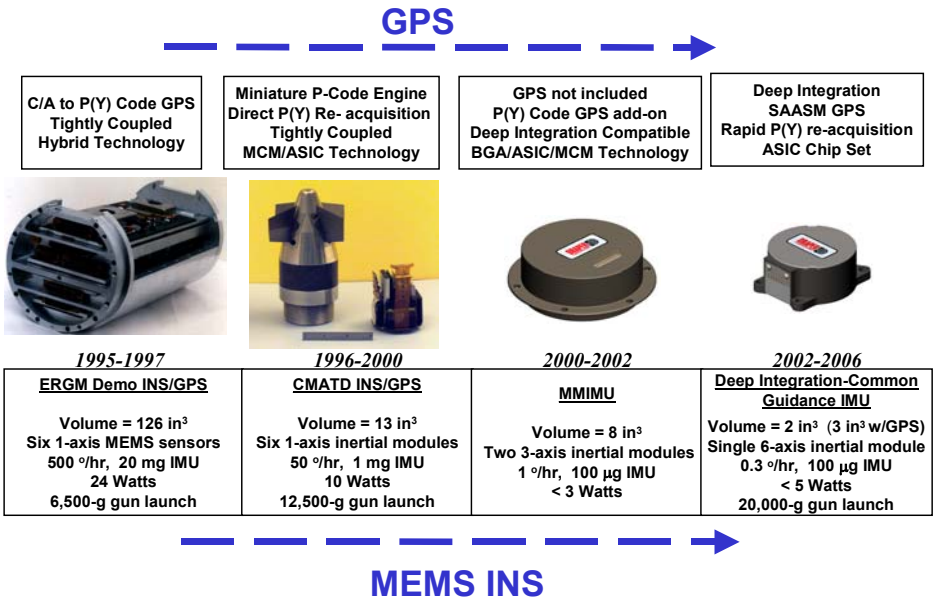


Figure 10. INS/GPS guidance system evolution.

3.0 GPS Accuracy and Other Improvements

The accuracy specification that is currently applicable to the GPS results in a precise positioning (PPS) of a GPS receiver operating with the military P(Y) code of approximately 10 m (CEP) in the WGS-84 coordinate system. Recent advances and planned programs to improve GPS accuracy and new approaches on how to use GPS in relative or differential modes (Ref. [3]) have all contributed to the real possibility of developing a 3-m CEP system in the near term and, possibly, systems with smaller than 1-m CEP in the far term. This section will discuss these items.

The accuracy of the GPS PPS provides impressive navigation performance, especially when multiple GPS measurements are combined in a Kalman filter to update an INS. The Kalman filter provides an opportunity to calibrate the GPS errors, as well as the inertial errors, and when properly implemented, CEPs better than either system are achievable.

In assessing GPS accuracy, the largest error sources today are in the space and control segment. The space segment dominant errors are: ionospheric errors, tropospheric errors, satellite clock errors, and satellite ephemeris. The ionospheric errors can be reduced by using a two-frequency receiver (L_1 and L_2) and tropospheric errors can be reduced by using a deterministic compensation model. Table 1 gives a typical absolute GPS error budget (Ref. [4], p. 105).

Horizontal Dilution of Precision (HDOP) is a geometrical factor that is a function of the geometry between the GPS receiver and the tracked satellites. For tracking four satellites, HDOP is typically 1.5. Then with a user equivalent range error (UERE) of 3.8m, and applying the approximate formula, CEP = (0.83)(HDOP)(UERE), the resulting CEP is 4.7 m.

Table 1. "Typical" absolute GPS error budget.

GPS Noise-Like Range Errors	1σ Values (m)
Multipath	0.6
Receiver noise	0.3
RMS noise-like error	0.7
GPS Bias-Like Range Errors	**1σ Values (m)**
Satellite ephemeris	1.4
Satellite clock	3.4
Atmospheric residual	0.2
RMS bias-like error	3.7
User equivalent range error (UERE) = $(0.7^2 + 3.7^2)^{1/2}$=3.8m	
CEP = (0.83) (UERE) (HDOP) = 4.7m if HDOP = 1.5	

In the near future, improvements are contemplated to clock and ephemeris accuracy (Ref. [4], p. 102 and Ref. [5]). In this later phase, the data from five or more National Imagery and Mapping Agency (NIMA) GPS monitoring sites will be integrated with data from the existing Air Force monitoring sites in the operational control segment. By including additional data from the NIMA sites, which are located at higher latitudes than the Air Force sites, an additional 15-percent improvement in combined clock and ephemeris accuracy could be anticipated. Improvements to the Kalman filter that is used in the ground control segment to process all the satellite tracking information can be expected to further reduce the errors by 15 percent. In addition, by incorporating more dynamical models in the filter, another 5-percent improvement may be anticipated. Table 2 summarizes these improvements (Ref. [4], p. 102).

Table 2. Reduction of combined clock and ephemeris errors.

Enhancement	Anticipated Combined Clock and Ephemeris Error Improvement over Existing Combined Error of 3.7 m (1σ)
Correction Updates (50% reduction)	1.8 m
Additional Monitor Stations (additional 15% reduction)	1.5 m
Non partitioned Kalman Filter (additional 15% reduction)	1.3 m
Improved Dynamic Model (additional 5% reduction)	1.2 m

Thus, a ranging error on the order of 1.4 m is a reasonable possibility with the atmospheric residual unchanged. With all-in-view tracking (HDOP approximately 1.0), CEPs on the order of 1 m appear quite possible in the near term. CEP=(0.83) (1.0) (1.4) = 1.1 m. If then, multiple GPS measurements are combined with an inertial system and Kalman Filter, better than 1 m accuracy should result.

To illustrate the benefits of the various GPS improvements, a simulation was conducted with an error model for a typical INS whose errors would result in 1.0 nmi/h error growth rate without GPS aiding. After 30 minutes of air vehicle flight, with all of the GPS accuracy improvements included, less than 1 meter CEP is obtained as shown in Table 3.

Table 3. Tightly coupled INS/GPS System-Air Vehicle Trajectory (@30 min).

CLOCK AND EPHEMERIS ERROR (1σ) ALL IN VIEW TRACKING	CEP (m) 8 SATELLITES
Current Model – 3.7 m	2.97 m
Correction Updates – 1.8 m	1.46 m
Additional Monitor Stations – 1.5 m	1.22 m
Non -partitioned Kalman Filter – 1.3 m	1.06 m
Improved Dynamic Model – 1.2 m	0.98 m

Another significant improvement in GPS for military systems will be the introduction of the M-code, which is designed to be more secure and have better jamming resistance than the current Y code (Ref. [6]). The system is being designed such that a higher power signal (+20 dB over current signal levels) will be available for localized coverage over an area of operations to boost signal jamming resistance. This significant improvement (M-code spot beam) is scheduled for the GPS-III phase of the GPS modernization process (circa 2016).

4.0 INS/GPS Integration

Many military inertial navigation systems could be replaced with less accurate inertial systems if it were guaranteed that GPS would be continuously available to update the inertial system to limit its error growth. A less accurate inertial system usually means a less costly system. However, given the uncertainty in the continuous availability of GPS in most military scenarios, an alternate way to reduce the avionics system cost is to attack the cost issue directly by developing lower-cost inertial sensors while improving their accuracy and low noise levels, as described in the "Inertial Sensor Trends" section. For applications without an interference threat, in the future, GPS updating is expected to provide better than 1-m navigation accuracy (CEP) when used in conjunction with an INS. The benefits and issues in using INS augmented with GPS updates, including a discussion of interference issues, have been presented in many references. Systems currently in use tend to be classified as either "the loosely coupled approach" or "the tightly coupled approach" (Figures 11 and 12 and Ref. [7]).

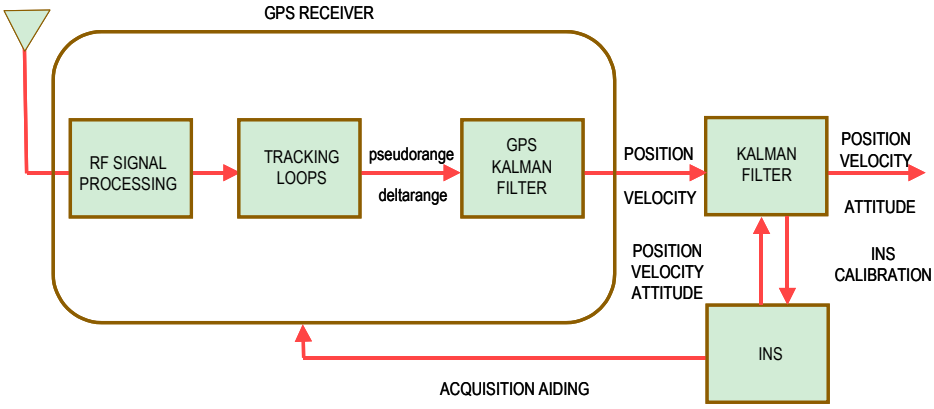


Figure 11. Loosely coupled approach.

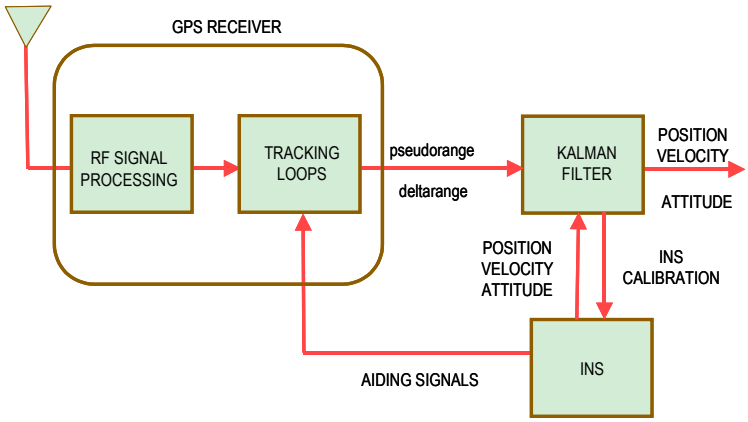


Figure 12. Tightly coupled approach.

The most recent research activity is a different approach called “deeply integrated” (Figure 13, Ref. [8]). In this approach, the problem is formulated directly as a navigation problem in which the optimum (minimum-variance) solution is sought for each component of the multidimensional navigation state vector. By formulating the problem in this manner, the navigation algorithms are derived directly from the assumed dynamical models, measurement models, and noise models. The solutions that are obtained are not based on the usual notions of tracking loops and operational modes (e.g., State 3, State 5, etc.). Rather, the solution employs a nonlinear filter that operates efficiently at all jammer/signal (J/S) levels and is a significant departure from traditional extended Kalman filter designs. The navigator includes adaptive algorithms for estimating postcorrelation signal and noise power using the full correlator bank. Filter gains continuously adapt to changes in the J/S environment, and the error covariance propagation is driven directly by measurements to enhance robustness under high jamming conditions.

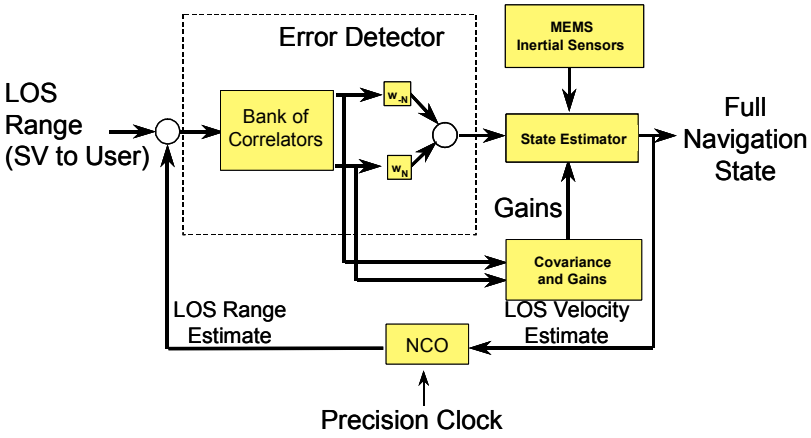


Figure 13. INS/GPS deep integration.

In this system, individual satellite phase detectors and tracking loop filters are eliminated. Measurements from all available satellites are processed sequentially and independently, and correlation among the line-of-sight distances to all satellites in view are fully accounted for. This minimizes problems associated with unmodeled satellite signal or ephemeris variations and allows for full Receiver Autonomous Integrity Monitoring (RAIM) capability.

Extended-range correlation may be included optionally to increase the code tracking loss-of-lock threshold under high jamming and high dynamic scenarios. If excessively high jamming levels are encountered (e.g., beyond 80 dB J/S at the receiver input for P(Y) code tracking), the GPS measurements may become so noisy that optimal weights given to the GPS measurements become negligible. In this situation, navigation error behavior is essentially governed by current velocity errors and the characteristics of any additional navigation sensors that are employed, such as an INS. Code tracking is maintained as long as the line-of-sight delay error remains within the maximum allowed by the correlator bank. If there is a subsequent reduction in J/S so that the optimal weights become significant, optimum code tracking performance is maintained without the need for reacquisition. Detector shapes for each correlator depend on the correlator lag and rms line-of-sight delay error.

Experiments have shown an improvement in code tracking of about 15 to 20 dB in wideband A/J capability for this architecture. Given that the implementation is done in software, it would be expect to be used in many future INS/GPS implementations.

5.0 INS/GPS Interference Issues

Interference to the reception of GPS signals can be due to many causes such as telecommunication devices, local interference from signals or oscillators on the same platform, or possibly radar signals in nearby frequency bands. Attenuation of the GPS signal can be caused by trees, buildings, or antenna orientation, and result in reduced signal/noise ratio even without interference. This loss of signal can result in an increase in effective jammer/signal (J/S) level even without intentional jamming or interference. The power of the GPS signals at the surface of the Earth is about 10^{-16} W, a level easily overcome by a jammer source.

Military receivers are at risk due to intentional jamming. Jammers as small as 1 W located at 100 km from the receiver can possibly prevent a military receiver from acquiring the satellite signals and “locking-on” to C/A code. Representative jammers are shown in Figure 14. Larger jammers are good targets to find and to attack because of their large radiation. Smaller jammers, which are hard to find, need to be defended against by improved anti-jam (A/J) technologies within the receiver, improved antennas, or by integration with an inertial navigation system. Proponents of high-accuracy inertial systems will generally argue that a high anti-jam GPS receiver is not required, while receiver proponents will argue that using a higher A/J receiver will substantially reduce inertial system accuracy requirements and cost. Both arguments depend entirely on the usually ill-defined mission and jamming scenario.

What has generally become accepted is that the GPS is remarkably vulnerable to jamming during the C/A code acquisition phase where conventional receiver technology has only limited jammer tolerability (J/S - 27 dB) (Refs. [9], [10], [11]). A 1-W (ERP) jammer located at 100 km from the GPS antenna terminals could prevent acquisition of the C/A code. Figure 15 is very useful in determining trade-offs between required A/J margin and jammer power. A 1-W jammer is "cheap" and potentially the size of a hockey puck. Furthermore, the C/A code can be spoofed by an even smaller power jammer. So generally, a GPS receiver cannot be expected to acquire the C/A code in a hostile environment.

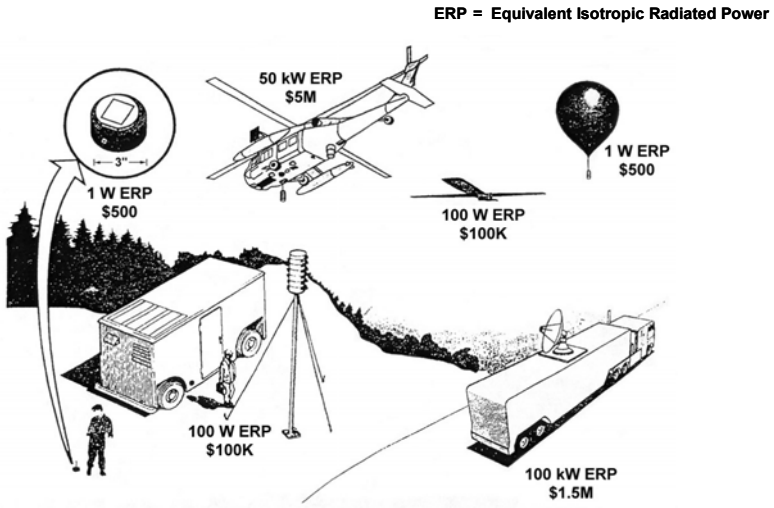


Figure 14. Jammer possibilities.

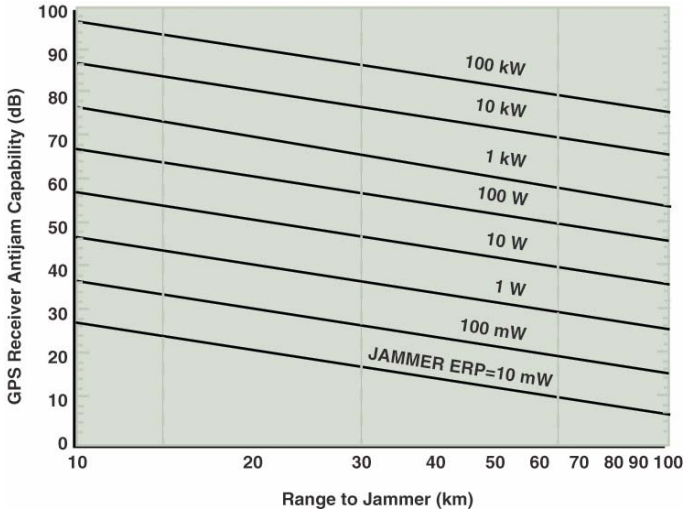


Figure 15. GPS jamming calculations.

For long-range cruise missile type applications, the C/A code could be acquired outside hostile territory and then the receiver would transition to P(Y) code lock, which has a higher level of jamming immunity. A 1-kW (ERP) jammer at about 100 km would now be required to break inertially-aided receiver code lock at 54 to 57 dB. As the weapon approaches the jammer, jammer power levels of about 10 W would be effective in breaking P(Y) code lock at 10 km (see Figure 16).

As previously mentioned, the "deeply integrated" architecture for combining INS and GPS may allow for tracking GPS satellites up to 70 – 75 dB J/S, an improvement of 15 to 20 dB above conventional P(Y) code tracking of 54 to 57 dB. If future increases of 20 dB in broadcast satellite power using the M-code spot beam (M spot) are also achieved, nearly 40 dB of additional performance margin would be achieved, so a jammer of nearly 100 kW would be required to break lock at 10 km.

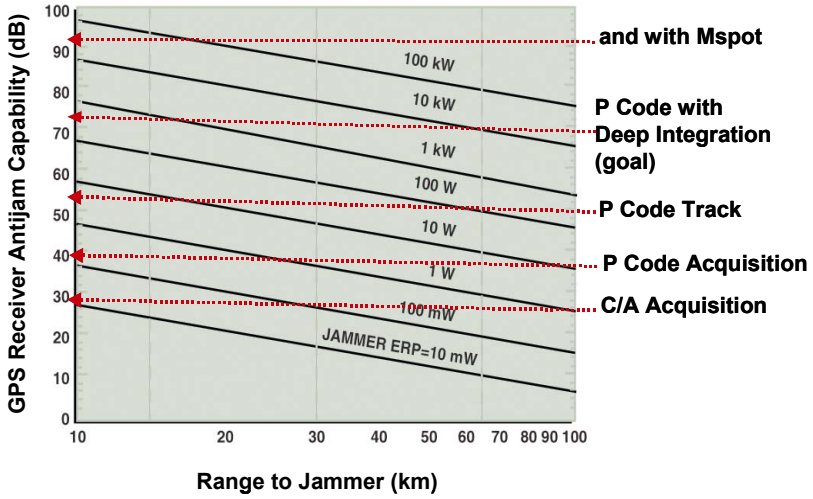


Figure 16. Possible A/J capabilities.

Furthermore, new receiver technology with advanced algorithms and space-time adaptive or nulling antenna technologies might also be incorporated into the system, further increasing its A/J capability significantly above 100 dB. If A/J performance is increased significantly, then the jammer power must also be increased significantly. A large jammer would present an inviting target to an antiradiation, homing missile. In the terminal area of flight against a target, the jammer located at the target will eventually jam the receiver, and the vehicle will have to depend on inertial-only guidance or the use of a target sensor. Thus, it is important to ensure that accurate guidance and navigation capability is provided to meet military mission requirements against adversaries who are willing to invest in electronic countermeasures (ECM). This fact is true today and is expected to remain so in the foreseeable future. Figure 17 summarizes electronic counter-countermeasures (ECCM) techniques.

- **Lower Cost, High-Accuracy IMU's**
- **Improve Signals in Space**
  - Increased Accuracy
  - Mcode and Mspot
- **Improved Receivers**
  - Deep Integration With IMU
  - Anti-Spoof Techniques
  - Higher A/J Electronic
- **Direct P (Y) Code Acquisition, Lock-on Before Launch**
  - Improved Aircraft Interface To Munitions
  - Miniature On-board Clock
  - Multiple Correlators
- **Higher Performance, Lower Cost Adaptive Antennas**
  - Digital Beamforming
  - Modern Algorithms

Figure 17. Valuable ECCM technologies and techniques.

6.0 Concluding Remarks

Recent progress in INS/GPS technology has accelerated the potential use of these integrated systems, while awareness has also increased concerning GPS vulnerabilities to interference. In the near future, improvements in accuracy in the broadcast GPS signals will evolve to 1 m. Many uses will be found for this high accuracy. In parallel, lower-cost inertial components will be developed and they will also have improved accuracy. Highly integrated A/J architectures for INS/GPS systems will become common, replacing avionics architectures based on functional black boxes where receivers and inertial systems are treated as stand-alone systems.

For future military and civilian applications, it is expected that the use of INS/GPS systems will proliferate and ultimately result in worldwide navigation accuracy better than 1 m, which will need to be maintained under all conditions. It can be expected that applications such as personal navigation systems, micro air vehicles (MAV), artillery shells, and automobiles will be quite common, see Figure 18. Other applications will certainly include spacecraft, aircraft, missiles, commercial vehicles, and consumer items.



Figure 18. Examples of future applications.

Acknowledgments/Additional References

Thanks to Neil Barbour for assistance with the section on Inertial Sensor Trends. A history of inertial navigation is given in Ref. [12] and a history of the GPS program is given in Ref. [13].

References

[1] Barbour, N. and Schmidt, G., "Inertial Sensor Technology Trends," *IEEE Sensors Journal,* Vol. 1, No. 4, 2001, pp. 332-339.

[2] Anderson, R. et al. "Evolution of Low-Cost MEMS Inertial Systems," NATO RTO Symposium on *Military Capabilities Enabled by Advances in Navigation Sensors,* Istanbul, Turkey, October 2002.

[3] Phillips, R. and Schmidt, G., "Relative and Differential GPS," in NATO AGARD Lecture Series 207, *System Implications and Innovative Applications of Satellite Navigation*, June 1996, pp. 5.1-5.22.

[4] National Research Council, *The Global Positioning System – A Shared National Asset*, National Academy Press, Washington, D.C., 1995.

[5] McDonald, K. and Hegarty, C., "Post-Modernization GPS Performance Capabilities," *ION 56th Annual Meeting*, San Diego, California, June 2000.

[6] Fontana, R. and Latterman, D., "GPS Modernization and the Future," *ION 56th Annual Meeting,* San Diego, CA, June 2000. Also see Aviation Week & Space Technology, September 23,2002, pp. 56-58.

[7] Schmidt, G. and Phillips, R., "INS/GPS Integration Architectures," Draper Laboratory Report, 4104, Cambridge, Massachusetts, February 2003. Also in NATO RTO Lecture Series 232, *Advances in Navigation Sensors and Integration Technology*, October 2003, pp. 5-1 – 5-15.

[8] Gustafson, D. et al., "A Deeply Integrated Adaptive GPS-Based Navigator with Extended Range Code Tracking," *IEEE Plans Conference*, San Diego, CA, March 2000. Also, see U.S. Patent 6,331,835 B1, December 18, 2001.

[9] NAVSTAR-GPS Joint Program Office, *NAVSTAR GPS User Equipment*, February 1991.

[10] Mahmood, S. et al., "Analysis of Differential Global Positioning System (DGPS) Techniques and GPS Jamming on Precision Guided Munition (PGM) Performance," NATO/AGARD MSP Meeting, *Technologies for Precision Air Strike Operations in Rapid Reaction and Localized Conflict Scenarios*, Seville, Spain, October 1995.

[11] Sklar, J., "GPS Capability Projections" in *Defense Science Board 1996 Summer Study Task Force on Tactics and Technology for 21st Century Military Superiority*, Vol. 3, October 1996, III.43-III.53.

[12] Draper, C. S., "Origins of Inertial Navigation," *Journal of Guidance and Control*, Vol. 4, No. 5, 1981, pp. 449-463.

[13] Parkinson, B., "Origins, Evolution, and Future of Satellite Navigation," *Journal of Guidance, Control, and Dynamics*, Vol. 20, No. 1, 1997, pp. 11-25.

Inertial Navigation Sensors

Neil M. Barbour
The Charles Stark Draper Laboratory, Inc.
555 Technology Square
Cambridge, Massachusetts 02139-3563
USA

email: nbarbour@draper.com

ABSTRACT

For many navigation applications, improved accuracy/performance is not necessarily the most important issue, but meeting performance at reduced cost and size is. In particular, small navigation sensor size allows the introduction of guidance, navigation, and control into applications previously considered out of reach (e.g., artillery shells, guided bullets). In recent years, three major technologies have enabled advances in military and commercial capabilities. These are Ring Laser Gyros, Fiber Optic Gyros, and Micro-Electro-Mechanical Systems (MEMS). Technology developments in these fields are described with specific emphasis on MEMS sensor design and performance. Some aspects of performance drivers are mentioned as they relate to specific sensors. Finally, predictions are made of the future applications of the various sensor technologies.

INTRODUCTION

The science of guidance, navigation, and control has been under development for over 100 years. Many exciting developments have taken place in that time, especially in the area of navigation sensors. (Ref. 1, 2, 3) Today, to understand fully the entire range of navigation sensors, one needs to know a wide range of sciences such as mechanical engineering, electronics, electro-optics, and atomic physics. Recently, the development and wide use of GPS has enhanced the role of traditional navigation sensors, and is able to provide quick, inexpensive answers to the basic navigation questions of: (i) where did I start from and where do I want to go, and (ii) where is my position and what is my velocity now with respect to where I started. In fact, many navigation missions can be accomplished with GPS alone, with the inertial sensors used only for stabilization and control. However, the vulnerability of GPS to jamming means that navigation sensors are still required, and also for applications where GPS is unavailable (such as indoors or in tunnels and caves), or cannot be acquired quickly enough (such as very short-time-of-flight munitions). The fact that an inertial (gyroscope or accelerometer) sensor's output drifts over time means that inertial navigation alone has an upper bound to mission accuracy. Therefore, in the absence of GPS, various augmentation sensors are also tied into the inertial systems; e.g., velocity meters, seekers, star trackers, magnetometers, lidar, etc. In nearly all cases, however, these augmentation sensors are not required for an integrated INS/GPS system. The key driver for which systems to use is cost for performance, where cost includes not only purchase but also life cycle cost. Some mission applications are extremely size- and power-restricted, so that not all inertial technologies are competitive.

Sensors are often compared on the basis of certain performance factors, such as bias and scale-factor stability and repeatability or noise (random walk). Sensor selection is made difficult by the fact that many different sensor technologies offer a range of advantages and disadvantages while offering similar performance. Nearly all new applications are strapdown (rather than gimballed) and this places significant performance demands upon the gyroscope (specifically: gyro scale-factor stability, maximum angular rate capability,

minimum g-sensitivity, high BW). For many applications, improved accuracy/performance is not necessarily the driving issue, but meeting performance at reduced cost and size is. In particular, small sensor size allows the introduction of Guidance, Navigation, and Control into applications previously considered out of reach (e.g., artillery shells, 30-mm bullets). Many of these newer applications require production in much larger quantities at much lower cost. This paper discusses various ongoing gyroscope and accelerometer technology developments. Specific emphasis is given to the design and performance of MEMS sensors, which continues to be a very active development area.

In recent years, three major technologies in inertial sensing have enabled advances in military (and commercial) capabilities. These are the Ring Laser Gyro (since ~1975), Fiber Optic Gyros (since ~1985), and MEMS (since ~1995). The Ring Laser Gyro (RLG) moved into a market dominated by spinning mass gyros such as rate gyros, single-degree-of-freedom integrating gyros, and dynamically (or dry) tuned gyros, because it is ideal for strapdown navigation. The RLG was thus an enabling technology for high dynamic environmental military applications. Fiber Optic Gyros (FOGs) were developed primarily as a lower-cost alternative to RLGs, with expectations of leveraging technology advances from the telecommunications industry. FOGs are now beginning to match and even beat RLGs in performance and cost, and are very competitive in many military and commercial applications. However, apart from the potential of reducing the cost, the IFOG did not really enable the emergence of any new military capabilities beyond those already serviced by RLGs. Efforts to reduce size and cost resulted in the development of small-path-length RLGs and short-fiber-length FOGs. These did enable new military capabilities such as guided munitions (e.g., JDAM). MEMS Inertial sensors have the potential to be an extreme enabling technology for new military applications. The small size, extreme ruggedness, and potential for very low-cost means that numerous new applications will be able to incorporate inertial guidance, a situation unthinkable before MEMS.

RING LASER GYROS

Although the RLG was first demonstrated in a square configuration in 1963, it wasn't until the late 1970s and 1980s that RLG systems came into common use as strapdown inertial navigators. The RLG has excellent scale-factor stability and linearity, negligible sensitivity to acceleration, digital output, fast turn-on, excellent stability and repeatability across dormancy, and no moving parts. The RLG's performance is very repeatable under temperature variations so that a temperature compensation algorithm effectively eliminates temperature sensitivity errors. It is superior to spinning mass gyros in strapdown applications, and is an exceptional device for high-dynamic environments.

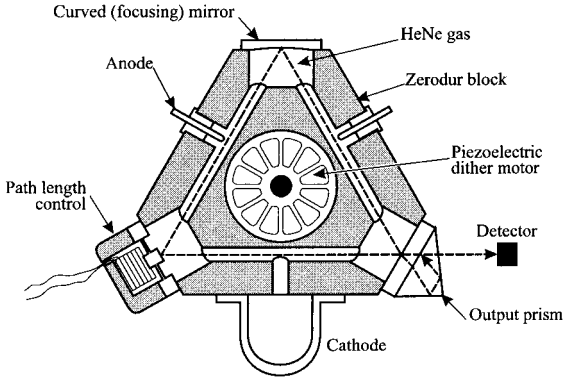


Figure 1: Ring Laser Gyroscope.

(© A. Lawrence, Modern Inertial Technology, Springer-Verlag 1998 used with permission of A. Lawrence)

The operating principles of the RLG are as follows. A low-pressure gas (usually helium-neon) inside the optical cavities lasers when an anode and cathode are excited, launching light waves in a clockwise (CW) and counterclockwise (CCW) direction. Thus the RLG is a laser itself and does not require an external light source. The Sagnac phase shift between the CW and CCW beams impinges on a split photo-detector. The zero crossings generated by the interference pattern moving across the detector, produce a pulse which is assigned to a CW or CCW change. Counting the pulses gives the accumulated angle. Therefore, the RLG is an open-loop integrating gyro. Taking samples over set time periods also provides angular rate information.

Backscatter from the mirrors causes the two counter-propagating waves to lock frequencies at very low input rates, known as lock-in. This can be overcome by introducing a frequency bias by means of a piezo-electric drive which dithers the RLG at several hundred hertz about its input axis. The Honeywell H-764G Embedded GPS/INS, which is based on GG1320 RLGs, is a 1-nautical-mile/hour navigator that has been installed on over 50 different aircraft types. Many ship navigation systems are being replaced with the Honeywell Mk45 RLG navigator.

Northrop Grumman's (Litton's) ZLG™ (Zero-Lock™ Laser Gyro) is a four-mirror device that avoids lock-in by using a Faraday rotator and a bent light path to provide a four-beam multi-oscillator. The ZLG™ is thus two laser gyros in one, sharing identical optical paths which reduces ARW uncertainty. The ZLG™ is used in Northrop Grumman's LN100G navigation system.

Efforts to reduce size and cost resulted in developments of small-path-length RLGs. Honeywell's 1308 and Kearfott's T-10 small-path-length systems have been widely used. As an example, the 1308 RLG system is used in JDAM. Kearfott's MRLG (monolithic RLG) systems comprise three RLGs in one block for size reduction; the T-10 three-axis RLG being approximately the size of a golf ball. An example of further miniaturization is the development of semiconductor ring lasers with a diameter of 3 mm (Ref. 4).

FIBER OPTIC GYROS

Interferometric Fiber Optic Gyro (IFOG)

In the 1970s, development of the Fiber Optic Gyro was started. The motivation was that the FOG was potentially less expensive and easier to build than the RLG, and might be more accurate. In 1976, IFOG feasibility was demonstrated when an interference pattern (Sagnac effect) was discerned from light traveling CW and CCW around an optical fiber at the University of Utah.

The Interferometric Fiber-Optic Gyro (IFOG) defines its light path by a wound coil of optical fibers in place of the RLG's mirrors and optical cavity. The IFOG has an external broadband light source (e.g., super-luminescent diode, doped fiber) that launches light into the fiber coil, which can be from 100m to 3km in length. Light from the optical source passes through a power splitter and into an integrated optics circuit which splits the light into counter-propagating beams and then recombines them after they have traveled through the fiber coil. The recombined beam then retraces its path to the optical detector. The open-loop IFOG is not an integrating gyro like the RLG, and the phase-angle output from the detector is proportional to angular rate. However, the IFOG can be operated as an integrating gyro by the addition of a feedback loop from the detector to a frequency shifter in the integrated optics circuit. The feedback loop shifts the frequency of the light entering the coil so that the detector reads at null. The IFOG is now operating closed-loop and the frequency shift measurement from the feedback loop is directly proportional to angle, provided feedback is at rates faster than the coil transit time.

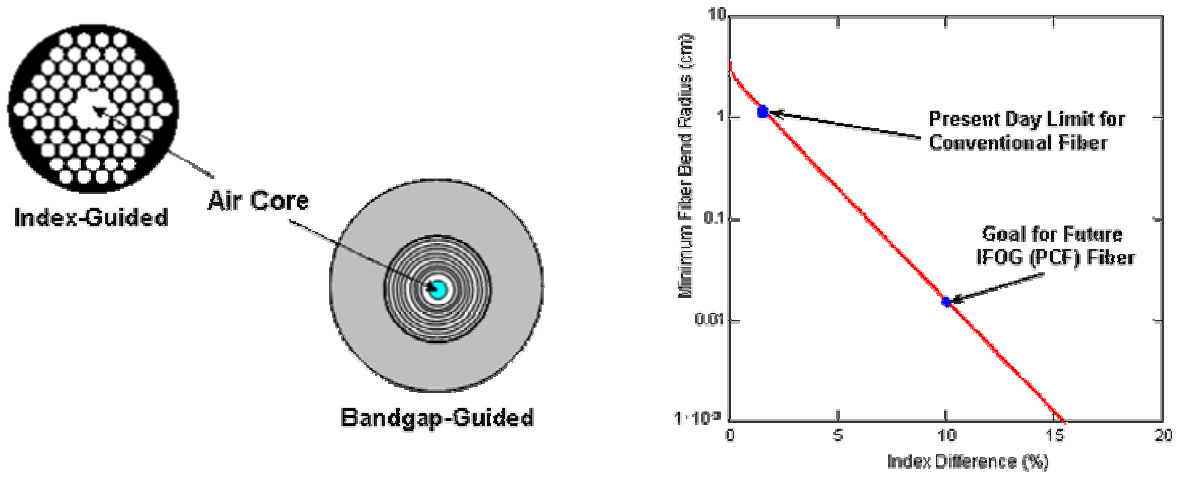
The IFOG has some advantages over the RLG in that: the light source does not require high voltage; the broadband light source prevents backscatter so there is no lock-in at low input rates; it has the potential for lower cost and lighter weight. A unique feature of the IFOG is the ability to scale performance up and down. For example, doubling the coil length will decrease angle random walk by a factor of two. However, unlike the RLG, the open-loop IFOG is limited in dynamic range and only has moderate scale factor stability. Thus, for most applications, closed-loop operation is preferred.

The IFOG has not yet superseded the RLG due partly to the large existing RLG-based industrial infrastructure. However, as costs decrease, IFOGs will further penetrate the market. IFOGs have found applications in lower-performing areas, especially in tactical and commercial applications, such as Unmanned Underwater Vehicles (UUVs) and Unmanned Air Vehicles (UAVs), camera and antenna stabilization, land navigation, AHRS, gyrocompasses, and oil drilling. For example, Northrop Grumman has built more than 24,000 tactical-grade (1 deg/h bias error) fiber gyros. There are numerous manufacturers of short-fiber-length FOGs such as KVH, Honeywell, Northrop Grumman (Litton), LITEF (Germany), Photonetics (France) (Ref. 5), JAE (Japan), etc. The Northrop Grumman LN200 series IMUs may be the most widely known; some of which have silicon accelerometers.

Performance is now comparable to that of the RLG, and over the last few years, it has become apparent that IFOGs can also achieve extremely high performance (<0.0003°/hr bias stability, <0.00008 deg/√hr ARW, and <0.5 ppm scale factor inaccuracy) (Ref. 6) at reasonable cost. This makes IFOGs suitable for precise aiming of telescopes, imaging systems, and antennas, or for strategic-grade navigation of submarines (Ref. 7). Advances in Fiber Optic Gyros development continue to be aimed at cost and size reduction, while maintaining performance. Some of the potentially enabling technologies are presented below.

Photonic Crystal IFOG

Photonic crystal fibers (PCF) (Figure 2[a]) offer the potential to be one of the enabling technologies for the next generation of IFOG instruments. There are two basic categories of PCF: bandgap guided (Bragg fibers, microstructured fibers) and index guided (microstructured fibers). Bragg fibers utilize multilayer interference to produce an omnidirectional mirror effect over a given wavelength band. Index-guided fiber, sometimes referred to as “holey” fiber due to its glass capillary structure, provides tight mode confinement by using a large index contrast (such as at an air/silica interface). Polarization-maintaining versions of holey fiber have demonstrated 10 times the birefringence of silica polarization-maintaining fiber. There are several key advantages of PCFs for IFOG applications: (1) tight mode confinement results in bend losses much lower than conventional fiber (Figure 2[b]); the limit on IFOG coil diameter is primarily due to fiber winding losses and fiber size, (2) cladding diameters less than that for conventional fiber provide the potential for tighter fiber packing, resulting in smaller coils, (3) dispersion compensation can be incorporated into the PCF resulting in less spectral distortion, and (4) light guiding in an air-core photonic bandgap fiber offers the potential utilizing mid-infrared optical wavelengths. The lowest reported losses to date are 13 dB/km for air-core bandgap fiber at 1.5 μm (Corning) and 0.58 dB/km for silica index-guided holey fiber at 1.55 μm. In addition to IFOGs, PCFs have many other applications, including ring laser gyros, broadband optical sources, chem/bio sensing, biomedicine, E-textiles, and telecom devices (WDM, variable optical attenuators, tunable optical filters).



(a) PCF Examples **(b) PCF Bending Limit**

Figure 2: Photonic Crystal Fibers (PCFs).

INTEGRATED OPTIC GYROSCOPES

Integrated Optic Gyros (or optical gyros on a chip) have been a sought-after goal for several years. Currently, the IO gyro is targeted for 0.1 to 1 deg/hr applications met by ring laser gyros and IFOGs. The IOG is an optical waveguide based Sagnac effect gyroscope in which two beams of light travel around a waveguide ring resonator in opposite directions (Figure 3). The relative position of the resonances is a measure of rotation rate about an axis that is perpendicular to the plane of the ring resonator. The IO gyros are fabricated on wafers, combining the capabilities of integrated optic fabrication and MEMS fabrication. Specialty glass layers are produced in an IO Fabrication lab by RF and Reactive Sputtering, and Flame Hydrolysis Deposition (FHD). FHD allows tailoring of the glass refractive index and incorporation of rare earth dopants such as erbium, ytterbium, and neodymium allowing the fabrication of laser sources and amplifiers. Waveguide definition is done with MEMS fabrication processes, utilizing photolithography and RIE capabilities. The RIE requirements for optical waveguides provide some unique challenges including vertical sidewalls with very low edge roughness, and etch processes that can be used with a variety of glass compositions and dopant levels. Figure 4 indicates the dramatic reduction in weight and volume expected for an IOG vs. an IFOG of comparable performance. Currently, IOGs are several years away.

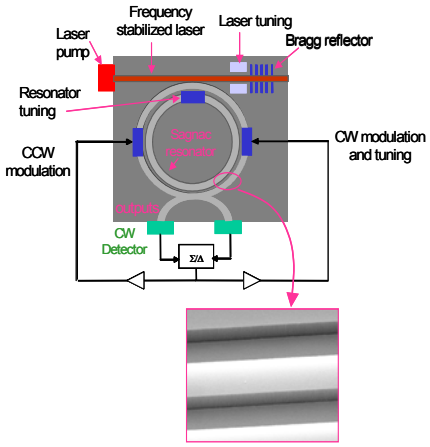


Figure 3: Integrated Optic Gyro (IOG).

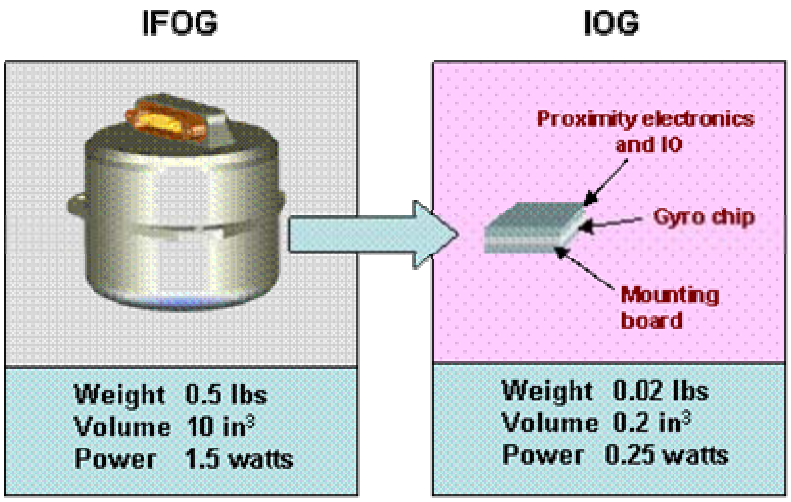


Figure 4: IFOG vs. IOG.

Integrated Optic technology also leads to improvements in IO chips for Fiber Optic Gyroscopes (FOGs) both tactical and strategic grade. A large part of the cost of current FOGs involves purchasing and connecting a variety of fiber pigtailed components. A planar lightwave circuit (PLC) can replace 21 components, significantly reducing cost.

OPTICAL ACCELEROMETERS

Although optical readouts have very high sensitivity, optical accelerometers have not found a niche and none is available commercially. Several efforts continue on the development of fiber optic (FO) and fiber Bragg grating (FBG) accelerometers (Ref. 8, 9, 10, 11). At present, none can be considered an enabling technology for military applications. Measurement of acceleration has been demonstrated using optical microspheres, in which the changes in light coupled into an optically resonant microsphere, as the sphere moves toward a waveguide, is detected. Incorporating optical readouts into MEMS devices has also been tried with varying success. The advantages of an optical readout may only become apparent when resolving accelerations in the nano-g range for measuring seismic disturbances or gravity gradients. This means that the rest of the accelerometer's components must also be very low-noise. Optical accelerometers are expected to have similar applications to tunneling accelerometers.

HEMISPHERICAL RESONANT GYRO (HRG)

In the 1980s, Delco (now Northrop Grumman [Litton]) developed the Hemispherical Resonator Gyro (HRG), which is a high-performance vibratory gyro whose inertially sensitive element is a fused silica hemispherical shell covered with a thin film of metallization. Electrostatic forcers surrounding the shell establish a standing resonant wave on the rim of the shell. As the gyro is rotated about its axis, the standing wave pattern does not rotate with the peripheral rotation of the shell but counter-rotates by a constant fraction (~0.3) of the input angle. Thus, the change in position of the standing wave, detected by capacitive pick-offs, is directly proportional to the angular movement of the resonator. In this mode of operation, termed whole angle mode, the HRG is an integrating sensor. The HRG can also be caged in a force rebalance mode to restrain the

standing wave to a particular location, and acts as a rate sensor. The whole angle mode is useful when excellent scale factor stability and linearity are required over a wide dynamic range. The force rebalance mode offers excellent angle resolution for pointing operations.

The advantages of the HRG is that it is lightweight, very compact, operates in a vacuum, and has no moving parts, so that life expectance limited only by the electronics, which are provided redundantly for expected lifetimes of more than 15 years. It is a very high-Q device so that vibrations of the shell persist for several minutes after power interruptions. This tends to make it immune to radiation and electromagnetic disturbances, since the pick-off can find the pattern mode and position when power is restored. It has negligible sensitivity to acceleration. Since its debut in space in the mid-1990s, the HRG has been used on many spacecraft, including the Near Earth Asteroid Rendezvous (NEAR) spacecraft and the Cassini mission. Figure 5 shows a Space Inertial Reference Unit containing four HRGs whose hemispherical shells are 30 mm in diameter.

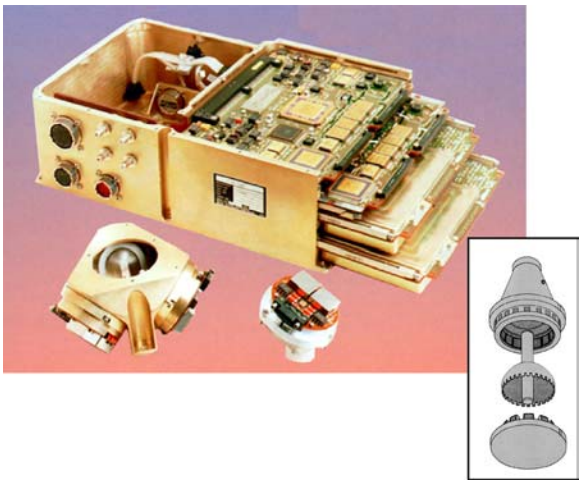


Figure 5: HRG Space Inertial Reference Unit.

© Northrop Grumman, printed with permission

INERTIAL MEMS SENSORS

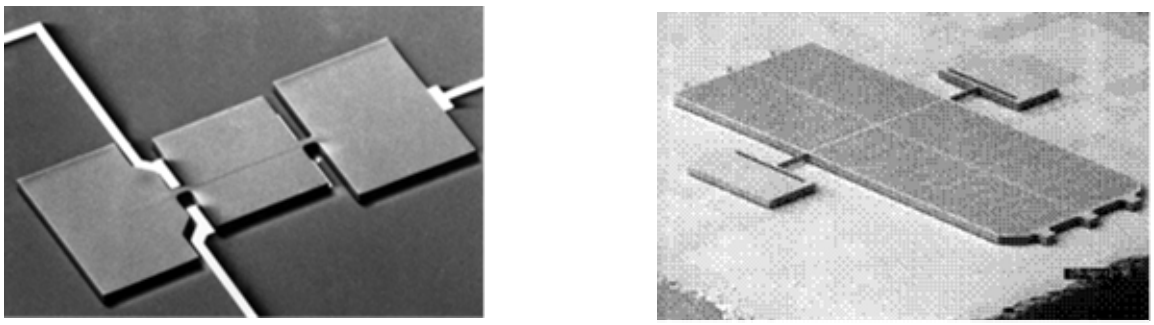
MEMS inertial sensors are expected to enable so many emerging military and commercial applications that are becoming too numerous to list. MEMS is probably the most exciting new inertial sensor technology ever and development is a worldwide effort (Ref. 12). Apart from size reduction, MEMS technology offers many benefits such as batch production and cost reduction, power (voltage) reduction, ruggedization, and design flexibility, within limits. However, the reduction in size of the sensing elements creates challenges for attaining good performance. In general, as size decreases, then sensitivity (scale factor) decreases, noise increases, and driving force decreases. Also, the change in Young's Modulus of silicon is ~100 ppm/°C, which leads to thermal sensitivity concerns. However, it appears that a MEMS system with performance of around 1 deg/hr and hundreds of μg will be available by 2006 (Ref. 13). This will be a serious threat to tactical RLG and IFOG systems.

MEMS ACCELEROMETERS

MEMS accelerometers detect acceleration in two primary ways: (i) the displacement of a hinged or flexure-supported proof mass under acceleration results in a change in a capacitive or piezoelectric readout; (ii) the change in frequency of a vibrating element is caused by a change in the element's tension induced by a change of loading from a proof mass. The former includes the class known as pendulous accelerometers and the latter are usually known as resonant accelerometers, or VBAs (Vibrating Beam Accelerometers). The pendulous types can meet a wide performance range from 1 mg for tactical systems down to aircraft navigation quality (25 μg). VBAs, or resonant accelerometers, have the potential for higher performance down to 1 μg. Numerous types of MEMS accelerometers are being developed throughout the world at universities, government organizations, and in industry.

MEMS Pendulous Mass (Z-Axis) Accelerometers

Figure 6 shows typical out-of-plane (z-axis) MEMS accelerometers, in which a hinged pendulous proof mass, suspended by torsional spring flexures over a glass substrate, rotates under acceleration perpendicular to the plane of the device. Motion is detected via change in the capacitance gap using electrodes on an insulator substrate. Under a 1g acceleration, typically the change in angle of the proof mass is 70 microradians; i.e., a $3x10^{-8}$ meter change in sense gap, which results in a 12 femtofarad (10^{-15}) peak change in capacitance. For a dynamic range of 15 g to 100 μg, it is necessary to resolve motion of $3x10^{-12}$ meters, or about 22.5 electrons charge change on the proof mass per carrier cycle.



(a) 10g - 100,000g Accelerometer (open loop) **(b) 100μg - 2g Accelerometer (closed loop)**

Figure 6: MEMS Pendulous Accelerometers.

A well-known example of this type of accelerometer is Northrop Grumman's SiAc™, of which over 20,000 have been produced. Two versions have been developed (tactical grade and inertial grade) and have wide usage, such as AMRAAM, GMLRS, and Commanche helicopter. Other examples are Draper/Honeywell, Applied MEMS Inc. Si-Flex™, Silicon Designs, and numerous others. Draper's pendulous accelerometers have been evaluated in the Extended Range Guided Munition and CMATD Guided Artillery Shell.

There is much interest in finding out how well commercially available (e.g., automotive) sensors could perform in military systems. Figure 7 shows how a temperature compensation algorithm can reduce the effects of temperature on accelerometer scale factor for a pendulous accelerometer.

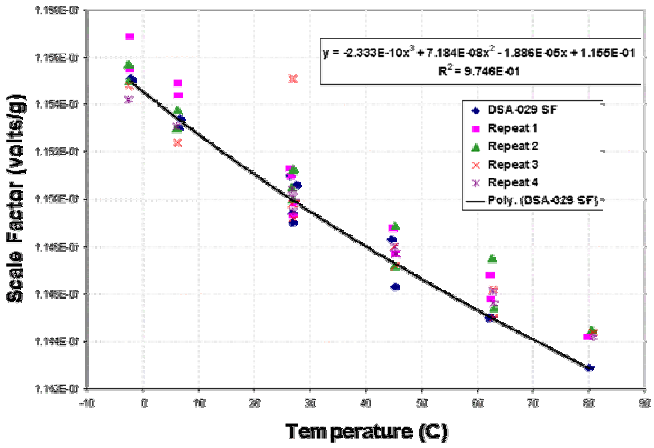
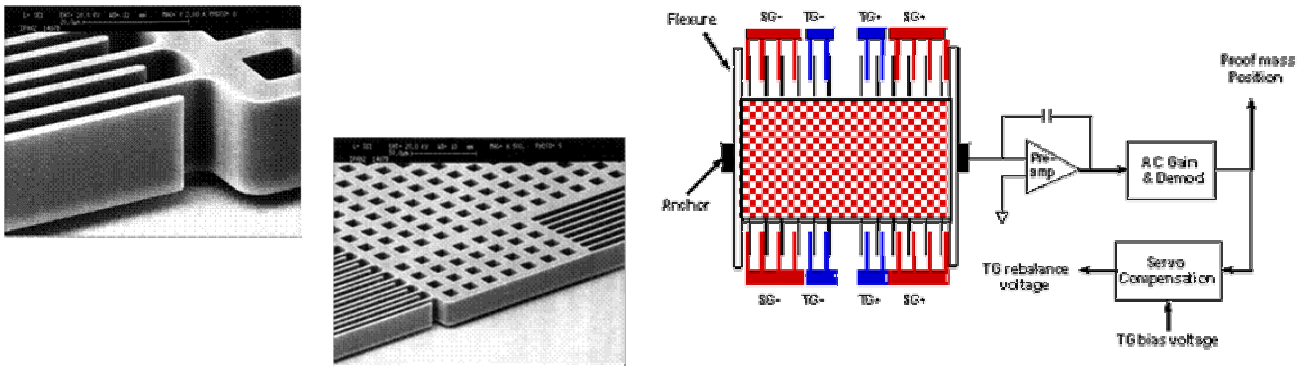


Figure 7: MEMS Pendulous Accelerometer – Scale Factor vs. Temperature.

MEMS Lateral Mass-Displacement Accelerometers

Figure 8 shows an in-plane (lateral) accelerometer in which proof mass displacement is measured by the change in capacitance across the comb fingers. This accelerometer is much more sensitive to accelerations in the left-to-right (rather than top-to-bottom) direction. The combination of z-axis and lateral accelerometers results in optimized system volume, since three axes of acceleration measurement can be achieved from three planar chips.



(a) In-Plane Accelerometer **(b) In-Plane Accelerometer Schematic**

Figure 8: MEMS Lateral Accelerometer.

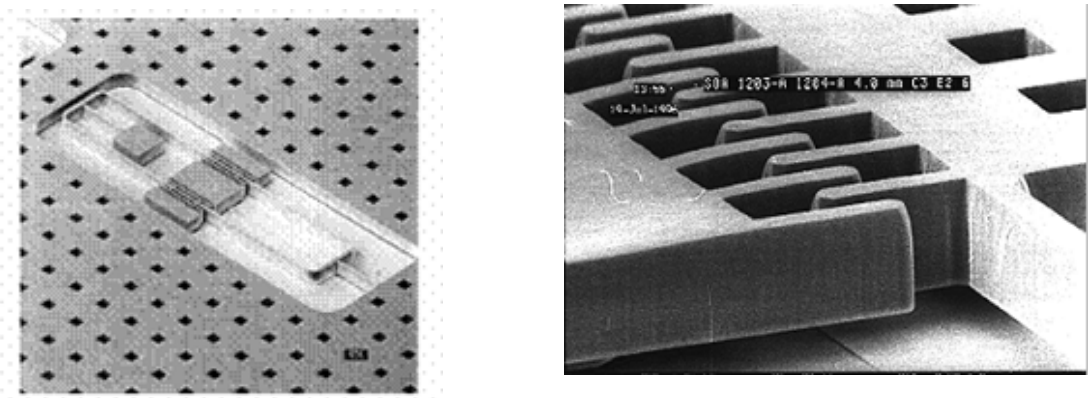
The most well-known of the in-plane accelerometers are probably the Analog Devices ADXL150 and ADXL 250. The latter measures lateral accelerations in two axes with a noise floor of 1mg/√Hz.

MEMS Resonant Accelerometers

'Resonant accelerometers' covers the general category of vibrating beam accelerometers (VBA), and can be z-axis or lateral. In resonant accelerometers, acceleration is sensed as a change in the resonant frequency of beam oscillators under the inertial loading of a proof mass, rather than measuring the mass displacement.

Z-axis resonant accelerometers have been achieved by micromachining a piezoelectric resonator in an area of high stress on one or more beams or flexures. As the flexure is bent under proof mass motion, the resonant frequency changes accordingly. Examples of this type are Kearfott's Silicon Micromachined Vibrating Beam Accelerometer (MVBA), Honeywell's SiMMA, and ONERA's Quartz Vibrating Inertial Accelerometer (VIA). ONERA's VIA design is of particular interest because it has an interesting mechanical isolating system which insulates the vibrating beam from the mounting base and protects the active part from thermal stresses due to the thermal expansion differences between quartz and the case material (Ref. 14). In-run bias stability of ~100 μg has been reported.

Figure 9(a) shows the in-plane (lateral) vibrating beam structure of Draper Laboratory's electrostatically driven Silicon Oscillating Accelerometer (SOA). The vibrating "tuning fork" is monolithic with the large silicon proof mass; the beams are axially loaded under acceleration in the wafer plane (Ref. 15). Oscillator resonance is actuated and sensed through low noise electronics acting through silicon comb drives (Figure 9[b]). The SOA integrates MEMS sensor fabrication, packaging, and high-performance electronics technologies to enable 1 micro-g performance.



(a) Capacitively Driven Resonator **(b) Comb Drives**

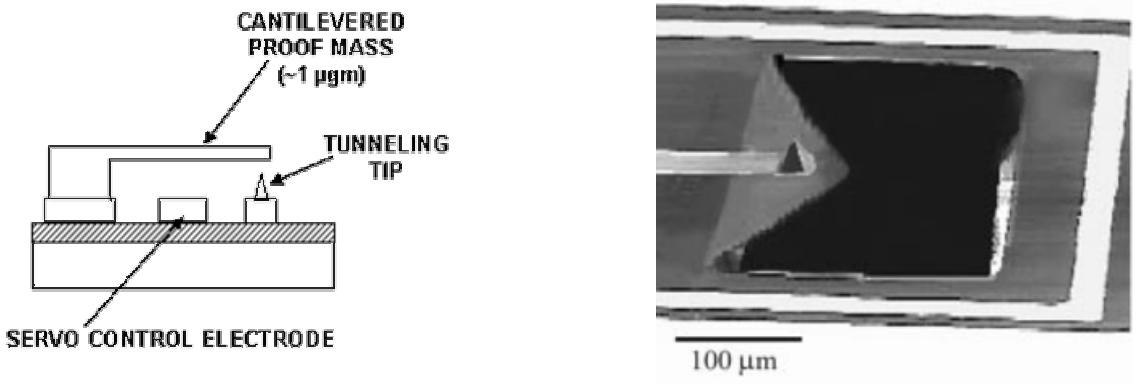
Figure 9: Silicon Oscillating Accelerometer.

The SOA MEMS fabrication process is silicon-on-glass; the silicon is crystalline quality and perfectly elastic leading to very high precision frequency control and stability. The SOA is packaged in a high reliability ceramic vacuum package to achieve high oscillator Q, and quality factors above 100,000 are typical. SOA sensor actuation and readout requires less than 1W of power. For a 100 Hz/g scale factor and a nominal oscillator frequency of 20 kHz, a frequency stability of 5 ppb is needed for 1 μg bias stability.

MEMS Tunneling Accelerometers

A technology under development (by Hughes Research Laboratory, Stanford University, and others) that offers a very high sensitivity readout and therefore better resolution, smaller size, and higher BW than capacitive accelerometers, is the tunneling accelerometer. Figure 10(a) shows a schematic of a tunneling accelerometer. The control electrode electrostatically deflects the cantilever into the tunneling position (<1 μm and ~20V). A servo mechanism holds constant the gap between the tunneling tip (Figure 10[b]) and the cantilever, and hence holds constant the tunneling current (~1 nA). The output signal is the change in voltage at the electrode under acceleration. These devices are designed to resolve accelerations in the nano-g range,

and require low-resonant frequency proof masses and sub-angstrom resolution readouts. Recent microfabricated tunneling accelerometers have resolved 20ng/√Hz over 5 Hz to 1.5 kHz (Ref. 16) with a closed-loop dynamic range of over 90dB. However, maximum acceleration measurement capability is very low (~1 mg) without further loop modification.



(a) Output is voltage required to keep cantilevered beam in fixed tunneling position during acceleration

(b) A scanning electron microscopic (SEM) view of triangular nitride cantilever and tunneling tip

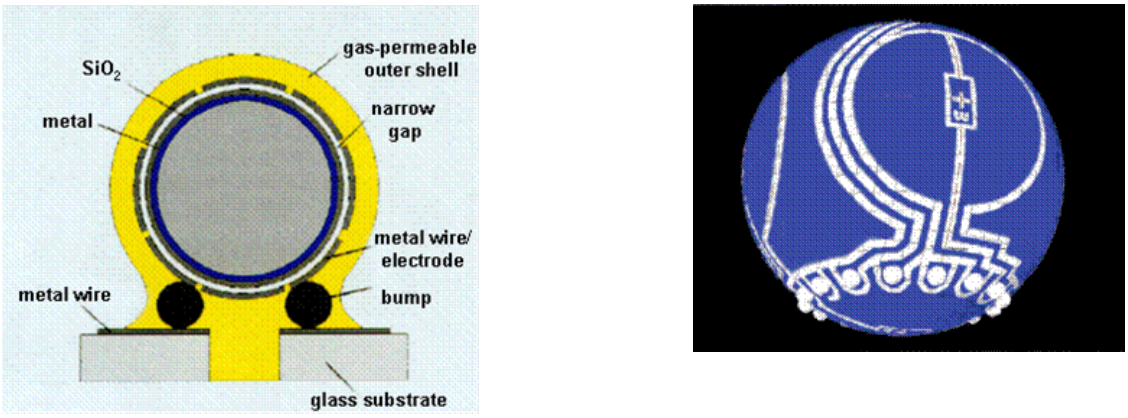
(See Ref. 16 © IEEE 2001)

Figure 10: MEMS Tunneling Accelerometer.

Electrostatically Levitated MEMS Accelerometers

Electrostatically levitating a proof mass eliminates the need to overcome the elastic restraint of mechanical supports. Theoretically, this would result in much higher sensitivity, less dependence on certain fabrication tolerances, and more flexibility in adjusting the device characteristics to BW and sensitivity without the need to redesign flexures. A further advantage is the potential for multi-axis sensing from one device. The major obstacle to development is the complexity of the control loop.

Figure 11 (Ref. 17) shows a cross-section of a 1-mm dia., 1.2 milligram proof mass supported electrostatically. Position of the ball is sensed capacitively and closed-loop electrostatic forces maintain its position. During the MEMS fabrication process, the gap between the ball and outer shell is formed by a sacrificial layer of polysilicon, subsequently etched through the outer shell. This device is under development by Ball Semiconductor, Tokinec, Inc., Japan, and Tokohu University, Japan. For high-performance microgravity measurements in space, a noise floor of better than 40 μg/√Hz is expected. A levitated disk concept is under development at the University of Southampton, UK (Ref. 18), as well as at other organizations. A spinning levitated MEMS mass technology, if perfected, could result in an extremely accurate gyroscope.



(a) Cross-sectional View of Accelerometer (1-mm dia. proof mass)

(b) Electrode Pattern

Figure 11: Electrostatically Levitated MEMS Sphere.

(See Ref. 17 © IEEE 2002)

MEMS GYROSCOPES

For inertial MEMS systems, attaining suitable gyro performance is more difficult to achieve than accelerometer performance. The Coriolis force is what causes Foucalt's pendulum to rotate about the vertical, and is the basis for all vibratory gyroscopes. Basically, if a mass is vibrated sinusoidally in a plane, and that plane is rotated at some angular rate Ω , then the Coriolis force causes the mass to vibrate sinusoidally perpendicular to the frame with amplitude proportional to Ω. Measurement of the Coriolis-induced motion provides knowledge of Ω. This measurement is the underlying principle of all quartz and silicon micromachined gyros. There are numerous MEMS gyros under development at present (Ref. 19); however, fundamentally MEMS gyros fall into four major areas: vibrating beams, vibrating plates, ring resonators, and dithered accelerometers.

MEMS Vibrating Beam (Tuning Fork) Gyros

In 1990, Systron-Donner started initial production for the USAF Maverick missile, with 18,000 quartz rate gyros produced in 2 years. In the mid-1990s, the technology was applied to low-cost, high-volume production of yaw rate sensors, the first application being for Cadillac in 1997. Figure 12 shows Systron Donner's well-known H-shaped quartz gyro. By 2000, over 10,000 rate gyros per day were being produced, and are being used for platform stabilization. High g versions have been developed for smart munitions. A six-degree-of-freedom IMU, containing 3 gyros and 3 vibrating accelerometers, called the Digital Quartz IMU (DQI), was developed in 1992 and beyond. The DQI has been inserted in Rockwell's C-MIGITS (Ref. 20).

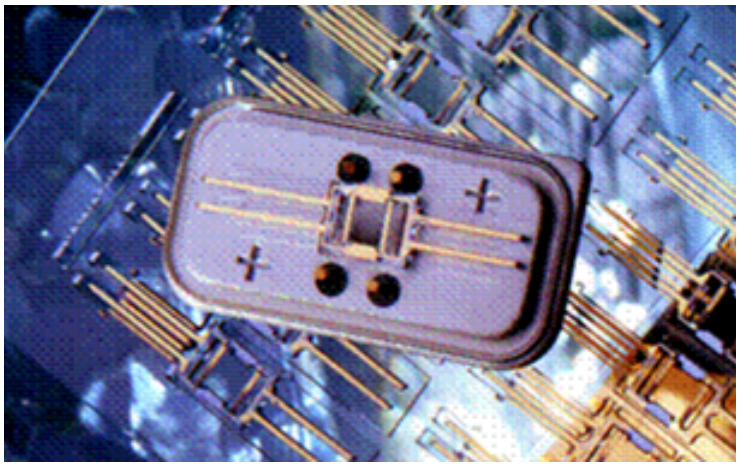


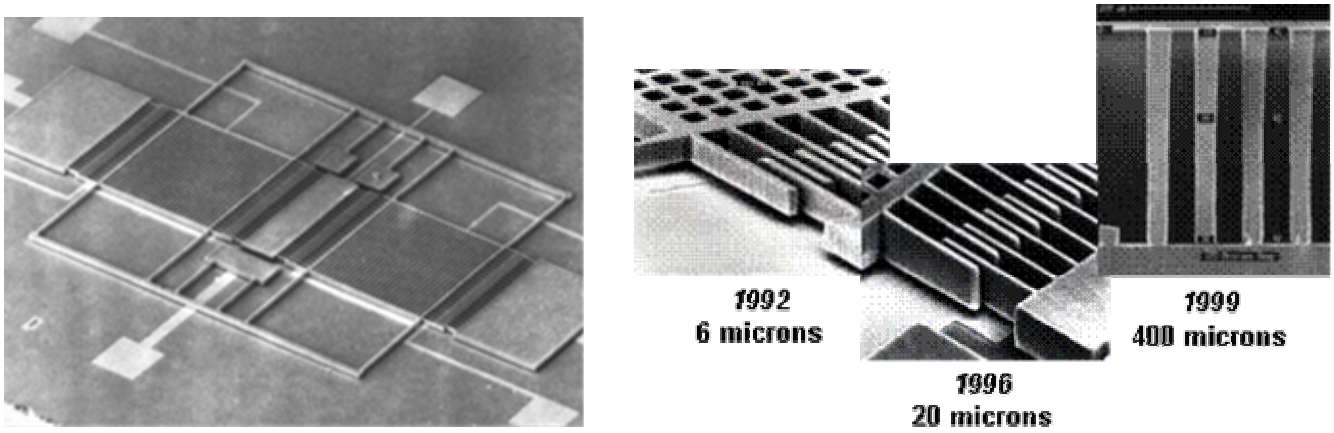
Figure 12: Systron Donner Quartz Rate Sensor (QRS).

(© BEI Systron Donner Inertial Division, printed with permission)

Sagem's Quapason gyro has four quartz tines extending upward from a common base. The advantage is the ability to reduce unwanted cross-coupling from drive to sense (Ref. 21).

Vibrating Plate MEMS Gyros

The gyroscope in Figure 13(a) consists of two silicon proof mass plates suspended over a glass substrate by folded beams and vibrating in-plane 180° out of phase. This design is also referred to as a double-ended tuning fork gyro. Dimensions are on the order of 300 microns by 400 microns. The out-of-plane motion induced by the Coriolis force is detected by changes in capacitance between the proof mass and the substrates. For a typical MEMS gyro, a 1-radian-per-second (in-plane) input rate results in a force of ~$9x10^{-8}$ N on the proof mass, ~$1x10^{-9}$ m of peak motion perpendicular to the sense electrodes, ~3 autofarads (10^{-18}) peak change in capacitance. Measuring 1 deg/h requires resolving motions of ~$5x10^{-15}$ m and about 0.25 electrons per cycle of motor motion. The Draper/Honeywell TFG series are a proven design for high-g applications and have undergone many iterations incorporating performance-enhancing features and fabrication improvements. Performance data indicate that the TFG currently performs at levels in the 3 to 50 deg/h range (3σ, compensated), over temperature ranges of -40°C to 85°C for many months, and over shock inputs of up to 12,000 g. These have been evaluated in both the Extended Range Guided Munition and the CMATD Guided Artillery Shell, and are currently under development for the U. S. Army's 2 cu. in. (33 cc) Common Guidance IMU (Ref. 22).



(a) Top view of MEMS vibrating plate gyroscope (TFG-2)

(b) Gyro comb fingers, highlighting aspect ratios and etch improvements over time

Figure 13: Vibrating Plate MEMS Gyro.

There are many kinds of vibrating plate gyros driven by the comb drive invented by the University of California, Berkeley. Many of the configurations have been designed to minimize coupling between sense and drive. Some are in-plane and some are z-axis gyros; some are oscillating circular disks. Studies indicate that the optimal gyro performance is achieved at a thickness of between 50 and 100 μm. Continued evolution of advanced processes to build thicker, more 3-dimensional parts that are less susceptible to fabrication tolerances is critical to the performance and cost targets. Initially this was hindered by the inability to perform deep high aspect ratio etching. However key improvements in fabrication equipment and process development have resulted in major advances, as depicted in Figure 13(b). Imperfections in the MEMS fabrication process can easily introduce unwanted performance errors. Optical techniques are being developed to characterize as-built geometry, alignments and symmetry, as well as behavior under temperature and electrostatic drive excitation (Ref. 23, 24).

Other types of vibrating plate MEMS gyros are under development. JPL's MEMS gyro (Ref. 25), in which a two degree-of-freedom resonating 4-leaf clover shape, suspended by four springs and containing a vertical post providing the main inertial mass, is driven in a rocking motion about an axis in the plane of the cloverleaf. This design is also referred to as a Foucault pendulum gyroscope. Rate about the z-axis (i.e., about the vertical post) is detected by the Coriolis acceleration-induced rocking about an axis 90° to the drive axis. JPL, in conjunction with Boeing Space Systems, have a joint objective to achieve 0.01 deg/hr performance in an IMU that will be less than 10 in^3, weighs less than 0.5 lb. (0.23 kg), and be available in volume production for less than $2500 (Ref. 26). Analog Devices now has a commercially available ADXRS gyro whose sense and drive axes are both parallel to the substrate which allows operation in one atmosphere of gas, but at limited performance. Northrop Grumman's MEMS gyro consists of a symmetrical sensing element (plate), suspended by torsion bars. The plate is dithered by an external drive about an axis perpendicular to the plate. An applied rate in the plane of the plate causes the plate to oscillate about the axis passing through the torsion bars. Upper and lower electrodes sense the motion, and torquing electrodes can close the loop. Prototype bias stability performance of <36°/hr was reported (Ref. 27).

Resonant Ring MEMS Gyros

Resonant ring MEMS gyroscopes have an advantage in that the ring structure maintains the drive and sense vibrational energy all in one plane. However, there is also a disadvantage in that the ring has a low vibrating mass and hence lower SF. Figure 14(a) shows a single crystal silicon vibrating ring gyro from U. Michigan (Ref. 28). The ring vibrates at 20 kHz and is 2.7 mm diameter, 50 µm wide, and 150 µm high. The ring is electrostatically vibrated by the forcer electrodes into an in-plane, elliptically shaped, primary flexural mode. A rate about the z-axis (normal to the plane of the ring) excites the Coriolis force which causes energy to be transferred from the primary to the secondary flexural mode, 45° apart. The amplitude of the secondary mode is detected capacitively. Any frequency mismatches arising during fabrication can be electronically compensated by the balancing electrodes. Figure 14(b) shows the drive and sense flexural modes before and after electronic balancing. This device has a SF of 132 mV/deg/s, resolution of 7.2 deg/h, and output noise of 10.4 deg/hr/√Hz.

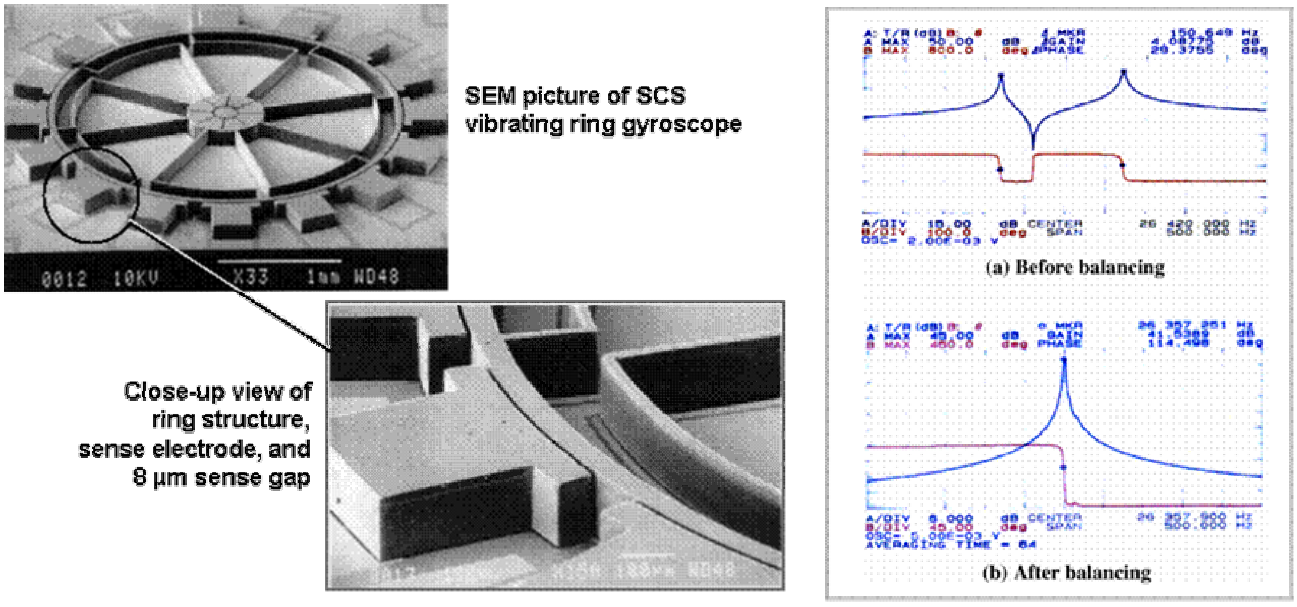


Figure 14: U. Michigan Vibrating Ring Gyroscope. (See Ref. 28 © IEEE 2002)

BAE SYSTEMS has a SiVSG (Silicon Vibrating Structure Gyro) which consists of a ring resonator supported by compliant spokes. Coriolis-induced motion of the ring is detected by change in the magnetic field supplied by a central magnet. BAE SYSTEMS, UK, and Sumitomo, Japan, are producing silicon gyro products. In May 1999, pilot production was 3,000 gyros/month. BAE SYSTEMS' inductive vibrating ring gyro (Ref. 29) was successfully used in an attitude reference system to control a production-standard, medium-range TRI-Nation Guided Anti-Tank (MR-TRIGAT) missile in flight in June 2000. It has also been evaluated in other military systems as well as part of the stabilization of the Segway™ Human Transporter. An all-silicon capacitive vibrating ring gyro is under development.

Dithered Accelerometers

A novel way of obtaining the gyro function has been developed by IEC/L-3 Communications with the µSCIRAS (Micro-machined Silicon Coriolis Inertial Rate and Acceleration Sensor) IMU (Ref. 30). Three opposing pairs of monolithic MEMS resonating beam accelerometers are dithered on a vibrating structure. The acceleration is sensed from the change in resonant frequency of the accelerometers, and rate is extracted through a synchronous demodulation of the Coriolis force acting on the accelerometers. A similar techniques is used in Kearfott's Micromachined Vibrating Beam Multisensor (MVBM) (Ref. 31).

MULTI-AXES GYRO AND ACCELEROMETER CHIPS

Further size reductions are underway through the combination of two in-plane (x- and y-axis) and one out-of-plane (z-axis) sensors on one chip. Draper Laboratory has demonstrated working devices of two TFGs and one OPG on one chip, and two IPAXs and one out-of-plane pendulum accelerometer on another single chip (Figure 15). These will result in IMUs around 0.2 cu. in (3.3 cc), but further development is required to develop high-performance chips. This is likely to be the ultimate in small IMUs enabling such things as personal navigation and guided bullets. It is likely that commercial investment will push this size-reduction technology, since there is a much stronger sized-based commercial need, rather than performance-based military need at this time.

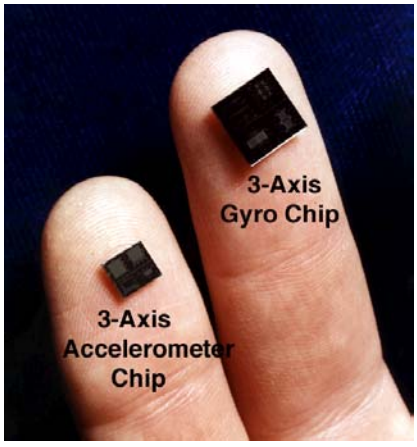


Figure 15: Photo of 3-Axis MEMS Chips.

ATOM INTERFEROMETER SENSORS

A potentially promising technology, which is in its infancy stages, is inertial sensing based upon atom interferometry (sometimes known as cold atom sensors). A typical atom de Broglie wavelength is 30,000 times smaller than an optical wavelength, and because atoms have mass and internal structure, atom interferometers are extremely sensitive (Ref. 32, 33). Accelerations, rotations, electromagnetic fields, and interactions with other atoms change the atom interferometric fringes. In theory, this means that atom interferometers could make the most accurate gyroscopes, accelerometers, gravity gradiometers, and precision clocks, by orders of magnitude. Much of the development to date has been at universities (Yale, Stanford, MIT, U. Arizona). Atom interferometer inertial sensors to date have used incoherent atoms propagating in free space; in the future, it may be possible to use coherent Bose-Einstein condensates propagating in a guiding

structure. Figure 16 shows a schematic of an atom interferometer If this technology can be developed, then it could result in a 5-meter/hour navigation system without GPS, in which the accelerometers are also measuring gravity gradients. The potential may ultimately exist for an all-accelerometer (including gradiometry) inertial navigation (Ref. 34).

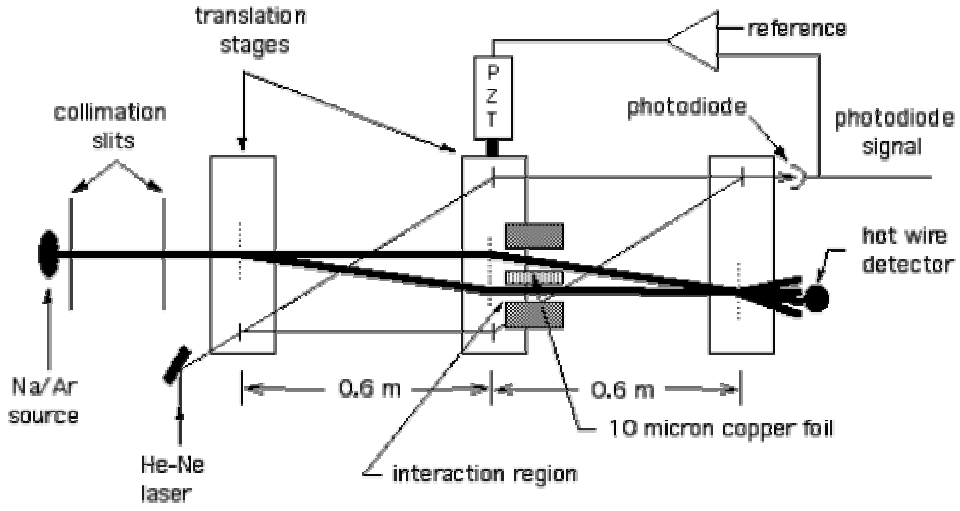


Figure 16: Atom Interferometer Schematic.

(Courtesy A. Cronin, University of Arizona, and David Pritchard, MIT)

There is significant interest in accurate gravity gradient measurements for detecting underground facilities as well as to improve navigation accuracy, which is ultimately limited by imperfect knowledge of the gravity vector. A superconducting gravity gradiometer (comprising nine superconducting accelerometers, six linear and three angular) has been developed at University of Maryland (Ref. 35) and has shown performance of $2x10^{-11}$ s^{-2} $Hz^{-½}$.

AUGMENTATION SENSORS

An integrated INS/GPS system, especially with ultra-tight (or deep) integration, can perform many, if not most, of the military missions, provided GPS is available. In just a few years, INS/GPS systems will provide 1m accuracy and have significant (75 dB J/S) anti-jam capability. However, for many missions, GPS will not be available for significant periods of time, and perhaps never (e.g., underground). In this case, augmentation sensors will be necessary to maintain accuracy. Consider a personal navigation application where horizontal position needs to be known to 1 meter after 1 hour in the absence of GPS. This means that the gyro and accelerometer bias performance needs to be about 5 micro-deg/hr and 15 nano-g, respectively. This is clearly not feasible given the desired low cost, size, and weight for a personal navigation system. Current MEMS technology is four to five orders-of-magnitude away in performance, although only a few years away from suitable size and power. Another situation when augmentation sensors are required is when the inertial sensors have insufficient performance for navigation, although are suitable for control.

Examples of augmentation sensors (or aiding devices) are velocity sensors, odometers, baroaltimeters, magnetometers, ranging devices, and GPS pseudolites. There can also be improvements from using special

procedures such as ZUPTs (Zero Velocity Updates) or path crossings. Velocity sensors and odometry, such as doppler radar or wheel counts, control the low-frequency drift of the inertial solution. Baroaltimeters stabilize the inertial navigation in the vertical direction, and today's devices provide 15cm resolution. Magnetometers provide a heading reference and inclination and can help bound the roll gyro errors in determining down in a spinning munition. It is interesting to note that the automotive industry is one of the major drivers for these technologies, and personal communications is driving packaging technology and low-power electronics. Augmentation sensors are not discussed in this paper, but their future development will be key to achieving many missions.

THE FUTURE

Inertial sensor maturity is depicted in Figure 17. Most of the technologies are in the lower-right hand corner, which represents a high maturity level. No new sensor technology appears to be on the near horizon, so what is next for the sensor designer? The desire for much lower cost and smaller size exists at all performance levels. Therefore, development over the next few years will continue to emphasize performance improvement and efficient packaging of MEMS sensors. Commercial applications require extremely low cost so the payback will come from selling very large quantities (billions). Military applications desire low cost but the quantities are not so large (thousands to millions). The payback will be from providing the entire GN&C system, not just the sensors. We may expect to see the development of various MEMS-based arrays to augment and support the inertial solution (Ref. 36, 37). This will be a worldwide effort with potential markets in the billions.

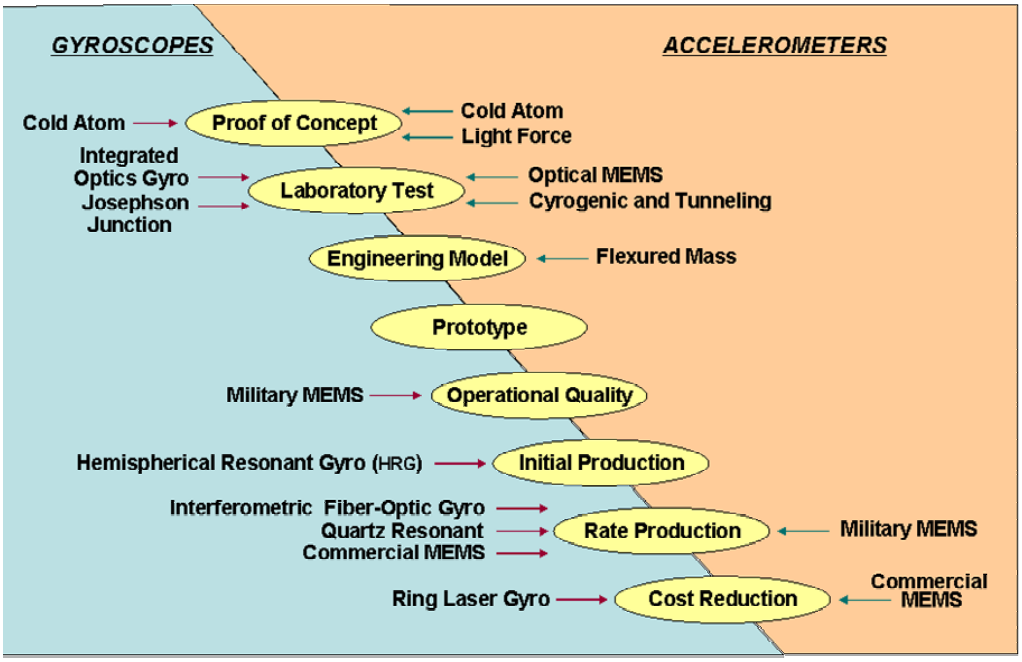


Figure 17: Inertial Sensor Maturity.

Fiber-optic gyros will continue pushing into areas traditionally held by RLGs. However, the 2 cu. in (33 cc). MEMS CGIMU is being developed for potential use in up to 80 percent of the tactical military applications after 2006. Some of these potential applications are described in Ref. 38. This will have a significant impact

on the tactical RLG and tactical FOG market. The relatively large production number of these MEMS IMUs will result in some of the promised cost benefits from MEMS being realized. RLG and FOG systems will maintain a niche in areas where they have better performance than MEMS. FOGs may hold their ground if higher bend-radius fiber, such as photonic crystal fiber, results in smaller FOGs. The integrated optics gyro (IOG) is a true solid-state, optics-on-a-chip sensor, manufactured with MEMS-like batch processing, with the potential (theoretically) to provide navigation-grade performance or higher. This has the potential to be a winning technology.

MEMS still needs performance improvement in turn-on repeatability and initial transient response for certain applications, such as short time-of-flight and rapid reaction weapons (e.g., guided bullets). In 1998 (Ref. 12), it was pointed out that MEMS performance enhancement (noise) had improved by a factor of 10, every two years since 1991. While this has slowed recently, MEMS inertial sensors still have the potential for one to two orders-of-magnitude performance improvement over the next decade by improved precision micro-fabrication, reduced sensitivity to packaging, and improved electronics.

Figure 18 shows possible future application areas for inertial sensor technology. Areas where FOGs are likely to remain unchallenged is in the field of precision pointing and tracking, and precision navigation (e.g., submarine). However, cold atom sensors have been mentioned as a very high performance, long-term competitor, but it is too early to predict with confidence. In the very long term, we may possibly develop NEMS (Nano-Electro-Mechanical Systems), or Optical NEMS, or even biological NEMS. In a few years, we may all have our own personal navigators in our pockets. In fact, navigation and position knowledge will soon become a commercial commodity item; everyone will expect to have it at all times. However, military navigation needs will continue to require higher-performance navigation sensors than commercially available, and it will be a difficult and expensive challenge to meet all requirements.

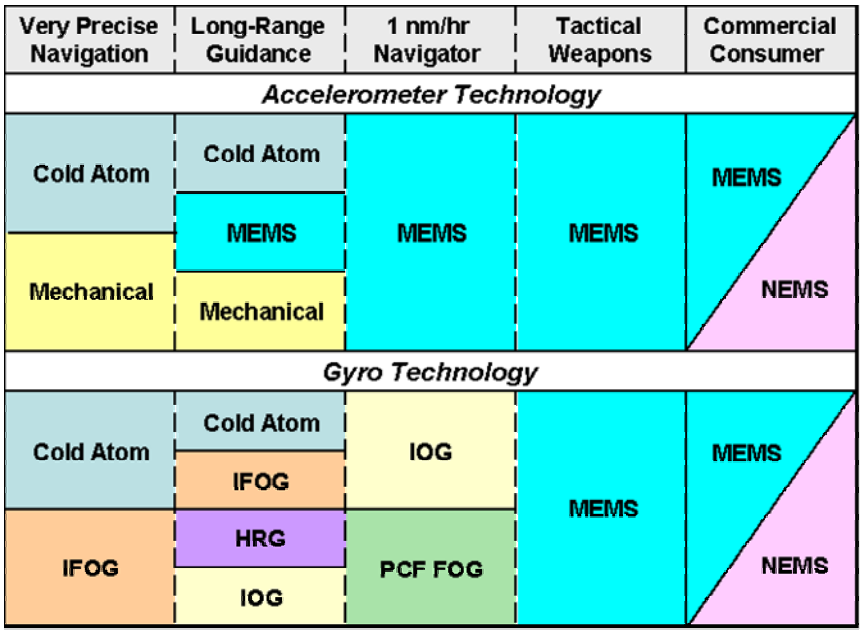


Figure 18: Future Applications for Inertial Sensor Technology.

NB/lah

ACKNOWLEDGEMENTS

Tony Lawrence for permission to use the RLG schematic from his book (Ref. 1). Charles Tapalian and Jack Haavisto from Draper Laboratory for information on Photonic Crystal Fibers (PCFs) and Integrated Optic Gyroscopes (IOG), respectively. Christine Doyle and Scott Licoscos, Northrop Grumman, for approval of the section on the HRG. The IEEE for use of copyrighted material in Figures 10(b) and 11. Alex Cronin for permission to use the atom interferometer schematic (Figure 16) from his website, and which originated from Dave Pritchard's Atom Interferometer Group at MIT. Mark Chamberlain, Systron Donner, for material relating to Systron Donner's quartz rate sensors. Khalil Najafi, University of Michigan, and the IEEE for permission to use elements of Figure 14.

REFERENCES

[1] Lawrence, A., *Modern Inertial Technology – Navigation, Guidance and Control*, Springer-Verlag, Second Edition, 1998.

[2] Barbour, N., *Inertial Components – Past, Present and Future*, Invited Paper, AIAA Guidance, Navigation and Control Conference, Montreal, Canada, August 2001.

[3] Mackenzie, D., *Inventing Accuracy – A Historical Sociology of Nuclear Missile Guidance*, MIT Press, 1990.

[4] Armenise, M. and Laybourn, P., *Design and Simulation of a Ring Laser for Miniaturized Gyroscopes*, SPIE Conference on Acousto-Optic and Magneto-Optic Devices for Telecommunications, Signal Processing and Remote Sensing, San Diego, CA, July 1998.

[5] Gaiffe, T., *From R&D Brassboards to Navigation Grade FOG-Based INS: The Experience of Photonetics/Ixsea*, Invited Paper, 2002 15th Optical Fiber Sensors Conference Technical Digest, Vol. 1, 2002, pp. 1-4, Vol. 1, 2 Vol., May 2002.

[6] Sanders, S., Strandjord, L. and Mead, D., *Fiber-Optic Gyro Technology Trends – A Honeywell Perspective*, Invited Paper, 2002 15th Optical Fiber Sensors Conference Technical Digest, Vol. 1, 2002, pp. 5-8, Vol. 1, 2 Vol., May 2002.

[7] Hans, K. et al, *A Submarine Navigator for the 21st Century*, IEEE PLANS, Palm Springs, CA, April 2002.

[8] Waters, R., Aklufi, M. and Jones, T., *Electro-Optical Ultra Sensitive Accelerometers*, IEEE PLANS, Palm Springs, CA, April 2002.

[9] Wang, T. and Zhang, S., *(Study of the) Silicon Micromechanical Accelerometer Using an Optical Fiber*, Proc. SPIE, MEMS/MOEMS Technologies and Applications, 2002, Vol. 4928, pp. 264-266, Conference, Shanghai, China, October 2002.

[10] Loh, N., Schmidt, M. and Manalis, S., *Sub-10 Cu. Cm. Interferometric Accelerometer with Nano-g Resolution*, Journal of Microelectromechanical Systems, Vol. 11, No. 3, pp. 182-187, June 1992.

[11] Morikawa, S., Ribeiro, A., Regazzi, R., Valente, L., and Braga, A., *Triaxial Bragg Grating Accelerometer*, 2002 15th Optical Fiber Sensors Conference Technical Digest, Vol. 1, 2002, pp. 95-98 Vol. 1, 2 Vol., May 2002.

[12] Yazdi, N., Ayazi, F. and Najafi, K., *Micromachined Inertial Sensors*, Proc. of the IEEE, Vol. 86, No. 8, August 1998.

[13] Warnasch, A. and Killen, A., *Low-Cost, High G, MEMS IMU Program*, IEEE PLANS 2002, Palm Springs, CA, April 2002.

[14] LeTraon, O., Janiaud, D., Muller, S., Bouniol, P., *The VIA Vibrating Beam Accelerometer: Concept and Performance*, IEEE PLANS 2002, Palm Springs, CA, April 1998.

[15] Hopkins, R., Borenstein, J., Antkowiak, B., Ward, P., Elliott, R., Weinberg, M., DePiero, M., and Miola, J., *The Silicon Oscillating Accelerometer: A MEMS Inertial Instrument for Strategic Missile Guidance*, Draper Technology Digest, Draper Report No. R-2907, July 2001.

[16] Liu, C. and Kenny, T., *A High-Precision, Wide-Bandwidth Micromachined Tunneling Accelerometer*, IEEE Journal of Microelectromechanical Systems (ISSN 1057-7157), Vol. 10, No. 3, pp. 425-433, September 2001.

[17] Toda, R.M., et al, *Electrostatically Levitated Spherical 3-Axis Accelerometer*, MEMS 2002 – 15th IEEE International Conference on MEMS, Las Vegas, NV, Jan 2002.

[18] Houlihan, R., *Modelling of an Accelerometer Based on a Levitated Proof Mass*, Journal of Micromechanics and Microengineering, Vol. 13, No. 4, July 192, pp. 495-503.

[19] Shkel, A., *Micromachined Gyroscopes: Challenges, Design Solutions, and Opportunities*, Smart Structures and Materials 2001, Proceedings of SPIE, Vol. 4334, 2001.

[20] Madni, A., Costlow, L. and Jaffe, R., *Aerospace Technology and Low Automotive Costs Benefit Quartz Micromachined Gyros*, ION 57th Annual Meeting and CIGTF 20th Biennial Guidance Test Symposium, Albuquerque, NM, June 2001.

[21] Leger, P., *QUAPASON™ – A New Low-Cost Vibrating Gyroscope*, 3rd St. Petersburg International Conference on Integrated Navigation Systems, St. Petersburg, Russia, May 1996.

[22] Anderson, R., Barbour, N., Connelly, J., Hanson, D., Kourepenis, A., Sitomer, J., and Ward, P., *Evolution of Low-Cost MEMS Inertial Systems*, NATO SET Symposium on Emerging Military Capabilities Enabled by Advances in Navigation Sensors, Istanbul, Turkey, October 2002.

[23] Hanson, D., Marinis, T., Furlong, C., and Pryputniewicz, R., *Advances in Optimization of MEMS Inertial Sensor Packaging*, repr. from Proc. Internat. Congress on Experimental and Applied Mechanics in Emerging Technologies, pp. 821-825, Portland, OR, June 2001.

[24] Gannon, J., Goldberg, H., Lawrence, E. and Speller, K., *Unique MEMS Characterization Solutions Enabled by Laser Doppler Vibrometer Measurements*, Proc. SPIE, Fifth International Conference on Vibration Measurements by Laser Techniques: Advances and Applications, Ancona, Italy, June 2002.

[25] Bae, S., Hayworth, K., Yee, K., Shcheglov, K. and Wiberg, D., *High Performance MEMS Micro-Gyroscope*, Proc. SPIE, Design, Test, Integration, and Packaging of MEMS/MOEMS 2002, Cannes, France, 2002.

[26] Challoner, D. et al, *A Highly Miniaturized Inertial Grade Gyroscope for Space Applications*, NASA Forum on Innovative Approaches to Outer Planetary Exploration 2001-2020, Houston, TX, February 2001.

[27] Matthews, A., Patterson, R., Goldman, A., Abbink, H., and Stewart, R., *A New Paradigm in Guidance, Navigation, and Control Systems based on Bulk Micromachined Inertial Sensors*, AIAA GN&C Conference, Montreal, Canada, August 2000.

[28] He, G. and Najafi, K., *A Single-Crystal Silicon Vibrating Ring Gyroscope*, MEMS 2002 – 15th IEEE International Conference on Micro Electro Mechanical Systems, Las Vegas, NV, January 2002.

[29] Gripton, A., *The Application and Future Development of a MEMS SiVSG for Commercial and Military Inertial Products*, IEEE PLANS, Palm Springs, CA, April 2002.

[30] Hulsing, R., *MEMS Inertial Rate and Acceleration Sensor*, ION National Technical Meeting, Long Beach, CA, January 1998.

[31] Roszhart, T., Sherman, P., Williams, D., Brand, A., Joress, P., Wing, B., and Berarducci, M., *Development of a Micromachined Vibrating Beam Multisensor (MVBM) for Tactical Guidance and Navigation Applications*, 2000 AIAA Guidance Navigation and Control Conference, Denver, CO, August 2000.

[32] Gustavson, T., Bouyer, P. and Kasevich, M., *A Dual Atomic Beam Matter-Wave Gyroscope*, SPIE Vol. 3270, pp. 62-68, 1998.

[33] McGuirk, J., Foster, G., Fixter, J., Snadden, M. and Kasevich, M., *Sensitive Absolute Gravity Gradiometry Using Atom Interferometry*, Physics, May 2001.

[34] Zorn, A., *A Merging of System Technologies – All-Accelerometer Inertial Navigation and Gravity Gradiometry*, IEEE PLANS, Palm Springs, CA, April 2002.

[35] Moody, M. and Ho Jung Paik, Canavan, E., *Three-Axis Superconducting Gravity Gradiometer for Sensitive Gravity Experiments*, J. Review of Scientific Instruments, (USA), Vol. 73, No. 11, November 2002.

[36] Ruffin, P. and Burgett, S., *Recent Progress in MEMS Technology Development for Military Applications*, Smart Structure and Materials 2001: Smart Electronics and MEMS, Proc. of SPIE, Vol. 4334, 2001.

[37] Ruffin, P., *MEMS-Based Sensor Arrays for Military Applications*, Smart Structure and Materials 2002: Smart Electronics, MEMS, and Nanotechnology, Proc. of SPIE, Vol. 4700, 2002.

[38] Ruffin, P. and Baeder, J., *Army Applications for MEMS Inertial Instruments*.

Strapdown System Computational Elements

Paul G. Savage
Strapdown Associates, Inc.
Maple Plain, Minnesota 55359 USA

ABSTRACT

This paper provides an overview of the primary strapdown inertial system computational elements and their interrelationship. Using an aircraft type strapdown inertial navigation system as a representative example, the paper provides differential equations for attitude, velocity, position determination, associated integral solution functions, and representative algorithms for system computer implementation. For the inertial sensor errors, angular rate sensor and accelerometer analytical models are presented including associated compensation algorithms for correction in the system computer. Sensor compensation techniques are discussed for coning, sculling, scrolling computation algorithms and for accelerometer output adjustment for physical size effect separation and anisoinertia error. Navigation error parameters are described and related to errors in the system computed attitude, velocity, position solutions. Differential equations for the navigation error parameters are presented showing error parameter propagation in response to residual inertial sensor errors (following sensor compensation) and to errors in the gravity model used in the system computer.

COORDINATE FRAMES

As used in this paper, a coordinate frame is an analytical abstraction defined by three mutually perpendicular unit vectors. A coordinate frame can be visualized as a set of three perpendicular lines (axes) passing through a common point (origin) with the unit vectors emanating from the origin along the axes. In this paper, the physical position of each coordinate frame's origin is arbitrary. The principal coordinate frames utilized are the following:

B Frame = "Body" coordinate frame parallel to strapdown inertial sensor axes.
N Frame = "Navigation" coordinate frame having Z axis parallel to the upward vertical at the local position location. A "wander azimuth" N Frame has the horizontal X, Y axes rotating relative to non-rotating inertial space at the local vertical component of earth's rate about the Z axis. A "free azimuth" N Frame would have zero inertial rotation rate of the X, Y axes around the Z axis. A "geographic" N Frame would have the X, Y axes rotated around Z to maintain the Y axis parallel to local true north.
E Frame = "Earth" referenced coordinate frame with fixed angular geometry relative to the rotating earth.
I Frame = "Inertial" non-rotating coordinate frame.

NOTATION

$\underline{V}$ = Vector without specific coordinate frame designation. A vector is a parameter that has length and direction. Vectors used in the paper are classified as "free vectors", hence, have no preferred location in coordinate frames in which they are analytically described.

$\underline{V}^A$ = Column matrix with elements equal to the projection of $\underline{V}$ on Coordinate Frame A axes. The projection of $\underline{V}$ on each Frame A axis equals the dot product of $\underline{V}$ with the coordinate Frame A axis unit vector.

$\left(\underline{V}^A \times\right)$ = Skew symmetric (or cross-product) form of $\underline{V}^A$ represented by the square matrix $\begin{bmatrix} 0 & -V_{ZA} & V_{YA} \\ V_{ZA} & 0 & -V_{XA} \\ -V_{YA} & V_{XA} & 0 \end{bmatrix}$ in which V_{XA}, V_{YA}, V_{ZA} are the components of $\underline{V}^A$. The matrix product of $\left(\underline{V}^A \times\right)$ with another A Frame vector equals the cross-product of $\underline{V}^A$ with the vector in the A Frame.

$C_{A_2}^{A_1}$ = Direction cosine matrix that transforms a vector from its Coordinate Frame A_2 projection form to its Coordinate Frame A_1 projection form.

$\underline{\omega}_{A_1A_2}$ = Angular rate of Coordinate Frame A_2 relative to Coordinate Frame A_1. When A_1 is non-rotating, $\underline{\omega}_{A_1A_2}$ is the angular rate that would be measured by angular rate sensors mounted on Frame A_2.

$\dot{(\,)} = \frac{d(\,)}{dt}$ = Derivative with respect to time.

t = Time.

1. INTRODUCTION

The primary computational elements in a strapdown inertial navigation system (INS) consist of integration operations for calculating attitude, velocity and position navigation parameters using strapdown angular rate and specific force acceleration for input. The computational form of these operations originate from two basic sources: time rate differential equations for the navigation parameters and analytical error models describing the error characteristics of the strapdown inertial angular rate sensors and accelerometers providing the angular rate and specific force acceleration measurement data. The latter is the source for compensation algorithms used in the system computer to correct predictable errors in the inertial sensor outputs. The former is the source for digital integration algorithms resident in system software for computing the navigation parameters. Both are the source for error propagation equations used to describe the behavior of navigation parameter errors in the presence of residual sensor errors remaining after compensation.

This paper provides examples of each of the aforementioned computational elements and their interrelationship. For the digital integration algorithms, the examples are selected to emphasize a structural goal of being based (to the greatest extent possible) on closed-form analytically exact integral solutions to the navigation parameter time rate differential equations. Such a structure significantly simplifies the integration algorithm software validation process based on a comparison with closed-form exact solution dynamic model simulators designed to thoroughly exercise the exact solution algorithms under test (Reference 20). For properly derived and programmed algorithms, the comparison will yield identically zero difference, thereby providing a clear unambiguous algorithm software validation. Once validated, such algorithms can be used as a generic set suitable for all strapdown inertial applications. Associated algorithm documentation is also simplified because algorithm derivations are classical analytical formulations and explanations/numerical-error-analysis justification for application dependent approximations are not required because there are none. Modern day strapdown system computer technology (high throughput, long floating point word-length) allows the general use of such exact solution algorithms without penalty. Similarly, the sensor compensation algorithms shown in the paper are a generic set based on the exact inverse of classical sensor error models without first order approximations (as has been commonly used in the past to save on computer throughput).

The form of the navigation error propagation equations are based on analytical definitions of the attitude, velocity, position error parameters. Several choices are possible. Two of the most common sets are

illustrated in the paper and equivalencies between the two described. An example of the error propagation equations based on one of the sets is provided.

This paper is a condensed version of material originally published in the two volume textbook *Strapdown Analytics* (Reference 18) which provides a broad detailed exposition of the analytical aspects of strapdown inertial navigation technology. Equations in the paper are presented without proof. Their derivations are provided in Reference 18 as delineated throughout the paper by Reference 18 section number. Documents delineated in the paper's References listing that are not cited in the body of the paper are those cited in Reference 18 that are specifically related to the paper's subject matter.

2. REPRESENTATIVE STRAPDOWN INERTIAL NAVIGATION DIFFERENTIAL EQUATIONS

This section describes a typical set of basic attitude/velocity/position integration and acceleration transformation operations performed in a strapdown INS. The integration operations are described in the form of continuous differential equations that when integrated in the classical analytical continuous sense, provide the attitude, velocity and position data generated digitally in the strapdown system computer. The algorithms described in Section 4 are designed to achieve the same numerical result by digital integration as the continuous integration of the differential equations presented in this section.

2.1 Attitude

For a terrestrial (earth) based inertial navigation system (e.g., for aircraft), sensor assembly angular attitude orientation is usually described as an "attitude direction cosine matrix" (or attitude quaternion) relating sensor assembly axes (the "body" or B Frame) to locally level attitude reference coordinates (N Frame). Attitude determination consists of integrating the associated time rate differential equations for the selected attitude parameters. For an attitude reference formulation based on direction cosines the attitude time rate differential equations are given by (Ref. 18 Sects. 4.1 and 4.1.1):

$$\dot{C}_B^N = C_B^N \left(\underline{\omega}_{IB}^B \times\right) - \left(\underline{\omega}_{IN}^N \times\right) C_B^N$$

$$\underline{\omega}_{IE}^N = \left(C_N^E\right)^T \underline{\omega}_{IE}^E \qquad \underline{\omega}_{EN}^N \equiv \underline{\rho}^N = F_C^N \left(\underline{u}_{Up}^N \times \underline{v}^N\right) + \rho_{ZN}\, \underline{u}_{ZN}^N \qquad (1)$$

$$\underline{\omega}_{IN}^N = \underline{\omega}_{IE}^N + \underline{\omega}_{EN}^N$$

where

$\underline{\rho}^N$ = Conventional notation for $\underline{\omega}_{EN}^N$, also known as "transport rate", and analytically defined as the angular rate of Frame N relative to Frame E.

ρ_{ZN} = Vertical component of $\underline{\rho}^N$. For a "wander azimuth" N Frame, ρ_{ZN} is zero. For a "free azimuth" N Frame, ρ_{ZN} is the downward vertical component of earth's inertial angular rate.

F_C^N = Curvature matrix in the N Frame that is a function of position location over the earth.

$\underline{v}$ = Velocity (rate of change of position) relative to the earth.

$\underline{u}_{Up}$ = Unit vector upward at the current position location (parallel to the N Frame Z axis).

The equivalent quaternion formulation (Ref. 18 Sect. 4.1) is as follows:

$$\dot{q}_B^N = \frac{1}{2} q_B^N \omega_{IB}^B - \frac{1}{2} \omega_{IN}^N q_B^N \qquad (2)$$

where

q_B^N = Attitude quaternion relating coordinate Frames B and N.

$\omega_{IB}^B, \omega_{IN}^N$ = Quaternions with vector components equal to $\underline{\omega}_{IB}^B, \underline{\omega}_{IN}^N$ and zero for the scalar components.

The C_N^E matrix in Equations (1) defines the system angular position location in earth reference coordinates, hence, is sometimes denoted as the "position" direction cosine matrix (or the equivalent position quaternion). The C_N^E matrix is calculated by integrating its differential equation (described in Section 2.3) using $\underline{\omega}_{IN}^N$ (N Frame "platform" rotation rate) as input. For earth's zero altitude surface reference modeled as an ellipsoid of revolution around earth's rotation axis (i.e., the conventional approach), Reference 18 Sections 5.2.4 and 5.3 develop the following exact expression for the F_C^N curvature matrix in Equations (1) based on an E Frame definition having Y axis parallel to earth's axis of rotation:

$$F_C^N = \begin{bmatrix} F_{C11} & F_{C12} & 0 \\ F_{C21} & F_{C22} & 0 \\ 0 & 0 & 0 \end{bmatrix}$$

$$F_{C11} = \frac{1}{r_l}\left(1 + D_{21}^2 f_{eh}\right) \qquad F_{C12} = \frac{1}{r_l} D_{21} D_{22} f_{eh}$$

$$F_{C21} = \frac{1}{r_l} D_{21} D_{22} f_{eh} \qquad F_{C22} = \frac{1}{r_l}\left(1 + D_{22}^2 f_{eh}\right) \tag{3}$$

$$r_l = R_0 \frac{(1 - e)^2}{\left\{1 + D_{23}^2\left[(1 - e)^2 - 1\right]\right\}^{3/2}} + h$$

$$f_{eh} \equiv \frac{(1 - e)^2 - 1}{\left(1 + D_{23}^2\left[(1 - e)^2 - 1\right]\right)\left(1 + \frac{h}{R_0}\sqrt{1 + D_{23}^2\left[(1 - e)^2 - 1\right]}\right)}$$

where

D_{ij} = Element in row i column j of C_N^E.

e = Ellipticity of earth's reference surface ellipsoid.

R_0 = Earth's equatorial radius.

r_l = Local radius of curvature at altitude in the North/South (latitude change) direction.

h = Altitude from earth's reference surface ellipsoid to the current position location (positive above the earth's surface).

2.2 Velocity

The velocity data in an inertial navigation system is typically computed as an integration of velocity rate described in the navigation N Frame. The velocity of interest is usually defined as the time rate of change of position relative to the earth in a coordinate frame that rotates at earth's rotation rates (i.e., the E Frame):

$$\underline{v}^E \equiv \dot{\underline{R}}^E \tag{4}$$

where

$\underline{R}$ = Position vector from earth's center to the current position location.

In the N Frame, the velocity is then:

$$\underline{v}^N = C_E^N \underline{v}^E \tag{5}$$

Based on this definition, the time rate differential equation for velocity is (Ref. 18 Sect. 4.3):

$$\dot{\underline{v}}^N = C_B^N \underline{a}_{SF}^B + \underline{g}^N - \underline{\omega}_{IE}^N \times \left(\underline{\omega}_{IE}^N \times \underline{R}^N\right) - \left(\underline{\omega}_{IN}^N + \underline{\omega}_{IE}^N\right) \times \underline{v}^N \tag{6}$$

where

$\underline{a}_{SF}$ = Specific force acceleration defined as the instantaneous time rate of change of velocity imparted to a body relative to the velocity it would have sustained without disturbances in local gravitational vacuum space. Sometimes defined as total velocity change rate minus gravity. Accelerometers measure $\underline{a}_{SF}$.

$\underline{g}$ = Mass attraction gravity at the current position location minus mass attraction gravity at the center of the earth. Sometimes denoted as "gravitation" (Ref. 2 Sect. 4.4).

For the quaternion attitude formulation approach in Section 2.1, the $C_B^N \underline{a}_{SF}^B$ term in Equation (6) would be replaced by the vector part of the quaternion product $q_B^N \underline{a}_{SF}^B q_B^N{}^*$ in which $q_B^N{}^*$ is the conjugate of q_B^N and a_{SF}^B is the quaternion with $\underline{a}_{SF}^B$ for its vector component and zero for its scalar component. Alternatively, once q_B^N is calculated by integrating Equation (2), it can be converted to the equivalent C_B^N direction cosine matrix (Ref. 18 Sect. 7.1.2.4) which is then directly compatible with Equation (6) as shown.

Reference 18 Section 5.4.1 shows how $\underline{g}^N - \underline{\omega}_{IE}^N \times \left(\underline{\omega}_{IE}^N \times \underline{R}^N\right)$ in Equation (6) can be calculated without singularities based on a classical gravity model defined in the E Frame (Ref. 2 Sect. 4.4 and Ref. 3). The latter references model gravity on and above earth's zero altitude surface. Reference 18 Section 5.4 extends the model for negative altitudes (i.e., below earth's surface).

2.3 Position

Position relative to the earth is often described by altitude above the earth and the angular orientation of the current local vertical direction in earth coordinates (the E Frame). The angular position parameters are commonly represented by latitude and longitude, however, to avoid mathematical singularities, the angular position parameters are frequently represented in the form of the N to E position direction cosine matrix (or the equivalent quaternion). The time rate differential equations for the position direction cosine matrix and altitude are as follows (Ref. 18 Sects. 4.4.1.1 and 4.4.1.2):

$$\dot{C}_N^E = C_N^E \left(\underline{\rho}^N \times\right) \qquad \dot{h} = \underline{u}_{Up}^N \cdot \underline{v}^N \tag{7}$$

2.4 Attitude, Velocity, Position Output Conversion

An advantage for using C_B^N, C_N^E (or their quaternion equivalents), $\underline{v}^N$, and h as the basic navigation parameters calculated by integration is that the associated differential equations have no singularities for all INS attitude orientations and position locations. Once calculated, they can be output from the INS directly and/or converted into other formats for output (e.g., roll, pitch, heading attitude; north, east, vertical velocity; latitude, longitude, altitude position - Ref. 18 Sects. 4.1.2, 4.3.1, and 4.4.2.1).

3. INTEGRAL SOLUTIONS FOR THE NAVIGATION PARAMETERS

The digital integration algorithms resident in the strapdown system computer are based on integrated forms of the Section 2 navigation parameter differential equations over a digital integration update cycle. For modern day algorithms, the integrated form is structured into two operations; 1. Basic digital updating operations used to increment the attitude/velocity/position parameters over each update cycle, and 2. High speed integration operations that account for high frequency angular-rate/acceleration inputs between each update cycle (coning effects in attitude determination, sculling effects in velocity determination, and scrolling effects in position determination). The bulk of the computations are contained in the basic operations that can be structured based on closed-form exact integral solutions to the Section 2 differential equations for particular idealized angular-rate/acceleration characteristics. The high speed integration operations measure variations from the idealized characteristics and provide corrections thereof to the basic updating operations. Use of exact closed-form solutions for the basic operations translates directly into computer integration algorithm forms that are easily verified by simple and direct simulation techniques (Ref. 20).

3.1 Attitude

The classical integral solution to the Section 2.1 direction cosine attitude rate equation is as follows (Ref. 18 Sects. 7.1.1, 7.1.1.1, and 7.1.1.2):

$$
\begin{aligned}
C_{B_m}^{N_{m-1}} &= C_{B_{m-1}}^{N_{m-1}} C_{B_{I(m)}}^{B_{I(m-1)}} \\
C_{B_m}^{N_m} &= C_{N_{I(m-1)}}^{N_{I(m)}} C_{B_m}^{N_{m-1}} \\
C_{B_{I(m)}}^{B_{I(m-1)}} &= I + \frac{\sin \phi_m}{\phi_m} (\underline{\phi}_m \times) + \frac{(1 - \cos \phi_m)}{\phi_m^2} (\underline{\phi}_m \times)^2 \\
C_{N_{I(m-1)}}^{N_{I(m)}} &= I - \frac{\sin \zeta_m}{\zeta_m} (\underline{\zeta}_m \times) + \frac{(1 - \cos \zeta_m)}{\zeta_m^2} (\underline{\zeta}_m \times)^2
\end{aligned}
\tag{8}
$$

where

m = System computer cycle time index for basic navigation parameter updating.

B_m, N_m = Coordinate Frame B and N orientations at navigation computer cycle time m.

$B_{I(m)}$, $N_{I(m)}$ = Discrete orientation of the B and N Frames in non-rotating inertial space (I) at computer cycle time t_m.

I = Identity matrix.

$\underline{\phi}_m$, $\underline{\zeta}_m$ = Rotation angle vector equivalents to the $C_{B_{I(m)}}^{B_{I(m-1)}}$ and $C_{N_{I(m-1)}}^{N_{I(m)}}$ direction cosine matrices (See Reference 18 Section 3.2.2 for rotation vector definition).

ϕ_m, ζ_m = Magnitudes of $\underline{\phi}_m$, $\underline{\zeta}_m$.

Reference 18 Sections 7.1.2, 7.1.2.1 and 7.1.2.2 provide the equivalent quaternion formulation integral solution which also is a function of the identical $\underline{\phi}_m$, $\underline{\zeta}_m$ rotation angle vectors.

The $\underline{\phi}_m$ and $\underline{\zeta}_m$ vectors are calculated as the integral from time t_{m-1} to t_m of the general $\dot{\underline{\phi}}$ and $\dot{\underline{\zeta}}$ equations (Ref. 18 Sect. 7.1.1.1):

$$\dot{\underline{\phi}} = \underline{\omega}_{IB}^{B} + \frac{1}{2}\underline{\phi} \times \underline{\omega}_{IB}^{B} + \frac{1}{\phi^2}\left(1 - \frac{\phi \sin \phi}{2(1-\cos\phi)}\right)\underline{\phi} \times \left(\underline{\phi} \times \underline{\omega}_{IB}^{B}\right)$$

$$\dot{\underline{\zeta}} = \underline{\omega}_{IN}^{N} + \frac{1}{2}\underline{\zeta} \times \underline{\omega}_{IN}^{N} + \frac{1}{\zeta^2}\left(1 - \frac{\zeta \sin \zeta}{2(1-\cos\zeta)}\right)\underline{\zeta} \times \left(\underline{\zeta} \times \underline{\omega}_{IN}^{N}\right) \qquad (9)$$

The $\dot{\underline{\phi}}$ equation, commonly referred to as the Bortz equation, relates the change in body B Frame attitude to the B Frame angular rate (as would be measured by strapdown angular rate sensors). The $\dot{\underline{\zeta}}$ equation relates the change in navigation N Frame attitude to the N Frame angular rate (as would be calculated in the strapdown system computer). The $\underline{\phi}_m$ and $\underline{\zeta}_m$ rotation vectors for Equations (8) are then obtained as the integral of Equations (9) from time t_{m-1}, evaluated at time t_m:

$$\underline{\phi}(t) = \int_{t_{m-1}}^{t} \dot{\underline{\phi}}(\tau)\, d\tau \qquad \underline{\phi}_m = \underline{\phi}(t_m)$$

$$\underline{\zeta}(t) = \int_{t_{m-1}}^{t} \dot{\underline{\zeta}}(\tau)\, d\tau \qquad \underline{\zeta}_m = \underline{\zeta}(t_m) \qquad (10)$$

where

t = General time in navigation.
t_m = Time t at computer cycle m.
τ = Dummy integration time parameter.

To reduce the number of computations involved in calculating $\dot{\underline{\phi}}$ and $\dot{\underline{\zeta}}$ with Equations (10), simplifying assumptions are typically incorporated. For example (Ref. 18 Sects. 7.1.1.1 and 7.1.1.2):

$$\dot{\underline{\phi}} \approx \underline{\omega}_{IB}^{B} + \frac{1}{2}\underline{\alpha(t)} \times \underline{\omega}_{IB}^{B} \qquad \underline{\alpha}(t) \equiv \int_{t_{m-1}}^{t} \underline{\omega}_{IB}^{B}\, d\tau$$

$$\dot{\underline{\zeta}} \approx \underline{\omega}_{IN}^{N} \qquad (11)$$

The simplified $\dot{\underline{\phi}}$ form in (11) has second order accuracy (i.e., in error to third order in $\underline{\alpha}$) even though it contains only first order $\underline{\alpha}$ terms (Ref. 18 Sect. 7.1.1.1). The simpler form of the $\dot{\underline{\zeta}}$ equation (compared to $\dot{\underline{\phi}}$) is possible due to the much smaller value of $\underline{\omega}_{IN}^{N}$ compared to $\underline{\omega}_{IB}^{B}$. The error in both the $\dot{\underline{\phi}}$ and $\dot{\underline{\zeta}}$ approximations is minimized by using a small value for the computer update cycle time interval t_{m-1} to t_m, thereby assuring small values of $\underline{\phi}$ and $\underline{\zeta}$. Based on the simplified forms and using Equations (1) for $\underline{\omega}_{IN}^{N}$ with a trapezoidal integration algorithm, the integral of Equations (11) over a computer update cycle become (Ref. 18 Sects. 7.1.1.1 and 7.1.1.2.1):

$$\underline{\phi}_m = \underline{\alpha}_m + \underline{\beta}_m$$

$$\underline{\alpha}(t) = \int_{t_{m-1}}^{t} \underline{\omega}_{IB}^{B}\, d\tau \qquad \underline{\alpha}_m = \underline{\alpha}(t_m) \qquad (12)$$

(Continued)

$$\underline{\beta}_m = \frac{1}{2}\int_{t_{m-1}}^{t_m} \left(\underline{\alpha}(t) \times \underline{\omega}_{IB}^{B}\right) dt$$

$$\underline{\zeta}_m \approx \int_{t_{m-1}}^{t_m} \underline{\omega}_{IN}^{N}\, dt \approx \frac{1}{2}\left[\underline{\omega}_{IE_{m-1}}^{N} + \underline{\omega}_{IE_m}^{N} + \left(\rho_{ZN_{m-1}} + \rho_{ZN_m}\right)\underline{u}_{Up}^{N}\right] T_m + \frac{1}{2}\left(F_{C_{m-1}}^{N} + F_{C_m}^{N}\right)\left(\underline{u}_{Up}^{N} \times \Delta\underline{R}_m^{N}\right) \quad (12)$$

(Continued)

$$\Delta\underline{R}_m^{N} \equiv \int_{t_{m-1}}^{t_m} \underline{v}^{N}\, dt$$

where

T_m = Time interval between m cycle updates.

$\underline{\alpha}_m$ = Integrated sensed B Frame angular rate vector from computer cycle m-1 to m.

$\underline{\beta}_m$ = Coning contribution to $\underline{\phi}_m$.

The $\Delta\underline{R}_m^{N}$ term is calculated as part of position updating operations (See Section 3.3). The approximate form shown for $\underline{\zeta}_m$ is based on position being updated before attitude.

The $\underline{\beta}_m$ term has been coined the "coning" term because it measures the effect of "coning motion" components present in $\underline{\omega}_{IB}^{B}$. "Coning motion" is defined as the condition when an angular rate vector is itself rotating. For $\underline{\omega}_{IB}^{B}$ exhibiting pure coning motion (the $\underline{\omega}_{IB}^{B}$ magnitude being constant but the vector rotating) a fixed axis in the B Frame that is approximately perpendicular to the plane of the rotating $\underline{\omega}_{IB}^{B}$ vector will generate a conical surface in the I Frame as the angular rate motion ensues (hence, the term "coning" to describe the motion). Under coning angular motion conditions, B Frame axes perpendicular to $\underline{\omega}_{IB}^{B}$ appear to oscillate (in contrast with non-coning or "spinning" angular motion in which axes perpendicular to $\underline{\omega}_{IB}^{B}$ rotate around $\underline{\omega}_{IB}^{B}$). Note that the neglected terms in the $\dot{\underline{\zeta}}$ equation can also be identified as coning associated with the $\underline{\omega}_{IN}^{N}$ rate vector.

For situations when $\underline{\omega}_{IB}^{B}$ is not rotating (i.e., parallel to an inertially non-rotating line) it is easily seen from Equations (12) that $\underline{\alpha}(t)$ will be parallel to $\underline{\omega}_{IB}^{B}$, hence, the cross-product in the $\underline{\beta}_m$ integrand will be zero and $\underline{\beta}_m$ will be zero. Under these conditions, $\underline{\phi}_m$ reduces to the simplified form:

$$\underline{\phi}_m = \underline{\alpha}_m \qquad \text{When } \underline{\omega}_{IB}^{B} \text{ is not rotating} \quad (13)$$

It should be noted that Equation (13) also applies to the exact $\underline{\phi}_m$ computation using Equations (9) and (10) (i.e., without approximation). This is readily verified by observing from Equation (9) that $\underline{\phi}(t)$ will initially be aligned with $\underline{\omega}_{IB}^{B}$ as the $\dot{\underline{\phi}}(t)$ integration begins, and will then remain parallel to $\underline{\omega}_{IB}^{B}$ because its cross-products with $\underline{\omega}_{IB}^{B}$ in the $\dot{\underline{\phi}}(t)$ expression will remain zero. Under these conditions, Equations (9) and (10) for $\underline{\phi}_m$ also reduce to (13). Also note that the basis for the $\dot{\underline{\zeta}}$ approximation in Equation (11) is zero coning

of the $\underline{\omega}^{N}_{IN}$ rate vector which makes the $\underline{\zeta}_m$ expression in (12) exact under zero $\underline{\omega}^{N}_{IN}$ coning conditions (except for the small error associated with the trapezoidal integration of small slowly varying terms).

3.2 Velocity

The velocity algorithm implemented in the navigation software can be formulated from the integral of Equation (6) using a trapezoidal integration approximation for the small and/or slowly varying terms (Ref. 18 Sects. 7.2, 7.2.2, 7.2.2.2 and 7.2.2.2.1 - note correction to Equation (7.2.2-4)):

$$\underline{v}^{N}_{m} = \underline{v}^{N}_{m-1} + \Delta\underline{v}^{N}_{SF_m} + \Delta\underline{v}^{N}_{G/COR_m}$$

$$\Delta\underline{v}^{N}_{G/COR_m} = \int_{t_{m-1}}^{t_m} \dot{\underline{v}}^{N}_{G/COR}\, dt \approx \frac{1}{2}\left(3\,\dot{\underline{v}}^{N}_{G/COR_{m-1}} - \dot{\underline{v}}^{N}_{G/COR_{m-2}}\right) T_m$$

$$\dot{\underline{v}}^{N}_{G/COR} \equiv \underline{g}^{N} - \underline{\omega}^{N}_{IE} \times \left(\underline{\omega}^{N}_{IE} \times \underline{R}^{N}\right) - \left(\underline{\omega}^{N}_{IN} + \underline{\omega}^{N}_{IE}\right) \times \underline{v}^{N}$$

$$\Delta\underline{v}^{N}_{SF_m} = \frac{1}{2}\left(C^{N_{I(m)}}_{N_{I(m-1)}} + I\right)\Delta\underline{v}^{N_{m-1}}_{SF_m} \approx \frac{1}{2}\left(2\,C^{N_{I(m-1)}}_{N_{I(m-2)}} - C^{N_{I(m-2)}}_{N_{I(m-3)}} + I\right)\Delta\underline{v}^{N_{m-1}}_{SF_m}$$

$$\Delta\underline{v}^{N_{m-1}}_{SF_m} = C^{N_{m-1}}_{B_{m-1}}\,\Delta\underline{v}^{B_{m-1}}_{SF_m}$$

$$\Delta\underline{v}^{B_{m-1}}_{SF_m} = \int_{t_{m-1}}^{t_m} C^{B_{I(m-1)}}_{B_{I(t)}}\,\underline{a}^{B}_{SF}\, dt = \underline{\upsilon}_m + \Delta\underline{v}_{Rot_m} + \Delta\underline{v}_{Scul_m} \qquad (14)$$

$$\underline{\upsilon}(t) \equiv \int_{t_{m-1}}^{t} \underline{a}^{B}_{SF}\, d\tau \qquad \underline{\upsilon}_m = \underline{\upsilon}(t_m)$$

$$\Delta\underline{v}_{Rot_m} = \frac{\left(1 - \cos\alpha_m\right)}{\alpha_m^2}\,\underline{\alpha}_m \times \underline{\upsilon}_m + \frac{1}{\alpha_m^2}\left(1 - \frac{\sin\alpha_m}{\alpha_m}\right)\underline{\alpha}_m \times \left(\underline{\alpha}_m \times \underline{\upsilon}_m\right)$$

$$\Delta\underline{v}_{Scul}(t) = \int_{t_{m-1}}^{t} \frac{1}{2}\left(\underline{\alpha}(\tau) \times \underline{a}^{B}_{SF} + \underline{\upsilon}(\tau) \times \underline{\omega}^{B}_{IB}\right) d\tau \qquad \Delta\underline{v}_{Scul_m} = \Delta\underline{v}_{Scul}(t_m)$$

where

$B_{I(t)}$ = B Frame orientation in non-rotating inertial space at time t after t_{m-1}.

$\Delta\underline{v}_{SF_m}$ = Velocity change from computer cycle m-1 to m due to specific force acceleration.

$\Delta\underline{v}_{G/COR_m}$ = Velocity change from computer cycle m-1 to m due to gravity and Coriolis acceleration. The approximate form shown is an extrapolation based on past (not yet updated) values of velocity and position.

$\Delta\underline{v}_{Rot_m}$ = "Velocity rotation compensation" contribution to $\Delta\underline{v}_{SF_m}$.

$\Delta\underline{v}_{Scul_m}$ = "Sculling" contribution to $\Delta\underline{v}_{SF_m}$.

$\underline{\upsilon}_m$ = Integrated sensed B Frame specific force acceleration vector from computer cycle m-1 to m.

The approximate form shown for $\Delta\underline{v}^{N}_{SF_m}$ in Equations (14) is based on $C^{N_{I(m)}}_{N_{I(m-1)}}$ (part of the Equations (8) and (12) attitude computations) being updated following the velocity and position update.

The $\Delta\underline{v}_{Scul_m}$ term in Equations (14), denoted as "sculling", measures the "constant" contribution to $\Delta\underline{v}^{B_{m-1}}_{SF_m}$ created from combined dynamic angular-rate/specific-force rectification. The rectification is a maximum under classical sculling motion defined as sinusoidal angular-rate/specific-force in which the $\underline{\alpha}(t)$ angular excursion about one B Frame axis is at the same frequency and in phase with the $\underline{a}^{B}_{SF}$ specific force along another B Frame axis (with a constant acceleration component then produced along the average third axis direction). This is the same principle used by mariners to propel a boat in the forward direction using a single oar operated with an undulating motion (also denoted as "sculling", the original use of the term). The notation "velocity" rotation compensation has been adopted for $\Delta\underline{v}_{Rot_m}$ to denote that this rotation compensation term feeds the "velocity" update equation (in contrast with an analogous "position rotation compensation" term in Section 3.3 that feeds the position update equation).

Under general motion, $\Delta\underline{v}_{Rot_m}$ may contain second order errors (e.g., on the order of $\alpha^2\,\upsilon$). Under conditions of constant B Frame angular-rate/specific-force-acceleration vector direction and magnitude ratio, the $\Delta\underline{v}_{Scul_m}$ sculling term is zero and the $\Delta\underline{v}_{Rot_m}$ expression becomes analytically exact. Except for the small trapezoidal integration error and a linearization approximation for the small $\frac{1}{2}$ term in the $\Delta\underline{v}^{N}_{SF_m}$ equation, all of Equations (14) are analytically exact under the previous conditions.

3.3 Position

The position algorithm implemented in the navigation software can be formulated from the integral of Equations (7) using an extrapolated trapezoidal approximation for the small and/or slowly varying terms (Ref. 18 Sects. 7.3.1, 7.3.3 and 7.3.3.1 - note correction to Equations (7.3.3-4)):

$$h_m = h_{m-1} + \Delta h_m$$

$$C^{E}_{N_{E(m)}} = C^{E}_{N_{E(m-1)}}\, C^{N_{E(m-1)}}_{N_{E(m)}}$$

$$C^{N_{E(m-1)}}_{N_{E(m)}} = I + \frac{\sin\xi_m}{\xi_m}\left(\underline{\xi}_m\times\right) + \frac{(1-\cos\xi_m)}{\xi_m^{\,2}}\left(\underline{\xi}_m\times\right)\left(\underline{\xi}_m\times\right)$$

$$\underline{\xi}_m \approx \int_{t_{m-1}}^{t_m} \underline{\rho}^{N}\, dt \approx \frac{1}{2}\left[\left(3\,\rho_{ZN_{m-1}} - \rho_{ZN_{m-2}}\right)\underline{u}^{N}_{Up}\,T_m + \left(3\,F^{N}_{C_{m-1}} - F^{N}_{C_{m-2}}\right)\left(\underline{u}^{N}_{Up}\times\Delta\underline{R}^{N}_{m}\right)\right]$$

$$\Delta h_m = \underline{u}^{N}_{Up}\cdot\Delta\underline{R}^{N}_{m} \qquad (15)$$

$$\Delta\underline{R}^{N}_{m} \equiv \int_{t_{m-1}}^{t_m} \underline{v}^{N}\, dt \approx \left(\underline{v}^{N}_{m-1} + \frac{1}{2}\Delta\underline{v}^{N}_{G/COR_m}\right)T_m + \Delta\underline{R}^{N}_{SF_m}$$

(Continued)

$$\Delta\underline{R}^{N}_{SF_m} = \frac{1}{6}\left(C^{N_m}_{N_{m-1}} - I\right)\Delta\underline{v}^{N_{m-1}}_{SF_m} T_m + C^{N_{m-1}}_{B_{m-1}}\Delta\underline{R}^{B}_{SF_m}$$

$$\approx \frac{1}{6}\left(2\,C^{N_{m-1}}_{N_{m-2}} - C^{N_{m-2}}_{N_{m-3}} - I\right)\Delta\underline{v}^{N_{m-1}}_{SF_m} T_m + C^{N_{m-1}}_{B_{m-1}}\Delta\underline{R}^{B}_{SF_m}$$

$$\Delta\underline{R}^{B}_{SF_m} = \underline{S}\upsilon_m + \Delta\underline{R}_{Rot_m} + \Delta\underline{R}_{Scrl_m}$$

$$\Delta\underline{R}_{Rot_m} = \left[\frac{1}{\alpha_m^2}\left(1 - \frac{\sin\alpha_m}{\alpha_m}\right)I + \frac{1}{\alpha_m^2}\left(\frac{1}{2} - \frac{(1-\cos\alpha_m)}{\alpha_m^2}\right)(\underline{\alpha}_m\times)\right]\left(\underline{S}\alpha_m\times\underline{\upsilon}_m + \underline{\alpha}_m\times\underline{S}\upsilon_m\right)$$

$$\Delta\underline{R}_{Scrl_m} = \int_{t_{m-1}}^{t_m}\frac{1}{6}\left[6\,\Delta\underline{v}_{Scul}(t) - \underline{S}\alpha(t)\times\underline{a}^{B}_{SF} + \underline{S}\upsilon(t)\times\underline{\omega}^{B}_{IB} + \underline{\alpha}(t)\times\underline{\upsilon}(t)\right]dt \qquad (15)$$

(Continued)

$$\underline{S}\alpha(t) = \int_{t_{m-1}}^{t}\int_{t_{m-1}}^{\tau}\underline{\omega}^{B}_{IB}\,d\tau_1\,d\tau \qquad \underline{S}\alpha_m = \underline{S}\alpha(t_m)$$

$$\underline{S}\upsilon(t) = \int_{t_{m-1}}^{t}\int_{t_{m-1}}^{\tau}\underline{a}^{B}_{SF}\,d\tau_1\,d\tau \qquad \underline{S}\upsilon_m = \underline{S}\upsilon(t_m)$$

where

$N_{E(m)}$ = Discrete orientation of the N Frame in rotating earth space (E) at computer cycle time t_m.

$\underline{\xi}_m$ = Rotation angle vector equivalent to the $C^{N_{E(m-1)}}_{N_{E(m)}}$ direction cosine matrix. The computation is an extrapolated trapezoidal approximation to the exact integral of $\dot{\underline{\xi}}$ over an m cycle (similar to the Section 3.1 Equation (12) approximation for the integral of $\dot{\underline{\zeta}}$ in Equation (9), but using $\underline{\rho}^{N}$ in place of $\underline{\omega}^{N}_{IN}$).

ξ_m = Magnitude of $\underline{\xi}_m$.

$\underline{\zeta}_m$ = Calculated in velocity update Equations (12).

$\Delta\underline{R}_m$ = Position vector change from computer cycle m-1 to m.

Δh_m = Altitude change from computer cycle m-1 to m.

$\Delta\underline{R}_{SF_m}$ = Specific force acceleration contribution to $\Delta\underline{R}_m$.

$\Delta\underline{R}_{Rot_m}$ = "Position rotation compensation" contribution to $\Delta\underline{R}_m$.

$\Delta\underline{R}_{Scrl_m}$ = "Scrolling" contribution to $\Delta\underline{R}_m$.

$\underline{S}\upsilon_m$ = Doubly integrated sensed B Frame specific force acceleration vector from cycle m-1 to m.

$\underline{S}\alpha_m$ = Doubly integrated sensed B Frame angular rate vector from cycle m-1 to m.

The $\Delta\underline{R}_{Scrl_m}$ term in (15), denoted as “scrolling”, is analogous to sculling in the velocity update equations. It measures the “constant” contribution to $\Delta\underline{R}_{SF_m}$ created from combined dynamic angular-rate/specific-force rectification. (The term “scrolling” was coined by the author merely to have a name for the term and also to have one that sounds like “sculling”, but for position integration (change in the position vector $\underline{R}$ stressing the “R” sound). The complex mathematical formulations that accompany “scrolling” may be a more appropriate reason for the name). The $\Delta\underline{R}_{Rot_m}$ “position" rotation compensation term is analogous to the velocity rotation compensation term in Section 3.2 that feeds the velocity update equation.

Under general motion, $\Delta\underline{R}_{Rot_m}$ may contain second order errors (e.g., on the order of $\alpha^2 S_\upsilon$). Under conditions of constant B Frame angular-rate and specific-force-acceleration, the $\Delta\underline{R}_{Scrl_m}$ scrolling term is zero and the $\Delta\underline{R}_{Rot_m}$ expression becomes analytically exact. Except for small trapezoidal integration errors and a linearization approximation for the small $\frac{1}{6}$ term in the $\Delta\underline{R}^N_{SF_m}$ equation, all of Equations (15) are analytically exact under the previous conditions.

3.4 Summary of Main Terms Requiring Integration Algorithms

Equations (8), (12), (14) and (15) are integral solutions to Equations (3), (6) and (7) over a computer update cycle. For the most part, they consist of exact closed form expressions fed by the integrated sensor output terms summarized below.

$$\underline{\beta}_m = \frac{1}{2}\int_{t_{m-1}}^{t_m} \left(\underline{\alpha}(t) \times \underline{\omega}^B_{IB}\right) dt \qquad \text{Coning} \tag{16}$$

$$\Delta\underline{v}_{Scul}(t) = \int_{t_{m-1}}^{t} \frac{1}{2}\left(\underline{\alpha}(\tau) \times \underline{a}^B_{SF} + \underline{\upsilon}(\tau) \times \underline{\omega}^B_{IB}\right) d\tau \qquad \Delta\underline{v}_{Scul_m} = \Delta\underline{v}_{Scul}(t_m) \qquad \text{Sculling} \tag{17}$$

$$\Delta\underline{R}_{Scrl_m} = \frac{1}{6}\int_{t_{m-1}}^{t_m} \left(6\,\Delta\underline{v}_{Scul}(t) - \underline{S}_\alpha(t) \times \underline{a}^B_{SF} + \underline{S}_\upsilon(t) \times \underline{\omega}^B_{IB} + \underline{\alpha}(t) \times \underline{\upsilon}(t)\right) dt \qquad \text{Scrolling} \tag{18}$$

$$\underline{S}_\alpha(t) = \int_{t_{m-1}}^{t}\int_{t_{m-1}}^{\tau} \underline{\omega}^B_{IB}\, d\tau_1\, d\tau \qquad \underline{S}_{\alpha_m} = \underline{S}_\alpha(t_m) \qquad \text{Doubly integrated angular rate} \tag{19}$$

$$\underline{S}_\upsilon(t) = \int_{t_{m-1}}^{t}\int_{t_{m-1}}^{\tau} \underline{a}^B_{SF}\, d\tau_1\, d\tau \qquad \underline{S}_{\upsilon_m} = \underline{S}_\upsilon(t_m) \qquad \begin{array}{c}\text{Doubly integrated}\\ \text{specifice force acceleration}\end{array} \tag{20}$$

$$\underline{\alpha}(t) = \int_{t_{m-1}}^{t} \underline{\omega}^B_{IB}\, d\tau \qquad \underline{\upsilon}(t) = \int_{t_{m-1}}^{t} \underline{a}^B_{SF}\, d\tau \qquad \text{Integrated inertial sensor inputs} \tag{21}$$

$$\underline{\alpha}_m = \underline{\alpha}(t_m) \qquad \underline{\upsilon}_m = \underline{\upsilon}(t_m)$$

The $\underline{\alpha}$, $\underline{\upsilon}$ integrated angular rate and specific force acceleration signals (measured by summing (integrating) angular rate sensor and accelerometer integrated output increments) are the normal basic inputs to most strapdown inertial system algorithms. The remaining terms (coning, sculling, scrolling, doubly integrated sensor signals) represent functions to be implemented by high speed digital computation algorithms operating within the basic m cycle update period.

4. DIGITAL INTEGRATION ALGORITHMS

Digital algorithms in the strapdown system computer are structured to provide integral solutions to the Section 2 differential equations based on repetitive processing at a specified computation rate. The integral

solutions in Section 3 to the Section 2 equations have such a repetitive processing structure, hence, for the most part, are the digital algorithm forms to be programmed directly in the strapdown computer. These are exact solution forms, hence, have no algorithm error if programmed as shown (except for minor trapezoidal integration algorithm errors for the small/slowly varying terms). Exceptions are the coning, sculling, scrolling and doubly integrated sensor signal integrals in Section 3.4 needing high speed digital integration algorithms for implementation. The high speed algorithm errors are a function of the high speed digital integration update frequency. Additionally, Taylor series expansion algorithms are needed for the trigonometric function coefficients in Equations (8), (14) and (15) that avoid singularities when ϕ_m, ζ_m, ξ_m or α_m are near zero. Taylor series truncation error can be designed to be negligible by carrying sufficient terms.

An important point to recognize in the previous algorithm formulation discussion is that direction cosine and quaternion based attitude algorithms are structured similarly. Both formulations are exact except for errors in the same coning digital integration algorithm input to each. Hence, contrary to outdated popular belief, modern day quaternion and direction cosine attitude algorithm formulations have equal accuracy.

Integration algorithms for the coning, sculling, scrolling and doubly integrated sensor signal terms are typically designed based on assumed approximate forms for the angular rate and specific force acceleration history during the computer update period. Commonly assumed forms for $\underline{\omega}^{B}_{IB}$ and $\underline{a}^{B}_{SF}$ are general polynomials in time:

$$\begin{aligned} \underline{\omega}^{B}_{IB} &= \underline{A}_{0_l} + \underline{A}_{1_l}\left(t - t_{l-1}\right) + \underline{A}_{2_l}\left(t - t_{l-1}\right)^2 + \cdots \\ \underline{a}^{B}_{SF} &= \underline{B}_{0_l} + \underline{B}_{1_l}\left(t - t_{l-1}\right) + \underline{B}_{2_l}\left(t - t_{l-1}\right)^2 + \cdots \end{aligned} \tag{22}$$

where

l = High speed computer cycle time index for high speed digital integration algorithms (within the slower m cycles).

$\underline{A}_{i_l}$, $\underline{B}_{i_l}$ = Coefficient vectors selected to match the $\underline{\omega}^{B}_{IB}$ and $\underline{a}^{B}_{SF}$ signals from computer cycle l-1 to l.

The high speed updating algorithms can be structured based on truncated versions of Equations (22). The advantage of this approach is that the resulting digital algorithms are easily validated by simulation testing using the truncated forms they have been designed for as inputs. The algorithm solution should match the equivalent result obtained by analytical evaluation of the Section 3.4 integrals under the same truncated polynomial inputs (Ref. 18 Sect. 11.1). Exact numerical correspondence should be the result for correctly structured and programmed algorithms.

The subsections to follow describe coning, sculling, scrolling and doubly integrated sensor signal digital integration algorithms designed to exactly match the Section 3.4 true continuous integrals under Equations (22) polynomial inputs truncated after the $\underline{A}_1$ and $\underline{B}_1$ terms. Based on the discussion in the previous paragraph, Reference 20 Section 2.3 describes specialized simulators for validating algorithms of this structure.

4.1 Coning Digital Integration Algorithm

A coning computation algorithm for Equation (16) based on:

$$\underline{\omega}^{B}_{IB} \approx \underline{A}_{0_l} + \underline{A}_{1_l}\left(t - t_{l-1}\right) \tag{23}$$

is given by (Ref. 18 Sect. 7.1.1.1.1):

$$\underline{\beta}_m = \sum_l \left[\frac{1}{2}\left(\underline{\alpha}_{l\text{-}1} + \frac{1}{6}\Delta\underline{\alpha}_{l\text{-}1}\right) \times \Delta\underline{\alpha}_l\right] \quad \text{From } t_{m-1} \text{ to } t_m$$

$$\underline{\alpha}_l = \sum_l \Delta\underline{\alpha}_l \quad \text{From } t_{m-1} \text{ to } t_l \qquad \Delta\underline{\alpha}_l = \int_{t_{l-1}}^{t_l} d\underline{\alpha} \tag{24}$$

where

$\Delta\underline{\alpha}_l$ = Summation of integrated angular rate sensor output increments from cycle l-1 to l.

4.2 Sculling Digital Integration Algorithm

A sculling computation algorithm for Equation (17) based on:

$$\overset{B}{\underline{\omega}}_{IB} \approx \underline{A}_{0_l} + \underline{A}_{1_l}(t - t_{l\text{-}1}) \qquad \overset{B}{\underline{a}}_{SF} \approx \underline{B}_{0_l} + \underline{B}_{1_l}(t - t_{l\text{-}1}) \tag{25}$$

is given by (Ref. 18 Sect. 7.2.2.2.2):

$$\Delta\underline{v}_{Scul_m} = \Delta\underline{v}_{Scul_l} \quad \text{At } t_m$$

$$\Delta\underline{v}_{Scul_l} = \sum_l \frac{1}{2}\left[\left(\underline{\alpha}_{l\text{-}1} + \frac{1}{6}\Delta\underline{\alpha}_{l\text{-}1}\right) \times \Delta\underline{\upsilon}_l + \left(\underline{\upsilon}_{l\text{-}1} + \frac{1}{6}\Delta\underline{\upsilon}_{l\text{-}1}\right) \times \Delta\underline{\alpha}_l\right] \quad \text{From } t_{m-1} \text{ to } t_l \tag{26}$$

$$\underline{\upsilon}_l = \sum_l \Delta\underline{\upsilon}_l \quad \text{From } t_{m-1} \text{ to } t_l \qquad \Delta\underline{\upsilon}_l = \int_{t_{l-1}}^{t_l} d\underline{\upsilon}$$

where

$\Delta\underline{\upsilon}_l$ = Summation of integrated accelerometer output increments from cycle l-1 to l.

Note the similarity in form between the Equations (24) coning algorithm and Equations (26) sculling algorithm. Reference 12 provides a general formula for deriving the equivalent sculling algorithm (e.g., Equations (26)) from a previously derived coning algorithm (e.g., Equations (24)).

4.3 Scrolling and Doubly Integrated Sensor Signal Algorithms

Algorithms for scrolling computation and doubly integrated sensor signals for Equations (18) - (20) based on:

$$\overset{B}{\underline{\omega}}_{IB} \approx \underline{A}_{0_l} + \underline{A}_{1_l}(t - t_{l\text{-}1}) \qquad \overset{B}{\underline{a}}_{SF} \approx \underline{B}_{0_l} + \underline{B}_{1_l}(t - t_{l\text{-}1}) \tag{27}$$

are given by (Ref. 18 Sect. 7.3.3.2):

$$\Delta\underline{R}_{Scrl_m} = \sum_l \left(\delta\underline{R}_{ScrlA_l} + \delta\underline{R}_{ScrlB_l}\right) \quad \text{From } t_{m-1} \text{ to } t_m$$

$$\begin{aligned}\delta\underline{R}_{ScrlA_l} = {} & \Delta\underline{v}_{Scul_{l-1}} T_l + \frac{1}{2}\left[\underline{\alpha}_{l\text{-}1} - \frac{1}{12}\left(\Delta\underline{\alpha}_l - \Delta\underline{\alpha}_{l\text{-}1}\right)\right] \times \left(\Delta\underline{S}_{\upsilon_l} - \underline{\upsilon}_{l\text{-}1} T_l\right) \\ & + \frac{1}{2}\left[\underline{\upsilon}_{l\text{-}1} - \frac{1}{12}\left(\Delta\underline{\upsilon}_l - \Delta\underline{\upsilon}_{l\text{-}1}\right)\right] \times \left(\Delta\underline{S}_{\alpha_l} - \underline{\alpha}_{l\text{-}1} T_l\right)\end{aligned} \tag{28}$$

(Continued)

$$\delta\underline{R}_{ScrlB_l} = \frac{1}{6}\left[\underline{S}_{\upsilon_{l-1}} + \frac{T_l}{24}\left(\Delta\underline{\upsilon}_l - \Delta\underline{\upsilon}_{l-1}\right)\right]\times\Delta\underline{\alpha}_l - \frac{1}{6}\left[\underline{S}_{\alpha_{l-1}} + \frac{T_l}{24}\left(\Delta\underline{\alpha}_l - \Delta\underline{\alpha}_{l-1}\right)\right]\times\Delta\underline{\upsilon}_l$$
$$+\frac{T_l}{6}\left[\underline{\alpha}_{l-1} - \frac{1}{6}\left(\Delta\underline{\alpha}_l - \Delta\underline{\alpha}_{l-1}\right)\right]\times\left[\underline{\upsilon}_{l-1} - \frac{1}{6}\left(\Delta\underline{\upsilon}_l - \Delta\underline{\upsilon}_{l-1}\right)\right] - \frac{T_l}{2160}\left(\Delta\underline{\alpha}_l - \Delta\underline{\alpha}_{l-1}\right)\times\left(\Delta\underline{\upsilon}_l - \Delta\underline{\upsilon}_{l-1}\right)$$

$$\underline{S}_{\alpha_l} = \sum_l \Delta\underline{S}_{\alpha_l} \quad \text{From } t_{m-1} \text{ to } t_l \qquad \underline{S}_{\alpha_m} = \underline{S}_{\alpha_l} \quad \text{at } t_m$$
$$\Delta\underline{S}_{\alpha_l} = \underline{\alpha}_{l-1}T_l + \frac{T_l}{12}\left(5\,\Delta\underline{\alpha}_l + \Delta\underline{\alpha}_{l-1}\right)$$
$$\underline{S}_{\upsilon_l} = \sum_l \Delta\underline{S}_{\upsilon_l} \quad \text{From } t_{m-1} \text{ to } t_l \qquad \underline{S}_{\upsilon_m} = \underline{S}_{\upsilon_l} \quad \text{at } t_m$$
$$\Delta\underline{S}_{\upsilon_l} = \underline{\upsilon}_{l-1}T_l + \frac{T_l}{12}\left(5\,\Delta\underline{\upsilon}_l + \Delta\underline{\upsilon}_{l-1}\right)$$

(28) (Continued)

where

T_l = Time interval between computer high speed l cycles.

4.4 Trigonometric Coefficient Algorithms

To assure that no singularities occur when ϕ_m, ζ_m, α_m or ξ_m are near zero, the following Taylor series expansion formulas can be used for the Equations (8), (14) and (15) $C_{B_{I(m)}}^{B_{I(m-1)}}$, $C_{N_{I(m-1)}}^{N_{I(m)}}$, $\Delta\underline{v}_{Rot_m}$, $C_{N_{E(m-1)}}^{N_{E(m)}}$, $\Delta\underline{R}_{Rot_m}$ trigonometric function coefficients (Ref. 18 Sects. 7.1.1.1, 7.1.1.2, 7.2.2.2.1, 7.3.1 and 7.3.3.1):

$$\frac{\sin\chi}{\chi} = 1 - \frac{\chi^2}{3!} + \frac{\chi^4}{5!} - \ldots \qquad \frac{(1-\cos\chi)}{\chi^2} = \frac{1}{2!} - \frac{\chi^2}{4!} + \frac{\chi^4}{6!} - \ldots$$
$$\frac{1}{\chi^2}\left(1 - \frac{\sin\chi}{\chi}\right) = \frac{1}{3!} - \frac{\chi^2}{5!} + \frac{\chi^4}{7!} - \ldots \qquad \frac{1}{\chi^2}\left(\frac{1}{2} - \frac{(1-\cos\chi)}{\chi^2}\right) = \frac{1}{4!} - \frac{\chi^2}{6!} + \frac{\chi^4}{8!} - \ldots \qquad (29)$$

$$\chi = \phi_m, \zeta_m, \xi_m \text{ or } \alpha_m$$

Corresponding computational algorithms are then structured from truncated versions of the former. The series can be truncated with a sufficient number of terms to assure "error free" performance. For example, to assure overall eleventh order accuracy in $C_{B_{I(m)}}^{B_{I(m-1)}}$ (Equations (8)), this would entail carrying $\frac{\sin\chi}{\chi}$ out to tenth order (in ϕ_m) and $\frac{(1-\cos\chi)}{\chi^2}$ out to eighth order (note, there is no ninth order term in $\frac{(1-\cos\chi)}{\chi^2}$).

4.5 Orthogonality and Normalization Algorithms

Orthogonality and normalization correction algorithms can be applied to computed direction cosine matrices (e.g., C_B^N and C_N^E) to preserve the proper characteristics of their rows and columns (Ref. 18 Sect. 7.1.1.3). Similarly, normalization algorithms can be applied to quaternion attitude representations (Ref. 18 Sect. 7.1.2.3). One of the advantages in using exact formulated attitude updating algorithms (e.g., Equations (8)) is that direction cosines and equivalent quaternion formulations calculated by integration,

will remain orthogonal and normal if initialized as such, independent of sensor error (Ref. 18 Sect. 3.5.1). Consequently, if computer register round-off error is negligible (as it is for most applications using modern day processors), there is no need for orthogonality/normality compensation.

5. STRAPDOWN SENSOR ERROR COMPENSATION

A fundamental problem with all inertial navigation systems is the inability to manufacture inertial components with the inherent accuracy required to meet system requirements. To correct for this deficiency, compensation algorithms are included in the INS software for correcting sensor outputs for known predictable error effects. The compensation algorithms represent the inverse of the inertial sensor analytical model equations.

This section describes error models and compensation algorithms that can be used to correct for errors in the strapdown inertial sensors (angular rate sensors and accelerometers), relative displacement between accelerometers ("size effect"), misalignment of the strapdown sensor assembly relative to the system mount, and alignment of the system mount in the user vehicle relative to vehicle reference axes. Included is a discussion of the application of the sensor compensation algorithms to the Section 4 strapdown inertial navigation integration routines and their associated coning, sculling, scrolling and accelerometer size-effect/anisoinertia elements.

5.1 Sensor Error Models

This section characterizes the errors typically present in the raw inertial sensor outputs (angular rate sensors and accelerometers) and then describes a general form of compensation equations for correcting the errors. All vectors in this section are represented in the B Frame, the designation for which has been omitted for analytical simplicity.

The output vector from strapdown angular rate sensor and accelerometer triads can be characterized as a function of their inputs as (Ref. 18 Sects. 8.1.1.1 and 8.1.1.2):

$$\begin{aligned} \underline{\omega}_{IB_{Puls}} &= \frac{1}{\Omega_{Wt_0}} (I + F_{Scal}) \left(F_{Algn}\, \underline{\omega}_{IB} + \delta\underline{\omega}_{Bias} + \delta\underline{\omega}_{Quant} + \delta\underline{\omega}_{Rand}\right) \\ \underline{a}_{SF_{Puls}} &= \frac{1}{A_{Wt_0}} (I + G_{Scal}) \left(G_{Algn}\, \underline{a}_{SF} + \delta\underline{a}_{Bias} + \delta\underline{a}_{Size} + \delta\underline{a}_{Aniso} + \delta\underline{a}_{Quant} + \delta\underline{a}_{Rand}\right) \end{aligned} \tag{30}$$

where

$\underline{\omega}_{IB_{Puls}}$, $\underline{a}_{SF_{Puls}}$ = Angular rate sensor and accelerometer triad output vector in pulses per second. Each axis output pulse is a digital indication that the sensor associated with that axis has received an integrated input increment equal to that particular sensor's pulse size.

Ω_{Wt_0}, A_{Wt_0} = Nominal pulse weight (a positive value) for each angular rate sensor (radians per pulse) and accelerometer (fps per pulse).

F_{Scal}, G_{Scal} = Angular rate sensor and accelerometer triad scale factor correction matrices; diagonal matrices in which each element adjusts the output pulse scaling to correspond to the actual scaling for the particular sensor output. May include non-linear scale factor effects and temperature dependency. Nominally, F_{Scal} and G_{Scal} are zero.

F_{Algn}, G_{Algn} = Alignment matrices for the angular rate sensor and accelerometer triads. Each row represents a unit vector along a particular sensor input axis as projected onto the

B-Frame. May include specific force acceleration dependency. Nominally, F_{Algn} and G_{Algn} are identity.

$\delta\underline{\omega}_{Bias}$, $\delta\underline{a}_{Bias}$ = Angular rate sensor and accelerometer triad bias vectors. Each element equals the systematic output from a sensor under zero input conditions. May have environmental sensitivities (e.g., temperature, specific force acceleration for angular rate sensors, angular rate for accelerometers).

$\delta\underline{\omega}_{Quant}$, $\delta\underline{a}_{Quant}$ = Instantaneous angular rate sensor and accelerometer triad pulse quantization error vectors associated with the output only being provided when the cumulative input equals the pulse weight per axis.

$\delta\underline{\omega}_{Rand}$, $\delta\underline{a}_{Rand}$ = Angular rate sensor and accelerometer triad random error output vectors.

$\delta\underline{a}_{Size}$ = Accelerometer triad size effect error created by the fact that due to physical size, the accelerometers in the triad cannot be collocated, hence, do not measure components of identically the same acceleration vector.

$\delta\underline{a}_{Aniso}$ = Accelerometer triad anisoinertia error effect (present in pendulous accelerometers) created by mismatch in the moments of inertia around the input and pendulum axes.

References 19 and 18 Section 8.1.3 analytically describe the Equations (30) $\delta\underline{\omega}_{Quant}$, $\delta\underline{a}_{Quant}$ quantization error effects in strapdown inertial sensors. The $\delta\underline{a}_{Size}$ size effect term (Ref. 18 Sect. 8.1.4.1) and for pendulous accelerometers, the $\delta\underline{a}_{Aniso}$ anisoinertia term (Ref. 14 and Ref. 18 Sect. 8.1.4.2), are given by :

$$\delta\underline{a}_{Size} \equiv \sum_{k=1,3} \left\{ \underline{G}^{T}_{Algn_k} \cdot \left[\dot{\underline{\omega}}_{IB} \times \underline{l}_k + \underline{\omega}_{IB} \times \left(\underline{\omega}_{IB} \times \underline{l}_k \right) \right] \right\} \underline{u}_k$$

$$\delta\underline{a}_{Aniso} = K_{Aniso} \sum_{k=1,3} \omega_{IB_k} \omega_{IB_{kp}} \underline{u}_k \qquad (31)$$

where

$\underline{u}_k$ = Unit vector parallel to the accelerometer k input axis.

$\underline{l}_k$ = Position vector from INS navigation center to accelerometer k center of seismic mass.

$\underline{G}^{T}_{Algn_k}$ = Vector formed from the k^{th} column of G^{T}_{Algn}, the transpose of the G_{Algn} accelerometer triad alignment matrix

K_{Aniso} = Accelerometer anisoinertia coefficient (a generic property of the accelerometer design).

ω_{IB_k}, $\omega_{IB_{kp}}$ = Angular rate $\underline{\omega}_{IB}$ projections on the accelerometer k input and kp pendulum axes.

5.2 Generic Strapdown Sensor Compensation Forms

The inverse of Equations (30) form the basis for compensating the $\underline{\omega}_{IB_{Puls}}$, $\underline{a}_{SF_{Puls}}$ raw sensor outputs to calculate the true $\underline{\omega}_{IB}$, $\underline{a}_{SF}$ angular-rate/specific-force-acceleration inputs for the strapdown inertial integration operations (Ref. 18 Sects. 8.1.1.1 and 8.1.1.2). First, Equations (30) are solved for the B Frame angular rate and acceleration input vector:

$$\underline{\omega}'_{IB} = \Omega_{Wt_0} \left(I + F_{Scal} \right)^{-1} \underline{\omega}_{IB_{Puls}}$$

$$\underline{a}'_{SF} = A_{Wt_0} \left(I + G_{Scal} \right)^{-1} \underline{a}_{SF_{Puls}} \qquad (32)$$

$$\begin{aligned} \underline{\omega}_{IB} &= F_{Algn}^{-1}\left(\underline{\omega}'_{IB} - \delta\underline{\omega}_{Bias} - \delta\underline{\omega}_{Quant} - \delta\underline{\omega}_{Rand}\right) \\ \underline{a}_{SF} &= G_{Algn}^{-1}\left(\underline{a}'_{SF} - \delta\underline{a}_{Bias} - \delta\underline{a}_{Size} - \delta\underline{a}_{Aniso} - \delta\underline{a}_{Quant} - \delta\underline{a}_{Rand}\right) \end{aligned} \tag{33}$$

where

$\underline{\omega}'_{IB}, \underline{a}'_{SF}$ = Scale factor compensated angular rate sensor and accelerometer output vectors.

Equations (32) represent the scale factor compensation equation for the raw angular rate sensor and accelerometer triad $\underline{\omega}_{IB_{Puls}}$, $\underline{a}_{SF_{Puls}}$ outputs. Compensation for the remaining predictable errors in $\underline{\omega}_{IB_{Puls}}$ and $\underline{a}_{SF_{Puls}}$ is achieved using a simplified form of (33) in which it is recognized that the $\delta\underline{\omega}_{Rand}$ and $\delta\underline{a}_{Rand}$ components are unpredictable, hence, can only be approximated by zero:

$$\begin{aligned} \underline{\omega}_{IB} &\approx F_{Algn}^{-1}\left(\underline{\omega}'_{IB} - \delta\underline{\omega}_{Bias} - \delta\underline{\omega}_{Quant}\right) \\ \underline{a}_{SF} &= G_{Algn}^{-1}\left(\underline{a}'_{SF} - \delta\underline{a}_{Bias} - \delta\underline{a}_{Size} - \delta\underline{a}_{Aniso} - \delta\underline{a}_{Quant}\right) \end{aligned} \tag{34}$$

Compensation Equations (34) are further refined to a more familiar form by introducing the following definitions:

$$\begin{aligned} \Omega_{Wt} &\equiv \Omega_{Wt_0}\left(I + F_{Scal}\right)^{-1} & A_{Wt} &\equiv A_{Wt_0}\left(I + G_{Scal}\right)^{-1} \\ K_{Mis} &\equiv I - F_{Algn}^{-1} & L_{Mis} &\equiv I - G_{Algn}^{-1} \\ \underline{K}_{Bias} &\equiv F_{Algn}^{-1}\,\delta\underline{\omega}_{Bias} & \underline{L}_{Bias} &\equiv G_{Algn}^{-1}\,\delta\underline{a}_{Bias} \end{aligned} \tag{35}$$

Substituting (35) into (32) and (34) obtains the equivalent compensation equations:

$$\begin{aligned} \underline{\omega}'_{IB} &= \Omega_{Wt}\,\underline{\omega}_{IB_{Puls}} \\ \underline{\omega}_{IB} &\approx \underline{\omega}'_{IB} - K_{Mis}\,\underline{\omega}' - \underline{K}_{Bias} - F_{Algn}^{-1}\,\delta\underline{\omega}_{Quant} \\ \underline{a}'_{SF} &= A_{Wt}\,\underline{a}_{SF_{Puls}} \\ \underline{a}_{SF} &\approx \underline{a}'_{SF} - L_{Mis}\,\underline{a}'_{SF} - \underline{L}_{Bias} - G_{Algn}^{-1}\left(\delta\underline{a}_{Size} + \delta\underline{a}_{Aniso} + \delta\underline{a}_{Quant}\right) \end{aligned} \tag{36}$$

In many systems, the form of the compensation equations so derived contain linearization approximations to the exact inverse relations (to conserve on computer throughput). The approach taken above is the analytically simpler expedient of using the exact inverse of the complete error model (without linearization approximation) based on the assumption that modern day computers can easily handle the workload.

5.3 Generic Strapdown Sensor Compensation Algorithms

Equations (36) are the basis for the following algorithms used to form the inputs to the Section 3 navigation parameter m cycle updating operations (Ref. 18 Sects. 8.1.2.1 and 8.1.2.2):

$$
\begin{aligned}
&\underline{\alpha}'_m = \Omega_{Wt}\, \underline{\alpha}_{Cnt_m} \\
&\underline{\alpha}_m \approx \underline{\alpha}'_m - K_{Mis}\, \underline{\alpha}'_m - \underline{K}_{Bias}\, T_m - \delta\underline{\alpha}_{QuantC_m} \\
&\underline{S}'_{\alpha_m} = \Omega_{Wt}\, \underline{S}_{\alpha Cnt_m} \\
&\underline{S}_{\alpha_m} \approx \underline{S}'_{\alpha_m} - K_{Mis}\, \underline{S}'_{\alpha_m} - \frac{1}{2}\left(\underline{K}_{Bias}\, T_m + \delta\underline{\alpha}_{QuantC_m}\right) T_m \\
&\underline{\upsilon}'_m = A_{Wt}\, \underline{\upsilon}_{Cnt_m} \\
&\underline{\upsilon}_m \approx \underline{\upsilon}'_m - L_{Mis}\, \underline{\upsilon}'_m - \underline{L}_{Bias}\, T_m - \delta\underline{\upsilon}_{SizeC_m} - \delta\underline{\upsilon}_{AnisoC_m} - \delta\underline{\upsilon}_{QuantC_m} \\
&\underline{S}'_{\upsilon_m} = A_{Wt}\, \underline{S}_{\upsilon Cnt_m} \\
&\underline{S}_{\upsilon_m} \approx \underline{S}'_{\upsilon_m} - L_{Mis}\, \underline{S}'_{\upsilon_m} - \frac{1}{2}\left(\underline{L}_{Bias}\, T_m + \delta\underline{\upsilon}_{SizeC_m} + \delta\underline{\upsilon}_{AnisoC_m} + \delta\underline{\upsilon}_{QuantC_m}\right) T_m
\end{aligned}
\tag{37}
$$

in which (with Equations (31)) the following definitions apply:

$$
\begin{aligned}
\delta\underline{\upsilon}_{SizeC_m} &\equiv G_{Algn}^{-1} \int_{t_{m-1}}^{t_m} \delta\underline{a}_{Size}\, dt \approx \int_{t_{m-1}}^{t_m} \delta\underline{a}_{Size}\, dt \\
&= \sum_k \int_{t_{m-1}}^{t_m} \left\{ \underline{u}_k \cdot \left[\dot{\underline{\omega}}_{IB} \times \underline{l}_k + \underline{\omega}_{IB} \times \left(\underline{\omega}_{IB} \times \underline{l}_k\right)\right]\right\} \underline{u}_k\, dt \\
\delta\underline{\upsilon}_{AnisoC_m} &\equiv G_{Algn}^{-1} \int_{t_{m-1}}^{t_m} \delta\underline{a}_{Aniso}\, dt \approx \int_{t_{m-1}}^{t_m} \delta\underline{a}_{Aniso}\, dt = K_{Aniso} \sum_{k=1,3} \underline{u}_k \int_{t_{m-1}}^{t_m} \omega_{IB_k}\, \omega_{IB_{kp}}\, dt \\
\delta\underline{\alpha}_{QuantC_m} &\equiv F_{Algn}^{-1} \int_{t_{m-1}}^{t_m} \delta\underline{\omega}_{Quant}\, dt \approx \int_{t_{m-1}}^{t_m} \delta\underline{\omega}_{Quant}\, dt \\
\delta\underline{\upsilon}_{QuantC_m} &\equiv G_{Algn}^{-1} \int_{t_{m-1}}^{t_m} \delta\underline{a}_{Quant}\, dt \approx \int_{t_{m-1}}^{t_m} \delta\underline{a}_{Quant}\, dt \\
\underline{\alpha}_{Cnt_m} &\equiv \int_{t_{m-1}}^{t_m} d\underline{\alpha}_{Cnt} \qquad \underline{\upsilon}_{Cnt_m} \equiv \int_{t_{m-1}}^{t_m} d\underline{\upsilon}_{Cnt}
\end{aligned}
\tag{38}
$$

Summation of raw sensor output pulses over computer cycle m

where

$d\underline{\alpha}_{Cnt}$, $d\underline{\upsilon}_{Cnt}$ = Angular rate sensor and accelerometer instantaneous pulse output vectors.

Reference 18 Sect. 8.1.3 (and its subsections) describe various methods for calculating the $\delta\underline{\alpha}_{QuantC_m}$, $\delta\underline{\upsilon}_{QuantC_m}$ sensor quantization compensation terms. Representative algorithms for the $\delta\underline{\upsilon}_{SizeC_m}$, $\delta\underline{\upsilon}_{AnisoC_m}$ accelerometer size effect and anisoinertia compensation terms are described next.

5.3.1 Representative Accelerometer Size Effect And Anisoinertia Computation Algorithms

The size effect and anisoinertia terms in Equations (38) can be calculated at the high speed l cycle rate within each m cycle as follows (Ref. 18 Sects. 8.1.4.1.1.1 and 8.1.4.2):

$$\eta_{ij_m} = \sum_{l} \Delta\alpha_{i_l} \Delta\alpha_{j_l} \qquad \text{From } t_{m-1} \text{ to } t_m$$

$$\begin{aligned} \delta\upsilon_{SizeCY_m} = f_{Size} \Big[& - l_{Z_2} \left(\Delta\alpha_{X_m} - \Delta\alpha_{X_{m-1}}\right) + l_{X_2} \left(\Delta\alpha_{Z_m} - \Delta\alpha_{Z_{m-1}}\right) \\ & + l_{Z_2} \eta_{YZ_m} + l_{X_2} \eta_{XY_m} - l_{Y_2} \left(\eta_{ZZ_m} + \eta_{XX_m}\right) \Big] \end{aligned} \qquad (39)$$

$\delta\upsilon_{SizeCZ_m}, \delta\upsilon_{SizeCX_m}$ = Similarly by permuting subscripts.

$$\underline{\delta\upsilon}_{AnisoC_m} = f_{Size} K_{Aniso} \sum_{k=1,3} \eta_{kp_m} \underline{u}_k$$

where

l_{i_k} = Component of l_k along B Frame axis i.

f_{Size} = Size effect algorithm computation frequency which equals the reciprocal of T_l.

$\Delta\alpha_{i_l}$ = Integrated angular rate around B Frame axis i over the l-1 to l computer cycle time interval.

$\Delta\alpha_{i_m}, \Delta\alpha_{i_{m-1}}$ = $\Delta\alpha_{i_l}$ for the l-1 to l cycle time intervals immediately preceding the m and m-1 cycle times.

$\delta\upsilon_{SizeCi_m}$ = i^{th} B Frame component of $\underline{\delta\upsilon}_{SizeC_m}$.

The previous algorithm is designed to compute the high frequency dependent terms (η_{ij}) at the l cycle rate, use them to calculate size effect at the m cycle rate, and apply the size effect correction at the m cycle rate in Equations (37). This implies that size-effect compensation is not being applied at the l cycle rate, hence, will not be provided on the acceleration data used for high speed sculling calculations (Equations (26)). The associated sculling error is of the same order of magnitude as the basic Equations (39) size-effect correction, thus, cannot be ignored. Section 5.4 describes an algorithm for correcting the associated sculling error at the m cycle rate. Alternatively, the full Equations (39) size-effect correction can be computed and applied at the high speed l cycle rate with η_{ij_m} replaced by $\Delta\alpha_{i_l} \Delta\alpha_{j_l}$. The sculling computation would then be performed with the size-effect compensated accelerometer data, thereby eliminating the previously described sculling error.

5.4 Compensation of High Speed Algorithms for Sensor Error

The high speed algorithms described in Sections 4.1- 4.3 and 5.3.1 for coning, sculling, scrolling, doubly integrated sensor signals, size effect and anisoinertia are based on error free values for the $\Delta\underline{\alpha}_l$ and $\Delta\underline{\upsilon}_l$ integrated angular rate sensor and accelerometer increment inputs. This implies that compensated sensor signals are being used, thereby implying sensor compensation to be performed at the l cycle rate in forming $\Delta\underline{\alpha}_l$ and $\Delta\underline{\upsilon}_l$. The equivalent result can also be obtained by performing the high speed computations with uncompensated sensor data, then compensating the result at the slower m cycle rate. A savings in throughput can thereby be achieved if needed for a particular application. For the coning algorithm, the associated operations would be as follows (Ref. 18 Sect. 8.2.1.1):

$$\underline{\beta}_{Cnt_m} \equiv \int_{t_{m-1}}^{t_m} \frac{1}{2} \underline{\alpha}_{Cnt}(t) \times d\underline{\alpha}_{Cnt}$$

$$\underline{\beta}'_m = \Omega_{ConeWt}\, \underline{\beta}_{Cnt_m} \qquad \underline{\beta}_m = \left(I - K_{MisCone}\right) \underline{\beta}'_m \qquad (40)$$

in which

$$K_{MisCone} \equiv \begin{bmatrix} (K_{Mis_{YY}} + K_{Mis_{ZZ}}) & - K_{Mis_{YX}} & - K_{Mis_{ZX}} \\ - K_{Mis_{XY}} & (K_{Mis_{ZZ}} + K_{Mis_{XX}}) & - K_{Mis_{ZY}} \\ - K_{Mis_{XZ}} & - K_{Mis_{YZ}} & (K_{Mis_{XX}} + K_{Mis_{YY}}) \end{bmatrix}$$

$$\Omega_{ConeWt} \equiv \begin{bmatrix} \Omega_{Wt_Y}\,\Omega_{Wt_Z} & 0 & 0 \\ 0 & \Omega_{Wt_Z}\,\Omega_{Wt_X} & 0 \\ 0 & 0 & \Omega_{Wt_X}\,\Omega_{Wt_Y} \end{bmatrix} \qquad (41)$$

where

$\underline{\alpha}_{Cnt}(t) = \underline{\alpha}(t)$ as defined in Equations (11) but based on angular rate sensor output counts.

Ω_{Wt_i}, $K_{Mis_{ij}}$ = Elements in row i of column i of Ω_{Wt} and row i column j of K_{Mis}.

Sensor compensation applied at the m cycle rate on uncompensated computed inputs to the accelerometer size effect and anisoinertia routines in Equations (39) would be (Ref. 18 Sect. 8.1.4.1.4):

$$\eta_{ij_m} = \Omega_{Wt_i}\,\Omega_{Wt_j}\,\eta_{ijCnt_m} \qquad \Delta\alpha_{i_m} = \Omega_{Wt_i}\,\Delta\alpha_{iCnt_m} \qquad (42)$$

where

η_{ijCnt_m}, $\Delta\alpha_{iCnt_m}$ = η_{ij_m}, $\Delta\alpha_{i_m}$ computed with uncompensated sensor pulse output data.

Similar but more complicated operations are required for post *l* cycle sculling and scrolling compensation for sensor error (Ref. 18 Sects. 8.2.2.1 and 8.2.3.1). In most applications, however, ignoring sensor misalignment effects in the sculling, scrolling (and size-effect/anisoinertia) calculations introduces negligible error. Based on this assumption, it then is reasonable to use the direct approach of performing scale factor compensation on the raw angular rate sensor and accelerometer input data (i.e., applying Ω_{Wt} and A_{Wt}) at the *l* cycle rate, and then applying the scale factor compensated signals as input to the sculling, scrolling (and accelerometer size effect/anisoinertia) *l* cycle computation algorithms (Equations (26), (28) and (39)). However, such an approach can still leave significant error in the sculling/scrolling computations executed using scale factor compensated sensor data without accelerometer size-effect compensation. Reference 18, Section 8.1.4.1 shows that the residual sculling error can be accurately approximated and corrected with:

$$\delta\underline{v}_{Scul\text{-}SizeC_m} \approx \int_{t_{m-1}}^{t_m} \frac{1}{2}\left(\underline{\alpha}(t) \times \delta\underline{a}_{Size} + \delta\underline{\upsilon}_{SizeC}(t) \times \underline{\omega}_{IB}\right) dt \qquad \delta\underline{\upsilon}_{SizeC}(t) \approx \int_{t_{m-1}}^{t} \delta\underline{a}_{Size}\, d\tau \qquad (43)$$

where

$\delta\underline{v}_{Scul\text{-}SizeC_m}$ = Size effect correction to be applied to a $\Delta\underline{v}_{Scul_m}$ sculling term calculated with accelerometer data not containing size effect compensation.

The $\delta\underline{v}_{Scul\text{-}SizeC_m}$ correction is applied at the m cycle rate by augmenting $\Delta\underline{v}_{SF_m}^{B_{m-1}}$ and $\Delta\underline{R}_{SF_m}^{B}$ in Equations (14) and (15) as follows:

$$\Delta\underline{v}_{SF_m}^{B_{m-1}} = \underline{\upsilon}_m + \Delta\underline{v}_{Rot_m} + \Delta\underline{v}_{Scul_m} - \delta\underline{v}_{Scul\text{-}SizeC_m}$$

$$\Delta\underline{R}_{SF_m}^{B} = \underline{S}\underline{\upsilon}_m + \Delta\underline{R}_{Rot_m} + \Delta\underline{R}_{Scrl_m} - \frac{1}{2}\,\delta\underline{v}_{Scul\text{-}SizeC_m}\,T_m \qquad (44)$$

Reference 18, Section 8.1.4.1.2 shows that $\delta\underline{v}_{Scul\text{-}SizeC_m}$ in (43) can be accurately approximated by the following algorithm whose form and magnitude is similar to the basic Equation (39) size-effect compensation algorithm:

$$\begin{aligned}\delta v_{Scul\text{-}SizeCY_m} = f_{Size}\Big\{ & \frac{1}{2}\alpha_{Z_m}\left[\left(\Delta\alpha'_{Y_m} + \Delta\alpha'_{Y_{m-1}}\right) l_{Z_1} - \left(\Delta\alpha'_{Z_m} + \Delta\alpha'_{Z_{m-1}}\right) l_{Y_1}\right] \\ & - \frac{1}{2}\alpha_{X_m}\left[\left(\Delta\alpha'_{X_m} + \Delta\alpha'_{X_{m-1}}\right) l_{Y_3} - \left(\Delta\alpha'_{Y_m} + \Delta\alpha'_{Y_{m-1}}\right) l_{X_3}\right] \\ & + \eta_{XX_m} l_{Y_3} + \eta_{ZZ_m} l_{Y_1} - \eta_{XY_m} l_{X_3} - \eta_{YZ_m} l_{Z_1}\Big\}\end{aligned} \tag{45}$$

$\delta v_{Scul\text{-}SizeCZ_m}$, $\delta v_{Scul\text{-}SizeCX_m}$ = Similarly by permuting subscripts.

where

$\delta v_{Scul\text{-}SizeCi_m}$ = i^{th} B Frame component of $\delta\underline{v}_{Scul\text{-}SizeC_m}$.

$\Delta\alpha'_{i_m}$ = i^{th} component of $\Delta\alpha_{i_m}$ with only scale factor compensation.

α_{i_m} = i^{th} component of $\underline{\alpha}_m$.

The alternative to using (44) with (45) is to apply the Equations (39) size-effect compensation at the high speed *l* cycle rate to the scale factor compensated accelerometer data (i.e., using scale factor compensated $\Delta\underline{\alpha}_l$ angular rate sensor data for $\Delta\alpha_{i_m}$ with η_{ij_m} replaced by $\Delta\alpha_{i_l}\Delta\alpha_{j_j}$). The sculling computation would then be performed with the size-effect compensated accelerometer data, thereby eliminating the Equations (43) error effect.

5.5 Compensation for Sensor Triad Attitude Error

The K_{Mis} and L_{Mis} misalignment error compensation coefficients described in Section 5.2 represent misalignment of the strapdown sensor axes relative to nominally defined B Frame sensor coordinates. An additional misalignment to be compensated in the INS is misalignment of the nominal B Frame relative to the reference axes of the user vehicle in which the INS is installed.

The attitude of the vehicle in which the strapdown inertial navigation system (INS) is installed is determined from the attitude direction matrix C_B^N, inertial sensor assembly mounting misalignments (relative to the INS mount), and the orientation of the INS mount relative to user vehicle reference axes. An attitude direction cosine matrix relating the user vehicle and locally level attitude reference axes can be written as (Ref. 18 Sect. 8.3):

$$C_{VRF}^N = C_B^N \left(C_B^M\right)^T C_{VRF}^M \tag{46}$$

where

M = INS mount coordinate frame (the B Frame is nominally aligned to the M Frame).
VRF = User vehicle reference axes.

The C_B^M direction cosine matrix can be defined without approximation in terms of the associated rotation vector components as follows:

$$C_B^M = I + \frac{\sin J}{J}\left(\underline{J}\times\right) + \frac{(1 - \cos J)}{J^2}\left(\underline{J}\times\right)^2 \tag{47}$$

where

$\underline{J}$, J = Sensor triad mount misalignment rotation error vector and its magnitude.

The $\underline{J}$ components are compensation coefficients measured during system calibration (Ref. 18 Sect. 18.4.7.4). The C^M_{VRF} matrix is a function of the particular mount orientation in the user vehicle.

6. STRAPDOWN INERTIAL NAVIGATION ERROR PROPAGATION EQUATIONS

The overall strapdown INS design process requires supporting analyses to develop and verify performance specifications. This generally entails the use of a strapdown INS error model in the form of time rate differential equations that describe the error response of INS computed attitude/velocity/position data. Such error models are also fundamental to the design of Kalman filters used, in conjunction with other system inputs, for correcting the INS errors. This section describes strapdown INS error model equations that represent the INS attitude/velocity/position navigation parameter integration routine response to sensor errors (i.e., excluding the effect of algorithm and computer finite word-length error, errors that are generally negligible in a well designed modern day INS compared to sensor error effects). The term "sensor error" used in this section refers to the residual error in the sensor signals after applying the Section 5 compensation corrections. It is only the residual sensor errors that generate INS navigation parameter output errors. The residual sensor errors arise from inaccuracy in measuring the sensor compensation coefficients, sensor random noise outputs that are not accounted for in the compensation algorithms, short and long term sensor instabilities, and variations in actual sensor performance from the analytical models in Section 5.1 that formed the basis for the sensor compensation algorithms.

6.1 Typical Strapdown Error Parameters

An important part of strapdown INS error model development is the definition (and selection) of attitude/velocity/position error parameters used in the error model and their relationship to the INS integration computed navigation parameters (or to a hypothetical set of INS navigation parameters that are analytically related to the INS computed set). The INS computed navigation parameters described in Sections 2 - 4 are the C^N_B matrix for attitude, the $\underline{v}^N$ vector for velocity, the C^E_N matrix for horizontal earth referenced position, and altitude h for vertical earth referenced position. These contain 22 individual scalar parameters, each of which develop errors in response to sensor error. Furthermore, the 18 error parameters associated with the C^N_B and C^E_N matrices (9 elements each) are not independent due to natural orthogonality/normality constraints that govern all direction cosine matrices. To circumvent the problem of dealing with the attendant complexities, navigation error is typically described in terms of three navigation error vectors (for attitude, velocity, and position), each consisting of three independent error components. The error in the INS computed navigation parameters (in this case, C^N_B, $\underline{v}^N$, C^E_N and h) are analytical functions of the independent error vector parameters. For example, the N Frame components of a commonly used set of attitude, velocity, and position error parameters is (Ref. 18 Sects. 12.2.1-12.2.3 and 12.5) :

$$\left(\underline{\psi}^N\times\right) \equiv C^N_E \left[I - \hat{C}^E_B\, C^B_E\right] C^E_N + \left[\left(C^N_B\, \delta\underline{\alpha}^B_{Quant}\right)\times\right]$$

$$\delta\underline{V}^N \equiv C^N_E \left(\hat{\underline{v}}^E - \underline{v}^E\right) - C^N_B\, \delta\underline{\upsilon}^B_{Quant} \qquad (48)$$

$$\delta\underline{R}^N \equiv C^N_E \left(\hat{\underline{R}}^E - \underline{R}^E\right) = R\left(C^N_E\, \hat{C}^E_N - I\right) \underline{u}^N_{Up} + \delta h\, \underline{u}^N_{Up}$$

where

$\hat{}$ = Designator for a system computer calculated quantity containing error. The quantity without the $\hat{}$ designation is by definition error free (e.g., C_B^A is error free and $\hat{C}_B^A$ contains errors).

$\underline{\psi}$ = Small angle error rotation vector associated with the computed C_B^E attitude matrix.

$\delta\underline{V}$ = Error in the computed $\underline{v}$ velocity vector relative to the earth measured in the E Frame.

$\delta\underline{R}$ = Error in the computed position vector from earth's center $\underline{R}$ measured in the E Frame.

$\delta\underline{\alpha}_{Quant}$, $\delta\underline{\upsilon}_{Quant}$ = Angular rate sensor and accelerometer triad quantization error residual (remaining after applying quantization compensation - Ref. 18 Sect. 8.1.3 and subsections).

The quantization terms in the $\underline{\psi}$ and $\delta\underline{V}$ equations are included to facilitate differential error equation modeling (See further explanation at conclusion of Section 6.2 to follow).

An equivalent set of attitude, velocity, position error parameters can also be defined that are more directly related to the C_B^N, $\underline{v}^N$, C_N^E, h navigation parameters computed by direct integration of Equations (1), (6) and (7) (previous references):

$$\left(\underline{\gamma}^N\times\right) \equiv I - \hat{C}_B^N C_N^B + \left[\left(C_B^N \delta\underline{\alpha}_{Quant}^B\right)\times\right]$$

$$\delta\underline{v}^N \equiv \hat{\underline{v}}^N - \underline{v}^N - C_B^N \delta\underline{\upsilon}_{Quant}^B \qquad (49)$$

$$\left(\underline{\varepsilon}^N\times\right) \equiv C_E^N \hat{C}_N^E - I$$

$$\delta h \equiv \hat{h} - h$$

where

$\underline{\gamma}$ = Small angle error rotation vector in the computed C_B^N attitude matrix.

$\delta\underline{v}$ = Error in computed velocity measured in the N Frame.

$\underline{\varepsilon}$ = Small angle error rotation vector in the computed C_N^E position matrix.

δh = Error in computed altitude.

The two sets of navigation error parameters are analytically related through (previous references):

$$\underline{\psi}^N = \underline{\gamma}^N - \underline{\varepsilon}^N$$

$$\delta\underline{V}^N = \delta\underline{v}^N + \underline{\varepsilon}^N \times \underline{v}^N \qquad (50)$$

$$\delta\underline{R}^N = R\left(\underline{\varepsilon}^N \times \underline{u}_{Up}^N\right) + \delta h\, \underline{u}_{Up}^N$$

or the equivalent inverse relationships:

$$\underline{\varepsilon}^N = \frac{1}{R}\left(\underline{u}_{Up}^N \times \delta\underline{R}^N\right) + \varepsilon_{ZN}\,\underline{u}_{Up}^N$$

$$\delta h = \underline{u}_{Up}^N \cdot \delta\underline{R}^N \qquad (51)$$

$$\delta\underline{v}^N = \delta\underline{V}^N - \underline{\varepsilon}^N \times \underline{v}^N$$

$$\underline{\gamma}^N = \underline{\psi}^N + \underline{\varepsilon}^N$$

where

ε_{ZN} = Local vertical component of $\underline{\varepsilon}$ (projection on the N Frame Z axis along $\underline{u}_{Up}$).
R = Distance from earth's center to the current position location (magnitude of $\underline{R}$).

6.2 Inertial Sensor Error Parameters

Classical error models for the angular rate sensor and accelerometer triad outputs following compensation (in which the error in accelerometer size effect and anisoinertia compensation is ignored as negligible) are as follows (Ref. 18 Sects. 12.4 - 12.5):

$$\delta\underline{\omega}_{IB}^B = \delta K_{Scal/Mis}\;\underline{\omega}_{IB}^B + \delta\underline{K}_{Bias} + \delta\,\underline{\omega}_{Rand}$$

$$\delta\underline{a}_{SF}^B = \delta L_{Scal/Mis}\;\underline{a}_{SF}^B + \delta\underline{L}_{Bias} + \delta\underline{a}_{Rand} \qquad (52)$$

where

$\delta\underline{\omega}_{IB}^B$, $\delta\underline{a}_{SF}^B$ = Angular rate sensor and accelerometer triad vector error residuals following sensor compensation but excluding $\delta\underline{\alpha}_{Quant}$, $\delta\underline{\upsilon}_{Quant}$ quantization compensation error residuals.

$\delta K_{Scal/Mis}$, $\delta L_{Scal/Mis}$ = Residual angular rate sensor and accelerometer scale-factor/misalignment error matrices remaining after applying Ω_{Wt}, K_{Mis}, A_{Wt}, L_{Mis} compensation in Equations (36).

$\delta\underline{K}_{Bias}$, $\delta\underline{L}_{Bias}$ = Residual angular rate sensor and accelerometer bias error vectors remaining after applying $\underline{K}_{Bias}$, $\underline{L}_{Bias}$ compensation in Equations (36).

Note that the $\delta\underline{\alpha}_{Quant}$, $\delta\underline{\upsilon}_{Quant}$ quantization compensation error residuals do not appear in the Equations (52) $\delta\underline{\omega}_{IB}^B$, $\delta\underline{a}_{SF}^B$ error definitions, but instead, show in the Equations (48) - (49) navigation parameter error vectors. Reference 19 and Reference 18 Section 12.5 show that this form results in the navigation error parameter time rate propagation equations being in standard error state dynamic format (with quantization noise inputs appearing directly, not as their derivatives) as shown next.

6.3 Error Parameter Propagation Equations

The $\underline{\psi}$, $\delta\underline{V}$, $\delta\underline{R}$ error parameters defined in Section 6.1 propagate in N Frame coordinates as (Ref. 18 Sects. 12.3.3 and 12.5.1):

$$\dot{\underline{\psi}}^{N} = - C_B^N \, \delta\underline{\omega}_{IB}^B - \underline{\omega}_{IN}^N \times \underline{\psi}^N + C_B^N \left(\underline{\omega}_{IB}^B \times \delta\underline{\alpha}_{Quant} \right)$$

$$\delta\dot{\underline{V}}^{N} = C_B^N \, \delta\underline{a}_{SF}^B + \underline{a}_{SF}^N \times \underline{\psi}^N - \frac{g}{R} \delta\underline{R}_H^N + F(h) \frac{g}{R} \delta R \, \underline{u}_{Up}^N - \left(\underline{\omega}_{IE}^N + \underline{\omega}_{IN}^N \right) \times \delta\underline{V}^N + \delta\underline{g}_{Mdl}^N$$
$$- \left(\underline{a}_{SF}^N \times \right) C_B^N \, \delta\underline{\alpha}_{Quant} - \left[\left(C_B^N \, \underline{\omega}_{IB}^B + \underline{\omega}_{IE}^N \right) \times \right] C_B^N \, \delta\underline{\upsilon}_{Quant}$$

$$F(h) = 2 \quad For \quad h \geq 0 \qquad\qquad F(h) = -1 \quad For \quad h < 0 \qquad\qquad (53)$$

$$\delta\dot{\underline{R}}^{N} = \delta\underline{V}^N - \underline{\omega}_{EN}^N \times \delta\underline{R}^N + C_B^N \, \delta\underline{\upsilon}_{Quant}$$

$$\delta\underline{R}_H^N = \delta\underline{R}^N - \delta R \, \underline{u}_{Up}^N$$

$$\delta R = \underline{u}_{Up}^N \cdot \delta\underline{R}^N$$

where

$\delta\underline{R}_H$, δR = Horizontal and upward vertical components of $\delta\underline{R}$.

$\delta\underline{g}_{Mdl}$ = Modeling error in $\underline{g}$ produced by variations in true gravity from the model used in the system computer.

Note that the vertical velocity error equations are different for positive compared to negative altitudes. This is a manifestation of the difference in gravity model below versus above the earth's surface (Ref. 18 Sect. 5.4).

Equations (53) can be integrated to calculate the response of the attitude, velocity, position errors in a strapdown INS as impacted by accelerometer, angular rate sensor, and gravity model approximation errors. The equations are based on the assumption that the INS navigation parameter integration algorithm error and computer round-off error is negligibly small.

A similar set of N Frame error propagation equations exist for the Equations (49) $\underline{\gamma}$, $\delta\underline{v}$, $\underline{\varepsilon}$, δh error parameters (Ref. 18 Sects. 12.3.4 and 12.5.2). Equations (53) for $\underline{\psi}$, $\delta\underline{V}$, $\delta\underline{R}$ and the equivalent set for $\underline{\gamma}$, $\delta\underline{v}$, $\underline{\varepsilon}$, δh can be derived from the differential of any set of strapdown inertial navigation error propagation equations (e.g., the set given in Section 2) with the appropriate definitions substituted for the navigation parameter error terms (e.g., Equations (48) or (49)). Alternatively, Reference 18 Section 12.3.6 (and subsections) shows that one set of error parameter propagation equations can be derived from another by applying the equivalency equations relating the parameters (e.g., Equations (50) or (51)). It is important to recognize that the parameters selected to describe the error characteristics of a particular INS can be any convenient set and not necessarily those derived from the navigation parameter differential equations actually implemented in the INS software. Thus, any set of error propagation equations can be used to model the error characteristics of any INS, provided that the error propagation equations and INS navigation parameter integration algorithms are analytically correct without singularities over the range of interest, and that the sensor error models are appropriate for the application.

7. CONCLUDING REMARKS

Computational operations in strapdown inertial navigation systems are analytically traceable to basic time rate differential equations of rotational and translational motion as a function of angular-rate/specific-force-acceleration vectors and local gravitation. Modern day strapdown INS computer capabilities allow the use of navigation parameter integration algorithms based on exact solutions to the differential equations.

This considerably simplifies the software validation process and can result in a single set of universal algorithms that can be used over a broad range of strapdown applications. Exact attitude updating algorithms based on direction cosines or an attitude quaternion are analytically equivalent with identical error characteristics that are a function of the error in the same computed attitude rotation vector input to each. Modern day strapdown computational algorithms and computer capabilities render the computational error negligible compared to sensor error effects.

The angular-rate/specific-force-acceleration vectors input to the strapdown INS digital integration algorithms are measured by angular rate sensors and accelerometers whose errors are compensated in the strapdown system computer based on classical error models for the inertial sensors. Strapdown INS attitude/velocity/position output errors are produced by errors remaining in the inertial sensor signals following compensation (due to sensor error model inaccuracies, sensor error instabilities, sensor calibration errors) and to gravity modeling errors. Resulting INS navigation error characteristics can be defined by various attitude, velocity, position error parameters that are analytically equivalent. Any set of navigation parameter error propagation equations can be used to predict the error performance of any strapdown INS. The navigation error parameters used in the error propagation equations do not have to be directly related to the navigation parameters used in the strapdown INS computer integration algorithms.

REFERENCES

1. Bortz J. E., "A New Mathematical Formulation for Strapdown Inertial Navigation", *IEEE Transactions on Aerospace and Electronic Systems*, Volume AES-7, No. 1, January 1971, pp. 61-66.

2. Britting, K. R., *Inertial Navigation System Analysis*, John Wiley and Sons, New York, 1971.

3. "Department Of Defense World Geodetic System 1984", NIMA TR8350.2, Third Edition, 4 July 1997.

4. Ignagni, M. B., "Optimal Strapdown Attitude Integration Algorithms", *AIAA Journal Of Guidance, Control, And Dynamics*, Vol. 13, No. 2, March-April 1990, pp. 363-369.

5. Ignagni, M. B., "Efficient Class Of Optimized Coning Compensation Algorithms", *AIAA Journal Of Guidance, Control, And Dynamics*, Vol. 19, No. 2, March-April 1996, pp. 424-429.

6. Ignagni, M. B., "Duality of Optimal Strapdown Sculling and Coning Compensation Algorithms", *Journal of the ION*, Vol. 45, No. 2, Summer 1998.

7. Jordan, J. W., "An Accurate Strapdown Direction Cosine Algorithm", NASA TN-D-5384, September 1969.

8. Kachickas, G. A., "Error Analysis For Cruise Systems", *Inertial Guidance*, edited by Pitman, G. R., Jr., John Wiley & Sons, New York, London, 1962.

9. Litmanovich, Y. A., Lesyuchevsky, V. M. & Gusinsky, V. Z., "Two New Classes of Strapdown Navigation Algorithms", *AIAA Journal Of Guidance, Control, And Dynamics*, Vol. 23, No. 1, January- February 2000.

10. Mark, J.G. & Tazartes, D.A., "On Sculling Algorithms", 3rd St. Petersburg International Conference On Integrated Navigation Systems, St. Petersburg, Russia, May 1996.

11. Miller, R., "A New Strapdown Attitude Algorithm", *AIAA Journal Of Guidance, Control, And Dynamics*, Vol. 6, No. 4, July-August 1983, pp. 287-291.

12. Roscoe, K. M., "Equivalency Between Strapdown Inertial Navigation Coning and Sculling Integrals/Algorithms", *AIAA Journal Of Guidance, Control, And Dynamics*, Vol. 24, No. 2, March-April 2001, pp. 201-205.

13. Savage, P. G., “A New Second-Order Solution for Strapped-Down Attitude Computation”, AIAA/JACC Guidance & Control Conference, Seattle, Washington, August 15-17, 1966.

14. Savage, P. G., “Strapdown Sensors”, *Strapdown Inertial Systems - Theory And Applications*, NATO AGARD Lecture Series No. 95, June 1978, Section 2.

15. Savage, P. G., “Strapdown System Algorithms”, *Advances In Strapdown Inertial Systems*, NATO AGARD Lecture Series No. 133, May 1984, Section 3.

16. Savage, P. G., “Strapdown Inertial Navigation System Integration Algorithm Design Part 1 - Attitude Algorithms”, *AIAA Journal Of Guidance, Control, And Dynamics*, Vol. 21, No. 1, January-February 1998, pp. 19-28.

17. Savage, P. G., “Strapdown Inertial Navigation System Integration Algorithm Design Part 2 - Velocity and Position Algorithms”, *AIAA Journal Of Guidance, Control, And Dynamics*, Vol. 21, No. 2, March-April 1998, pp. 208-221.

18. Savage, P. G., *Strapdown Analytics*, Strapdown Associates, Inc., Maple Plain, Minnesota, 2000

19. Savage, P. G., "Analytical Modeling of Sensor Quantization in Strapdown Inertial Navigation Error Equations", *AIAA Journal Of Guidance, Control, And Dynamics*, Vol. 25, No. 5, September-October 2002, pp. 833-842.

20. Savage, P. G., "Strapdown System Performance Analysis", *Advances In Navigation Sensors and Integration Technology*, NATO RTO Lecture Series No. 232, October 2003, Section 4.

Strapdown System Performance Analysis

Paul G. Savage
Strapdown Associates, Inc.
Maple Plain, Minnesota 55359 USA

ABSTRACT

This paper provides an overview of assorted analysis techniques associated with strapdown inertial navigation systems. The process of strapdown system algorithm validation is discussed. Closed-form analytical simulator drivers are described that can be used to exercise/validate various strapdown algorithm groups. Analytical methods are presented for analyzing the accuracy of strapdown coning, sculling and position integration algorithms (including position algorithm folding effects) as a function of algorithm repetition rate and system vibration inputs. Included is a description of a simplified analytical model that can be used to translate system vibrations into inertial sensor inputs as a function of sensor assembly mounting imbalances. Strapdown system static drift and rotation test procedures/equations are described for determining strapdown sensor calibration coefficients. The paper overviews Kalman filter design and covariance analysis techniques and describes a general procedure for validating aided strapdown system Kalman filter configurations. Finally, the paper discusses the general process of system integration testing to verify that system functional operations are performed properly and accurately by all hardware, software and interface elements.

COORDINATE FRAMES

As used in this paper, a coordinate frame is an analytical abstraction defined by three mutually perpendicular unit vectors. A coordinate frame can be visualized as a set of three perpendicular lines (axes) passing through a common point (origin) with the unit vectors emanating from the origin along the axes. In this paper, the physical position of each coordinate frame's origin is arbitrary. The principal coordinate frames utilized are the following:

B Frame = "Body" coordinate frame parallel to strapdown inertial sensor axes.
N Frame = "Navigation" coordinate frame having Z axis parallel to the upward vertical at the local position location. A "wander azimuth" N Frame has the horizontal X, Y axes rotating relative to non-rotating inertial space at the local vertical component of earth's rate about the Z axis. A "free azimuth" N Frame would have zero inertial rotation rate of the X, Y axes around the Z axis. A "geographic" N Frame would have the X, Y axes rotated around Z to maintain the Y axis parallel to local true north.
E Frame = "Earth" referenced coordinate frame with fixed angular geometry relative to the earth.
I Frame = "Inertial" non-rotating coordinate frame.

NOTATION

$\underline{V}$ = Vector without specific coordinate frame designation. A vector is a parameter that has length and direction. The vectors used in the paper are classified as "free vectors", hence, have no preferred location in coordinate frames in which they are analytically described.

$\underline{V}^A$ = Column matrix with elements equal to the projection of $\underline{V}$ on Coordinate Frame A axes. The projection of $\underline{V}$ on each Frame A axis equals the dot product of $\underline{V}$ with the coordinate Frame A axis unit vector.

$\left(\underline{V}^A \times\right)$ = Skew symmetric (or cross-product) form of $\underline{V}^A$ represented by the square matrix $\begin{bmatrix} 0 & -V_{ZA} & V_{YA} \\ V_{ZA} & 0 & -V_{XA} \\ -V_{YA} & V_{XA} & 0 \end{bmatrix}$ in which V_{XA}, V_{YA}, V_{ZA} are the components of $\underline{V}^A$. The matrix product of $\left(\underline{V}^A \times\right)$ with another A Frame vector equals the cross-product of $\underline{V}^A$ with the vector in the A Frame.

$C_{A_2}^{A_1}$ = Direction cosine matrix that transforms a vector from its Coordinate Frame A_2 projection form to its Coordinate Frame A_1 projection form.

$\underline{\omega}_{A_1A_2}$ = Angular rate of Coordinate Frame A_2 relative to Coordinate Frame A_1. When A_1 is non-rotating, $\underline{\omega}_{A_1A_2}$ is the angular rate that would be measured by angular rate sensors mounted on Frame A_2.

$\dot{(\,)} = \frac{d(\,)}{dt}$ = Derivative with respect to time.

t = Time.

1. INTRODUCTION

An important part of strapdown inertial navigation system (INS) analysis deals with performance assessment of particular technology elements. One of the most common is covariance simulation analysis which determines the expected system errors based on statistical estimation. This paper discusses performance analysis methods which, although infrequently reported, are a fundamental part of the design and accuracy assessment of aided and unaided inertial systems: inertial computation algorithm validation, system vibration effects analysis, system testing for inertial sensor calibration error, and Kalman filter validation.

The primary computational elements in a strapdown inertial navigation system consist of integration operations for calculating attitude, velocity and position navigation parameters using strapdown angular rate and specific force acceleration for input. These operations are resident in the system computer and are comprised of computational algorithms designed to perform the required digital integration operations. An important part of the algorithm design is the validation process used to assure that the digital integration operations accurately create an attitude, velocity, position history corresponding to a continuous integration of time rate differential equations for the navigation parameters. Structuring the algorithms such that they are primarily based on exact closed-form solutions to the differential equations significantly simplifies the validation process, allowing it to be executed using simple closed-form exact solution reference truth models that are application independent. This paper provides examples of such truth models describing there use in validating representative strapdown algorithms.

The accuracy of well-structured strapdown computational algorithms is ultimately limited by their ability to perform their designated functions in the presence of sensor vibrations. The algorithm repetition rate is a determining factor in this regard which must be selected small enough to meet specified software accuracy requirements. This paper describes some simple analytical techniques for predicting strapdown inertial sensor dynamic motion and resulting algorithm error in the presence of angular/linear inertial sensor vibrations. Included is a description of a simplified sensor-assembly/mount structural dynamic analytical model for translating INS input vibration into strapdown sensor inputs.

Following inertial sensor calibration and strapdown inertial system final assembly, the system must be tested to verify proper performance and in the process, assess the residual calibration errors remaining in the inertial sensor compensation coefficients. The paper describes two commonly used system level tests, the Strapdown Drift Test (for measuring angular rate sensor bias residuals), and the Strapdown Rotation Test

(for measuring angular-rate-sensor/accelerometer misalignment/scale-factor-error and accelerometer bias). Both tests are structured based on measurements from a stabilized "platform" created by software operations on the strapdown sensor signals. This method considerably reduces the accuracy requirements for rotation test fixtures used in the tests.

Kalman filtering has become the standard method for updating inertial system navigation parameters (and sensor compensation coefficients) during operation (i.e., the "aided" inertial navigation system configuration). A Kalman filter is a sophisticated set of software operations processed in parallel with the normal strapdown inertial navigation integration algorithms. Proper operation of an aided inertial system depends on thorough validation of the Kalman filter software. Such a validation process is described in the paper based on a generic model of a real time Kalman filter. Included is an overview of covariance analysis techniques for assessing aided (and unaided) system performance on a statistical basis.

The paper concludes with a general discussion of system integration procedures to assure that all system hardware, software and associated interface elements function properly and accurately.

This paper is a condensed version of material originally published in the two volume textbook *Strapdown Analytics* (Reference 6) which provides a broad detailed exposition of the analytical aspects of strapdown inertial navigation technology. Equations in the paper are presented without proof. Their derivations are provided in Reference 6 as delineated throughout the paper by Reference 6 section number (or by Reference 7 Equation number which, in Reference 7, are also referenced to sections in Reference 6 for their derivation source).

2. STRAPDOWN ALGORITHM VALIDATION

A key aspect of the strapdown inertial navigation software design process is validation of the digital integration algorithms. In general this consists of operating the integration algorithms in a test computer at their specified repetition rate with inertial sensor inputs provided by a "truth model" having a corresponding navigation parameter profile (e.g., attitude, velocity, position). The navigation parameter solution generated with the strapdown algorithms under test is compared numerically against the equivalent truth model profile parameters to validate the algorithms.

The success of the validation depends on the accuracy of the truth model navigation reference solution profile accompanying the truth model sensor data. Ideally, the reference solution should be completely error free with the attitude, velocity, position parameters representing an error free integration of the truth model inertial sensor signals. In addition, the reference solution profile(s) should be designed to exercise all elements of the computational algorithms under test. In general, this dictates reference profile(s) that do not represent realistic conditions encountered in normal navigation system use. It also generally involves several simulation profiles, each designed to exercise different groupings of the computational algorithms under test.

In general, two methods can be considered for the truth model; 1. A digital integration approach in which the truth model integration algorithms are more accurate than the INS integration algorithms being validated, and 2. Closed-form analytical equations representing exact integral solutions of the inertial sensor angular-rate/linear-acceleration inputs to the INS integration algorithms. The problem with the Method 1 approach is the dilemma it presents in demonstrating the accuracy of a truth model that also contains digital integration algorithm error. This section addresses the Method 2 approach, and provides two examples from Reference 6 of closed-form analytically exact truth models for evaluating classical groupings of INS algorithms used to execute basic integration operations; 1. Attitude updating under dynamic coning conditions, 2. Attitude updating, acceleration transformation, velocity/position updating under sculling/scrolling dynamic conditions (including accelerometer size effect separation) - See Reference 6 Sections 7.1.1.1, 7.2.2.2, 7.3.3 for coning, sculling, scrolling definitions. These truth models (described in the Sections 2.1 and 2.2 to follow) are denoted as SPIN-CONE and SPIN-ROCK-SIZE.

Additional closed-form analytically exact truth models developed in Reference 6 are SPIN-ACCEL (Sect. 11.2.2) for evaluating strapdown attitude update, acceleration transformation, velocity update algorithms under constant B Frame inertial angular-rate, constant B Frame specific-force-acceleration, constant N Frame inertial angular rate; and GEN NAV (Sect. 11.2.4) for evaluating strapdown attitude update, acceleration transformation, velocity/position update algorithms during long term navigation over an ellipsoidal earth surface shape model. The SPIN-ACCEL model can be easily expanded to also provide an analytically exact position solution.

Reference 6 Section 11.2 shows how the previous defined analytical routines can be used to validate all subroutines typically utilized in a strapdown INS for attitude, velocity, position updating and associated system outputs.

Reference 6 Section 11.1 also illustrates how specialized simulators can be designed for validating high speed strapdown integration algorithms that have been designed to identically match the equivalent true continuous integrals under particular angular-rate/specific-force-acceleration input conditions. This methodology is applied in Section 2.3 to follow for the Reference 6 coning, sculling, scrolling algorithms.

2.1 SPIN-CONE Truth Model

The SPIN-CONE truth model provides exact closed-form attitude and corresponding continuous integrated body frame angular rates for a spinning body with coning motion. The difference between integrated body rates at successive strapdown software sensor sampling cycles simulate the inputs from strapdown angular rate sensors used in the attitude update routines for the software under test. The SPIN-CONE and strapdown software computed attitude solutions are compared to establish strapdown software attitude algorithm accuracy.

The SPIN-CONE truth model is based on a closed-form solution to the attitude motion described by a body spinning at a fixed magnitude rotation rate and whose spin axis is rotating at a fixed precessional rate. The geometry of the motion is described in Figure 1 which shows the spin-axis and precessional-axis to be separated by an angle β. The spin axis rotates about the precessional axis which is defined to be perpendicular to a non-rotating inertial plane. A set of body reference axes is implied in Figure 1 that rotates relative to a defined set of non-rotating coordinates. In Figure 1,

N = Non-rotating coordinate frame that is fixed to the non-rotating plane with X_N, Y_N axes in the plane and the Z_N axis perpendicular to the plane in the direction opposite the precessional rate vector.

R = Body "reference" coordinate axes fixed to the body with the X axis (X_R) along the spin axis. The R Frame is at a fixed orientation relative to B Frame sensor axes. A distinction is made between the B and R Frames so that the angular rate generated by the Figure 1 motion can have selected projections on B Frame sensor axes to test the general response of the strapdown attitude algorithms.

β = Angle between the precessional axis and the R-Frame X_R spin axis (the "cone angle") - considered constant.

ω_s = Inertial rotation rate of the body about X_R ("spin rate") - considered constant.

ω_c = Inertial precessional rate of the body X_R axis about the precessional axis which corresponds to a coning condition.

ϕ, θ, ψ = Roll, pitch, heading Euler angles of the R Frame axes relative to the N Frame.

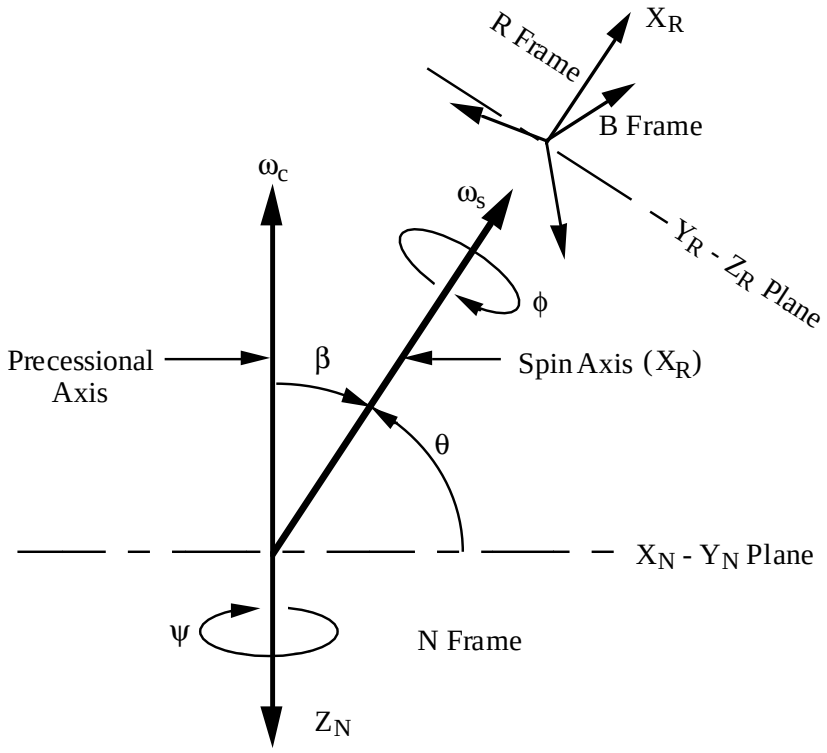


Figure 1 - SPIN-CONE Geometry

The analytical solution corresponding to the Figure 1 motion is (Ref. 6 Sects. 11.2.1.1 and 11.2.1.2):

$$\phi = (\omega_s - \omega_c \cos\beta)\, t + \phi_0 \qquad \theta = \pi/2 - \beta \qquad \psi = -\omega_c\, t \tag{1}$$

$$I\underline{\omega}^R_{IB}(t) \equiv \int_0^t \underline{\omega}^R_{IB}\, dt = \begin{bmatrix} \omega_s\, t \\ \dfrac{\omega_c \sin\beta}{(\omega_s - \omega_c \cos\beta)}(\cos\phi - \cos\phi_0) \\ -\dfrac{\omega_c \sin\beta}{(\omega_s - \omega_c \cos\beta)} \sin(\phi - \phi_0) \end{bmatrix} \tag{2}$$

$$I\underline{\omega}^B_{IB}(t) \equiv \int_0^t \underline{\omega}^B_{IB}\, dt = C^B_R\, I\underline{\omega}^R_{IB}(t) \qquad \Delta\underline{\alpha}_l \equiv \int_{t_{l-1}}^{t_l} \underline{\omega}^B_{IB}\, dt = I\underline{\omega}^B_{IB}(t_l) - I\underline{\omega}^B_{IB}(t_{l-1}) \tag{3}$$

$$\begin{aligned} C_{RN_{11}} &= \cos\theta \cos\psi \\ C_{RN_{12}} &= -\cos\phi \sin\psi + \sin\phi \sin\theta \cos\psi \\ C_{RN_{13}} &= \sin\phi \sin\psi + \cos\phi \sin\theta \cos\psi \\ C_{RN_{21}} &= \cos\theta \sin\psi \\ C_{RN_{22}} &= \cos\phi \cos\psi + \sin\phi \sin\theta \sin\psi \\ C_{RN_{23}} &= -\sin\phi \cos\psi + \cos\phi \sin\theta \sin\psi \end{aligned} \tag{4}$$

(Continued)

$$C_{RN_{31}} = -\sin\theta$$
$$C_{RN_{32}} = \sin\phi\cos\theta \qquad (4)\ \text{(Continued)}$$
$$C_{RN_{33}} = \cos\phi\cos\theta$$

$$C_B^N = C_R^N C_B^R \qquad (5)$$

where

ϕ_0 = Initial value for ϕ. The initial value for ψ is assumed to be zero.
t = Time from simulation start.
l = Truth model output cycle time index corresponding to the highest speed computation repetition rate for the algorithms under test.
$\Delta\underline{\alpha}_l$ = Integrated B Frame $\underline{\omega}_{IB}$ inertial angular rate vector from cycle l-1 to l.
$C_{RN}(i,j)$ = Element in row i column j of C_R^N.
C_B^R = Constant direction cosine matrix relating the B and R Frames.

The $\Delta\underline{\alpha}_l$ output vector would be used as the simulated angular rate sensor input to the attitude algorithms under test (e.g., Reference 7 Equations (8), (12) and (24) with zero setting for the N Frame rotation rate and l corresponding to the high speed coning algorithm computation cycle index). The C_B^N matrix represents the truth solution corresponding to the $\Delta\underline{\alpha}_l$ history for comparison with the equivalent C_B^N generated by the algorithms under test. Comparison is performed by multiplying the algorithm computed C_B^N (on the left) by the transpose of the truth model C_B^N (on the right) and comparing the result with the identity matrix (the correct value of the product when the algorithm computed C_B^N is error free) - See Reference 6 Section 11.2.1.4 for details and how results can be equated to equivalent normality, orthogonality and misalignment errors.

If the algorithms being tested are exact and properly programmed, the comparison described previously with the SPIN-CONE truth solution should show identically zero error. The attitude algorithms in Reference 7 Equations (8) and (12) are exact under zero coning motion and zero N Frame rotation rate. Hence, an exact comparison with SPIN-CONE should be obtained when using zero coning rate (i.e., setting ω_c to zero). With non-zero ω_c, the comparison with SPIN-CONE measures the error in the coning computation portion of the algorithms being tested (a function of the l cycle rate). If the coning computation algorithm is an analytically exact solution to an assumed form of the angular rate input profile (e.g., Ref. 7 Eqs. (24)), Section 2.3 to follow shows how the associated coning algorithm software can be exactly validated (i.e., with zero error).

2.2 SPIN-ROCK-SIZE Truth Model

The SPIN-ROCK-SIZE truth model provides exact closed form integrated angular rates, integrated linear accelerations, attitude, velocity and position simulating a strapdown sensor assembly undergoing spinning/sculling/scrolling dynamic motion with the individual accelerometers mounted at specified lever arm locations within the sensor assembly (i.e., simulating size effect separation). The integrated rates and accelerations are used as inputs to strapdown software algorithms under test to compute body attitude, accelerometer size effect lever arm compensation to the body navigation reference center, transformation of compensated specific force acceleration to navigation coordinates, and transformed acceleration integration to velocity and position. The strapdown software algorithm accuracy is evaluated by comparing the SPIN-

ROCK-SIZE truth model computed position, velocity and attitude with the equivalent data generated by the strapdown software algorithms under test.

The SPIN-ROCK-SIZE truth model generates navigation and inertial sensor outputs under dynamic motion around an arbitrarily specified and fixed rotation axis (Figure 2). The rotation axis is defined to be non-rotating and non-accelerating. The dynamic motion is characterized as rigid body motion around the specified axis with the specified axis located within the rotating rigid body. The strapdown sensor assembly being simulated is located in the rigid body and has its navigation reference center at a specified lever arm location from the rotation axis. Each accelerometer within the sensor assembly is located at an arbitrarily selected lever arm position. The accelerations measured by the accelerometers are created by centripetal and tangential acceleration effects produced by their lever arm displacement from the rotation axis under rigid body dynamic angular motion around the rotation axis. For this truth model, the N Frame is inertially non-rotating and gravity is zero.

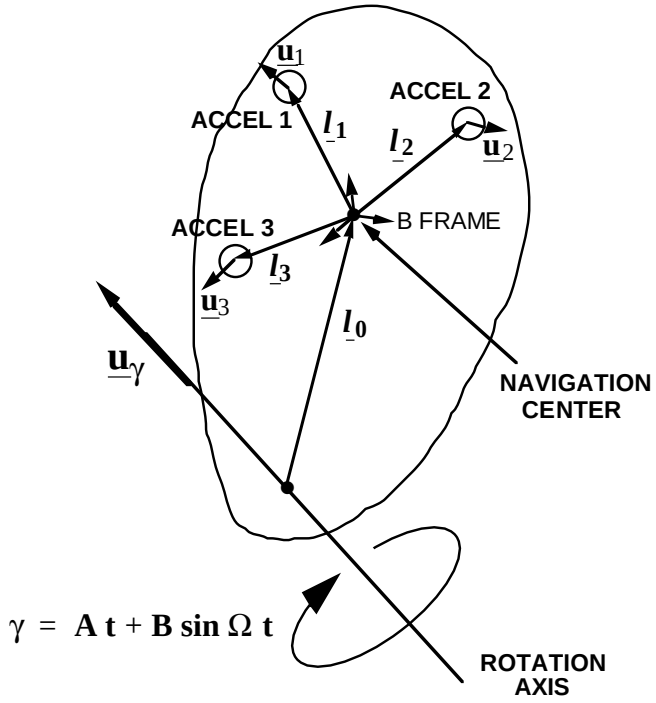


Figure 2 - SPIN-ROCK-SIZE Parameters

In Figure 2,

$\underline{l}_0$ = Position vector from the rotation axis to the navigation center.

$\underline{l}_i$ = Position vector from the navigation center to the accelerometer i (Accel i) center of seismic mass.

$\underline{u}_i$ = Accelerometer i input axis.

$\underline{u}_\gamma$ = Unit vector along the angular rotation axis.

γ = Angle of rotation about $\underline{u}_\gamma$.

A, B, Ω = Constants.

The analytical solution corresponding to the Figure 2 motion is (Ref. 6 Sects. 11.2.3.1 - 11.2.3.3):

$$\gamma = A\,t + B \sin \Omega\, t \qquad \dot{\gamma} = A + B\,\Omega \cos \Omega\, t \tag{6}$$

$$\Delta\underline{\alpha}_l = \int_{t_{l-1}}^{t_l} \underline{\omega}_{IB}^{B}\, dt = \left(\gamma(t_l) - \gamma(t_{l-1})\right) \underline{u}_\gamma^{B} \tag{7}$$

$$\Delta\upsilon_{i_l} = \int_{t_{l-1}}^{t_l} \underline{u}_i^B \cdot \underline{a}_{SF_i}^B \, dt = \underline{u}_i^B \cdot \left\{ \left[\left(f_a(t_l) - f_a(t_{l-1})\right)\left(\underline{u}_\gamma^B\times\right) + \left(f_b(t_l) - f_b(t_{l-1})\right)\left(\underline{u}_\gamma^B\times\right)^2 \right] \left(\underline{l}_0^B + \underline{l}_i^B\right) \right\} \quad (8)$$

$$f_a(t) = B\,\Omega\cos\Omega t \qquad f_b(t) = \left(A^2 + \frac{1}{2}B^2\,\Omega^2\right)t + 2\,A\,B\sin\Omega t + \frac{1}{2}B^2\,\Omega\sin\Omega t\cos\Omega t \quad (9)$$

$$C_B^N = C_{B_0}^N C_B^{B_0} \qquad C_B^{B_0} = I + \sin\gamma\left(\underline{u}_\gamma^B\times\right) + \left(1 - \cos\gamma\right)\left(\underline{u}_\gamma^B\times\right)^2 \quad (10)$$

$$\underline{v}^N = \dot{\gamma} C_B^N \left(\underline{u}_\gamma^B \times \underline{l}_0^B\right) \qquad \underline{R}^N = C_B^N \underline{l}_0^B \quad (11)$$

where

I = Identity matrix.

$C_{B_0}^N$ = Initial value of C_B^N.

$\underline{a}_{SF_i}$ = Specific force acceleration vector at the accelerometer i location. Specific force acceleration is defined as the instantaneous time rate of change of velocity imparted to a body relative to the velocity it would have sustained without disturbances in local gravitational vacuum space. Sometimes defined as total velocity change rate minus gravity. Accelerometers measure $\underline{a}_{SF}$.

$\Delta\upsilon_{i_l}$ = Integrated specific force acceleration along the accelerometer i input axis over the computation algorithm high speed l cycle time interval from l-1 to l.

The $\Delta\underline{\alpha}_l$, $\Delta\upsilon_{i_l}$ output vectors would be used as the simulated angular rate sensor and accelerometer inputs to the attitude update, acceleration transformation, velocity update, position update, size effect compensation algorithms under test (e.g., Reference 7 Equations (8), (12), (14), (15), (24), (26), (28), (37) and (39) with zero setting for the N Frame inertial rotation rate and l corresponding to the high speed coning/sculling/scrolling algorithm computation cycle index) The C_B^N matrix represents the attitude truth solution corresponding to the $\Delta\underline{\alpha}_l$ history for comparison with the equivalent C_B^N generated by the algorithms under test. Comparison is performed as described in Section 2.1. The $\underline{v}^N$ vector is the velocity truth solution used for comparison against the equivalent $\underline{v}^N$ generated by integration using the algorithms under test. The $\underline{R}^N$ vector is the truth model position solution used for comparison against the equivalent $\underline{R}^N$ generated by integration using the algorithms under test (e.g., summation of the $\Delta\underline{R}_m^N$ increments in Equations (15) of Reference 7).

If the algorithms being tested are exact and properly programmed, the comparison described previously with the SPIN-ROCK-SIZE truth solution should show identically zero error. The attitude algorithms in Reference 7 Equations (8), (12) and (24) are exact under zero N Frame rotation rate and zero coning (coning is zero when the angular rate vector is non rotating - Ref. 6 Sect. 7.1.1.1) Hence, since SPIN-ROCK-SIZE is based on constant angular rate vector direction, an exact comparison with the SPIN-ROCK-SIZE solution should be obtained. The acceleration-transformation/velocity-update/position-update algorithms in Reference 7 Equations (14), (15), (26) and (28) are exact under zero N Frame rotation rate and zero sculling/scrolling motion (sculling and scrolling are zero under constant B Frame angular rate and specific force acceleration - Ref. 6 Sects. 7.2.2.2.1 and 7.3.3.1). Constant B Frame angular rate and specific force acceleration can be generated with SPIN-ROCK-SIZE by setting the B coefficient to zero. Under this condition and zero accelerometer lever arms, an exact comparison with the SPIN-ROCK-SIZE attitude/velocity/position solution should be obtained. With non-zero B coefficient and simulated accelerometer lever arms, the comparison with SPIN-ROCK-SIZE measures the error in the

sculling/scrolling and accelerometer size effect compensation portion of the algorithms being tested. If the sculling and scrolling computation algorithms are analytically exact solutions to an assumed form of the angular-rate/specific-force-acceleration input profile (e.g., Ref. 7 Eqs. (26) and (28)), Section 2.3 to follow shows how the associated sculling/scrolling algorithm software can be exactly validated (i.e., with zero error).

2.3 Specialized Simulators For High Speed Algorithm Validation

High speed strapdown inertial digital integration algorithms designed to be exact under assumed analytic forms of their inertial sensor inputs can be validated numerically using specialized simulators. The general methodology is described in Reference 6 Section 11.1. For example, consider the strapdown inertial high speed coning, sculling, scrolling integration functions derived in Reference 6, Sections 7.1.1.1, 7.2.2.2, 7.3.3 and summarized in Section 3.4 of Reference 7:

$$\underline{\alpha}(t) = \int_{t_{m-1}}^{t} \underline{\omega}_{IB}^{B}\, d\tau \qquad \underline{\upsilon}(t) = \int_{t_{m-1}}^{t} \underline{a}_{SF}^{B}\, d\tau \qquad \text{Integrated inertial sensor signals}$$

$$\underline{S}_{\alpha}(t) = \int_{t_{m-1}}^{t} \int_{t_{m-1}}^{\tau} \underline{\omega}_{IB}^{B}\, d\tau_1\, d\tau \qquad \underline{S}_{\upsilon}(t) = \int_{t_{m-1}}^{t} \int_{t_{m-1}}^{\tau} \underline{a}_{SF}^{B}\, d\tau_1\, d\tau \qquad \begin{matrix}\text{Doubly integrated}\\ \text{inertial sensor signals}\end{matrix}$$

$$\underline{\beta}_m = \frac{1}{2}\int_{t_{m-1}}^{t_m} \left(\underline{\alpha}(t) \times \underline{\omega}_{IB}^{B}\right) dt \qquad (12)$$

$$\Delta\underline{v}_{Scul}(t) = \int_{t_{m-1}}^{t} \frac{1}{2}\left(\underline{\alpha}(\tau) \times \underline{a}_{SF}^{B} + \underline{\upsilon}(\tau) \times \underline{\omega}_{IB}^{B}\right) d\tau \qquad \Delta\underline{v}_{Scul_m} = \Delta\underline{v}_{Scul}(t_m)$$

$$\Delta\underline{R}_{Scrl_m} = \frac{1}{6}\int_{t_{m-1}}^{t_m} \left(6\,\Delta\underline{v}_{Scul}(t) - \underline{S}_{\alpha}(t) \times \underline{a}_{SF}^{B} + \underline{S}_{\upsilon}(t) \times \underline{\omega}_{IB}^{B} + \underline{\alpha}(t) \times \underline{\upsilon}(t)\right) dt$$

where

m = Navigation parameter (i.e., attitude, velocity, position) update cycle time index.
$\underline{a}_{SF}$ = Specific force acceleration vector that would be measured by the strapdown accelerometers.
$\underline{\beta}_m$ = Coning contribution to attitude motion from cycle time m-1 to m.
$\Delta\underline{v}_{Scul_m}$ = Sculling contribution to velocity motion from cycle time m-1 to m.
$\Delta\underline{R}_{Scrl_m}$ = Sculling contribution to position motion from cycle time m-1 to m.

In Reference 6 Sections 7.1.1.1.1, 7.2.2.2.2 and 7.3.3.2, digital integration algorithms are designed to implement the previous operations using a high speed *l* cycle computation rate between attitude, velocity, position m cycle updates. The algorithms (summarized in Reference 7 Equations (24), (26) and (28)) are designed to provide exact solutions to the above operations under linearly ramping angular rate and specific force acceleration profiles between *l* cycles. Algorithm inputs are integrated angular rate and specific force acceleration increments between *l* cycles, representing the input signals from strapdown angular rate sensors and accelerometers. A simple method for numerically validating that the algorithms perform as designed is to build a specialized simulator that generates integrated inertial sensor increment inputs to the algorithms based on a linear ramping angular-rate/specific-force-acceleration profile. The algorithms to be validated would then be operated in the simulation at their *l* cycle rate using the simulated sensor incremental inputs, and evaluated at the m cycle times. For correctly derived and software implemented algorithms, results

should exactly match the true analytic integral of Equations (12) under linear ramping angular-rate/specific-force-acceleration conditions:

$$\underline{\omega}_{IB}^{B} = \underline{A}_0 + \underline{A}_1 (t - t_{m-1}) \qquad \underline{a}_{SF}^{B} = \underline{B}_0 + \underline{B}_1 (t - t_{m-1}) \tag{13}$$

where

$\underline{A}_0, \underline{A}_1, \underline{B}_0, \underline{B}_1$ = Selected simulation constants.

Substituting Equations (13) into (12) and carrying out the integral operations analytically yields the true analytic solutions corresponding to the assumed linear ramping profiles:

$$\underline{\beta}_m = \frac{1}{12}\left(\underline{A}_0 \times \underline{A}_1\right) T_m^3 \qquad \Delta\underline{v}_{Scul_m} = \frac{1}{12}\left(\underline{A}_0 \times \underline{B}_1 + \underline{B}_0 \times \underline{A}_1\right) T_m^3$$
$$\Delta\underline{R}_{Scrl_m} = \frac{1}{72}\left(\underline{A}_0 \times \underline{B}_1 - 2\,\underline{A}_1 \times \underline{B}_0\right) T_m^4 - \frac{1}{360}\left(\underline{A}_1 \times \underline{B}_1\right) T_m^5 \tag{14}$$

where

T_m = Time interval between computation m cycles.

The *l* cycle incremental inputs to the algorithms being validated are the integrals of Equations (13) between *l* cycles:

$$\Delta\underline{\alpha}_l = \int_{t_{l-1}}^{t_l} \underline{\omega}_{IB}^{B}\, dt = \underline{A}_0 T_l + \frac{1}{2}\underline{A}_1 \left((t_l - t_{m-1})^2 - (t_{l-1} - t_{m-1})^2\right)$$
$$\Delta\underline{\upsilon}_l = \int_{t_{l-1}}^{t_l} \underline{a}_{SF}^{B}\, dt = \underline{B}_0 T_l + \frac{1}{2}\underline{B}_1 \left((t_l - t_{m-1})^2 - (t_{l-1} - t_{m-1})^2\right) \tag{15}$$

where

l = High speed algorithm computation cycle index (within the m update cycle).

T_l = Time interval between *l* cycles.

$\Delta\underline{\alpha}_l$ = Summation of integrated angular rate sensor output increments from cycle time *l*-1 to *l*.

$\Delta\underline{\upsilon}_l$ = Summation of integrated accelerometer output increments from cycle time *l*-1 to *l*.

Operating the Reference 6 Chapter 7 high speed digital integration algorithms with Equation (15) inputs should provide results at the m cycle times that identically match Equations (14) for any values selected for the $\underline{A}_0, \underline{A}_1, \underline{B}_0, \underline{B}_1$ constants.

3. VIBRATION EFFECTS ANALYSIS

Strapdown inertial navigation integration algorithms are designed to accurately account for three-dimensional high frequency angular and linear vibration of the sensor assembly. If not properly accounted for, such motion can lead to systematic attitude/velocity/position error build-up. The high speed algorithms described in Reference 7 Equations (24), (26), and (28) to measure these effects (i.e., coning, sculling, scrolling, doubly integrated sensor input) are based on approximations to the form of the angular-rate/specific-force profiles during the high speed update interval. An important part of the algorithm design is their accuracy evaluation under hypothesized vibration exposure of the strapdown INS in the user vehicle, the subject of this section. Algorithm performance evaluation results, used in design/synthesis iterative fashion, eventually set the order of the algorithm selected and its required repetition rate in the INS computer.

Since the sensor assembly is dynamically coupled to the INS mount through the INS structure (in many cases including mechanical isolators and their imbalances), vibrations input to the INS mount become dynamically distorted as they translate into inertial sensor outputs provided to the navigation algorithms. Included in this section is a description of a simplified analytical model for characterizing the dynamic response of an INS sensor assembly to input vibration and its use in system performance evaluation.

All equations in this section are written in B Frame coordinates whose explicit designation has been deleted for analytical simplicity.

3.1 System Response Under Sinusoidal Vibration

In this section we describe the effect of sensor assembly linear and angular sinusoidal vibration on system navigational performance. The section is divided into two major subsections covering true attitude, velocity, position motion vibration response, and the vibration response of particular algorithms used in the system attitude, velocity, position digital integration routines. The material is selected from Section 10.1 (and its subsections) of Reference 6 which also covers other vibration induced effects.

The attitude response discussion is based on the following B Frame input angular vibration designed to produce coning motion:

$$\underline{\theta}(t) = \underline{u}_x \theta_{0_x} \sin\left(\Omega t - \varphi_{\theta_x}\right) + \underline{u}_y \theta_{0_y} \sin\left(\Omega t - \varphi_{\theta_y}\right) \tag{16}$$

where

$\underline{\theta}(t)$ = B Frame vibration "angle" vector defined as the integrated B Frame inertial angular rate. Since we are addressing angular vibration effects that are by nature, small in amplitude, $\underline{\theta}(t)$ is approximately the rotation vector associated with the vibration motion, hence, represents an actual physical angle vector (See Reference 6 Section. 3.2.2 for rotation vector definition).

$\underline{u}_x, \underline{u}_y$ = Unit vectors along the B Frame X, Y axes.

Ω = Vibration frequency.

$\theta_{0_x}, \theta_{0_y}$ = Sinusoidal vibration "angle" vector amplitude around B Frame axes X and Y.

$\varphi_{\theta_x}, \varphi_{\theta_y}$ = Phase angle associated with each B Frame X, Y axis angular vibration.

The velocity response discussion is based on the following B Frame input linear and angular vibration designed to produce sculling motion:

$$\underline{\theta}(t) = \underline{u}_x \theta_{0_x} \sin\left(\Omega t - \varphi_{\theta_x}\right) \qquad \underline{a}_{SF}(t) = \underline{u}_y a_{SF0_y} \sin\left(\Omega t - \varphi_{a_{SF_y}}\right) \tag{17}$$

where

a_{SF0_y} = Sinusoidal vibration amplitude of the B Frame Y axis specific force acceleration vibration.

$\varphi_{a_{SF_y}}$ = Phase angle associated with the B Frame Y axis linear vibration.

Note that because the angular motion is about a fixed axis, there is no coning motion in the previous vibration profile.

The position response discussion is based on B Frame linear vibration which can produce folding effect amplification in the position update algorithms. Such effects are generally not present in the attitude/velocity algorithms because the inertial sensors are typically of the integrating type, providing their inputs to the navigation computer in the form of pre-integrated angular rate and specific force acceleration increments. The B Frame input vibration is as follows:

$$\underline{a}_{SF}(t) = \underline{u}_{Vib}\, a_{SF_0} \sin(\Omega t - \varphi_{a_{SF}}) \qquad \underline{\theta}(t) = 0 \tag{18}$$

where

$\underline{u}_{Vib}$ = Linear vibration input axis.

Note that because there is no angular motion in the previous vibration profile, there is no coning, sculling or scrolling effect on the resulting position response.

3.1.1 True System Response

Under the Equation (16) vibration profile, the following true attitude motion is generated (Ref. 6 Sect. 10.1.1.1):

$$\begin{aligned}\underline{\Phi}(t) = {} & \underline{u}_x \theta_{0_x}\left[\sin\left(\Omega t - \varphi_{\theta_x}\right) - \sin\left(\Omega t_0 - \varphi_{\theta_x}\right)\right] + \underline{u}_y \theta_{0_y}\left[\sin\left(\Omega t - \varphi_{\theta_y}\right) - \sin\left(\Omega t_0 - \varphi_{\theta_y}\right)\right] \\ & + \underline{u}_z \frac{1}{2}\Omega\, \theta_{0_x}\theta_{0_y} \sin\left(\varphi_{\theta_y} - \varphi_{\theta_x}\right)\left[(t - t_0) - \frac{\sin\left(\Omega (t - t_0)\right)}{\Omega}\right]\end{aligned} \tag{19}$$

where

t_0 = Initial time t.

$\underline{\Phi}(t)$ = Rotation vector describing the B Frame attitude at time t due to the Equation (16) vibration, relative to the B Frame attitude at t_0.

The attitude response has first order constant and oscillatory terms around the angular vibration input axes, a second order angular vibration around $\underline{u}_z$ (the axis perpendicular to the angular vibration input axes), and a linear time build-up term around axis $\underline{u}_z$ representing the coning effect. The average slope of the attitude response is the linear term coefficient denoted as the coning rate (previous reference):

$$\dot{\underline{\Phi}}_{Avg} = \underline{u}_z \frac{1}{2}\Omega\, \theta_{0_x}\theta_{0_y} \sin\left(\varphi_{\theta_y} - \varphi_{\theta_x}\right) = \text{Coning rate} \tag{20}$$

Under the Equation (17) vibration profile, the following true velocity motion is generated (Ref. 6 Sect. 10.1.2.1):

$$\begin{aligned}\underline{v}(t) = {} & \underline{u}_y\, a_{SF_{0_y}} \frac{1}{\Omega}\left[\cos\left(\Omega t_0 - \varphi_{a_{SF_y}}\right) - \cos\left(\Omega t - \varphi_{a_{SF_y}}\right)\right] \\ & + \underline{u}_z \frac{1}{2}\theta_{0_x}\, a_{SF_{0_y}} \left\{\frac{1}{\Omega}\left[\sin\left(\Omega t - \varphi_{\theta_x}\right) - \sin\left(\Omega t_0 - \varphi_{\theta_x}\right)\right]\left[\cos\left(\Omega t_0 - \varphi_{a_{SF_y}}\right)\right.\right. \\ & \left.\left. - \cos\left(\Omega t - \varphi_{a_{SF_y}}\right)\right] + \cos\left(\varphi_{a_{SF_y}} - \varphi_{\theta_x}\right)\left[(t - t_0) - \frac{\sin\left(\Omega (t - t_0)\right)}{\Omega}\right]\right\}\end{aligned} \tag{21}$$

where

$\underline{v}(t)$ = Velocity at time t in the time t_0 oriented B Frame due to the Equation (17) angular/linear vibration since time t_0.

The velocity response has first order constant and oscillatory terms along the linear vibration input axis, second order constant and oscillatory terms along $\underline{u}_z$ (the axis perpendicular to the linear/angular vibration input axes), and a linear time build-up term along axis $\underline{u}_z$ representing the sculling effect. The average slope of the velocity response is the linear term coefficient denoted as the sculling rate (previous reference):

$$\dot{\underline{v}}_{Avg} = \underline{u}_z \frac{1}{2}\theta_{0_x}\, a_{SF_{0_y}} \cos\left(\varphi_{a_{SF_y}} - \varphi_{\theta_x}\right) = \text{Sculling Rate} \tag{22}$$

Under the Equation (18) vibration profile, the following true velocity, position motion is generated (Ref. 6 Sect. 10.1.3.2.1):

$$\underline{v}(t) = \int_{t_0}^{t} \underline{a}_{SF}(\tau)\, d\tau = -\underline{u}_{Vib}\, a_{SF_0} \frac{1}{\Omega}\left[\cos(\Omega t_0 - \varphi_{a_{SF}}) - \cos(\Omega t - \varphi_{a_{SF}})\right] \quad (23)$$

$$\underline{R}(t) = \int_{t_0}^{t} \underline{v}(\tau)\, d\tau = -\underline{u}_{Vib}\, a_{SF_0} \frac{1}{\Omega}\left\{(t - t_0)\cos(\Omega t_0 - \varphi_{a_{SF}}) - \frac{1}{\Omega}\left[\sin(\Omega t - \varphi_{a_{SF}}) - \sin(\Omega t_0 - \varphi_{a_{SF}})\right]\right\} \quad (24)$$

where

$\underline{R}(t)$ = Position at time t in the time t_0 oriented B Frame due to Equation (18) vibration since time t_0.

3.1.2 System Algorithm Response

The response of the system attitude, velocity, position computational algorithms to the Section 3.1 input vibrations depends on the particular algorithms utilized. An important part of algorithm design is an analytical assessment of their response in comparison with the true kinematic response under hypothesized input motion. For the two-speed algorithms described in Reference 7, the low speed portions have been designed to be analytically exact such that algorithm errors are generated only by the high speed algorithms (except for minor small trapezoidal integration algorithm errors associated with Coriolis, gravity, N Frame rotation rate terms). The result is that under the Section 3.1 input profiles, the Reference 7 algorithm response should match the Section 3.1 truth solution plus an added high speed algorithm error.

For the Reference 7 (and 4) attitude computation, a high speed algorithm computes the coning contribution to attitude motion (Ref. 7 Eqs. (24)) based on a second order truncated Taylor series expansion as:

$$\underline{\beta}_m = \sum_l \frac{1}{2}\left(\underline{\alpha}_{l\text{-}1} + \frac{1}{6}\Delta\underline{\alpha}_{l\text{-}1}\right) \times \Delta\underline{\alpha}_l \quad \text{From } t_{m-1} \text{ to } t_m$$

$$\underline{\alpha}_l = \sum_l \Delta\underline{\alpha}_l \quad \text{From } t_{m-1} \text{ to } t_l \quad (25)$$

For the previous coning algorithm operating with an exact attitude updating algorithm (Ref. 4 and Ref. 7 Eqs. (8)), the average algorithm error response under the Equations (16) vibration profile is (Ref. 6 Sect. 10.1.1.2.2):

$$\dot{\delta\underline{\Phi}}_{Algo} = \dot{\delta\underline{\beta}}_{Algo} = \underline{u}_z \frac{1}{2}\Omega\, \theta_{0_x}\, \theta_{0_y} \sin\left(\varphi_{\theta_y} - \varphi_{\theta_x}\right)\left\{\left[1 + \frac{1}{3}(1 - \cos\Omega T_l)\right]\left(\frac{\sin\Omega T_l}{\Omega T_l}\right) - 1\right\} \quad (26)$$

where

$\dot{\delta\underline{\Phi}}_{Algo}$, $\dot{\delta\underline{\beta}}_{Algo}$ = Average attitude and coning algorithm error rate.

For the Reference 7 (and 5) velocity computation, a high speed algorithm computes the sculling contribution to velocity motion (Ref. 7 Eqs. (26)) based on a second order truncated Taylor series expansion as:

$$\Delta\underline{v}_{Scul_m} = \sum_l \frac{1}{2}\left[\left(\underline{\alpha}_{l\text{-}1} + \frac{1}{6}\Delta\underline{\alpha}_{l\text{-}1}\right) \times \Delta\underline{\upsilon}_l + \left(\underline{\upsilon}_{l\text{-}1} + \frac{1}{6}\Delta\underline{\upsilon}_{l\text{-}1}\right) \times \Delta\underline{\alpha}_l\right] \quad \text{From } t_{m-1} \text{ to } t_m$$

$$\underline{\upsilon}_l = \sum_l \Delta\underline{\upsilon}_l \quad \text{From } t_{m-1} \text{ to } t_l \quad (27)$$

For the previous sculling algorithm operating with an exact velocity updating algorithm (Ref. 5 and Ref. 7 Eqs. (14)), the average algorithm error response under the Equations (17) vibration profile is (Ref. 6 Sect. 10.1.2.2.2):

$$\delta\dot{\underline{v}}_{Algo} = \delta\dot{\underline{v}}_{ScullAlgo} = \underline{u}_z \frac{1}{2} \theta_{0_x} a_{SF0_y} \cos\left(\varphi_{a_{SF_y}} - \varphi_{\theta_x}\right) \left\{\left[1 + \frac{1}{3}\left(1 - \cos \Omega T_l\right)\right]\left(\frac{\sin \Omega T_l}{\Omega T_l}\right) - 1\right\} \qquad (28)$$

where

$\delta\dot{\underline{v}}_{Algo}, \delta\dot{\underline{v}}_{ScullAlgo}$ = Average velocity update and sculling algorithm error rate.

Because there is no coning motion in the Equations (17) vibration profile, the accompanying Reference 7 attitude algorithm response would be error free.

The Reference 7 (and 5) high resolution position computation uses a high speed algorithm to compute doubly integrated acceleration (Ref. 7 Eqs. (28)) based on a second order truncated Taylor series expansion as:

$$\underline{S}_{\upsilon_m} = \int_{t_{m-1}}^{t_m} \int_{t_{m-1}}^{\tau} \underline{a}_{SF}^{B} \, d\tau_1 \, d\tau \approx \sum_l \left[\underline{\upsilon}_{l-1} T_l + \frac{T_l}{12}\left(5\,\Delta\underline{\upsilon}_l + \Delta\underline{\upsilon}_{l-1}\right)\right] \quad \text{From } t_{m-1} \text{ to } t_m \qquad (29)$$

where

$\underline{\upsilon}_l$ = As defined previously in Equations (27).

For the previous doubly integrated acceleration algorithm operating with an exact position updating algorithm (Ref. 5 and Ref. 7 Eqs. (15)), the position error response under the Equations (18) vibration profile is (Ref. 6 Sects. 10.1.3.2.3):

$$\begin{aligned}\delta\underline{R}_{Algo}(t) = \sum_m \delta\underline{S}_{\upsilon_m} = -\underline{u}_{Vib} \frac{1}{\Omega^2} a_{SF_0} \Bigg\{\Bigg(&\frac{\Omega T_l \sin \Omega' T_l}{2\,(1 - \cos \Omega' T_l)} - 1 \\ &+ \frac{1}{12} \Omega T_l \sin \Omega' T_l\Bigg)\left[\sin\left(\Omega'(t - t_0) + \Omega t_0 - \varphi_{a_{SF}}\right) - \sin\left(\Omega t_0 - \varphi_{a_{SF}}\right)\right] \\ &- \frac{1}{12} \Omega T_l \left[\cos\left(\Omega'(t - t_0) + \Omega t_0 - \varphi_{a_{SF}}\right) - \cos\left(\Omega t_0 - \varphi_{a_{SF}}\right)\right](1 - \cos \Omega' T_l)\Bigg\}\end{aligned} \qquad (30)$$

$$\frac{\Omega' T_l}{2\pi} = \frac{\Omega T_l}{2\pi} - \left(\frac{\Omega T_l}{2\pi}\right)_{Intgr} \qquad k = \left(\frac{\Omega T_l}{2\pi}\right)_{Intgr} \qquad \Omega' \equiv \Omega - \frac{2\pi k}{T_l}$$

where

$\delta\underline{R}_{Algo}(t)$ = Position algorithm error.

$\delta\underline{S}_{\upsilon_m}$ = Error in the $\underline{S}_{\upsilon_m}$ acceleration double integration algorithm.

k = Nearest integer value of the ratio of Ω to $2\pi / T_l$.

$(\,)_{Intg}$ = ( ) rounded to the nearest integer value (e.g., $(0.3)_{Intgr} = 0$, $(0.5)_{Intgr} = 1$, $(0.7)_{Intgr} = 1$, $(1.3)_{Intgr} = 1$, $(1.5)_{Intgr} = 2$, $(1.7)_{Intgr} = 2$, etc.).

Ω' = Folded frequency.

Because there is no coning or sculling motion in the Equations (18) vibration profile, the accompanying Reference 7 attitude and velocity algorithm response would be error free.

Equations (30) show that the algorithm computed position error can be sizable when the folded frequency Ω' approaches zero (i.e., when Ω is close to an integer multiple of $2\pi / T_l$ for which $(1 - \cos \Omega' T_l)$ approaches zero). Reference 6 Section 10.1.3.2.3 shows that for k = 0, the term of concern $\dfrac{\Omega T_l \sin \Omega' T_l}{2\,(1 - \cos \Omega' T_l)}$

= 1 but for k > 0, $\frac{\Omega T_l \sin \Omega' T_l}{2 (1 - \cos \Omega' T_l)}$ equals $\frac{2 \pi k}{\Omega' T_l}$ which is infinite for zero folding frequency Ω'. The latter effect on position error is actually a build-up in time that only becomes infinite at infinite time (previous reference). To assess the effect for finite time, the equivalent to Equations (30) is (Ref. 6 Sect. 10.1.3.2.4):

$$\begin{aligned}\delta \underline{R}_{Algo}(t) = & - \underline{u}_{Vib} \frac{1}{\Omega^2} a_{SF_0} \left\{ \Omega(t - t_0) \left(\frac{f_1(\Omega' T_l)}{2 f_2(\Omega' T_l)} - \frac{\Omega'}{\Omega} \right.\right. \\ & \left. + \frac{1}{12} (\Omega' T_l)^2 f_1(\Omega' T_l) \right) \left[\cos (\Omega t_0 - \varphi_{a_{SF}}) f_1\left(\Omega'(t - t_0)\right) \right. \\ & \left. \left. - \sin (\Omega t_0 - \varphi_{a_{SF}}) \Omega'(t - t_0) f_2\left(\Omega'(t - t_0)\right) \right] \right. \\ & \left. - \frac{1}{12} \Omega T_l \left[\cos \left(\Omega'(t - t_0) + \Omega t_0 - \varphi_{a_{SF}}\right) - \cos (\Omega t_0 - \varphi_{a_{SF}}) \right] (1 - \cos \Omega' T_l) \right\}\end{aligned} \tag{31}$$

in which the f_1, f_2 functions are defined as:

$$f_1(x) \equiv \frac{\sin x}{x} = 1 - \frac{x^2}{3!} + \frac{x^4}{5!} - \cdots \qquad f_2(x) \equiv \frac{(1 - \cos x)}{x^2} = \frac{1}{2!} - \frac{x^2}{4!} + \frac{x^4}{6!} - \cdots \tag{32}$$

Equation (31) for the position algorithm error is singularity free for finite values of time t and for all values of Ω' (i.e., including k > 0 values).

3.2 System Vibration Analysis Model

The results of Section 3.1 are based on having knowledge of the INS sensor assembly B Frame vibration input amplitudes and phasing that are representative of expected system usage. Finding values for these terms can be a time consuming computer aided software design process involving complex mechanical modeling of the INS structure and how it mechanically couples to a user vehicle. Due to its complexity, the process is inherently prone to data input error that distorts results obtained. To provide a reasonableness check on the results, simplified dynamic models are frequently employed for comparison that lend themselves to closed-form analytical solutions. Once the detailed modeling results match the simplified model within its approximation uncertainty, the detailed model is deemed valid for use in estimating B Frame response.

From a broader perspective, it must be recognized that it is virtually impossible to develop an accurate mechanical dynamic model for an INS in a user vehicle due to variations in mechanical structural properties between INS's of a particular design (e.g., variations in stiffness/damping characteristics of electronic circuit boards in their respective card guides, variations in mechanical housings, variations in mounting interfaces, etc.), as well as variations in the characteristics for a particular INS over temperature and time. On the other hand, for performance analysis purposes, only "ball-park" accuracy is generally required for B Frame vibration characteristics. All things considered, it becomes reasonable to use the simplified analytical models for B Frame vibration, thereby eliminating the need for cumbersome computerized modeling.

Figure 3 illustrates such a simplified analytical model depicting the INS sensor assembly linear and angular response to linear INS input vibration exposure.

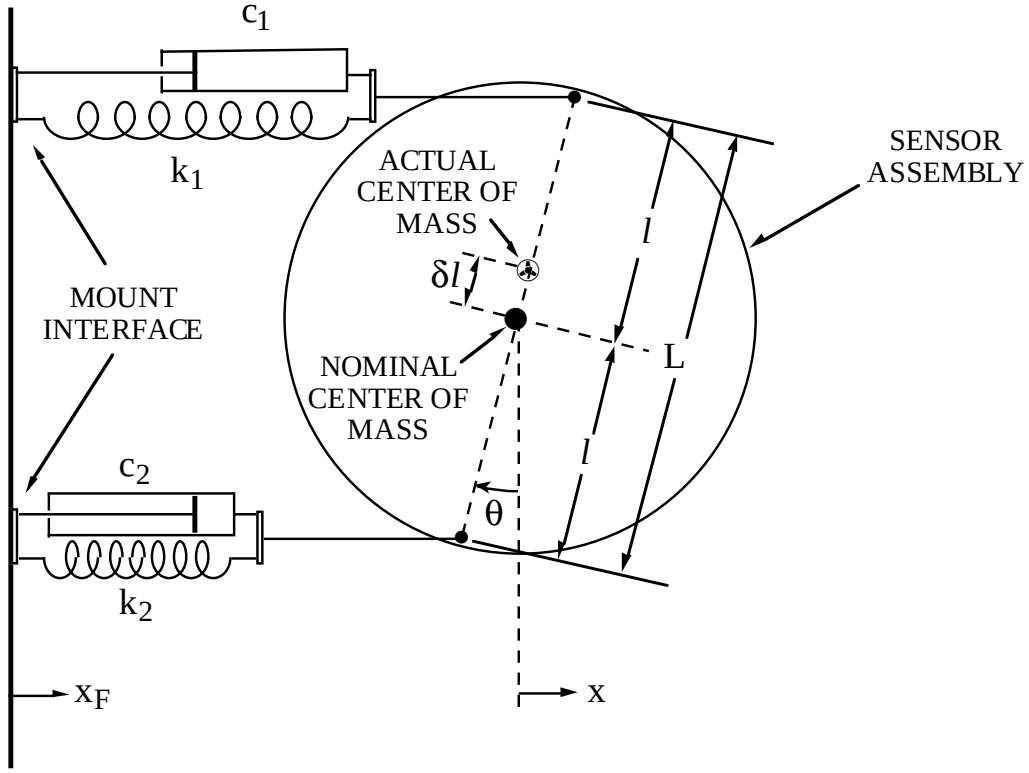


Figure 3 - Simplified Sensor Assembly Dynamic Response Model

In Figure 3

X_F, X = Vibration forcing function input position displacement and sensor assembly position response.

θ = Sensor assembly angular response to X_F input vibration.

k_i, c_i = Spring constants and damping coefficients for structure connecting the sensor assembly to the INS vibration input source.

δl = Variation of the actual sensor assembly center of mass from its nominal location.

Figure 3 depicts a sensor assembly that would be nominally mounted with a symmetrical attachment to the vibration source such that k_1, c_1 and k_2, c_2 are nominally equal with the actual sensor assembly center of mass collocated with the nominal center of mass (zero δl). Under such nominal "CG Mount" conditions, the input vibration X_F produces sensor assembly motion with zero angular response θ and with a linear X response of (Ref. 6 Sect. 10.5.1):

$$A(S) = \frac{(2\,c\,S + 2\,k)}{m\,S^2 + 2\,c\,S + 2\,k} A_F(S) \qquad (33)$$

where

$A_F(S)$, A(S) = Laplace transforms of the input vibration and sensor assembly response accelerations (the second derivatives of X_F, X).

S = Laplace transform variable.

k, c = Nominal values for k_i, c_i.

m = Sensor assembly mass.

Under off-nominal conditions, the same linear response is produced but an angular response is also generated given by (previous reference):

$$\vartheta(S) = - \frac{m\left[\left(l\,\delta c + 2\,c\,\delta l\right) S + l\,\delta k + 2\,k\,\delta l\right]}{\left(J\,S^2 + 2\,c\,l^2\,S + 2\,k\,l^2\right)\left(m\,S^2 + 2\,c\,S + 2\,k\right)} A_F(S) \tag{34}$$

in which $\delta k \equiv k_2 - k_1$ $\delta c \equiv c_2 - c_1$

where

$\vartheta(S)$ = Laplace transform of the sensor assembly θ angular vibration response.

For $A_F(S)$ as an input sinusoid, the amplitudes of the previous acceleration and angular response transfer functions (i.e., the polynomials multiplying $A_F(S)$) are (Ref. 6 Sect. 10.6.1):

$$B_A(\Omega) = \sqrt{\frac{\omega_y^4 + 4\,\zeta_y^2\,\omega_y^2\,\Omega^2}{\left(\omega_y^2 - \Omega^2\right)^2 + 4\,\zeta_y^2\,\omega_y^2\,\Omega^2}}$$

$$B_\vartheta(\Omega) = \frac{1}{L}\sqrt{\frac{\omega_\theta^4\left(\varepsilon_k + 4\,\varepsilon_l\right)^2 + 4\,\zeta_\theta^2\,\omega_\theta^2\left(\varepsilon_c + 4\,\varepsilon_l\right)^2\,\Omega^2}{\left[\left(\omega_\theta^2 - \Omega^2\right)^2 + 4\,\zeta_\theta^2\,\omega_\theta^2\,\Omega^2\right]\left[\left(\omega_y^2 - \Omega^2\right)^2 + 4\,\zeta_y^2\,\omega_y^2\,\Omega^2\right]}} \tag{35}$$

in which

$$\omega_x \equiv \sqrt{\frac{2\,k}{m}} \qquad \zeta_x \equiv \frac{c}{m\,\omega_x} \qquad \omega_\theta \equiv \sqrt{\frac{2\,k\,l^2}{J}} \qquad \zeta_\theta \equiv \frac{c\,l^2}{J\,\omega_\theta}$$

$$\varepsilon_k \equiv \frac{\delta k}{k} \qquad \varepsilon_c \equiv \frac{\delta c}{c} \qquad L \equiv 2\,l \qquad \varepsilon_l \equiv \frac{\delta l}{L} \tag{36}$$

where

Ω = $A_F(S)$ sinusoidal input vibration frequency.

$B_A(\Omega)$, $B_\vartheta(\Omega)$ = Magnitudes of the polynomials multiplying $A_F(S)$ in the A(S), $\vartheta(S)$ equations.

Under sinusoidal $A_F(S)$ excitation at frequency Ω, the A(S), $\vartheta(S)$ responses would be sinusoidal at frequency Ω with amplitudes equal to $B_A(\Omega)$, $B_\vartheta(\Omega)$ multiplied by the $A_F(S)$ sinusoid input amplitude, and with generally non-zero phasing relative to the $A_F(S)$ sinusoid (Ref. 6 Sect. 10.5.1 also provides the A(S), $\vartheta(S)$ phase angle response as a function of Ω).

Although Equations (35) were derived based on the simplified Figure 3 model, they can be applied as universal simplified formulas in which the coefficients and error terms are selected to represent actual sensor-assembly/mount parameters, e.g.,

ω_x, ζ_x = Undamped natural frequency and damping ratio for the actual sensor-assembly/mount linear vibration motion dynamic response characteristic.

ω_θ, ζ_θ = Undamped natural frequency and damping ratio for the actual sensor-assembly/mount rotary vibration motion dynamic response characteristic.

L = Distance between actual sensor assembly mounting points.

ε_k, ε_c = Actual sensor assembly mounting structure spring, damping cross-coupling error coefficients.

ε_l = Distance from the sensor assembly mount center of force to the sensor assembly center of mass, divided by L.

3.3 System Response Under Random System Vibration

Section 3.1 described analytical formulas for calculating strapdown INS performance parameters as a function of linear and angular sinusoidal vibrations of the sensor assembly. Section 3.2 described a simplified model of the structural dynamic characteristics for translating a linear sinusoidal vibration input source into resulting linear and angular sinusoidal vibration of the sensor assembly. A typical INS design specification defines the input vibration source as a random mixture of frequency components at frequency dependent amplitudes. The sensor assembly response to random vibration is a composite sum of its response to each frequency component. For the Section 3.1 performance equations, the Section 3.2 simplified sensor assembly dynamical model (interpreted to provide angular response around both axes perpendicular to the linear input vibration), and worst case approximations for phase response of the sensor assembly to vibration excitation, the following can be used to assess system performance under random vibration (Ref. 6 Sect. 10.6.1):

$$E\left(\dot{\Phi}_{Avg}\right) = \int_0^\infty \omega\, B_\vartheta^2(\omega)\, G_{aVib}(\omega)\, d\omega \quad \text{Coning attitude motion} \tag{37}$$

$$E\left(\dot{v}_{Avg}\right) = \int_0^\infty B_\vartheta(\omega)\, B_A(\omega)\, G_{aVib}(\omega)\, d\omega \quad \text{Sculling velocity motion} \tag{38}$$

$$E\left(\delta\dot{\underline{\Phi}}_{Algo}\right) = E\left(\delta\dot{\underline{\beta}}_{Algo}\right) = \int_0^\infty \omega\, B_\vartheta^2(\omega) \left| \left[1 + \frac{1}{3}\left(1 - \cos\omega T_l\right)\right]\left(\frac{\sin\omega T_l}{\omega T_l}\right) - 1 \right| G_{aVib}(\omega)\, d\omega$$

Attitude/coning algorithm error (39)

$$E\left(\delta\dot{\underline{v}}_{Algo}\right) = E\left(\delta\dot{\underline{v}}_{ScullAlgo}\right) = \int_0^\infty B_\vartheta(\omega)\, B_A(\omega) \left| \left[1 + \frac{1}{3}\left(1 - \cos\omega T_l\right)\right]\left(\frac{\sin\omega T_l}{\omega T_l}\right) - 1 \right| G_{aVib}(\omega)\, d\omega$$

Velocity/sculling algorithm error (40)

$$E\left(\delta R_{Algo}^2(t)\right) = (t - t_0)^2 \int_0^\infty B_A^2(\omega)\, \frac{2}{\omega^2} \left\{ E(\omega)^2 + \frac{1}{6}(\omega' T_l)^2 \left[E(\omega)\, f_1(\omega' T_l) + \frac{1}{12}(\omega' T_l)^2\, f_2(\omega' T_l) \right] \right\} f_2\left(\omega'(t - t_0)\right) G_{aVib}(\omega)\, d\omega$$

Position algorithm folding effect error (41)

$$\omega' \equiv \omega - \frac{2\pi}{T_l}\left(\frac{\omega T_l}{2\pi}\right)_{Intgr} \qquad E(\omega) \equiv \frac{f_1(\omega' T_l)}{2\, f_2(\omega' T_l)} - \frac{\omega'}{\omega}$$

where

$E(\,)$ = Expected value operator (i.e., average statistical value).

ω = Input random vibration frequency parameter.

ω' = Frequency folded version of ω.

$G_{aVib}(\omega)$ = Input linear vibration power spectral density. The integral of $G_{aVib}(\omega)$ from ω equal zero to plus infinity equals the expected value of the random vibration acceleration input squared.

The f_1, f_2 functions, $B_A(\omega)$ and $B_\vartheta(\omega)$ are defined in Equations (32) and (35). Note that $E\left(\delta R^2_{Algo}(t)\right)$ for the position error is based on the Equation (31) form to avoid singularities when the folded frequency ω' is zero.

The previous methodology for evaluating particular INS error characteristics under random (and sinusoidal) vibration can be applied to other INS error effects as well. Reference 6 Sections 10.6.1-10.6.3 provide several examples in addition to those discussed previously.

4. SYSTEM TESTING FOR INERTIAL SENSOR CALIBRATION ERRORS

After an INS (or its sensor assembly) is assembled and sensor compensation software coefficients have been installed (typically based on sensor calibration measurements), it is frequently required that residual sensor error parameters be measured to assess system level performance. For compensatable effects, the results can be used to update the sensor calibration coefficients. This section describes two INS system level tests that are typically conducted in the laboratory for measuring residual bias, scale-factor and misalignment errors: the Strapdown Drift Test and the Strapdown Rotation Test. The Strapdown Drift test is a static test performed on high performance sensor assemblies in which the attitude integration software in the INS computer is configured to constrain the average horizontal transformed specific force acceleration to zero. For a test of several hours duration, the averages of the constraining signals become accurate measures of horizontal angular rate sensor bias error. The Strapdown Rotation Test can be used on sensor assemblies of all accuracy grades. It consists of exposing the INS to a series of rotations, and recording its average transformed specific force acceleration output at static dwell times between rotations. By processing the recorded data, very accurate measurements can be made of the scale factor error and relative misalignment between all inertial sensors in the sensor assembly, the accelerometer bias errors, and misalignment of the sensor assembly relative to the INS mounting fixture. The details of these tests and others are described in Reference 6 Chapter 18.

4.1 Strapdown Drift Test

The Strapdown Drift test is designed to evaluate angular rate sensor error by processing data generated during extended self-alignment operations. The test is performed on a strapdown analytic platform during an extension of the normal self-alignment initialization mode. The principal measurement of the Strapdown Drift Test is the composite north horizontal angular rate sensor output, determined from the north component of angular rate bias applied to the strapdown analytic platform to render it stationary in tilt around North. Subtracting the known true value of north earth rate from the measurement evaluates the north component of angular rate sensor composite error. East and vertical angular rate sensor errors are ascertained by repeating the test with the previously east and vertical angular rate sensors in the horizontal north orientation.

The self-alignment process utilized in the Strapdown Drift Test creates a locally level rotation rate stabilized analytic "platform" (the N Frame) whose level orientation (relative to the earth) is sustained based on horizontal platform acceleration measurements (i.e., perpendicular to the accelerometer derived local gravity vertical). The test measurement is the biasing rate to the analytically stable platform to maintain it level in the presence of earth's rotation. As configured, the analytic platform remains angularly stable in the presence of B Frame angular rate, hence, angular rate sensor bias determined from stabilized platform measurements becomes insensitive to small physical angular movements of the sensor assembly during the test (caused for example by test-fixture/laboratory micro-motion relative to the earth or rotation of the sensor assembly internal mount (within the INS) due to thermal expansion under thermal exposure testing).

Angular rate sensor bias determined by the previous method is corrupted by angular rate sensor scale factor and misalignment compensation error residuals which are generally negligible in the Strapdown Drift

Test environment compared with typical high accuracy bias accuracy requirements. Also contained in the bias measurements are the effects of angular rate sensor random output noise which is reduced to an acceptable level by allowing a long enough extended self-alignment measurement period. If test accuracy requirements permit, a simpler version of the Strapdown Drift Test can be utilized in which the test measurement is the direct integral of the compensated angular rate from each sensor minus its earth rate component input. To reduce earth rate input misalignment error effects using the latter approach, the angular rate sensor can be oriented with its input axis aligned with earth's polar rotation axis. The simpler approach is directly susceptible to angular motion of the sensor assembly relative to the earth during the test measurement.

For situations when the biasing rate to the strapdown analytic platform is not an available INS output, an alternative procedure can be utilized based on INS computed true heading outputs (Ref. 6 Sect. 18.2.2). In this case the east angular rate sensor error is determined from the test based on the heading error it generates at the end of an extended self-alignment run. In order to discriminate east angular rate sensor error from North earth rate coupling (under test heading misalignment), the INS heading output is measured for two individual alignment runs. The second alignment run is performed at a heading orientation that is rotated 180 degrees from the first. The difference between the average heading measurements so obtained cancels the North earth rate coupling input, thereby becoming the measurement for east angular rate sensor error determination. North and vertical angular rate sensor errors are ascertained by repeating the test with the previously north and vertical angular rate sensors in the horizontal east orientation.

The following operations are integrated to implement the strapdown analytic platform function during the Strapdown Drift Test extended alignment computational process (Ref. 6 Sect. 6.1.2):

$$
\begin{aligned}
\dot{C}_B^N &= C_B^N \left(\underline{\omega}_{IB}^B \times\right) - \left(\underline{\omega}_{IN}^N \times\right) C_B^N \\
\underline{\omega}_{IN}^N &= \underline{\omega}_{IE}^N + \underline{\omega}_{Tilt}^N \\
\underline{\omega}_{Tilt}^N &= K_2 \, \underline{u}_{Up}^N \times \Delta\underline{R}_H^N \\
\underline{\omega}_{IE}^N &= \underline{\omega}_{IE_H}^N + \underline{u}_{Up}^N \, \omega_e \sin l \\
\dot{\underline{\omega}}_{IE_H}^N &= K_1 \, \underline{u}_{Up}^N \times \Delta\underline{R}_H^N \\
\dot{\underline{v}}_H^N &= \left(C_B^N\right)_H \underline{a}_{SF}^B - K_3 \, \Delta\underline{R}_H^N \\
\Delta\dot{\underline{R}}_H^N &= \underline{v}_H^N - K_4 \, \Delta\underline{R}_H^N
\end{aligned}
\qquad (42)
$$

where

$\underline{\omega}_{IB}^B$, $\underline{a}_{SF}^B$ = Angular rate sensor and accelerometer compensated input vectors.
H = Subscript indicating horizontal components (or rows)of the associated vector (or matrix).
K_i = Extended alignment analytical platform level maintenance coefficients.
ω_e = Earth inertial rotation rate magnitude.
l = Geodetic latitude.
$\underline{u}_{Up}$ = Unit vector upward along the geodetic vertical (i.e., along the N Frame Z axis).
$\underline{v}$, $\Delta\underline{R}$ = Velocity and position displacement during extended alignment.

The North angular rate sensor bias is calculated as an adjunct to the previous operations as (Ref. 6 Sect. 18.2.1):

$$
\hat{\underline{\phi}}_H^N \equiv \int_{t_{Start}}^{t_{End}} \hat{\underline{\omega}}_{IN_H}^N \, dt \qquad \delta\omega_{ARS/Cnst_{North}} \approx \frac{1}{(t_{End} - t_{Start})} \hat{\phi}_H - \omega_e \cos l \qquad (43)
$$

where

t_{Start}, t_{End} = Time at the start and end of the Strapdown Drift Test measurement period.

$\delta\omega_{ARS/Cnst_{North}}$ = North component of angular rate sensor constant bias residual error.

ω_e = Earth rotation rate magnitude.

l = Test site latitude.

$\hat{\phi}_H$ = Magnitude of $\underline{\hat{\phi}}_H$.

4.2 Strapdown Rotation Test

The basic concept for the Strapdown Rotation Test was originally published by the author in 1977 (Reference 3). Since then, variations of the concept have formed the basis in most strapdown inertial navigation system manufacturing organizations for system level calibration of accelerometer/angular-rate-sensor scale-factors/misalignments and accelerometer biases.

The Strapdown Rotation test consists of a series of rotations of the strapdown sensor assembly using a rotation test fixture for execution. During the test, special software operates on the strapdown angular rate sensor outputs from the sensor assembly to form an analytic angular rate stabilized wander azimuth "platform" (L Frame - See definition to follow) that nominally maintains a constant orientation relative to the earth. The analytic platform is implemented by processing strapdown attitude-integration/acceleration-transformation algorithms (e.g., Reference 7 Equations (8), (12), (14), (24) and (26) including inertial sensor compensation Equations (38)) with the platform horizontal inertial rotation rate components held constant. Platform horizontal rotation rates are calculated prior to rotation test initiation using special test software that implements strapdown initial alignment algorithms (e.g., Equations (42) using Kalman filter formulated K_i gains). Measurements during the Strapdown Rotation test are taken at stationary positions and computed from the averaged transformed accelerometer outputs plus gravity (i.e., the average computed total acceleration vector):

$$\Delta\underline{v}^L_m \equiv \int_{t_{m-1}}^{t_m} \left(\underline{a}^L_{SF} + \underline{g}^L\right) dt = \Delta\underline{v}^L_{SF_m} - g_{Tst}\,\underline{u}^L_{Up}\,T_m$$

$$\Delta\underline{v}^L_{SF_m} \equiv \int_{t_{m-1}}^{t_m} C^L_B\,\underline{a}^B_{SF}\,dt \qquad (44)$$

$$\underline{a}^L = \begin{pmatrix} a \\ b \\ c \end{pmatrix} \approx \frac{1}{T_m}\Delta\underline{v}^L_{Avg} \qquad \text{Test measurements}$$

where

L Frame = "Attitude Reference" coordinate frame aligned with the N Frame but having Z axis parallel to the downward (rather than upward) vertical and with X, Y axes interchanged (the L Frame X, Y axes are parallel to the N Frame Y, X axes). Reference 6 uses the L Frame for "attitude reference" outputs as an intermediate frame between the B and N Frames.

$\underline{g}$ = Plumb-bob gravity vector at the test site (mass attraction "gravitation" plus earth rotation effect centripetal acceleration).

g_{Tst} = Vertical component of $\underline{g}$.

$\Delta\underline{v}^L_{Avg}$ = Output from an averaging process performed on successive $\Delta\underline{v}^L_{SF_m}$'s (See Reference 6 Section 18.4.7.3 for process designed to attenuate accelerometer quantization noise).

$\underline{a}$ = Average total acceleration.

a, b, c = Components of $\underline{a}$ in the L Frame.

The fundamental theory behind the Strapdown Rotation test is based on the principle that for a perfectly calibrated sensor assembly, following a perfect initial alignment, the computed L Frame acceleration should be zero at any time the sensor assembly is stationary. Moreover, this should also be the case if the sensor assembly undergoes arbitrary rotations between the time periods that it is set stationary. Therefore, any deviation from zero stationary acceleration can be attributed to imperfections in the sensor assembly (i.e., sensor calibration errors) or in the initial alignment process. Initial alignment process errors create initial L Frame tilt which is removed from the Strapdown Rotation Test measurements by structuring the horizontal measurements as the difference between average horizontal L Frame acceleration readings taken before and after completing each of the test rotation sequences. As an aside, it is to be noted that in the original Reference 3 paper, the measurement for the rotation test was the average acceleration taken at the end of each rotation sequence, with a self-alignment performed before the start of each rotation sequence. The purpose of the realignment was to eliminate attitude error build-up caused by angular rate sensor error during previous rotation sequences. By taking the measurement as the difference between average accelerations before and after rotation sequence execution (as indicated above), the need for realignment is eliminated. The before/after measurement approach was introduced by Downs in Reference 1 for compatibility with an existing Kalman filter used to extract the acceleration measurements.

The principal advantage for this particular method of error determination derives from the combined use of the angular rate sensors and accelerometers to establish an angular rate stabilized reference for measuring accelerations. This implicitly enables the inertial sensors to measure the attitude of the rotation test fixture settings as the rotations are executed. Consequently, precision rotation test table readout or controls are not required (nor a stable test fixture base), hence, a significant savings can be made in test fixture cost. Inaccuracies in rotation fixture settings manifest themselves as second order errors in sensor error determination, which can be made negligibly small if desired through a repeated test sequence. It has been demonstrated, for example, with precision ring laser gyro strapdown inertial navigation systems, that the test method can measure and calibrate gyro misalignments to better than 1 arc sec accuracy with 0.1 deg rotation fixture orientation inaccuracies. In addition, because the orientation of the sensor assembly is being measured by the sensor assembly itself, it is not necessary that the sensor assembly be rigidly connected to the rotation test fixture. This is an important advantage for high accuracy applications in which the sensor assembly is attached to its chassis and mounting bracket through elastomeric isolators of marginal attitude stability.

While most of the sensor calibration errors evaluated by the Strapdown Rotation test can be measured on an individual sensor basis, the rotation test is the only direct method for measuring relative misalignments between the sensor input axes. It should also be noted that determination of sensor-assembly-to-mount misalignment is not an intrinsic part of the Strapdown Rotation Test, however, because the data taken during the test allows for this determination, it is easily included as part of test data processing (Ref. 6 Sect. 18.4.5).

Reference 6 Section 18.4 (and subsections) provides a detailed description of the Strapdown Rotation Test, its analytical theory, processing routines, and structure based on two sets of rotation sequences (a 16 rotation sequence set and a 21 rotation sequence set). The rotation sequences for the 16 set are summarized in Table 1.

Table 1 - 16 Set Rotation Test Sequences

SEQUENCE NUMBER	ROTATION SEQUENCE (Degrees, B Frame Axis)	STARTING ATTITUDE (+Z Down, Axis Indicated Along Outer Rotation Fixture Axis)
1	+360 Y	+Y
2	+360 X	+X
3	+90 Y, +360 Z, -90 Y	+Y
4	+180 Y, +90 Z, +180 X, -90 Z	+Y
5	+180 X, +90 Z, +180 Y, -90 Z	+X
6	+90 Y, +90 Z, -90 X, -90 Z	+Y
7	+90 Y	+Y
8	-90 Y	+Y
9	+90 Y, +90 Z	+Y
10	+90 Y, -90 Z	+Y
11	-90 Y, -90 Z	+Y
12	+90 X, +90 Z	+X
13	+90 X, -90 Z	+X
14	+180 Z	+Y
15	+180 Y	+Y
16	+180 X	+X

Based on the Table 1 rotation sequences, Reference 6 Section 18.4.3 develops the relationship between the test measurements and the sensor errors excited by the test; e.g., for Table 1 rotation sequences 1 and 9:

$$\Delta a_1 = -2\pi g \kappa_{yy}$$

$$\Delta b_1 = 0$$

$$c_1^1 = c_1^2 = -g\left(\lambda_{zz} - \lambda_{zzz}\right) + \alpha_z$$

$$\Delta a_9 = -g\left(\frac{1}{2}\upsilon_{zx} + \frac{1}{2}\upsilon_{yz} + \mu_{zy} - \mu_{xz} + \frac{\pi}{2}\kappa_{yy}\right) - \alpha_x + \alpha_z$$

$$\Delta b_9 = g\left(\frac{1}{2}\upsilon_{xy} + \frac{1}{2}\upsilon_{yz} + \mu_{yz} - \mu_{xy} + \frac{\pi}{2}\kappa_{zz}\right) + \alpha_x - \alpha_y \qquad (45)$$

$$c_9^1 = -g\left(\lambda_{zz} - \lambda_{zzz}\right) + \alpha_z$$

$$c_9^2 = -g\left(\lambda_{yy} - \lambda_{yyy}\right) + \alpha_y$$

where

$\Delta a_i, \Delta b_i$ = Difference between a, b horizontal acceleration measurements taken at the start and end of rotation sequence i.

c_i^1, c_i^2 = Vertical acceleration measurements taken immediately before (superscript 1) and after (superscript 2) rotation sequence i.

α_i = i axis accelerometer bias calibration error.

λ_{ii} = i axis accelerometer symmetrical scale factor calibration error.

λ_{iii} = i axis accelerometer scale factor asymmetry calibration error.

κ_{ii} = i axis angular rate sensor scale factor calibration error.

υ_{ij} = Orthogonality compensation error between the i and j angular rate sensor input axes, defined as $\pi/2$ radians minus the angle between the compensated i and j sensor input axes.

μ_{ij} = i axis accelerometer misalignment calibration error, coupling specific force from the j axis of the mean angular rate sensor axes into the i axis accelerometer input axis.

The mean angular rate sensor (MARS) axis frame in the previous μ_{ij} definition refers to a B Frame defined as the orthogonal triad that best fits symmetrically within the actual compensated angular rate sensor input axes. The "best fit" condition is specified as the condition (measured around angular rate sensor axis k) for which the angle between angular rate sensor input axis i and MARS axis i equals the angle between angular rate sensor input axis j and MARS axis j (Ref. 6 Sect. 18.4.3). As such, the overall angular misalignment of the actual angular rate sensor triad is defined to be zero relative to the MARS frame, and individual angular rate sensor misalignments affecting the Strapdown Rotation Test measurements are only due to orthogonality errors between the angular rate sensor axes.

Once the $\Delta a_i, \Delta b_i, c_i^1, c_i^2$ measurements are obtained, the individual sensor residual errors can be calculated deterministically as summarized in Figure 4 (Ref. 6 Sect. 18.4.4). The results so obtained can then be used to update the INS sensor calibration coefficients (Ref. 6 Sect. 18.4.6). If the B Frame is chosen to be the MARS Frame as described previously, the μ_{ij} accelerometer misalignments calculated from Figure 4 would be used directly to update the accelerometer misalignment calibration coefficients relative to the B Frame. For the angular rate sensors, selecting the B Frame as the MARS Frame equates to the following for individual angular rate sensor misalignments relative to the B Frame as:

$$\kappa_{xy} = \kappa_{yx} = \frac{1}{2}\upsilon_{xy} \qquad \kappa_{yz} = \kappa_{zy} = \frac{1}{2}\upsilon_{yz} \qquad \kappa_{zx} = \kappa_{xz} = \frac{1}{2}\upsilon_{zx} \qquad (46)$$

where

κ_{ij} = Angular rate sensor misalignment calibration error coupling B Frame j axis angular rate into the i angular rate sensor input axis.

ANGULAR RATE SENSOR CALIBRATION ERRORS

Scale Factor Errors

$$\kappa_{xx} = -\frac{1}{2\pi g}\Delta a_2$$

$$\kappa_{yy} = -\frac{1}{2\pi g}\Delta a_1$$

$$\kappa_{zz} = \frac{1}{2\pi g}\Delta b_3$$

Orthogonality Errors

$$\upsilon_{xy} = \frac{1}{g}\left(\Delta b_6 - \frac{1}{2}\Delta b_4 - \frac{1}{4}\Delta b_3\right)$$

$$\upsilon_{yz} = \frac{1}{4g}\left(\Delta b_5 + \Delta b_4\right)$$

$$\upsilon_{zx} = \frac{1}{4g}\left(\Delta b_5 - \Delta b_4\right)$$

ACCELEROMETER CALIBRATION ERRORS

Bias Errors

$$\alpha_x = \frac{1}{4}\Delta a_1 - \frac{1}{2}\Delta a_{15}$$

$$\alpha_y = \frac{1}{2}\Delta a_{16} - \frac{1}{4}\Delta a_2$$

$$\alpha_z = \frac{1}{2}\left(\Delta a_7 - \Delta a_8\right) - \frac{1}{4}\Delta a_1$$

Scale Factor Errors

$$\lambda_{xx} = -\frac{1}{2g}\left(c_{12}^2 + c_{13}^2\right)$$

$$\lambda_{yy} = -\frac{1}{2g}\left(c_9^2 + c_{10}^2\right)$$

$$\lambda_{zz} = -\frac{1}{2g}\left(c_{14}^2 + c_{15}^2\right)$$

Scale Factor Asymmetry

$$\lambda_{xxx} = \frac{1}{2g}\left(c_{12}^2 - c_{13}^2 + \Delta a_{15} - \frac{1}{2}\Delta a_1\right)$$

$$\lambda_{yyy} = \frac{1}{2g}\left(c_9^2 - c_{10}^2 - \Delta a_{16} + \frac{1}{2}\Delta a_2\right)$$

$$\lambda_{zzz} = \frac{1}{2g}\left(c_{14}^2 - c_{15}^2 - \Delta a_7 + \Delta a_8 + \frac{1}{2}\Delta a_1\right)$$

Misalignment Errors Relative To Mean Angular Rate Sensor Axes

$$\mu_{xy} = \frac{1}{2g}\left(\Delta b_{11} - \Delta b_{10} + \Delta b_6 - \frac{3}{4}\Delta b_3 - \frac{1}{2}\Delta b_4\right)$$

$$\mu_{yx} = \frac{1}{2g}\left(\Delta b_7 - \Delta b_8 - \Delta b_6 + \frac{1}{2}\Delta b_4 + \frac{1}{4}\Delta b_3\right)$$

$$\mu_{yz} = \frac{1}{2g}\left(\Delta b_{14} + \Delta a_{16} - \frac{1}{2}\Delta a_2 + \frac{1}{4}\Delta b_4 + \frac{1}{4}\Delta b_5\right)$$

$$\mu_{zy} = \frac{1}{2g}\left(\Delta a_{10} - \Delta a_9 - \frac{1}{4}\Delta b_4 - \frac{1}{4}\Delta b_5\right)$$

$$\mu_{zx} = \frac{1}{2g}\left(\Delta a_{13} - \Delta a_{12} - \frac{1}{4}\Delta b_5 + \frac{1}{4}\Delta b_4\right)$$

$$\mu_{xz} = \frac{1}{2g}\left(\Delta a_{14} - \Delta a_{15} + \frac{1}{2}\Delta a_1 + \frac{1}{4}\Delta b_5 - \frac{1}{4}\Delta b_4\right)$$

Figure 4 - Sensor Errors In Terms Of Measurements For The 16 Rotation Sequence Test

5. SYSTEM PERFORMANCE ANALYSIS

To assess the accuracy of inertial navigation systems, error analysis techniques are traditionally employed in which error equations are used to describe the propagation of system navigation error parameters in response to system error sources. The error equations also form the basis for performance improvement techniques in which the inertial system errors are estimated and controlled in real time based on navigation measurements taken from other navigation devices (e.g., GPS satellite range measurements). Such "aided" inertial navigation systems are structured using a Kalman filter in which system error estimates are based on a running statistical determination of the expected instantaneous errors (e.g., typically in the form of a "covariance matrix"). The covariance matrix computational structure used in the Kalman filter is also applied in "covariance analysis" simulators to statistically analyze both aided and unaided ("free inertial") system performance. Validation of the Kalman filter software is an important element in the aided inertial navigation system software design process.

5.1 Free Inertial Performance Analysis

The accuracy of all inertial navigation systems is fundamentally limited by instabilities in the inertial component error characteristics following calibration. Resulting residual inertial sensor errors produce INS navigation errors that are unacceptable in many applications. To predict Strapdown INS performance, linear time rate differential error propagation equations can be analyzed depicting the growth in INS computed attitude, velocity, position error as a function of residual inertial sensor and gravity modeling error (e.g., Ref. 7 Eqs. (50)). Modern formulations of such error propagation equations cast them in a standard error state dynamic equation format as follows (Ref. 2 Sect. 3.1 and Ref. 6 Sect. 15.1):

$$\dot{\underline{x}}(t) = A(t)\,\underline{x}(t) + G_P(t)\,\underline{n}_P(t) \tag{47}$$

where

$\underline{x}(t)$ = Error state vector treated analytically as a column matrix.
$A(t)$ = Error state dynamic matrix.
$\underline{n}_P(t)$ = Vector of independent white “process” spectral noise density sources driving $\underline{x}(t)$ (treated analytically as a column matrix).
$G_P(t)$ = Process noise dynamic coupling matrix that couples individual $\underline{n}_P(t)$ components into $\dot{\underline{x}}(t)$.

In general, $A(t)$ and $G_P(t)$ are time varying functions of the angular rate, acceleration, attitude, velocity and position parameters within the INS computer. To evaluate the solution to Equation (47) at discrete time instants, the following equivalent integrated form is utilized (Ref. 2 Sect. 3.4 and Ref. 6 Sect. 15.1.1):

$$\underline{x}_n = \Phi_n\,\underline{x}_{n-1} + \underline{w}_n \tag{48}$$

in which

$$\Phi(t, t_{n-1}) = I + \int_{t_{n-1}}^{t} A(\tau)\,\Phi(\tau, t_{n-1})\,d\tau \qquad \Phi_n \equiv \Phi(t_n, t_{n-1}) \tag{49}$$

$$\underline{w}_n = \int_{t_{n-1}}^{t_n} \Phi(t_n,\tau)\,G_P(\tau)\,\underline{n}_P(\tau)\,d\tau \tag{50}$$

where

n = Performance evaluation cycle time index.
$\underline{x}_n$ = Error state vector evaluated at cycle time n.
Φ_n = Error state transition matrix that propagates the error state vector from the n-1th to the nth time instant.

$\underline{w}_n$ = Change in $\underline{x}_n$ due to process noise input from the n-1th to the nth time instant.

For a strapdown INS, the elements of the $\underline{x}$ error state vector would include INS attitude, velocity, position error parameters, inertial sensor error parameters (e.g., bias, scale factor, misalignment) and gravity modeling error. Elements of the $\underline{n}_P$ process noise vector would include inertial sensor random output noise, noise source input to randomly varying inertial sensor error states, and noise source inputs to randomly varying gravity error modeling error states. Equations (50) of Reference 7 are an example of strapdown INS error propagation equations that are in the Equation (47) form. The sensor error terms in these equations are typically modeled as random constants (with random walk input white noise), first order Markov processes, or the sum of both (Ref. 6 Sect. 12.5.6). Reference 6 Section 16.2.3.3 provides an example of how the gravity error term in these equations can be modeled.

5.2 Kalman Filters For INS Aiding

To overcome the performance deficiencies in a free inertial navigation system, "inertial aiding" is commonly utilized in which the INS navigation parameters (and in some cases, the sensor calibration coefficients) are updated based on inputs from an alternate source of navigation information available in the user vehicle. The modern method for applying the inertial aiding measurement to the INS data is through a Kalman filter, a set of software that is typically resident in the INS computer. The Kalman filter is designed based on the Equation (48) $\underline{x}$ error state vector propagation model, to generate estimates for $\underline{x}$ and provide updates to the INS computer parameters to control $\underline{x}$ (ideally to zero). For an aided INS, the $\underline{x}$ error state vector would also include error terms associated with the aiding device. The basic structure of a real-time Kalman filter based on "delayed control resets" (to allow for finite computation time delay - Ref. 6 Sect. 15.1.2) is:

$$\begin{aligned} \xi_{INS_n}(+_c) &= \xi_{INS_n}(-) + g_{INS}\left(\xi_{INS_n}(-), \underline{u}_{c_n}\right) \\ \xi_{Aid_n}(+_c) &= \xi_{Aid_n}(-) + g_{Aid}\left(\xi_{INS_n}(-), \underline{u}_{c_n}\right) \end{aligned} \tag{51}$$

$$\underline{Z}_{Obs_n} = f\left(\xi_{INS_n}(+_c), \xi_{Aid_n}(+_c)\right) \tag{52}$$

$$\tilde{\underline{x}}_n(-) = \Phi_n \tilde{\underline{x}}_{n-1}(+_e) \tag{53}$$

$$\tilde{\underline{x}}_n(+_c) = \tilde{\underline{x}}_n(-) + \underline{u}_{c_n} \tag{54}$$

$$\tilde{\underline{z}}_n = H_n \tilde{\underline{x}}_n(+_c) \tag{55}$$

$$\tilde{\underline{x}}_n(+_e) = \tilde{\underline{x}}_n(+_c) + K_n\left(\underline{Z}_{Obs_n} - \tilde{\underline{z}}_n\right) \tag{56}$$

$$\underline{u}_{c_{n+1}} = \text{function of } \tilde{\underline{x}}_n(+_e) \tag{57}$$

$$\tilde{\underline{x}}_0 = 0 \qquad \text{Initial Conditions} \tag{58}$$

where

ξ_{INS} = INS navigation parameters.

ξ_{Aid} = Aiding device navigation parameters.

$g_{INS}(\ ), g_{Aid}(\ )$ = Non-linear functional operators used to apply $\underline{u}_{c_n}$ to the ξ_{INS}, ξ_{Aid} navigation parameters at time t_n such that the error in these parameters is controlled (typically to zero).

f( ) = Functional operator that compares designated equivalent elements of ξ_{INS} and ξ_{Aid}. The f( ) operator is designed so that for an error free INS, an error free aiding device, and a perfect (error free) f( ) software implementation, f( ) will be zero.

$\underline{Z}_{Obs}$ = Observation vector formed from the comparison between comparable INS and aiding device navigation parameters.

$\underline{u}_{c_{n+1}}$ = Control vector derived from the Kalman filter estimate of the time t_n value of $\underline{x}$ and applied at time t_{n+1} to constrain the actual value of $\underline{x}$.

$\tilde{}$ = Value for parameter estimated (or predicted) by the Kalman filter.

$(+_e)$ = Designation for parameter value at its designated time stamp (t_n in this case) immediately after ("a posteriori") the application of estimation resets (e subscript) at the same designated time.

$(+_c)$ = Designation for parameter value at its designated time stamp (t_n in this case) immediately after ("a posteriori") the application of control resets (c subscript) at the same designated time.

(-) = Designation for parameter value at its designated time stamp (t_n in this case) immediately prior to ("a priori") the application of any resets (estimation or control) at the same designated time.

K_n = Errors state estimation gain matrix.

n = Kalman filter software cycle time index.

$(\ )_n$ = $(\ )$ at the n^{th} Kalman filter cycle time.

$\underline{\tilde{z}}$ = Estimated "measurement vector" analytically represented as a column matrix. The $\underline{\tilde{z}}$ equation implemented in the Kalman filter represents a linearized version of the $\underline{Z}_{Obs}$ observation equation based on the expected (projected) value of the error state vector $\underline{x}$ when $\underline{Z}_{Obs}$ is measured.

H = The "measurement matrix". Generally a time varying function of the navigation parameters calculated in the INS computer. See further description in the paragraph following Equation (59) parameter definitions.

The previous Latin notation "a priori" and "a posteriori" has been adopted in Kalman filter terminology to add an element of "mysterioso". Identification of individual $(+_e)$ and $(+_c)$ "a posteriori" updates provides flexibility to allow for different Kalman filter estimation/control time points (e.g., for timing and synchronization of observation/measurement/control operations - Ref. 6 Sect. 15.1.2.4).

The estimation process described by Equation (56) is general and becomes a Kalman filter operation when the gain matrix K_n matrix is computed based on "optimally" estimating the error state vector as follows (Ref. 2 Sect. 4.2 and Ref. 6 Sect. 15.1.2.1):

$$K_n = P_n(-)\, H_n^T \left(H_n\, P_n(-)\, H_n^T + G_{M_n}\, R_n\, G_{M_n}^T \right)^{-1} \qquad (59)$$

in which

$$P \equiv E\left(\Delta\underline{x}\, \Delta\underline{x}^T\right) \qquad \Delta\underline{x} \equiv \tilde{\underline{x}} - \underline{x} \qquad R_n \equiv E\left(\underline{n}_{M_n}\, \underline{n}_{M_n}^T\right)$$

where

$\Delta\underline{x}$ = Error state vector estimation uncertainty.

P = Error state vector uncertainty covariance matrix.

$\underline{n}_M$ = Vector of independent white measurement noise sources (represented analytically as a column matrix). The $\underline{n}_M$ vector represents noise type error effects that may be introduced in the process of making the $\underline{Z}_{Obs}$ observation.

G_M = Measurement noise dynamic coupling matrix that couples $\underline{n}_M$ into the $\underline{Z}_{Obs}$ observation. Generally a time varying function of the navigation parameters calculated in the INS computer.

From an analytical standpoint, G_M and $\underline{n}_M$ in Equation (59) (and H in Equation (55)) are defined as part of $\underline{z}$, the linearized analytical form of the $\underline{Z}_{Obs}$ observation, which is denoted as the "measurement equation": $\underline{z}_n = H_n \underline{x}_n + G_{M_n} \underline{n}_{M_n}$ (Ref. 6 Sect. 15.1 and Ref. 2 Sect. 3.5). The covariance matrix P in Equation (59) is calculated by an integration operation based on the statistical uncertainty in the Equation (56) estimation process (using the previous $\underline{z}_n$ approximation for $\underline{Z}_{Obs_n}$) and the Equation (53) approximation for the actual Equation (48) error state vector propagation between estimation cycles (Ref. 2 Sect. 4.2 and Ref. 6 Sects. 15.1.2.1 and 15.1.2.1.1):

$$P_n(-) = \Phi_n P_{n-1}(+_e) \Phi_n^T + Q_n \tag{60}$$

$$P_n(+_e) = (I - K_n H_n) P_n(-) (I - K_n H_n)^T + K_n G_{M_n} R_n G_{M_n}^T K_n^T \tag{61}$$

in which

$$Q_n \equiv E\left(\underline{w}_n \underline{w}_n^T\right)$$

5.2.1 Covariance Simulation Analysis

The computational structure used in computing the Kalman filter covariance matrix (Eqs. (59) - (61)) can also be used in performance analysis time domain simulation programs for statistically estimating aided INS accuracy (or unaided performance by setting the K_n gain matrix to zero). Such covariance simulation programs (Ref. 6 Chpt. 16) are commonly used to provide numerical time histories depicting the accuracy of a given system configuration in terms of the covariance of its associated linearized error state vector. For a Kalman filter aided system, the covariance simulation is also utilized as a basic design tool during the synthesis and test of the "suboptimal" Kalman filter configuration used in the actual system. The suboptimal Kalman filter configuration is typically based on a simplified error state dynamic/measurement model (compared to the “real world” error state dynamics/measurements) with numerical values for its defining matrix elements that may differ from real world values. The covariance simulation is used to evaluate the performance of the suboptimal filter operating in a real world environment, and to provide the design engineer with useful sensitivities for identifying sources of undesirable performance characteristics during the design process.

5.3 Kalman Filter Validation

Although a Kalman filter is generally a complex software package, its validation process can be fairly straight-forward because of its fundamental underlying structure. The Kalman filter elements are well defined analytically and can be validated individually based on their intrinsic properties. Once the elements are validated, the proper operation of the filter is assured through its theoretical structure.

As an example, Reference 6 Section 15.1.4 discusses the following operations that can be performed using specialized test simulators for validating the Equations (51) - (58) and (59) - (61) Kalman filter algorithms:

- The state transition matrix Φ_n, estimated measurement $\underline{\tilde{z}}_n$, and observation $\underline{Z}_{Obs_n}$ algorithms can be validated by operating Equations (51) - (58) “open loop” (i.e., setting the Kalman gain K_n and

control vector $\underline{u}_c$ to zero) using simulators for ξ_{INS_n} and ξ_{Aid_n}. The ξ_{INS_n} simulator would consist of the strapdown inertial navigation algorithms upon which Φ_n is based. The ξ_{Aid_n} simulator would be built onto a previously validated trajectory generator; the trajectory generator would also provide the strapdown inertial sensor inputs to ξ_{INS_n}. The Kalman filter error state vector $\underset{\sim}{\underline{x}}_n$ components would be initialized to some arbitrary non-zero value; the same error values would be inserted into the ξ_{INS_n}, ξ_{Aid_n} parameters. Under these conditions, the Kalman filter estimated measurement $\underset{\sim}{\underline{z}}_n$ calculated with (55) should track the observation vector $\underline{Z}_{Obs_n}$ computed with (52), resulting in a zero value for the measurement residual $\underline{Z}_{Obs_n} - \underset{\sim}{\underline{z}}_n$ (within the fundamental linearization error in $\underset{\sim}{\underline{z}}_n$). A zero measurement residual validates the Φ_n, $\underset{\sim}{\underline{z}}_n$ and $\underline{Z}_{Obs_n}$ algorithms and associated timing structure in the simulation implementation.

- The covariance propagation algorithm (with process noise set to zero) can be validated as part of the previous process by initially setting the covariance matrix equal to the arbitrarily defined $\underset{\sim}{\underline{x}}_n$ error state vector times its transpose. The covariance matrix would then be propagated without resets using the Equation (60) algorithm or a Reference 6 Section 15.1.2.1.1.3 equivalent (several propagation cycles between estimation cycles). The propagated covariance matrix should then equal the propagated error state vector times its transpose.

- The algorithms for calculating the Kalman gain matrix K_n and resetting the covariance matrix can be validated by comparing the covariance reset algorithm output with the output from an equivalent alternative algorithm based on the analytical form of K_n (e.g., the Equation (61) "Joseph's" form compared with the Reference 6 Equation (15.1.2.1.1-4) optimal form). The results should be identical.

- The basic estimation capability of the Kalman filter can be validated by disabling the control vector (setting $\underline{u}_c$ to zero) and allowing the Kalman filter to estimate $\underset{\sim}{\underline{x}}_n$ in the presence of selected values for the error state components initially imbedded in ξ_{INS_n} and ξ_{Aid_n}. For this test, the process and measurement noise matrices in the Kalman filter covariance propagation/reset routines would be set to zero to heighten sensitivity (and better account for the error condition being simulated).

- Kalman filter estimation capability in the presence of process and measurement noise can be validated by repeating the previous test, but with random noise (from a software noise generator at the Kalman filter specified white noise source amplitudes) applied appropriately to the ξ_{INS_n}, ξ_{Aid_n} models (for process noise) and to the $\underline{Z}_{Obs_n}$ routine (for measurement noise). The Kalman filter process and measurement noise matrices would also be active for this test. In parallel, a "truth model" error state vector history would be generated using the same noise and initial conditions applied to a simulated version of error state dynamic Equation (47). The uncertainty in the Kalman filter estimated error state vector is evaluated by comparing the filter error state vector estimate with the "truth model" error state vector. Repeated runs with different random noise generator initial "seeds" provides an ensemble history of the error state uncertainty. The ensemble average of the uncertainty times its transpose (at common time points) should match the corresponding filter covariance matrix history.

- The control vector $\underline{u}_c$ interface in control reset Equations (51) and (54) can be validated by assigning an arbitrary value to $\underline{u}_c$ and applying it to the previous equations. If the control reset equations and the measurement/observation algorithms are consistent, the measurement residual $\underline{Z}_{Obs_n} - \underset{\sim}{\underline{z}}_n$ should be unaffected by the control reset application.

A previously validated trajectory generator is an important supporting software element in the Kalman filter validation process to provide truth model navigation parameter data over a user shaped trajectory profile. A trajectory generator is also required in covariance analysis programs to provide navigational parameters for computing the error-state-transition, measurement and noise matrices. Reference 6 Chapter 17 describes a trajectory generator based on exact strapdown inertial navigation integration algorithms that can be validated using the steps outlined in Section 2 (and subsections) of this paper.

6. SYSTEM INTEGRATION TESTING

System performance testing is conducted to verify that the system meets accuracy requirements under anticipated user environments (e.g., temperature, vibration, altitude, etc.). Prior to performance testing, system integration testing must be conducted to verify that functional operations are performed properly and accurately by all hardware, software, and interface elements. Based on direct experience, it is the author's firm contention that all software operations should be (and can be) completely validated prior to hardware/software integration of a strapdown INS. Otherwise, problems that will inevitably be encountered during final system integration (e.g., software errors due to programming flaws or algorithm error) may never be completely resolved (e.g., hardware designers may fault the software, software designers may fault the hardware - particularly the inertial components, thus discouraging meaningful problem resolution). For an aided strapdown INS, the software validation procedures discussed in Sections 2 and 5.3 can be utilized.

Hardware/software integration begins with software/system-computer integration. The purpose should be to verify identical performance in the system computer (within minuscule round-off error) as achieved in the computer used for software validation. Toward this end, the same simulators/truth-models used for the software validation process would be installed with the system software being integrated as the computer/software integration test driver/evaluator. The driver/evaluator should be designed/validated (as part of the software validation process) to fully exercise/verify all system software under simulated system inputs. In this regard, the driver/evaluator should be considered to be an integral part of the validated system software. For today's computer technology with associated high speed floating point architecture, long word-length, large memory capabilities and abundant software compiler/translator tools, computer/software integration should be a fairly straightforward task.

Hardware integration precedes hardware/software integration based on traditional methods in which functional elements are first individually tested, then interfaced/tested in functional groups until a fully integrated hardware assembly is verified. A critical part of hardware integration is the individual testing (by applied stimulus) of all functional element input/output interfaces to verify that proper signals are being transmitted to assigned locations with proper phasing. Analog signal inputs to the system computer must be individually tested to assure proper error free analog-to-digital conversion. Digital computer interfaces should be individually checked to assure immunity to system self-generated electrical noise and externally applied electro-magnetic interference (EMI). For a strapdown INS, common internal computer interfaces to be tested are for inertial sensor inputs, for individual temperature probe inputs (used for temperature sensitive sensor compensation software), and for special computer input/output signals used to control individual internal sensor operations (e.g., path length control resets for ring laser gyros). Successful interface testing requires pre-planning in the hardware design process for the ability to stimulate all interfaces to be tested. For an aided INS, interfaces with the aiding device must also be verified (e.g., GPS data).

A powerful technique for demonstrating satisfactory completion of the strapdown INS hardware/software integration process is to execute a system level laboratory calibration procedure (e.g., using the Section 4.1 and 4.2 Strapdown Rotation Test and Strapdown Drift Test). The system should perform accurately after re-calibration based on the test results. For a GPS aided INS, a successful GPS data interface can be demonstrated by a correct GPS data based position solution generated independently within the integrated system computer (compared with the same solution generated externally using an independent GPS receiver system).

For recent GPS aided INS micro-electronic "deeply integrated" architectures designed around MEMS (micro-machined electro-mechanical systems) inertial sensors, application of the previous integration test techniques poses new challenges.

7. CONCLUDING REMARKS

Strapdown inertial navigation computation algorithms can be accurately validated using simple closed-form exact solution truth models for reference. Algorithm validation can be greatly facilitated by structuring the algorithms based on exact integral solutions between update cycles of the continuous form navigation parameter time rate differential equations. This permits the algorithms to be validated using simple generic application independent truth models designed to exercise all algorithm elements. The truth models generally do not have to simulate realistic trajectory profiles.

Vibration induced inertial system error effects are easily analyzed using simplified analytical INS structural dynamic models. Simplified simulators based on these models can quickly generate numerical system performance measurements (e.g., coning/sculling motion, coning/sculling algorithm error, position integration algorithm folding effect error, vibration induced sensor error) as a function of system vibration power spectrum input, sensor assembly mounting dynamics/imbalance, and algorithm update frequency.

Several methods are available for INS system level performance analysis in the test laboratory to evaluate residual sensor errors remaining after system calibration. The Strapdown Drift Test and Strapdown Rotation Test provide simple methods for accurately measuring residual strapdown inertial sensor calibration errors without requiring elaborate precision test fixturing.

Kalman filters for strapdown INS aiding should be validated based on their natural internal structure using a simulated version of the INS being aided (interfaced to the Kalman filter) and a simulated aiding device. The software in the simulated INS should be validated prior to Kalman filter testing. Inputs to the INS and aiding device simulators would be provided by a previously validated trajectory generator. A trajectory generator is also required for covariance simulation analysis performance assessment of aided and unaided inertial navigation systems. Trajectory generator validation can be performed using the same methods used to validate the INS software.

System software should be thoroughly validated prior to system integration testing.

REFERENCES

1. Downs, H. B., “A Lab Test To Find The Major Error Sources In A Laser Strapdown Inertial Navigator”, 38th Annual Meeting of the ION, Colorado Springs, CO, June 15-17, 1982.

2. Gelb, A., *Applied Optimal Estimation*, The MIT Press, Cambridge Mass., London, England, 1978.

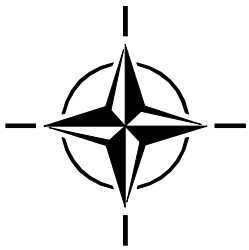
3. Savage, P. G., “Calibration Procedures For Laser Gyro Strapdown Inertial Navigation Systems”, 9th Annual Electro-Optics / Laser Conference and Exhibition, Anaheim, California, October 25-27, 1977.

4. Savage, P. G., “Strapdown Inertial Navigation System Integration Algorithm Design Part 1 - Attitude Algorithms”, *AIAA Journal Of Guidance, Control, And Dynamics*, Vol. 21, No. 1, January-February 1998, pp. 19-28.

5. Savage, P. G., “Strapdown Inertial Navigation System Integration Algorithm Design Part 2 - Velocity and Position Algorithms”, *AIAA Journal Of Guidance, Control, And Dynamics*, Vol. 21, No. 2, March-April 1998, pp. 208-221.

6. Savage, P. G., *Strapdown Analytics*, Strapdown Associates, Inc., Maple Plain, Minnesota, 2000

7. Savage, P. G., "Strapdown System Computational Elements", *Advances In Navigation Sensors and Integration Technology*, NATO RTO Lecture Series No. 232, October 2003, Section 3.



INS/GPS Integration Architectures

George T. Schmidt, Richard E. Phillips
The Charles Stark Draper Laboratory
555 Technology Sq. MS 57
Cambridge, Massachusetts 02139-3563
USA

ABSTRACT

An inertial navigation system (INS) exhibits relatively low noise from second to second, but tends to drift over time. Typical aircraft inertial navigation errors grow at rates between 1 and 10 nmi/h (1.8 to 18 km/h) of operation. In contrast, Global Positioning System (GPS) errors are relatively noisy from second to second, but exhibit no long-term drift. Using both of these systems is superior to using either alone. Integrating the information from each sensor results in a navigation system that operates like a drift-free INS. There are further benefits to be gained depending on the level at which the information is combined. This presentation will focus on integration architectures, including "loosely coupled," "tightly coupled," and "deeply integrated" configurations. The advantages and disadvantages of each level of integration will be listed. Examples of current and future systems will be cited. Examples of current and future systems will be cited.

1.0 INTRODUCTION

INS/GPS integration is not a new concept [Refs. 1, 2, 3, 4]. Measurements of noninertial quantities have long been incorporated into inertial navigation systems to limit error growth. Examples shown in Figure 1.1 are barometric "altitude" measurements, Doppler ground speed measurements, Doppler measurements to communications satellites, and range measurements to Omega stations.

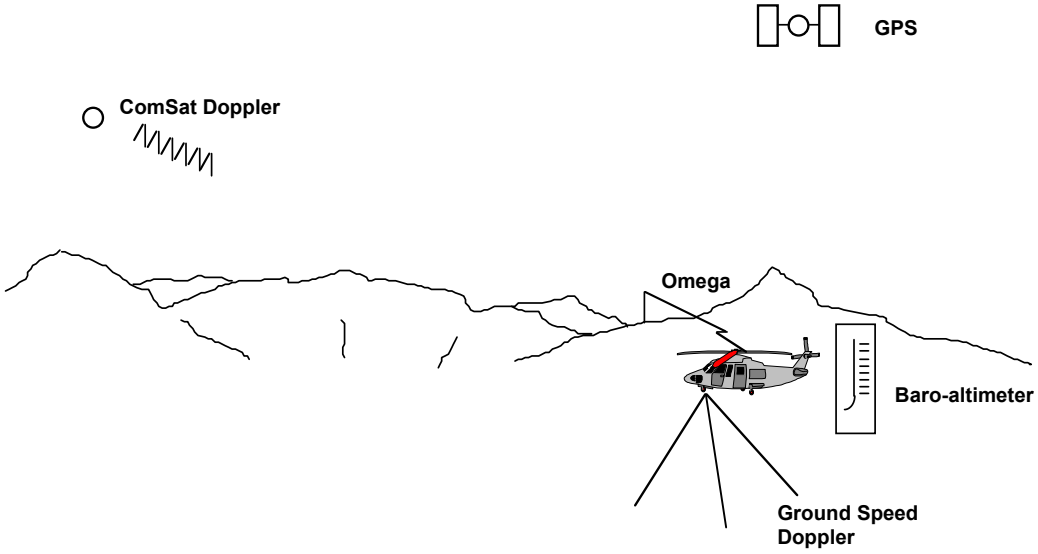


Figure 1.1: Inertial Navigation Systems can be Aided from a Variety of Sources.

Although GPS provides a deterministic solution for both position and velocity, it has its own shortcomings. Among them are: low data rate (typically 1 Hz), susceptibility to jamming (even unintentional interference), and lack of precision attitude information.

GPS and inertial measurements are complementary for two reasons. Their error characteristics are different and they are measures of different quantities. GPS provides measures of position and velocity. An accelerometer measures specific force. The gyroscopes provide a measure of attitude rate, and after initial alignment, they allow the accelerometer measurements to be resolved into a known coordinate frame.

GPS position measurement accuracy is limited due to a combination of low signal strength, the length of the pseudo-random code, which is about 300 m, and errors in the code tracking loop. Multipath, the phenomenon whereby several delayed copies of the signal arrive at the antenna after being reflected from nearby surfaces, is a source of correlated noise, especially for a moving vehicle. GPS position measurements also have constant or slowly changing biases due to satellite ephemeris and clock errors. These biases are bounded and are not integrated since they are already at the position level.

GPS velocity (position difference) measurements are also noisy, again due to variations in signal strength, the effects of changing multipath, and user clock instability.

In contrast, the accelerometers in an inertial navigation system measure specific force. They have relatively low-noise characteristics when compared with GPS measurements. The signals must be compensated for gravity and integrated twice before providing position estimates. This fundamental difference in radio navigation measurements and inertial measurements is a clue to the difference in the behavior of INS and GPS navigators.

Figure 1.2 shows accelerometer noise (and its first two integrals). The noise level was specified at 56 μg/√Hz, typical of a 10-nmi/h inertial system. The accelerometer noise itself is shown in the top graph.

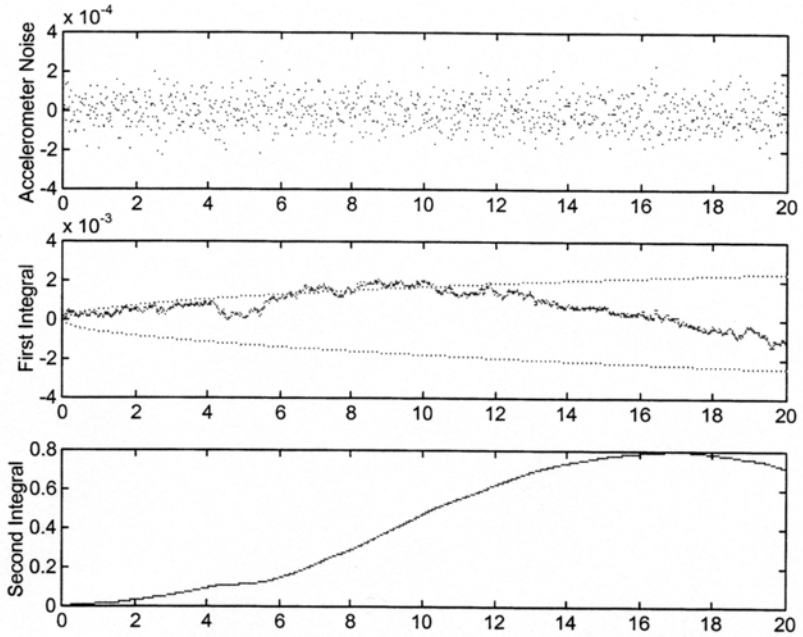


Figure 1.2: Accelerometer Noise and its First Two Integrals.

In these graphs, the accelerometer is read every 20 ms for 20 s. The integral of acceleration, the middle graph, shows the familiar "random walk" behavior of the integral of random noise. The dotted lines are the 1σ expected errors in the random walk. The second integral, the bottom graph, corresponds to position. (Units are metric: m, m/s and m/s^2)

GPS receivers typically produce solutions at 1 Hz or 10 Hz. The data bit rate of 50 Hz sets a "natural" minimum of 20 ms between position and velocity determinations. The middle graph in Figure 1.3 shows random noise in a set of measurements. The standard deviation of the velocity measurement is 0.01 m/s, typical of a good GPS receiver and strong signals in a benign environment.

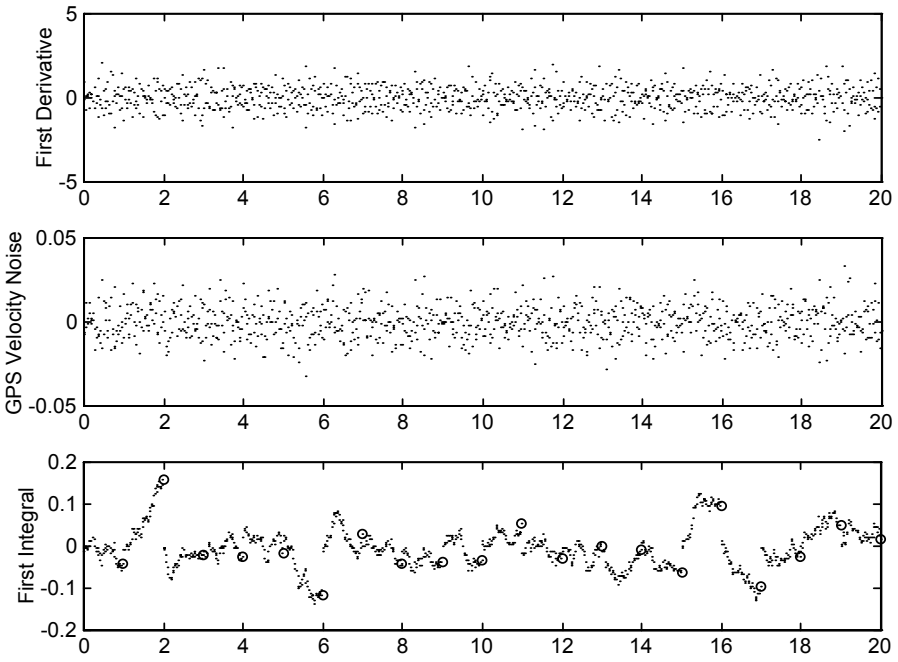


Figure 1.3: GPS Velocity Measurement Noise and its First Derivative and First Integral.

Back differencing these measurements to match the 50-Hz accelerometer output results in the noisy acceleration measurements as shown in the top graph of the figure. (Again, units are metric: m, m/s and m/s^2) The bottom graph of Figure 1.3 shows the first integral of the velocity over 1-s intervals as it might be used for carrier track smoothing of the GPS position measurement. The circles show the value of the integral after each 1-s interval. Thus, they indicate the error in the position difference from one GPS measurement (at 1 Hz) to the next. It is considerably smaller than the measurement error in the position measurement itself, thus the impetus for carrier track smoothing. The position measurement keeps the integral of the carrier track from diverging in the same "random walk" fashion as the integral of accelerometer noise.[1] Users will, quite naturally, want the features of both systems -- the high bandwidth and autonomy of inertial systems, and the long-term accuracy of GPS.

[1] It is not necessary to break the velocity measurement into 20-ms intervals. As suggested by Cox et al. [Ref. 1] it is possible to track the carrier phase continuously from satellite rise to satellite set. Another method for extracting a less noisy velocity would be to recognize that the error at the beginning of one interval is the negative of the error at the end of the preceding interval (if carrier tracking is continuous across the data bit).

Table 1.1 summarizes the features and shortcomings of inertial and GPS navigation systems.

Table 1.1: Inertial and GPS Attributes and Shortcomings.

	Attributes	Shortcomings
GPS	Errors are bounded	Low data rate No attitude information Susceptible to jamming (intentional and unintentional)
INS	High data rate Both translational and rotational information Self-contained (not susceptible to jamming)	Unbounded errors Requires knowledge of gravity

The goal of INS/GPS integration, besides providing the redundancy of two systems, is to take advantage of the synergy outlined as follows:

1. The conventional approach to aiding the receiver's carrier and code tracking loops with inertial sensor information allows the effective bandwidth of these loops to be reduced, even in the presence of severe vehicle maneuvers, thereby improving the ability of the receiver to track signals in a noisy environment such as caused by a jammer. The more accurate the inertial information, the narrower the bandwidth of the loops that can be designed. In a jamming environment, this allows the vehicle to more closely approach a jammer-protected target before losing GPS tracking.[2] A minimum of a factor of 3 to 4 improvement in approach distance is typical. A "deeply-integrated" approach to aiding will be shown to be even more robust. Outside a jamming environment, INS data provide high bandwidth accurate navigation and control information and allow a long series of GPS measurements to play a role in the recursive navigation solution. They also provide an accurate navigation solution in situations where "GPS only" navigation would be subject to "natural" short-term outages caused by signal blockage and antenna shading.

2. The inertial system provides the only navigation information when the GPS signal is not available. Then inertial position and velocity information can reduce the search time required to reacquire the GPS signals after an outage and to enable direct P(Y) code reacquisition in a jamming environment.

3. Low-noise inertial sensors can have their bias errors calibrated during the mission by using GPS measurements in an integrated navigation filter that combines inertial system and GPS measurements to further improve the benefits listed under (1) and (2). The accuracy achieved by the combined INS/GPS system should exceed the specified accuracy of GPS alone. The synergistic benefits of combining inertial data with GPS data as described in the previous paragraph are notionally shown in Figure 1.4.

4. Having inertial instruments at the core of the navigation system allows any number of satellites to play a role in the solution.

[2] Representative jammers are given in Reference 4.

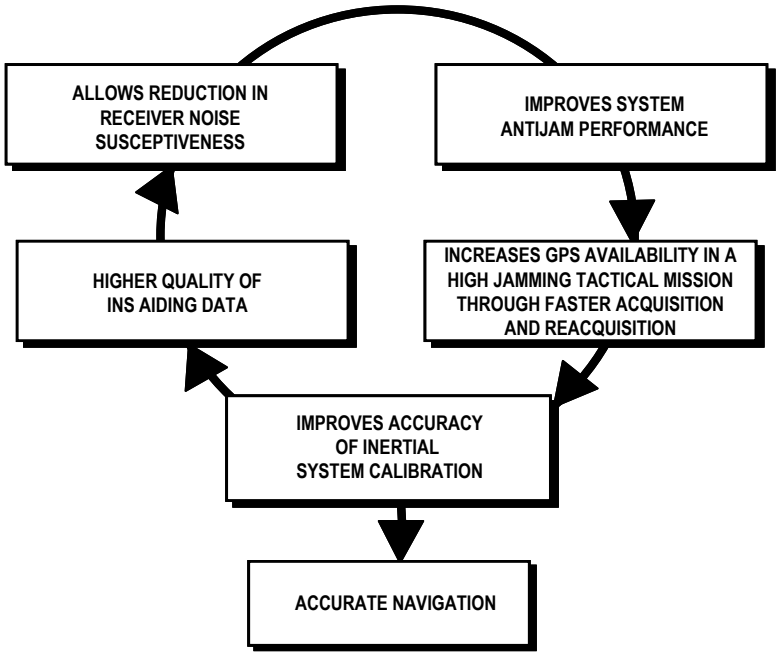


Figure 1.4: The Synergy of INS/GPS Integration.

The accuracy of the solution, the resistance to jamming, and the ability to calibrate the biases in low-noise inertial system components depends on the avionics system architecture. There have been many different system architectures that have been commonly implemented to combine the GPS receiver outputs and the INS information, thus obtaining inertial sensor calibration, to estimate the vehicle state. Different INS/GPS architectures and benefits will be discussed in the following section.

2.0 ALTERNATE INS/GPS ARCHITECTURES

Four architectures will be discussed in this paper: separate systems, loosely coupled, tightly coupled,[3] and deeply integrated systems. Several variations of loosely coupled and tightly coupled systems will be shown.

2.1 Separate Systems

The simplest way to get the features of both systems is to simply have both navigation systems integrated only in the mind of the user. Only slightly more complex would be to simply add a correction from the GPS to the inertial navigation solution. Figure 2.1 illustrates such a system.

[3] "Coupled" here refers to combining data from the GPS and INS systems into a single navigation solution. When retrofitting older aircraft with new navigation systems, there is often a problem with space and with power and data connections. For these reasons, it can be desirable to include GPS in the same box with the inertial navigator. This repackaging will be referred to as "embedding."

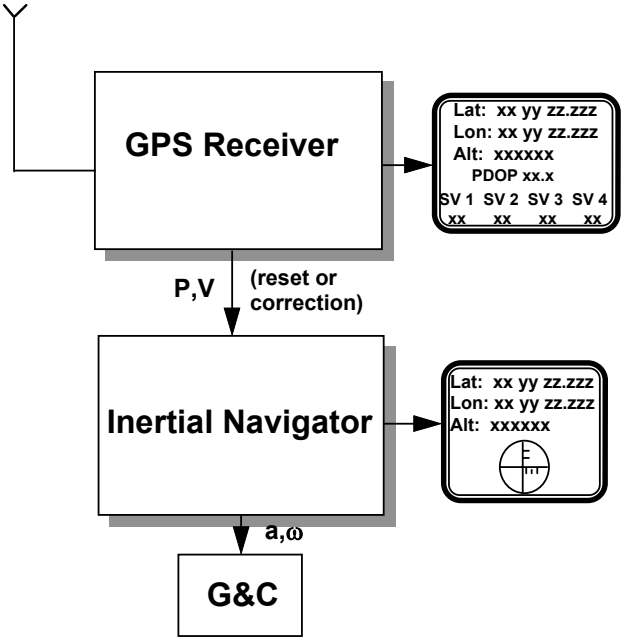


Figure 2.1: Separate GPS and INS Systems with a Possible INS Reset.

This mode of operation or coupling has the advantage of leaving the two systems independent and redundant. But as the Inertial Measurement Unit (IMU) drifts, the inertial solution becomes practically useless.

By using a GPS "reset" or correction, the inertial system errors are kept bounded, but after the first reset, the INS solution is no longer independent of the GPS system. Of course, the corrections could be monitored for reasonableness to prevent the contamination of the inertial solution with grossly incorrect GPS measurements should they occur. Even if not independent, the systems do remain redundant in the sense that they both still have dedicated displays, power supplies, etc., so that the failure of one does not affect the other or leave the vehicle with no navigator.

Inertial system resets provided the first mechanization for the U.S. Space Shuttle GPS integration. The Space Shuttle has a ground uplink capability in which the position and velocity are simply set to the uplinked quantities. For minimum change to the software, the GPS system simply provides a pseudo ground uplink. To make a minimal impact on existing software and hardware is a common rationale for the more loosely coupled systems.

In summary, this architecture offers redundancy, bounded position and velocity estimates, attitude and attitude rate information, high data rates for both translational and rotational information suitable for guidance and control functions, and (for existing systems) minimum impact on hardware and software.

2.2 Loosely Coupled

Most often, discussions of INS/GPS integration focus on systems that are more tightly coupled than the system described in the previous section. This will be true of the remaining architectures. Redundancy and solution independence can be maintained, but we will see more benefits from coupling than the simple sum of inertial and GPS navigation features. New software will be required, an integration filter for example.

2.2.1 Loosely Coupled – Conservative Approach

Figure 2.2 shows one version of a loosely coupled system. In this system, the functional division could correspond to the physical division with the GPS in a box, the INS in a box, and the computer that combines the navigation solutions in yet another box. Only low rates are required for data links between the boxes. Of course, the three functions could be packaged together if desired.

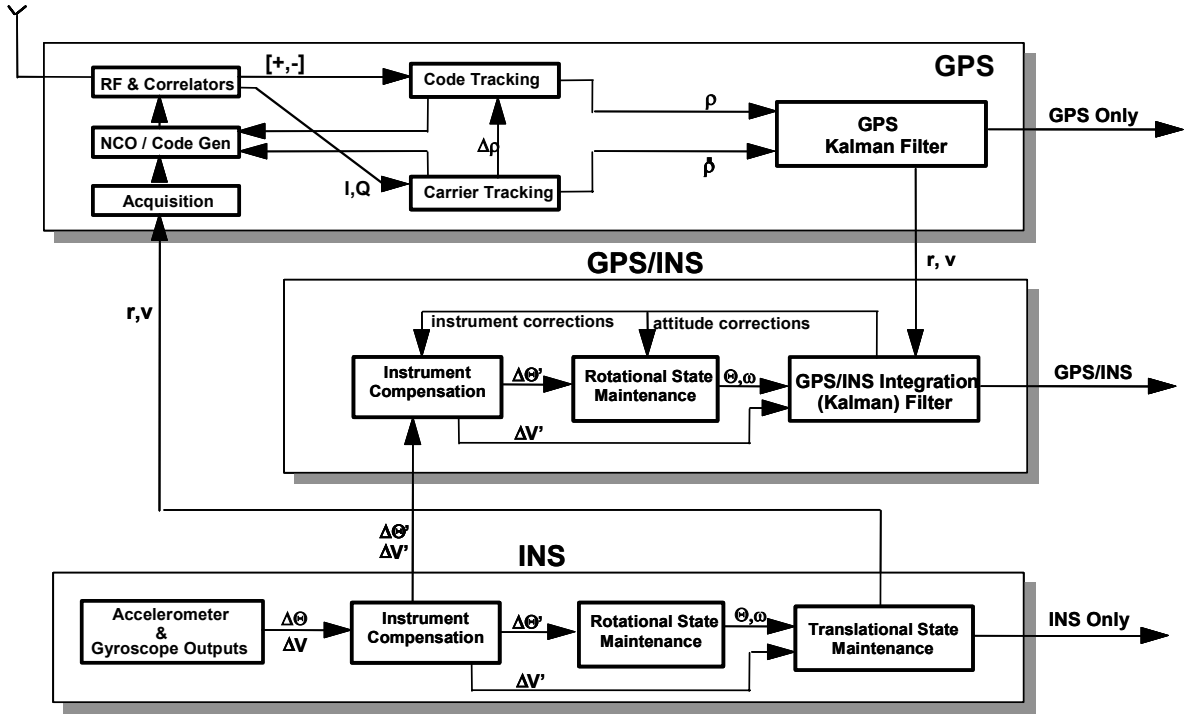


Figure 2.2: A Loosely Coupled INS/GPS Navigation System.

Simplified diagrams for each of the functions are shown. The following paragraphs consist of a high-level description of the operation of a receiver and inertial navigator. It is assumed that the reader has some familiarity with these sensors; thus, the discussion is intended to serve more as a reminder of pertinent features rather than a tutorial.

The receiver diagram shows signals coming into the radio frequency "front end" of the receiver. They are down converted to baseband and fed into the correlators. Meanwhile, a duplicate of the signal is generated internally in the receiver. In fact, three (or more) copies are generated. One of these copies is supposedly time synchronized so that it arrives at the "prompt" correlator at exactly the same time as the signal from the antenna. The other copies are intentionally either a little early or a little late compared with what is expected from the satellite. These copies are sent to the early and late correlators. The magnitude of the early and late correlations, indicated by [+,-] in the figure, is given to the code tracking function. The difference in these magnitudes is an indication of the timing error (and thus range error). This error signal is fed back into the code generator, which makes a correction to the code phase timing. This process is repeated as long as the signal is present. At some point, the phase error will be driven down to an acceptable level, and the code will be declared "in lock." While "in lock," the time difference between the broadcast of the signal and the receipt of the signal are a measure of the pseudo-range.

Similarly, the in-phase and quadrature signals are fed into the carrier tracking function. The arctangent of these two signals is a measure of the carrier tracking error. This signal is fed back to the numerically-controlled oscillator (NCO), and its frequency is adjusted accordingly. It might be noted that the carrier tracking loop is typically of third order, allowing it to "perfectly track" signals with constant range acceleration. Note that the carrier loop (when it is "in lock") "aids" the code loop as indicated by the arrow labeled $\Delta\rho$. In this mode, the code tracking loop can be of first order.

For this architecture, the receiver only uses INS data for the purpose of aiding in acquisition. Knowing the position and velocity of the vehicle enables the code generator and oscillator to make good initial guesses of the frequency and code phase of the incoming signal. The search time during acquisition can be reduced significantly depending on the accuracy of these estimates.

The output of the two tracking loops is an estimate of the range and range rate between the vehicle and the satellite. Range and range rate estimates from four satellites are sufficient to resolve the vehicle position, velocity, receiver clock bias, and receiver clock drift rate. For some receivers, these deterministic quantities are the ultimate receiver output. However, receivers that are expected to operate in a dynamic environment use a polynomial Kalman filter to estimate position, velocity, and acceleration, and clock bias and clock drift rate.

A (strapdown) INS diagram is shown at the bottom of the figure. Raw measurements from the accelerometers and gyroscopes are compensated using *a priori* values, or values derived from another mode of operation (e.g., a calibration and alignment mode). The gyroscope output is used to maintain the rotational state of the vehicle. Angular rates are integrated into either a quaternion or matrix, which relates the vehicle attitude to some reference coordinate system (e.g., local level). Corrected ΔV's are rotated into this coordinate system and integrated to maintain the translational state: position and velocity.

The INS/GPS integration function is shown in the middle diagram of the figure. It receives corrected inertial measurements, $\Delta\Theta$' and ΔV', from the INS and position and velocity measurements from the GPS receiver. The 1-Hz GPS measurements, coming from a Kalman filter, are highly correlated. The second Kalman filter in this "cascaded" architecture handles this problem by only incorporating these measurements every 10 s. The 10-s interval allows each position/velocity measurement to be more or less independent of the previous measurements. A performance comparison between this loosely coupled architecture and a tightly coupled architecture is given in Reference 5. Note that the integration Kalman filter includes calibration and alignment estimates that provide in-flight improvement of the INS calibration and alignment. This conservative approach to coupling yielded surprisingly good results in estimating these gyro and accelerometer parameters.

Table 2.1 summarizes the functions of the three components of the system. Table 2.2 lists the attributes of the system.

Table 2.1: Functions of the Three Components of the Loosely Coupled System.

Component	Function
GPS	The Kalman filter estimates: Position, velocity, acceleration Clock bias, clock drift
INS	The INS provides: Position, velocity, acceleration Attitude, attitude rate
Integration Filter	The integration filter estimates: Position, velocity Attitude corrections, instrument corrections

Table 2.2: Loosely Coupled System Attributes

System Attributes
All the attributes of the previous "uncoupled" architecture, including redundant and independent INS and GPS solutions
More rapid acquisition of code and carrier phase
Improved navigation performance
In-flight (and better) calibration and alignment, which results in improved navigation during satellite loss/jamming

We distinguish between jamming resistance and mitigation against jamming. By the latter term, we simply mean that the inertial bias and scale-factor parameters will be better calibrated so that if the GPS signal is lost, the INS/GPS solution (receiving only inertial data) will be accurate for longer than otherwise.

2.2.2 Loosely Coupled-Aggressive Approach

Figure 2.3 shows possible variations in what may still be considered a loosely coupled architecture. Inertial aiding of tracking loops has not yet been introduced, and the integration filter still uses position and velocity data rather than pseudo-range and range rate. Additional data transfer beyond that of the previous architecture is indicated by heavy lines. Either one or the other or both data transfers are viable options.

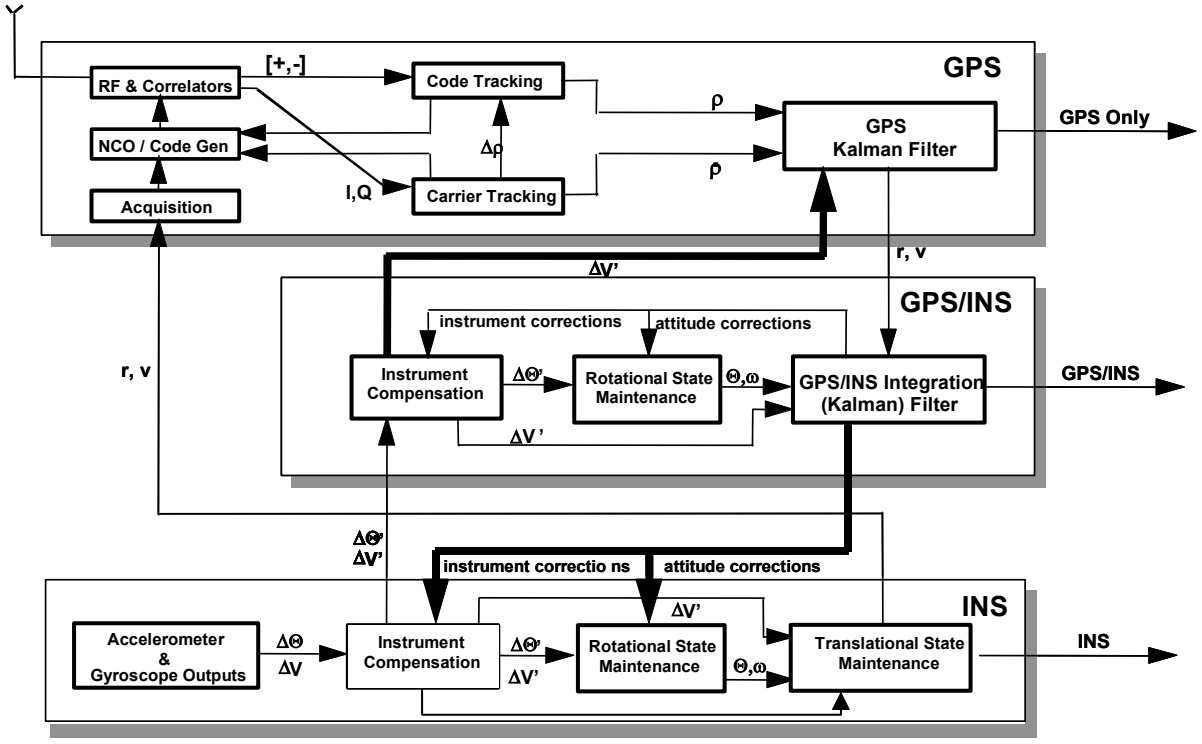


Figure 2.3: Loosely Coupled Variations use the Results of the Integration Filter in both the GPS and INS Solutions.

The first of these data transfers is of the corrected velocity increment ΔV' from the INS/GPS module to be used in the GPS module to propagate the solution between measurements. This provides a vast improvement in dynamic situations. Otherwise, the propagation must be done using the acceleration estimate from the GPS Kalman filter itself. This acceleration, although a component of the filter state, is derived by back differencing the velocity. Figure 1.3 showed the level of acceleration noise inherent in this operation. It is true that the filter offers some "smoothing." However, it cannot offer much due to the process noise, which must be added in the dynamic aircraft environment. There is a requirement by the U.S. GPS Joint Program Office that the receiver be able to maintain track at a jerk level of 10 g/s for 0.6 s. Although this requirement is on the tracking loops, it most certainly has implications for the process noise that must be added to the acceleration covariance term in the GPS Kalman filter. There is no substitute for using the measured acceleration.

The other optional data transfer is that of the in-flight calibration and alignment corrections from the INS/GPS estimator to the INS. This helps keep the INS in closer agreement with the INS/GPS solution. Of course, the independence of the two solutions is lost.

In summary, we have improved the navigation accuracy of the combined GPS and the INS at the cost of independence in their solutions. We have maintained redundant systems.

2.2.3 Loosely Coupled – Rockwell's MAGR Approach

This approach might actually be characterized somewhere between loosely and tightly coupled. Figure 2.4 shows the GPS and INS functions and interfaces between them. The MAGR (Military Airborne GPS

Receiver) has an INS mode and a PVA (Position, Velocity, and Acceleration) mode. The latter is a stand-alone mode independent of inertial measurements.

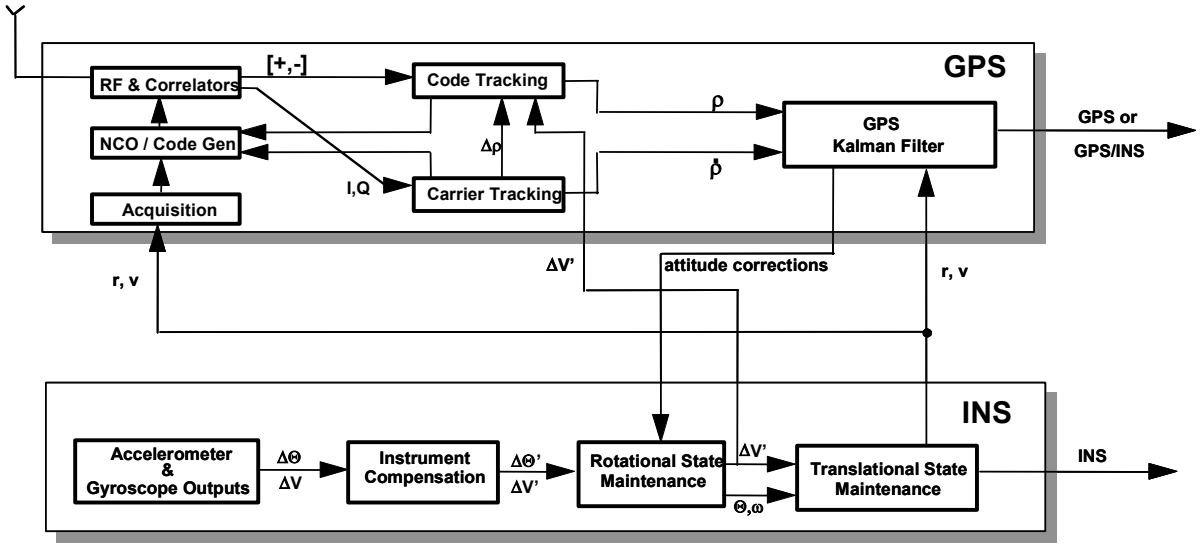


Figure 2.4: The Coupling Approach taken by the Rockwell MAGR.

In the INS mode, inertial measurements are used to aid the code tracking loop when the carrier loop is out of lock and unable to provide aiding. The GPS uses the inertial measurements to extrapolate the position and velocity between GPS measurements rather than estimating acceleration in a polynomial filter. The GPS estimates attitude corrections for the IMU. The MAGR (in the INS mode) thus has some of the features of a tightly coupled system. Table 2.3 lists the filter state elements for the PVA and INS mode of operation.

Table 2.3: Filter States for the MAGR

PVA Mode	INS Mode
Position	Position
Velocity	Velocity
Acceleration	Attitude corrections
Clock bias	Clock bias
Clock drift	Clock drift
Barometer bias	Barometer bias

2.3 Tightly Coupled

Finally, the two changes that define a tightly coupled system are introduced. The GPS range and delta range measurements are incorporated directly into the navigation estimate, and the position and velocity from the inertial system are used by the GPS receiver to reduce the tracking loop bandwidths even in the presence of

high dynamics.[4] First, a straightforward system that provides a single combined INS/GPS solution will be presented. Then a system that also maintains independent and redundant GPS and INS solutions will be presented.

2.3.1 Tightly Coupled – Combined INS/GPS Only

Figure 2.5 shows the architecture for a tightly coupled INS/GPS navigation system that offers a single navigation solution. The INS and GPS modules have been truncated. The inertial "system" now simply provides raw measurements. The GPS receiver does not have its own Kalman filter, but it does still have independent tracking loops that provide the values for pseudo-range and range rate. Although it has not been shown in any of the figures, it is of course understood that the pseudo-range and range rate to at least four satellites are required for a position and velocity determination. The GPS functions shown in the upper diagram of Figure 2.5 are duplicated for each satellite by having multiple "channels" in a receiver – only one of which is shown in the diagram.

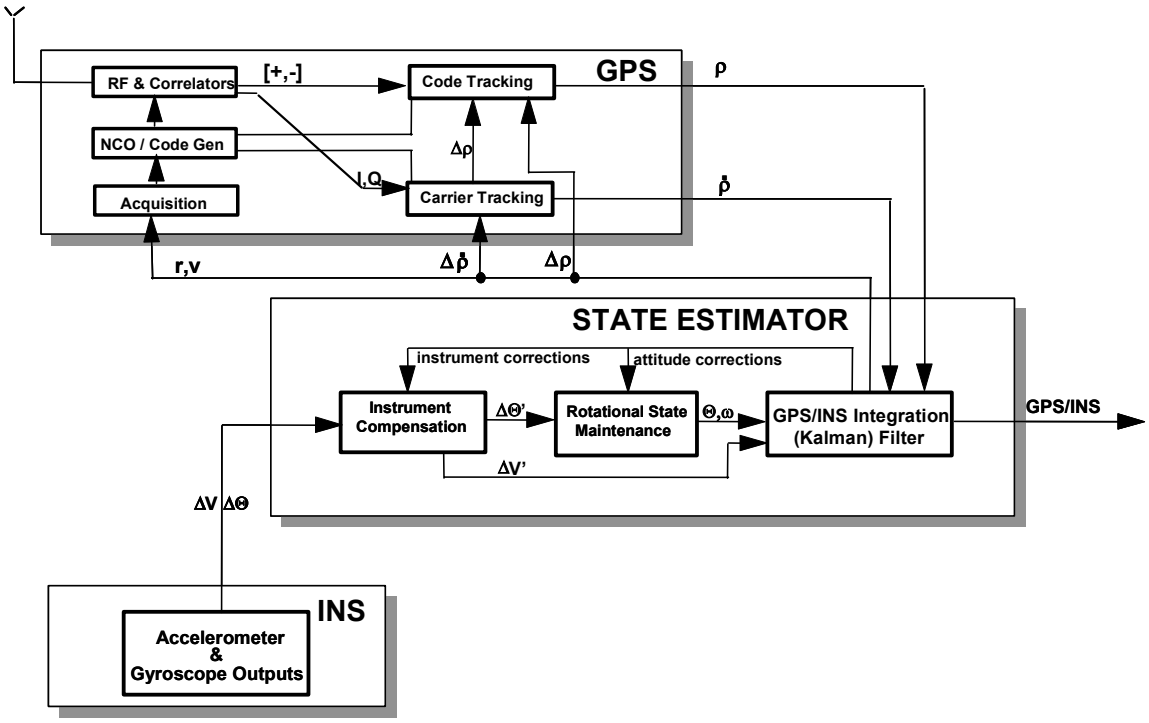


Figure 2.5: A Tightly Coupled INS/GPS Navigation System offering only One Combined Solution.

The tracking loops in the receiver are aided by data from the INS/GPS state estimator. These data are required at a high rate, thus the propagation from one measurement epoch to another is broken into many subintervals for the purpose of tracking loop aiding. The goal is to make these tracking loops "think" the receiver is sitting still. The quantities being estimated by the Kalman filter are position and velocity, whereas the data required by the tracking loops are code phase (range) and Doppler frequency shift (range rate). The estimated position and velocity and the satellite ephemerides are used to calculate the code phase and frequency shift.

[4] The definitions of tightly coupled are not universally agreed upon. The first round of "EGI" receivers were considered to be tightly coupled by some but they did not have inertial aiding of the carrier tracking loops.

The diagrams in this paper will show the transfer of r, v, and delta range and range rate, implying that these calculations are done in the receiver. They could as well be done in the "State Estimator" box. The bandwidth of the tracking loops must only accommodate the errors in the measured acceleration rather than the whole acceleration. These errors are many orders of magnitude less than the acceleration itself, depending on the quality of the inertial system and its calibration.

The tightly coupled navigation systems are more accurate. This can be seen in Reference 5, where tightly and loosely coupled systems are compared. We still have the gains or attributes of the loosely coupled systems except for the loss of redundancy. The bandwidth of the tracking loops can be reduced, thus increasing jamming resistance. The integration filter can make optimal use of any and all satellites that are being tracked, even if there are less than four of them. It should be said that GPS-only solutions can be maintained with either three or two satellites if one or two or both of the following assumptions are made: 1) the clock bias is constant and 2) the altitude is constant or is known by some other means (e.g., a baroaltimeter).

Only the redundancy offered by three complete systems is lost for this architecture. A summary of the benefits accrued by coupling will be given at the end of Section 2.3.2.

2.3.2 Tightly Coupled – Redundant Solutions

Figure 2.6 illustrates a tightly coupled architecture that also offers redundant navigation solutions from both the GPS and INS. This figure most closely resembles the Figure 2.3 for the loosely coupled architecture. The changes with reference to that earlier figure are inertial aiding of the tracking loops from the INS/GPS solution and the use of pseudo-range and range rate measurements rather than position and velocity in the integration filter.

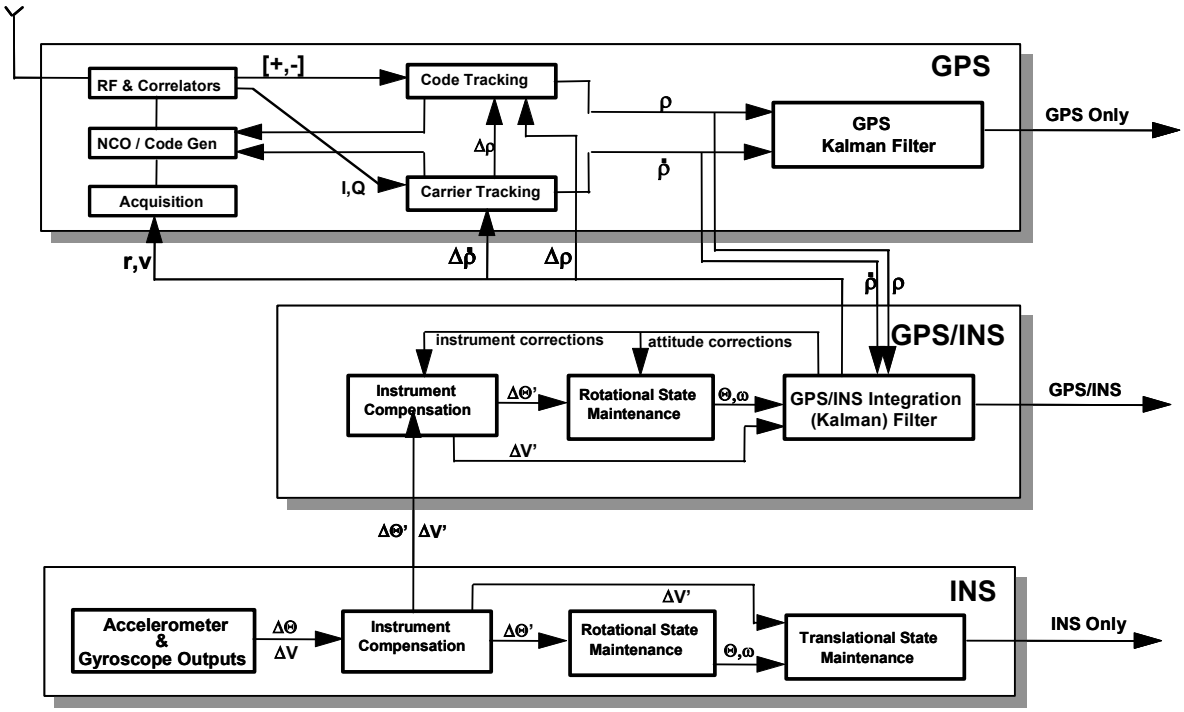


Figure 2.6: Tightly Coupled Architecture with Redundant GPS and INS-Only Solutions.

This more elaborate system requires more software. This is the price of the redundancy unless the software is already present in existing INSs and GPS. This can indeed be the case and was the case in the U.S. GPS Joint Program Office's Embedded GPS Inertial (EGI) program. The concept of the EGI program was to obtain a navigation system with GPS and inertial attributes at minimum cost. Specifications for such a (non-developmental) system were published. Several vendors have produced such embedded systems, among them are Litton's LN-100G [Ref. 6] and Honeywell's H-764G [Ref. 7] combinations of GPS with ring laser gyroscopes. The U.S. Advanced Research Projects Administration also sponsors a tightly coupled and embedded combination, the GPS Guidance Package, using fiber-optic gyroscopes.

Embedding the receivers allows the data transfer rates required for tight coupling. EGI specifications state that separate and independent inertial-only and GPS-only solutions are to be maintained. Although they do not specify the two characteristics we have used to define tight coupling, they do state that INS aiding of the tracking loops is allowed [Ref. 8]. This potentially makes the GPS solution dependent on the INS. Mathematical independence is maintained if the tracking loops have adequate signal strength to work with and can maintain lock such that the error in range rate (for example) is independent of the aiding value. If the error in the tracking loops is independent of the aiding, the GPS and INS/GPS solutions will be independent. Logic in the receivers attempts to recognize when lock is lost and not incorporate the resulting "bad" measurements into the GPS solution. This precaution also (arguably) keeps the GPS solution mathematically independent of the other solutions.

The tightly coupled receiver offers elevated jamming resistance. It offers the ability to continue operation when GPS is intermittent due to wing shadowing, foliage, or other natural or man-made obstructions. Table 2.4 summarizes the benefits that have been gained by coupling GPS with INS. The benefits are cumulative. That is, the benefits for each level also include those for the previous level. (The exception is loss of redundancy and independence for the simpler of the tight coupling architectures.)

Table 2.4: Cumulative Benefits of Increasingly Tight Coupling

Coupling Level	Benefit
Uncoupled/reset INS to GPS (Sum of system attributes)	Position, velocity, acceleration, attitude, and attitude rate information Redundant systems • A drift-free GPS • A high-bandwidth INS
Loosely coupled	More rapid GPS acquisition In-flight calibration and alignment Better inertial instrument calibration and alignment • Better attitude estimates • Longer operation after jamming
Tightly coupled	Better navigation performance Better instrument calibration Reliable tracking under high dynamics Reduced tracking loop bandwidth (jamming resistance) Optimum use of however many SVs available

2.4 Deeply Integrated

Figure 2.7 shows the architecture of a deeply integrated INS/GPS navigation system. This figure compares most closely with the first tightly coupled architecture shown in Figure 2.4. In the deeply integrated concept, independent tracking loops for the code and carrier have been eliminated.

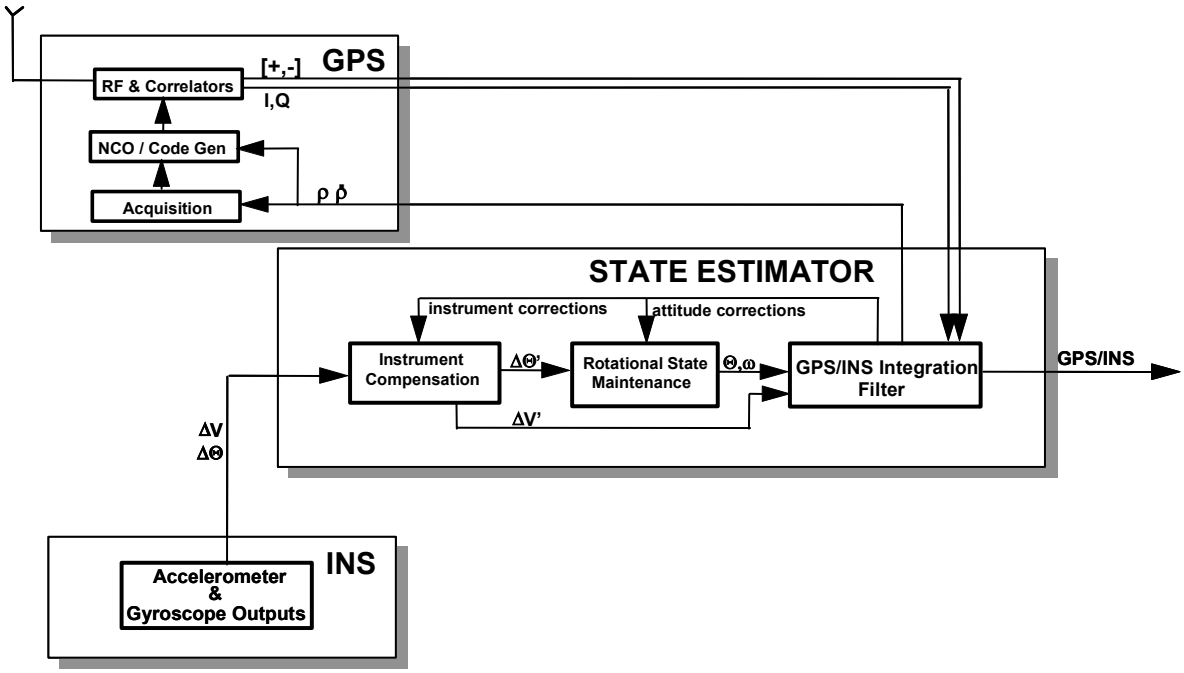


Figure 2.7: Deeply Integrated INS/GPS Systems feature a Single Estimator for both Detection and Navigation.

In the deeply integrated approach, the problem is formulated directly as a navigation problem in which the optimum (minimum-variance) solution is sought for each component of the multidimensional navigation state vector.[5] By formulating the problem in this manner, the navigation algorithms are derived directly from the assumed dynamical models, measurement models, and noise models. The solutions that are obtained are not based on the usual notions of tracking loops and operational modes (e.g., State 3, State 5, etc.). Rather, the solution employs a nonlinear filter that operates efficiently at all jammer/signal (J/S) levels and is a significant departure from traditional extended Kalman filter designs. The navigator includes adaptive algorithms for estimating pos-correlation signal and noise power using the full correlator bank. Filter gains continuously adapt to changes in the J/S environment, and the error covariance propagation is driven directly by measurements to enhance robustness under high jamming conditions (see Figure 2.8).

[5] The material in this section is from References 9 and 10.

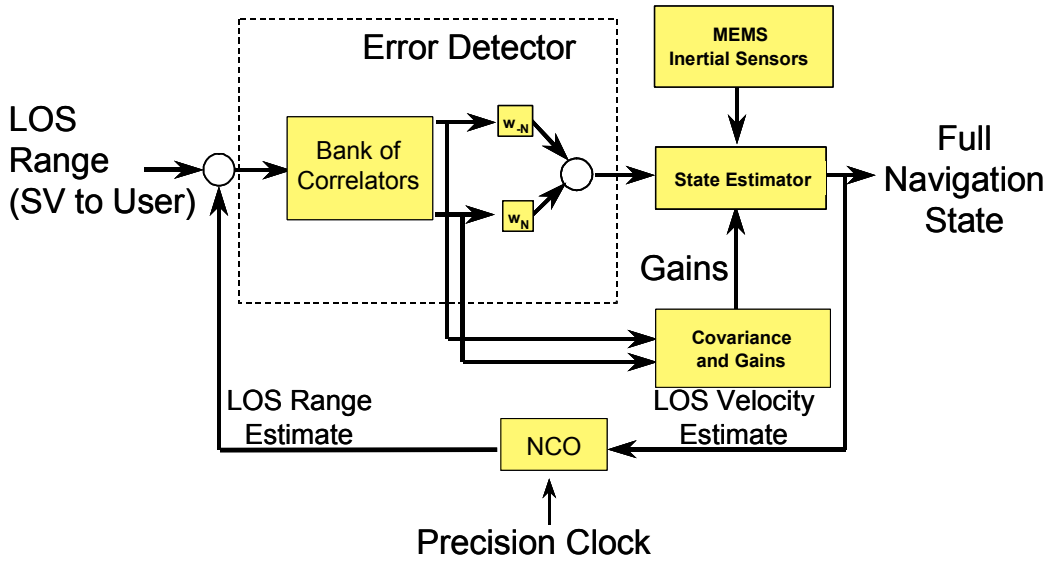


Figure 2.8: INS/GPS Deep Integration.

In this system, individual satellite phase detectors and tracking loop filters are eliminated. Measurements from all available satellites are processed sequentially and independently, and correlation among the line-of-sight distances to all satellites in view is fully accounted for. This minimizes problems associated with unmodeled satellite signal or ephemeris variations and allows for full Receiver Autonomous Integrity Monitoring (RAIM) capability.

The design offers several significant benefits at high J/S levels. The effects of measurement nonlinearities, which are significant at high J/S levels, are accounted for in an efficient manner. The estimator produces near-optimal state vector estimates as well as estimates of the state error covariance matrix. The estimator operates in real time using recursive algorithms for both state vector and error covariance matrix estimation. The J/S levels are estimated adaptively in real time to facilitate seamless transitions between course tracking and tight tracking without the use of artificial moding.

Extended-range correlation may be included optionally to increase the code tracking loss-of-lock threshold under high jamming and high dynamic scenarios. If excessively high jamming levels are encountered (e.g., beyond 75 to 80 dB J/S at the receiver input for P(Y) code tracking), the GPS measurements may become so noisy that optimal weights given to the GPS measurements become negligible. In this situation, navigation error behavior is essentially governed by current velocity errors and the characteristics of any additional navigation sensors that are employed. Code tracking is maintained as long as the line-of-sight delay error remains within the maximum allowed by the correlator bank. If there is a subsequent reduction in J/S so that the optimal weights become significant, optimum code tracking performance is maintained without the need for reacquisition. Detector shapes for each correlator depend on the correlator lag and rms line-of-sight delay error.

For navigators using GPS only, navigation errors will be reduced significantly by using algorithms that approximate the minimum-variance solutions at high J/S. For navigators employing other sensors, a fully integrated system will allow simpler, smaller, cheaper hardware to be employed. Superior sensor calibration capability will reduce sensor performance requirements, allowing lower-cost sensors to be used.

Figure 2.9 shows the information flow between the principal elements of the navigation system. The data from each satellite in view are processed sequentially; the figure illustrates processing for a single satellite. The GPS receiver front end performs filtering, carrier wipeoff and sampling to produce I/Q data. These data are processed by each correlator to produce the 50-Hz samples $I_{50}(j,k)$ and $Q_{50}(j,k)$ for the k^{th} correlator at the j^{th} time point. Square law detection and summation is then used to obtain $Z_k(n)$; currently, summation is over five samples so that $Z_k(n)$ is 10-Hz data. The processor uses inputs $Z_k(n)$ to calculate the navigation state estimate $\hat{x}(n)$. The state estimate is propagated to measurement update time using an assumed dynamical model. As shown in the figure (dashed lines), two types of sensors may be optionally added to the GPS-based navigator. Inertial sensor data may be incorporated during propagation to reduce the error bandwidth during periods of high dynamics and retard error growth if code lock is lost. If inertial sensors are used, the processor accepts raw sensor data (e.g., body frame specific force and angular rates for a strapdown configuration) and time-correlated sensor error states may be included in the navigation state vector in order to perform in-flight calibration of significant error sources. At measurement update time, the state is updated using the measurements $\{Z_k(n);\ k = -m,\ldots,m\}$ from $2m + 1$ correlators, satellite ephemeris data, and (optionally) measurements from other sensors (e.g., radars, altimeters, etc.). The estimated time delay $\hat{\tau}(n)$, which is a function of the state estimate and satellite ephemeris, is fed to the code NCO, which controls correlator code phase in order to maintain the mean code tracking error close to zero.

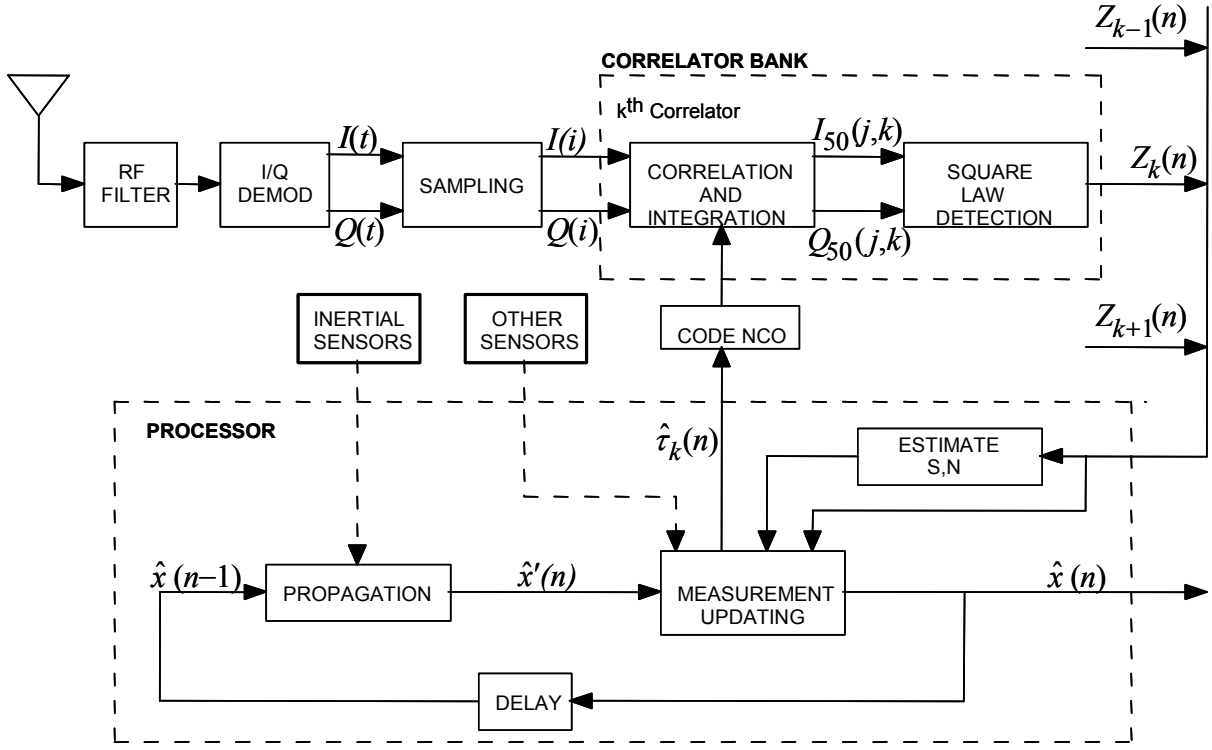


Figure 2.9: Code Tracking Information Flow Diagram for GPS-Based Navigator.

The navigator includes adaptive algorithms for estimating postcorrelation signal power (S) and noise power (N). Noise statistics are assumed to be the same for all correlators. Although the 50-Hz noises are uncorrelated over time, the noise in adjacent correlators is correlated.

3.0 SUMMARY

This paper has described INS/GPS integration architectures including loosely coupled, tightly coupled, and deeply integrated configurations. The advantages and disadvantages of each level of integration were listed. Examples of current and futures systems were cited. In a companion paper, Reference 5, performance comparisons between the three major INS/GPS system architectures for various mission scenarios will be presented in order to understand the benefits of each. The loosely coupled and tightly coupled systems will be compared in several scenarios including aircraft flying against jammers and a helicopter flying a scout mission. The tightly coupled and deeply integrated architectures will be compared for several jamming scenarios including that of a precision guided munition.

4.0 REFERENCES

[1] Cox, D.B., Kriegsman, B.A., Stonestreet, W.M., Kishel, J., and Calicchia, L.V., *Feasibility Study of GPS-Inertial Navigation for Helicopters and Study of Advanced GPS Signal Processing Techniques*, Draper Laboratory Report R-981, Cambridge, MA, March 1978.

[2] Cox, D.B., "Inertial Integration of GPS," *Global Position System – Papers Published in Navigation*, Vol. 1, Institute of Navigation, Alexandria, VA, 1980.

[3] Phillips, R. and Schmidt, G., "GPS/INS Integration," in NATO AGARD Lecture Series 207, *System Implications and Innovative Applications of Satellite Navigation*, June 1996, pp. 9-1 – 9-18.

[4] Schmidt, G., *INS/GPS Technology Trends*, Draper Laboratory Report P-4036, Cambridge, MA, October 2002. Also in NATO RTO Lecture Series 232, *Advances in Navigation Sensors and Integration Technology*, October 2003, pp. 1-1 – 1-16.

[5] Schmidt, G. and Phillips, R., *INS/GPS Integration Architecture Performance Comparisons,* Draper Laboratory Report P-4105, Cambridge, MA, February 2003. Also in NATO RTO Lecture Series 232, *Advances in Navigation Sensors and Integration Technology*, October 2003, pp. 6-1 – 6-18.

[6] Lipman, Jerome S., "Trade-Offs in the Implementation of Integrated GPS Inertial Systems," *Proceedings of the Institute of Navigation GPS-92 Technical Meeting*, The Institute of Navigation, Alexandria, VA, 1992.

[7] Moya, David C., Elchynski, Joseph J., "Evaluation of the World's Smallest Integrated Embedded INS/GPS, the H-764G," *Proceedings of the National Technical Meeting of the Institute of Navigation*, The Institute of Navigation, Alexandria, VA, 1993, pp. 275-286.

[8] *Systems Requirement Document for an Embedded Global Positioning System (GPS) Receiver in an Inertial Navigation System (INS) EGI*, ASC/SMEV Wright Patterson AFB, Ohio 45433-6503.

[9] Gustafson, D. et al., *A Deeply Integrated Adaptive GPS-Based Navigator with Extended Range Code Tracking,* Draper Laboratory Report P-3791, Cambridge, MA, January 2000.

[10] Gustafson, D. et al., *A High Antijam GPS-Based Navigator*, Draper Laboratory Report P-3776, Cambridge, MA, January 2000.

INS/GPS Integration Architecture Performance Comparisons

George T. Schmidt, Richard E. Phillips
The Charles Stark Draper Laboratory
555 Technology Sq. MS 57
Cambridge, Massachusetts 02139-3563
USA

ABSTRACT

Performance comparisons between the three major INS/GPS system architectures for various mission scenarios will be presented in order to understand the benefits of each. The loosely coupled and tightly coupled systems will be compared in several scenarios including aircraft flying against jammers and a helicopter flying a scout mission. The tightly coupled and deeply integrated architectures will be compared for several jamming scenarios including that of a precision guided munition.

1.0 INTRODUCTION

In Reference 1, INS/GPS integration architectures defined as loosely coupled, tightly coupled, and deeply integrated configurations were described. The advantages and disadvantages of each level of integration were listed. Examples of current and future systems were cited. In this paper, performance comparisons between the three major INS/GPS system architectures for various mission scenarios will be presented in order to understand the benefits of each. The loosely coupled and tightly coupled systems will be compared in several scenarios including aircraft flying against jammers and a helicopter flying a scout mission. The tightly coupled and deeply integrated architectures will be compared for several jamming scenarios including that of a precision guided munition.

2.0 LOOSELY COUPLED VS. TIGHTLY COUPLED PERFORMANCE COMPARISON

This section shows the jamming-related performance of loosely coupled and tightly coupled INS/GPS navigation systems in several hypothetical situations. In addition to comparing navigation architectures, the performance of inertial systems of varying quality was evaluated. The analysis considered only the performance of the combined INS/GPS solution and is thus appropriate to either of the loosely coupled architectures as they share the same INS/GPS solution. This particular example of an INS/GPS loosely coupled system has been the subject of numerous published studies [e.g., Ref. 2]. The tightly coupled system did not necessarily correspond to any particular existing system.

Several jamming scenarios were considered. The first scenario was designed to simply show the behavior of INS/GPS systems when GPS satellites are lost and reacquired one at a time. That is, there will be four satellites in track, then three, two, one, and finally zero. Then they were reacquired one at a time. For one of the scenarios, the navigation system was augmented with a Doppler ground speed measuring device.

2.1 Loosely Coupled System Definition

The loosely coupled GPS system consisted of a GPS receiver, an inertial navigation system, and an integration filter. The PVA solution from a typical receiver like the MAGR was used as the input to the INS/GPS integration Kalman filter. In order to avoid the problem of dealing with correlated measurements, the integration filter only used the position from the PVA solution, and this only once every 10 s and only if the Expected Horizontal Error (EHE), a receiver output and measure of horizontal navigation quality, was less than 100 m. The receiver did not compute a solution if there were fewer than four satellites in track. The state elements for the GPS receiver are shown in Table 2.1.

Table 2.1: State Elements for the Unaided GPS Receiver

State Element	Components
Position	3
Velocity	3
Acceleration	3
User clock bias	1
User clock drift	1
Altimeter bias	1
Total	12

Since the GPS receiver solution is the result of a (Kalman) filter, the velocity is correlated with the position, and both position and velocity are correlated in time. Process noise, which allows the filter to track changing acceleration, also decorrelates the output. The process noise is of such a magnitude that position solutions separated by 10-s intervals are not significantly correlated. The state elements of the integration filter that processes these measurements is shown in Table 2.2.

Table 2.2: State Elements for the Loosely Coupled Integration Filter

State Element	Components
Position	3
Velocity	3
Misalignment	3
Gyro drift	3
Gyro scale factor	3
Accel. bias	3
Accel. scale factor	3
Altimeter bias	1
Total	22

Most Kalman filters are suboptimal estimators. Some are less near optimal than others. The cascaded filter architecture of loosely coupled systems is certainly far from optimal. These systems are particularly sensitive to the procedure known as "tuning," in which the process noise is added and measurements are down-weighted or omitted. A considerable effort went into tuning the loosely coupled INS/GPS system such that it could be compared fairly with the tightly coupled systems.

2.2 Tightly Coupled System Definition

The tightly coupled system consists of a receiver, inertial instruments, and an integration filter. The integration filter accepts measurements of pseudo-range and pseudo-range rate from each satellite at a 1-Hz rate. The filter state is extrapolated forward in time using inertial measurements and a model for the earth's gravity field. The state elements for this most straightforward approach are shown in Table 2.3. These same states appear in the cascaded filters of the loosely coupled system.

Table 2.3: State Elements for the Tightly Coupled Integration Filter

State Element	Components
Position	3
Velocity	3
User clock bias	1
User clock drift	1
Misalignment	3
Gyro drift	3
Gyro scale factor	3
Accel. bias	3
Accel. scale factor	3
Altimeter bias	1
Total	24

2.3 Initial Errors, Modeling Errors, and Instrument Errors

These error sources influence the performance of the navigation system, some more than others. The initial errors in position, velocity, and misalignment in fact have very little effect on the performance of the system as long as it operates for a significant time. They are set to levels that are consistent with some kind of ground calibration and alignment mode, but are poor enough to show improvement as in-flight alignment progresses – with either system architecture. Other errors can have significant effect on navigation system performance. Those errors that are independent of INS quality are given in Table 2.4. The Markov processes in this table are characterized by two numbers, a standard deviation, and a distance constant.

Table 2.4: Error Values for INS Independent Models

Bias Errors	Modeled Value (1σ)	No. Components
Initial position	16 m (vertical) 600 m (horizontal)	1 2
Initial velocity	0.3 m/s	3
GPS user clock Initial offset Initial drift g-sensitive drift	 5000 ms 10^{-2} ppm 10^{-3} ppm/g	 3
GPS pseudo-range	3.0 m	4
GPS range rate	0.003 m/s	4
Gravity (Markov)	35 µg/37 km	3
Barometer (Markov)	150 m/460 km	1
Noise errors		
GPS pseudo-range	from receiver tracking	4
GPS range rate	loop simulation	4
Barometer	3 m	1

The performance of four different IMU qualities were analyzed. The four IMUs were characterized by their navigation error after 1 h of unaided (inertial-only) operation. The error characteristics of actual inertial instruments whose performance was close to 10, 1, 0.5 and 0.2 nmi/h were scaled proportionally to yield those exact values.

The error values for each of these hypothetical instruments are shown in Table 2.5.

Table 2.5: IMU Error Sources

	IMU Quality (All errors except random walk are 1σ biases)			
Error Source	**10 nmi/h**	**1.0 nmi/h**	**0.5 nmi/h**	**0.2 nmi/h**
Accel. bias	223 µg	37 µg	19 µg	4.2 µg
Accel. scale factor	223 ppm	179 ppm	90 ppm	21 ppm
Input axis misalign.	22 arcsec	3 arcsec	1.5 arcsec	0.4 arcsec
Random walk	56 µg/√Hz	15 µg/√Hz	7.5 µg/√Hz	4.2 µg/√Hz
Gyro bias	0.11 deg/h	0.0045 deg/h	0.0022 deg/h	0.00084 deg/h
Gyro scale factor	112 ppm	7.5 ppm	3.5 ppm	1.67 ppm
Input axis misalign.	22 arcsec	2.2 arcsec	1.1 arcsec	0.4 arcsec
Random walk	4.7 deg/h/√Hz	0.13 deg/h/√Hz	0.066 deg/h/√Hz	0.03 deg/h/√Hz

Initial misalignment error was derived from "gyrocompassing" each of the inertial units so it is instrument-dependent. Its values are not critical for the analysis because improvements in alignment due to in-flight maneuvers soon dominate the navigation results.

2.4 GPS Receiver Bandwidth, Loss of Lock and Reacquisition

For the loosely coupled receiver, the noise bandwidths of the code and carrier loop are fixed. The carrier was a third-order loop with bandwidth of 5.83 Hz. The code loop band is first order, but is aided by either the carrier loop if the carrier loop is in lock, or by the INS if the carrier loop is not in lock. During carrier loop aiding, the code loop bandwidth is 1.5 Hz. During inertial aiding, the bandwidth is 0.5 Hz.

The bandwidths for the tightly coupled receiver were set appropriate to the quality of inertial instruments. These bandwidths are determined by the requirement that the loops stay in lock for a 10-g/s jerk, which lasts for 0.6 s. (The carrier tracking bandwidth was actually set for this study by requiring that the phase error be less than 90 deg for a 6-g acceleration step. This is a slightly more stringent requirement, but is easier to analyze.) The next several paragraphs present the method used for setting the tracking loop bandwidths. We took maximum advantage of knowing the inertial instrument performance. Closely tuning the tracking loops to the inertial performance in this way may not always be practical for actual receivers.

The phase error in a third-order loop following an acceleration step is shown in the following equation. (Note that distance has been converted to phase error in degrees using the code length of 300 m.)

$$\Delta\Phi = \frac{R}{\omega_0^2}\left[e^{-\omega_0 t} + \frac{e^{-\omega_0 t 2}}{\sqrt{3}}\left(\sin\omega_0 t\frac{\sqrt{3}}{2} - \sqrt{3}\cos\omega_0 t\frac{\sqrt{3}}{2}\right)\right]$$

where: R is the step magnitude (deg/s^2)

ω_0 is the filter natural frequency (rad/s)

$\Delta\Phi$ is the phase error in degrees

The natural frequency should be selected to keep the peak phase error less than 90 deg. The graph in Figure 2.1 shows the response, $\Delta\Phi$, for a natural frequency of 17.67 rad/s, the maximum error is 90 deg.

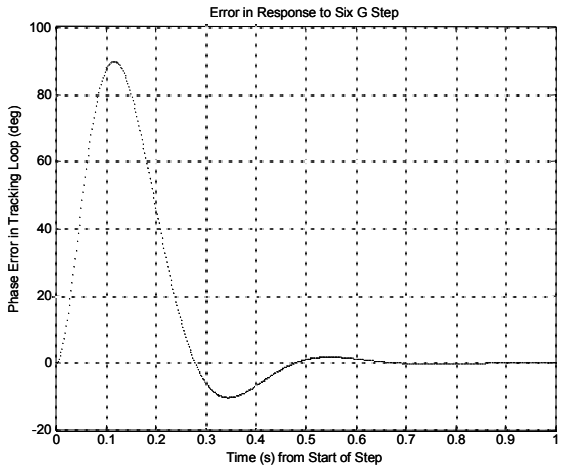


Figure 2.1: Error in Third-Order Loop Response to a 6-G Step in Acceleration.

With inertial aiding, the tracking loop will not be affected by the full magnitude of the step in acceleration. Only a residual part of the acceleration step due to imperfect inertial instruments will affect the tracking loop. The error, $\Delta\Phi$, is proportional to the step magnitude and inversely proportional to the square of the natural frequency. To maintain a 90-deg peak error, the natural frequency can be scaled by the square root of the ratio of aided to unaided step magnitude.

$$\omega_{0,aided} = \sqrt{\frac{R_{aided}}{R_{unaided}}}\,\omega_{0,unaided} \tag{2.1}$$

The residual error (post-calibration) accelerometer scale factor and IMU misalignment cause a residual acceleration step to be seen by the tracking loop. Lag in the inertial aiding would also add to the acceleration seen by the tracking loop. This lag was assumed to be negligible in this tightly coupled situation.

The residual acceleration seen by the tracking loop due to scale factor error is shown below.

$$\delta a_{sf} = \begin{bmatrix} sf_1 & 0 & 0 \\ 0 & sf_2 & 0 \\ 0 & 0 & sf_3 \end{bmatrix} a$$

IMU misalignment causes acceleration to be rotated incorrectly. The error in acceleration due to misalignment is shown below.

$$\delta a_{mis} = \begin{bmatrix} 0 & -\delta\theta_3 & \delta\theta_2 \\ \delta\theta_3 & 0 & -\delta\theta_1 \\ -\delta\theta_2 & \delta\theta_1 & 0 \end{bmatrix} a$$

The net error caused by scale factor and misalignment due to a unit acceleration step is thus:

$$\delta a = \delta a_{sf} + \delta a_{mis}$$

$$\delta a = \begin{bmatrix} 1 & 0 & 0 & 0 & -1 & 1 \\ 0 & 1 & 0 & 1 & 0 & -1 \\ 0 & 0 & 1 & -1 & 1 & 0 \end{bmatrix} \begin{bmatrix} sf_1 \\ sf_2 \\ sf_3 \\ \delta\theta_1 \\ \delta\theta_2 \\ \delta\theta_3 \end{bmatrix}$$

The covariance of residual acceleration error due to a unit acceleration step is shown below.

$$\left\langle \delta a \delta a^T \right\rangle = \begin{bmatrix} 1 & 0 & 0 & 0 & -1 & 1 \\ 0 & 1 & 0 & 1 & 0 & -1 \\ 0 & 0 & 1 & -1 & 1 & 0 \end{bmatrix} \begin{bmatrix} \sigma_{sf}^2 & c_{sf-mis} \\ c_{sf-mis} & \sigma_{mis}^2 \end{bmatrix} \begin{bmatrix} 1 & 0 & 0 \\ 0 & 1 & 0 \\ 0 & 0 & 1 \\ 0 & 1 & -1 \\ -1 & 0 & 1 \\ 1 & -1 & 0 \end{bmatrix}$$

The quantities $\sigma_{sf,}$ and σ_{mis} are the scale factor and misalignment standard deviations. The quantity $c_{sf\text{-}mis}$ is the covariance of these two quantities. This scale factor/misalignment matrix (the middle factor on the right) was taken from a covariance analysis after the aircraft had performed in-flight calibration maneuvers. If the scale factor is expressed as a fraction and the misalignment is in radians, the acceleration variance (on the left) will be the variance in acceleration seen by the tracking loop for a unit acceleration step. The radius of the sphere that enclosed 90% of these acceleration errors was taken to be the acceleration magnitude to which the tracking loops were tuned. Although a 90% level may not seem very robust, it should be remembered that tracking loop errors greater than 90 deg do not necessarily cause loss of lock.

For the four qualities of IMU studied, the radius of the acceleration sphere and the corresponding bandwidths are shown in Table 2.6. The error due to a unit acceleration step is given in parts per million.

Table 2.6: The Residual Acceleration Error and Corresponding Bandwidth for the Carrier Tracking Loop for Four IMU Qualities.

IMU	Residual Error (90%) Due to Scale Factor and Misalignment (ppm)	Acceleration Seen by Tracking Loop Due to 6-g Acceleration Step	Required Carrier Tracking Loop Bandwidth
No inertial aiding	Not applicable	6 g	18 rad/s
10 nmi/h	1880	0.011 g	0.77
1 nmi/h	431	0.0026 g	0.37
0.5 nmi/h	311	0.0019 g	0.32
0.2 nmi/h	225	0.0014 g	0.27

The quantity in the second column is the radius of the sphere that encloses 90% of the errors. The quantities in the third column are that error times the 6-g acceleration step, and the quantities in the third column are the required bandwidth as determined by Eq. 2.1. For example, the bandwidth for the 10-nmi/h system was computed as shown below.

$$\omega_{0,aided} = \sqrt{\frac{0.011\,g}{6\,g}}\,18\,rad/s = 0.77\,rad/s$$

For the purposes of the analysis, it was declared that the receiver had lost lock if the carrier phase error exceeded 90 deg or if the signal-to-noise ratio dropped below 19 dB. Loss of lock for the code phase was declared if the tracking error was greater then 1/2 chip (50 ns) or if the signal-to-noise ratio dropped below 18 dB. Conversely, reacquisition was dependent on achieving a signal-to-noise ratio of at least 21 dB for the code and 22 dB for the carrier for a required amount of time. The required time depends on the uncertainty in the range and range rate to each satellite and the rate at which each code phase and frequency combination could be searched.

At the given signal level, a 20-ms integration period should be adequate for accumulating signal energy. The size of the phase shift between 20-ms search intervals was 36 deg corresponding to 30 m. The size of the

frequency bandwidth was 50 Hz corresponding to 10 m/s. The approximate time required to search over this position-frequency space (±σ) is given below.

$$\Delta T = 0.020\left[\frac{2\sigma_{rng}}{30}\right]\times\left[\frac{2\sigma_{rng-rate}}{10}\right]$$

Some additional time must be added to allow for receiver moding. That is, the search process must be halted, and the receiver tracking loops cycled several times with an adequate signal-to-noise/jammer ratio.

2.5 Navigation Performance for Four Missions

Four missions were studied. The purpose of each of these mission scenarios was to observe the effects of jamming on loosely and tightly coupled INS/GPS systems and to observe the effect of IMU quality on tightly coupled systems. For the first scenario, the loss of lock and reacquisition for each of four satellites was spaced out so that the behavior of the navigation solution could be observed for extended periods of time between each loss. The other missions consisted of: 1) an aircraft flying past a jammer so that it loses lock then reacquires satellites as the jammer recedes into the distance, 2) an aircraft approaching a jammer head on, and 3) a helicopter operating in the vicinity of a jammer.

2.5.1 Sequential Outage

In this scenario, the loss of lock on satellite carrier and code phase was forced at 3-min intervals. Loss of code lock began after the fourth carrier tracking loop lost lock. Thus, the sequence began with loss of lock on a single carrier signal and ended with the loss of lock of the fourth code loop. Two variations in the study were considered at this point. In one of these, the signals were reacquired in inverse order after a total outage of 20 min. In the other variation, the mission was continued for 84 min using inertial measurements without the aid of GPS.

The behavior of the horizontal velocity error for the loosely and tightly coupled systems is shown in Figures 2.2 and 2.3.

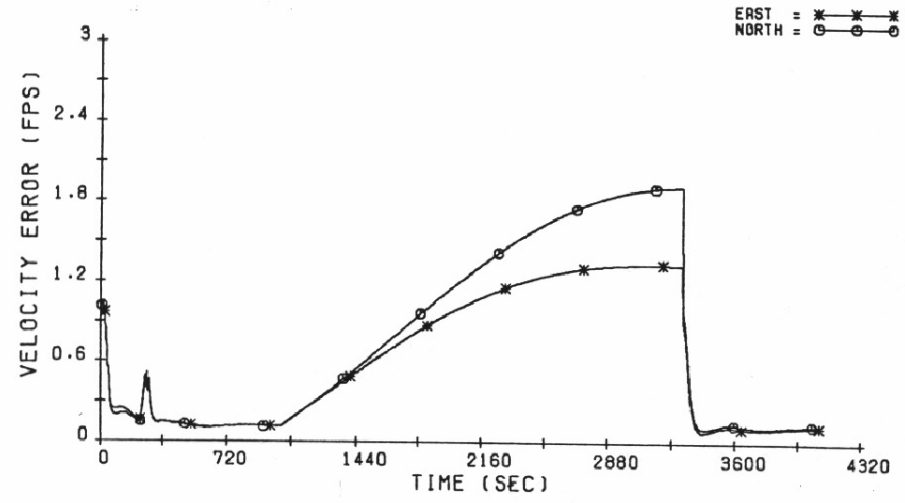


Figure 2.2: Horizontal Velocity Error for the Loosely Coupled Navigation Systems.

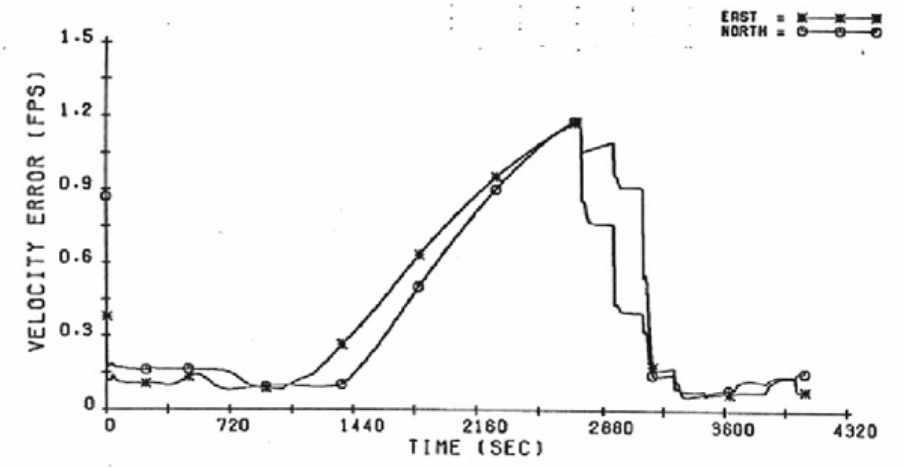


Figure 2.3: Horizontal Velocity Error for the Tightly Coupled Navigation Systems.

The first loss of carrier tracking occurs at 360 s. The first loss of code at 1020 s. One feature of this loosely coupled system is that it does not form a navigation solution if fewer than four satellites are in lock. Thus, the immediate rise in velocity error begins at this point in the bottom graph (loosely coupled system). In contrast, the increase in velocity error for the tightly coupled system is somewhat delayed. The sequence of code reacquisition begins at 2760 s. Since the tightly coupled system makes immediate use of the first code measurement, the step improvement in velocity is seen at that time. The correlations between position and velocity in the Kalman filter cause the decrease in velocity error, even though it is a range measurement that has been made. Each successive code loop reacquisition causes a step improvement in the velocity accuracy. In contrast, the loosely coupled system does not get the benefit of the recently reacquired code phase until four satellites are in lock. At this point (in the lower graph), the improvement in velocity accuracy is recognized easily.

With four satellites in lock, the loosely coupled system yields perfectly acceptable navigation performance. The response to jamming the tightly coupled system is somewhat better. The maximum horizontal position error for each system studied is shown in Figure 2.4.

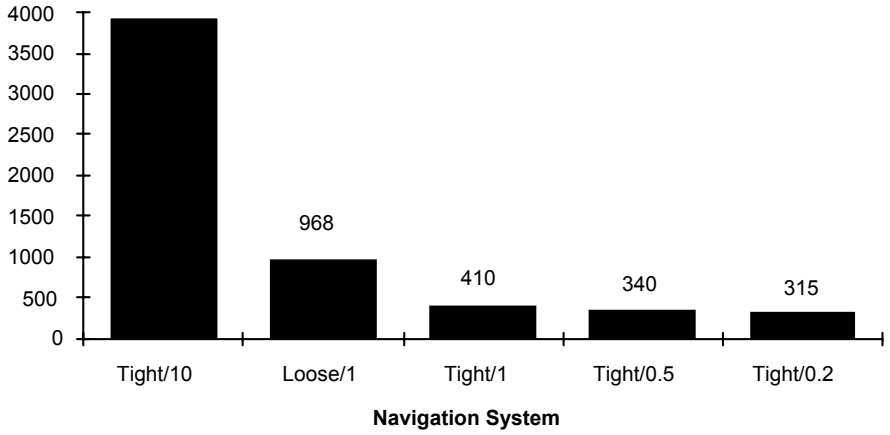


Figure 2.4: Horizontal Position Error at Time of Reacquisition.
(The units for the ordinates are meters)

If the navigation system is denied, GPS measurements for 84 min, the horizontal position errors grow to the levels shown in Figure 2.5.

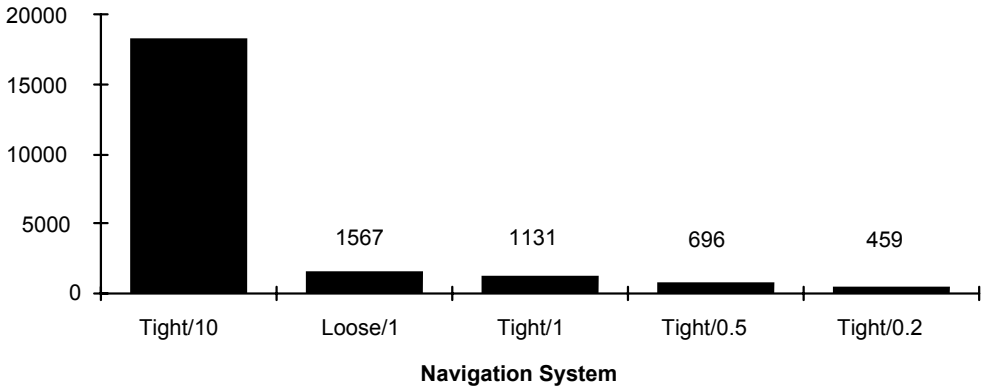


Figure 2.5: Horizontal Position Errors 1 Schuler Period after Loss of Last Satellite. (The units for the ordinates are meters)

In addition to the obvious correlation of navigation error to IMU quality, we can make the following general observations about these results. The tightly coupled 1.0-nmi/h system does perform better than the loosely coupled system. This is due to two factors: 1) the tightly coupled system makes use of measurements even when fewer than four satellites are in lock, and 2) the calibration of the inertial instruments is somewhat better with the tightly coupled system. This performance difference diminishes with time. A very long time after the last GPS measurement, the performance of the tightly coupled and loosely coupled systems would be identical – that of a 1-nmi/h system. The performance of the 1.0-nmi/h system is about 10 times better than that of the 1.0-nmi/h system at the end of the 20-min blackout interval. However, at the end of 84 min, the 1.0-nmi/h system has only drifted to a 0.6-nmi error. The 10-nmi/h system, however, has drifted to close to 10 nmi. This simply reflects the fact that the major source of error for the 10-nmi/h system is uncalibratable random errors.

2.5.2 Jammer Flyby

For this scenario, an aircraft flies by a jammer, thus losing and regaining lock in a somewhat more realistic fashion. A jammer was placed on the ground near the midpoint of the trajectory to cause an approximate 20-min outage. In contrast to the previous situation in which the period of the outage was specified, in this scenario, the actual loss of lock will be determined by the signal-to-noise ratio for each satellite. Reacquisition will be determined by the growing uncertainty in range and range rate to each satellite. The period of outage will also be a function of the bandwidth of the carrier tracking loops for each of the receivers. We will, again, observe position and velocity error growth as GPS measurements are lost.

Table 2.7 shows the number of range intervals to be searched for each satellite at the time the signal-to-noise threshold rose above 21 dB. In no case did the error growth in velocity cause the range rate uncertainty to any satellite to be greater than 10 m/s (one Doppler shift interval).

Table 2.7: Search for Range Phase as a Function of IMU Quality

Navigation System	Range (Code Phase) Intervals to be Searched — Satellite Identification						
	3	11	12	15	17	18	21
Tightly coupled 10 nmi/h	73	64	70	42	82	70	43
Loosely coupled 1.0 nmi/h	8	8	8	6	9	8	6
Tightly coupled 1.0 nmi/h	7	6	6	5	7	6	5
Tightly coupled 0.5 nmi/h	6	6	6	5	6	6	5
Tightly coupled 0.2 nmi/h	6	5	6	5	6	5	5

For a search time of 20 ms/chip (code phase interval), the better IMUs hold the search time to 0.2 s. The 10-nmi/h inertial system holds the search time to about 0.8 to 1.6 s. These numbers only reflect the error growth in position (and velocity) uncertainty and assume that the entire 1σ search area must be searched before lock on is achieved. Sometimes the signal will be found sooner, and of course, 32% of the time, it will be outside the 1σ bounds and require a longer search. Unfortunately, these results cannot be generalized. The placement of the jammer, its signal strength, the antenna orientation, and gain pattern are unique to the scenario and can only be considered typical.

The blackout period as a function of IMU architecture and IMU quality is shown in Figure 2.6.

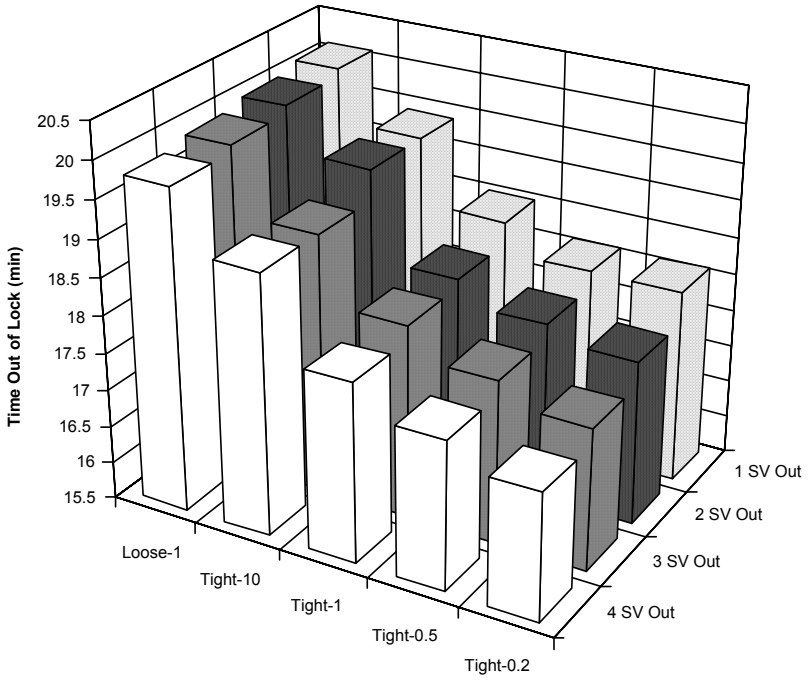


Figure 2.6. GPS Loss of Lock as a Function of IMU Architecture and Quality.

(Note the vertical scale does not begin at zero. The difference is not so striking, as the graph seems to indicate.) For this particular scenario, the performance difference is due to better calibration of the inertial instruments rather than jamming resistance. Even for the best IMU, the blackout time is reduced by only about 2 min from the 20-min blackout experienced by the loosely coupled receiver with full (unaided) bandwidth. Once again, it is difficult to generalize from these results.

For this jammer flyby scenario, the horizontal position errors (root-sum-squared (rss) 1σ) just prior to reacquisition are shown in Figure 2.7.

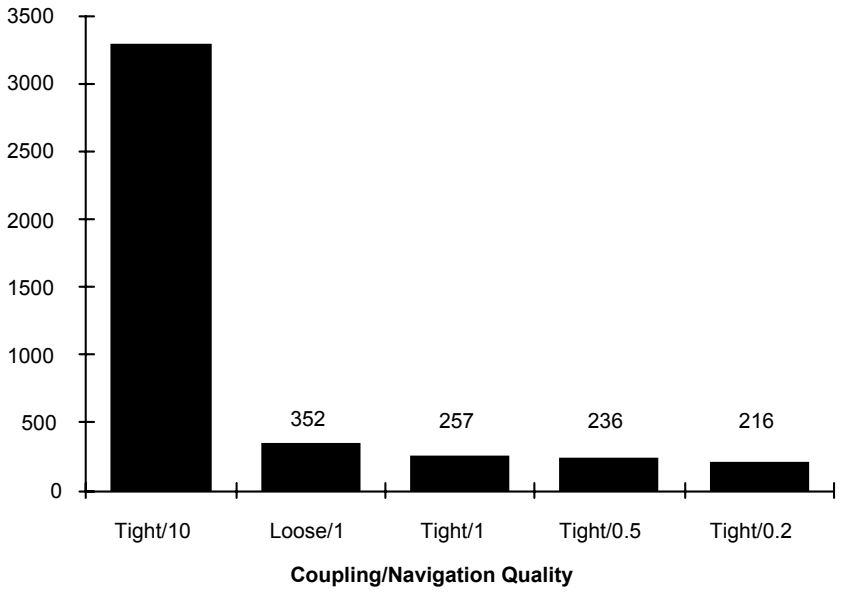


Figure 2.7: Horizontal Position Error just prior to Reacquisition.
(The units for the ordinates are meters)

The ratio of error level between the 10-nmi/h and the 1-nmi/h tightly coupled systems (3300:260) is greater than the 10 to 1 ratio implied by their characterization. Noise is a big error source in the 10-nmi/h system and cannot be calibrated by the GPS measurements as can biases and scale-factor errors. Thus, the better IMUs perform better yet when they are calibrated continuously by in-flight GPS measurements. The tightly coupled 1-nm/h system benefits somewhat more by the GPS in-flight calibration than the loosely coupled system.

2.5.3 Head-On Approach to Jammer

This scenario is meant to simulate the navigation performance of a fighter-bomber mission in which there is a jammer at the target. After take-off, the aircraft climbs to 40,000 ft, dodges a surface-to-air missile, then dives down to 200 ft to get below radar detection and to avoid GPS jamming. On approaching the target area, the aircraft then climbs to a few thousand feet to locate the target, then releases the bomb. The jammer at the target overwhelms all variations of IMU quality and architecture as soon as the aircraft climbs above its horizon. The time interval between loss of lock and bomb release is about 159 s for the loosely coupled system and 153 s for the tightly coupled systems. Figure 2.8 shows the position error at bomb release for the five navigation systems.

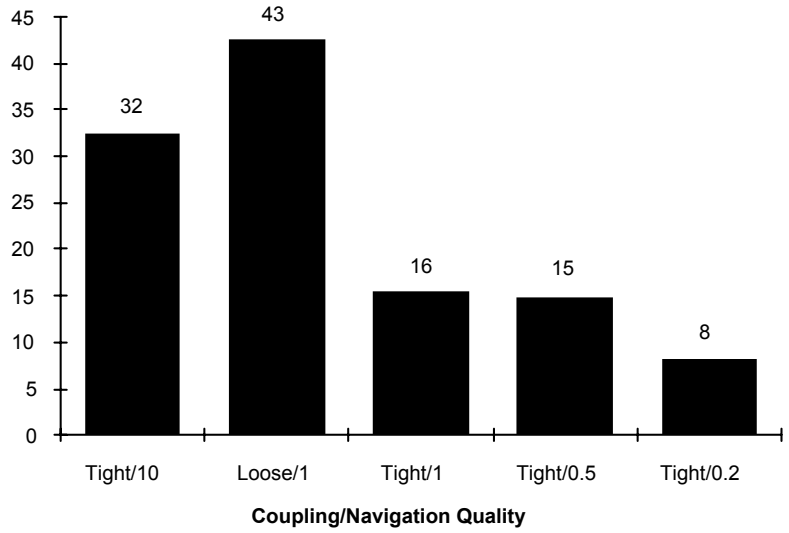


Figure 2.8: Position Error at Bomb Release after about 2.7 min of Free Inertial Navigation. (The units for the ordinates are meters)

In contrast to the previous scenarios, the IMU performance shortly after loss of lock is shown here. The tightly coupled 10 nmi/h system has better performance than this particular loosely coupled system when GPS measurements are available. After this short a time, 2.7 min, this advantage has not yet been lost. Another contributor to the difference is that the tightly coupled systems resisted the jamming for about 6 s longer than did the loosely coupled system.

2.5.4 Helicopter Performance in Jammer Vicinity

This scenario is meant to depict a helicopter on a scouting mission. The helicopter closely follows the terrain in order to avoid detection. The resulting flight profile has high levels of acceleration and jerk, which caused occasional momentary loss of carrier lock. No effect on mission performance can be seen.

The jamming scenario was simplified for this mission. GPS measurements were available until on-board estimates of IMU calibration and alignment had reached steady state. At that point, GPS was assumed to be jammed. The mission continued for another 19 min. In a variation from the previous scenarios, the navigation system of the helicopter was augmented with ground speed Doppler measurements. These Doppler measurements yield velocity in body coordinates. It will be seen that these measurements make a considerable difference in navigation performance after GPS is lost. The error model for the Doppler measurements is given in Table 2.8.

Table 2.8: Error Model for Doppler Ground Speed Measurements

Error Source	Vertical (1σ)	Horizontal (1σ) (two components)
Bias	0.05 nmi/h	0.1 nmi/h
Scale factor	0.1%	0.25%
Misalignment	2.0 mrad	2.0 mrad

At the end of the mission, the task of the helicopter is to define coordinates of a target at some distance (8 km) from its own position. The error in target coordinates, δr_{tgt}, is thus due to a combination of helicopter location error, $\delta r_{helicopter}$, and IMU misalignment, $\delta\alpha$.

$$\delta r_{tgt} = \delta r_{helicopter} + \delta\alpha \times r$$

where r is the vector from helicopter to target.

Figure 2.9 shows the error in helicopter position and target location as a function of two IMU qualities when no ground-speed Doppler measurements are included in the navigation solution.

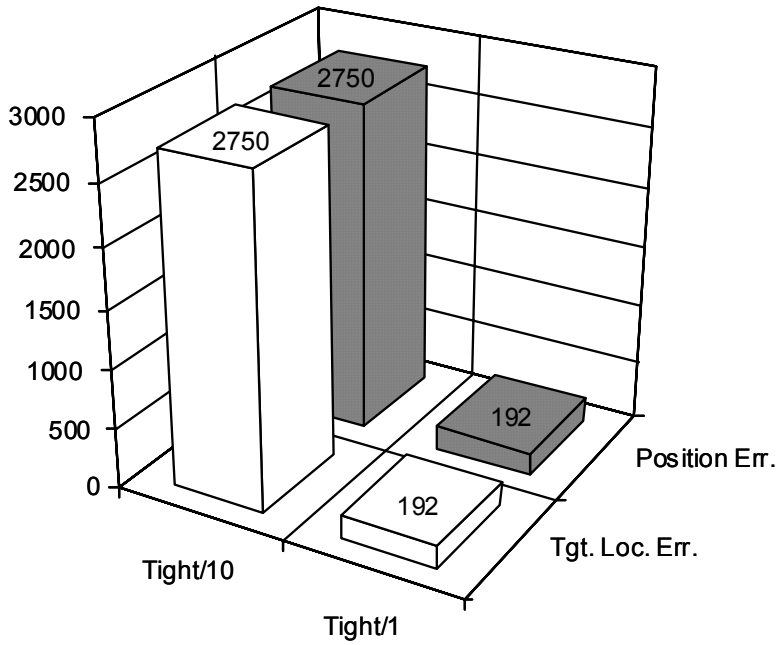


Figure 2.9: Position and Target Location Error for a Helicopter 19 min after GPS Loss of Lock without the Aid of Doppler Ground-Speed Measurements. (The units for the ordinates are meters)

As seen in an earlier scenario, the ratio of the errors between the 10 nmi/h and the 1 nmi/h navigation system, 2750:192 in this case, is greater than the characterization ratio, 10:1. The pointing error is negligible compared with the position error so that the target location errors and the aircraft position errors are essentially the same.

Figure 2.10 shows the same errors when the navigation solution is aided with ground-speed Doppler measurements. Results for both an INS/GPS system and for an INS/GPS system supplemented with Doppler ground-speed measurements are shown.

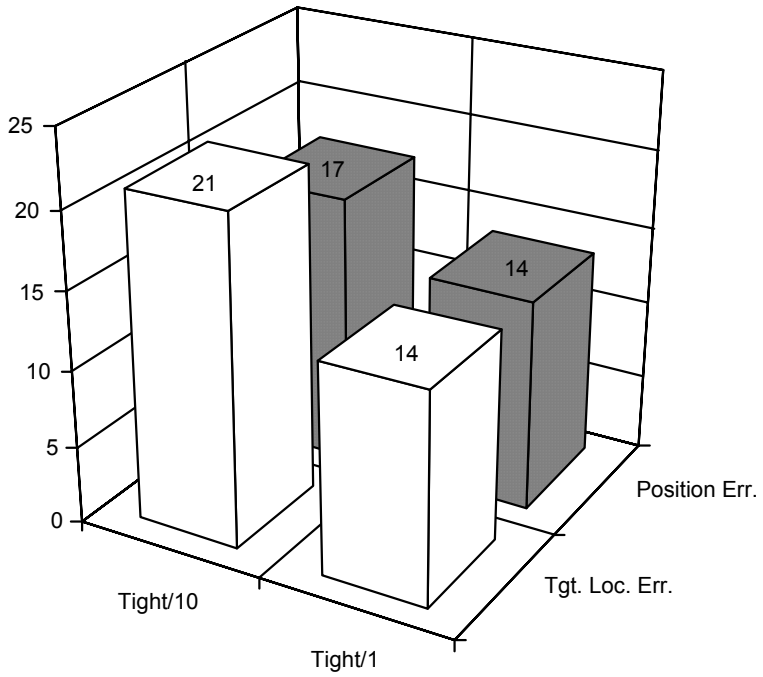


Figure 2.10: Position and Target Location Error for Scout Helicopter 19 min after GPS Loss of Lock with the Aid of Doppler Ground-Speed Measurements. (The units for the ordinates are meters)

As expected, the Doppler ground-speed measurements slow the error growth that is seen with the free inertial system. These errors in these velocity measurements integrate into growing position errors so they are not equivalent to GPS, which provides position as well as velocity. But they provide much better results than the inertial instruments whose measurements must be integrated twice before yielding position. The improvement with the Doppler ground-speed sensor is dramatic. Note that when aided by these measurements, the performance of the 10-nmi/h system is nearly the same (50% greater target location errors) as that of the 1-nmi/h system.

2.6 Summary of Comparison Results – Loosely Coupled vs. Tightly Coupled

This comparison has illustrated several features of INS/GPS systems that are true in many cases, but there is some danger in drawing general conclusions because the flight profiles and jamming scenarios are quite specific. A particular flight profile may allow more or less in-flight calibration, depending on aircraft maneuvers. These differences can be minimized by including maneuvers whose specific purpose is in-flight calibration and alignment. Jamming scenarios, however, are more difficult to characterize in a general way. Jammers can be on the ground, in which case, they are shadowed by the terrain for low-altitude approaches. They could also be airborne, in which case, their effective range will be greater, but for which their signal strength will grow with closing distance uncomplicated by shadowing considerations. Furthermore, there may be focused jammers and as a countermeasure to jamming, receiver antennas whose gain can be made a function of direction. All these variables make it difficult to generalize about how much longer a tightly coupled system will be able to maintain lock on the GPS signals. Perhaps the most general statement that can be made is to state the improvement in decibels in signal-to-noise (jammer) ratio that inertially aided receivers achieve.

The in-flight calibration and alignment of the tightly and loosely coupled receivers is simpler to assess. As in this study, loosely and tightly coupled architectures can be proposed. The resulting performance after loss of lock can then be assessed by either Monte Carlo techniques or, as in this study, by linearized covariance analysis.

After doing the analysis and observing simulation results, the following cautious assertions can be made:

1. When GPS is available, its measurements dominate navigation performance. The steady-state navigation error will be reduced by inertial aiding, which simply considered, allows GPS measurement noise to be "averaged out." Improvement of steady-state error with improving inertial quality is not as dramatic.
2. Tight coupling is superior to loose coupling for maintaining lock in a jamming environment, but the gain is hard to quantify, except by improvement in the signal-to-noise (jammer) ratio.
3. Better inertial instruments gain more from in-flight alignment and perform better after GPS is lost. This is because poorer instruments in general have larger proportions of uncalibratable noise.
4. For short time intervals after GPS loss, coupling architectures can make a difference in performance (because they affect calibration and alignment quality).
5. In the long run, basic IMU quality will dominate navigation accuracy due to instrument noise and loss of calibration accuracy.

Finally, it was shown that there is a dramatic difference in jammed performance if Doppler ground-speed measurements were available.

3.0 DEEPLY INTEGRATED VS. TIGHTLY COUPLED PERFORMANCE COMPARISON[1]

The inertial sensor error model used was representative of a particular Microelectromechanical System (MEMS) IMU capability. Rms accelerometer errors were characterized by 1-mg bias stability, 100-ppm scale-factor stability and 1-cm/s/$\sqrt{h}$ random walk. Rms gyro errors were 10-deg/h bias stability and 0.03-deg/$\sqrt{h}$ random walk. All stability errors were modeled as first-order Markov processes with a time constant of 5 min, which is representative of expected in-flight error characteristics. Accelerometer and gyro input axis nonorthogonalities of 1 mrad, rms were assumed and were treated as fixed biases.

A full 6-degree-of-freedom simulation was used with four satellites continuously in view. The navigation state vector consisted of 3 components of position, velocity, inertial sensor stability errors (bias, scale factor, and misalignment for both accelerometers and gyros), user clock, and clock rate. Clock errors were treated as biases. Satellite ephemeris errors were accounted for by including an unestimated range bias of two meters, rms.

The navigation algorithms are nonlinear. Thus, it was not possible to perform an accurate error covariance analysis based on linearization. As a consequence, the results in this section are based on Monte Carlo analysis.

The measurements from all correlators were processed simultaneously, while the measurements from each satellite were processed sequentially. An ideal correlation function was assumed in the navigation

[1] The material in this section is from References 3 and 4.

algorithms, with $R_c(\tau) = 1 - |\tau|$ for $|\tau| \leq 1$ and $R_c(\tau) = 0$ for $|\tau| > 1$. A correlator spacing of ½ chip was used throughout. Two types of jammers were assumed: 1) wideband Gaussian jammer with a 20 MHz bandwidth, and 2) narrowband jammer with a 1 kHz bandwidth. Jammer outputs were generated using a first-order Markov process driven by pseudorandom Gaussian noise.

In order to assess performance relative to conventional systems, a tightly coupled INS/GPS system was also simulated. The simulation model assumed a GPS receiver capable of calculating pseudo-range and delta-range. The receiver outputs and the simulated MEMS sensor outputs were fed to an INS/GPS integration filter. This filter was mechanized as a standard extended Kalman filter and used the same navigation state vector as the deeply integrated system. The receiver was velocity aided using the velocity components of the state vector estimate. The tightly coupled receiver filter bandwidth was 0.1 Hz while in State 3 tracking. Code loop loss-of-lock was assumed to occur at J/S = 54 dB. Above this threshold, GPS data were not used and free inertial navigation was assumed.

3.1 Constant Wide-Band Gaussian Jamming

Performance comparisons between the deeply integrated and tightly coupled systems were first conducted for two scenarios in which the navigator is subject to a constant wide-band Gaussian jamming. This allows the assessment of the additional loss-of-lock capability due to deep integration in a relatively straightforward manner. Dynamic maneuvers were simulated: body-frame specific force was pulsed between 0 and ±1 g along all axes; pulsewidth was 10 s with a period of 90 s.

Results for the first scenario are shown in Figure 3.1 using 27 Monte Carlo runs. J/S was maintained at 30 dB over the first 60 s of flight and then instantaneously switched to a higher value and held there for the remainder of the 5-min flight. Initial rms navigation errors were 30 m and 1 m/s along each axis. Initial rms clock errors were 20 m and 2 m/s. J/S levels used were 40 to 80 dB in increments of 5 dB, as shown outside the right edge of the figures. The deeply integrated system was able to maintain code lock up to 65 dB J/S, an improvement of approximately 15 dB over the tightly coupled system. Note also that the deeply integrated system achieves lower rss error during the 60-s initialization phase.

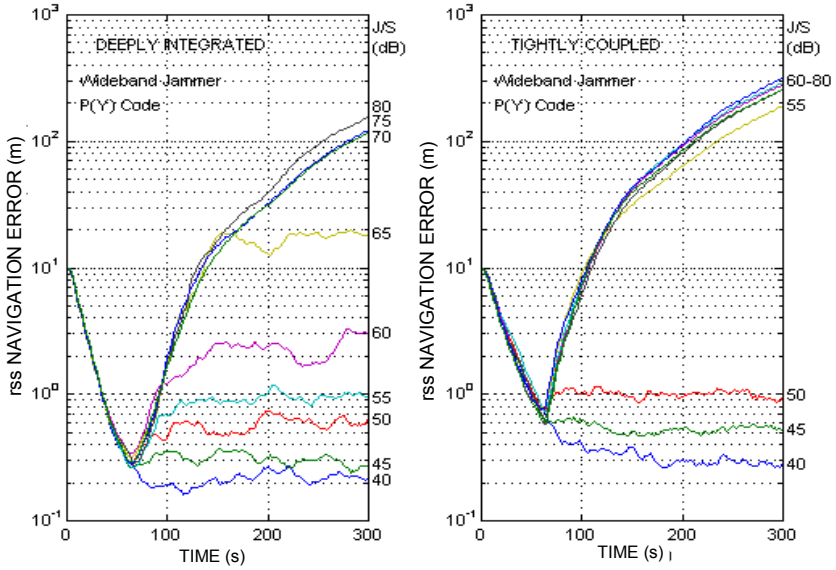


Figure 3.1. Navigation Performance Comparison: First Scenario.

The second scenario used a constant value of J/S over a 7-min flight. Initial rms position and velocity errors were 2 m and 1 m/s along all axes. The rms clock errors were 1 m and 0.1 m/s. J/S was varied between 50 and 80 dB in 5-dB increments. The results are shown in Figure 3.2, using 35 Monte Carlo runs and for both 10-deg/h and 1-deg/h INS error models. The results again indicate a significant improvement in loss-of-lock capability due to deep integration. This improvement is shown quantitatively in Figure 3.3, in which the results of Figure 3.2 are replotted vs. antijam (A/J) improvement. A/J improvement is in excess of 10 dB at all values of rss Error and exceeds 15 dB for rss Error greater than 35 m. Note that the A/J improvement also increases when higher quality inertial sensors are employed. This is primarily due to the enhanced in-flight error calibration capability of the deeply integrated system.

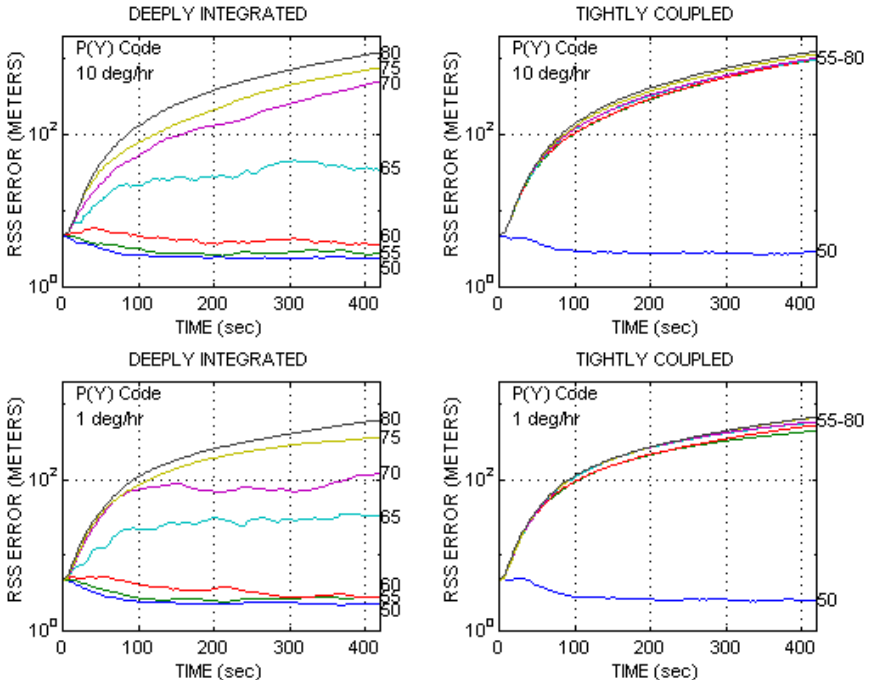


Figure 3.2: Navigation Performance Comparison: Second Scenario.

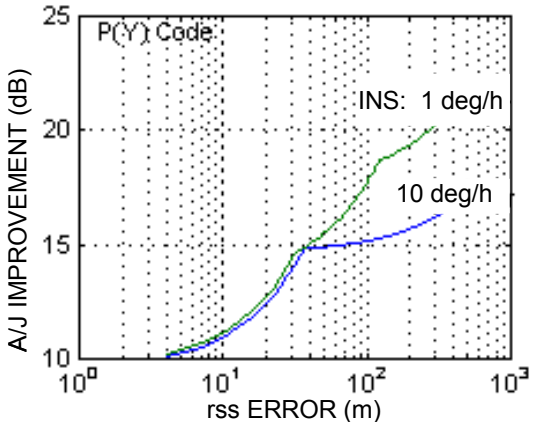


Figure 3.3: A/J Improvement due to Deep Integration.

3.2 Precision Guided Munition Scenario

The performance of the deeply integrated navigation system was evaluated for a precision guided munition (PGM) scenario in which the target was at a range of 63 nmi. The altitude profile is plotted in Figure 3.4. A single wideband Gaussian jammer was placed 10 km in front of the target in an attempt to simulate a worst-case scenario for a single jammer. This placement gives maximum J/S prior to final target approach with a resultant loss of navigation system performance just prior to target impact. The J/S history for a 100 W jammer is shown in Figure 3.5.

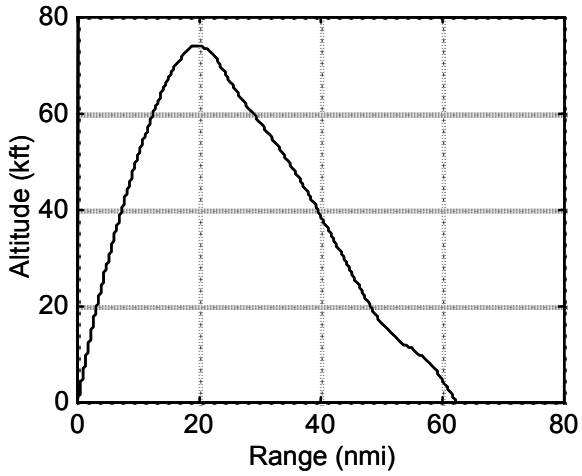


Figure 3.4: PGM Altitude Profile.

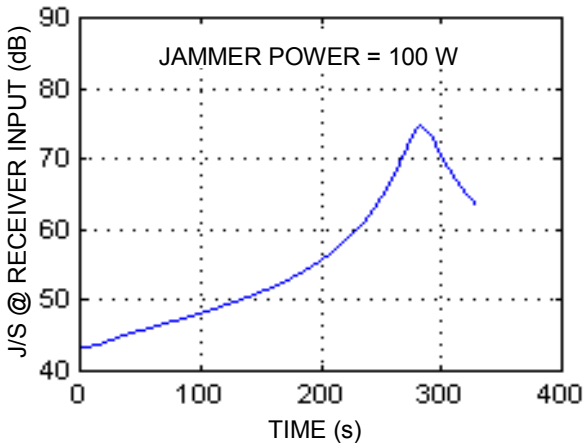


Figure 3.5: PGM Scenario: J/S vs. Time.

Performance was evaluated by varying the jammer power from 1 W to 10 kW. A total of 25 Monte Carlo runs was made at each power level. Initial rms navigation errors were 10 m and 0.2 m/s per axis; initial rms clock errors were 10 m and 0.2 m/s. The CEP at target impact is plotted vs. jammer power for wideband jamming in Figure 3.6 and for narrowband jamming in Figure 3.7. Comparing the results in the figures, it can be seen that the deeply integrated system offers significant improvement over the traditional tightly coupled system for both wideband and narrowband jamming. As an example, a 100-W wideband jammer results in a CEP of 11 m for the deeply integrated system, compared with a CEP of 120 m for the tightly coupled system. If the jammer power is reduced to 10 W, the CEP values are 2.6 m for the deeply integrated system and 71 m for the tightly coupled system.

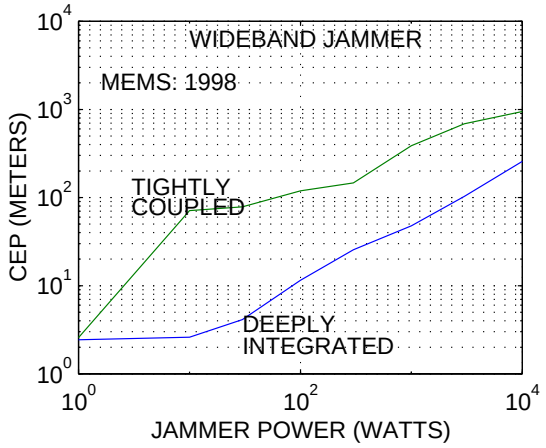


Figure 3.6: CEP vs. Jammer Power: Wideband Jammer.

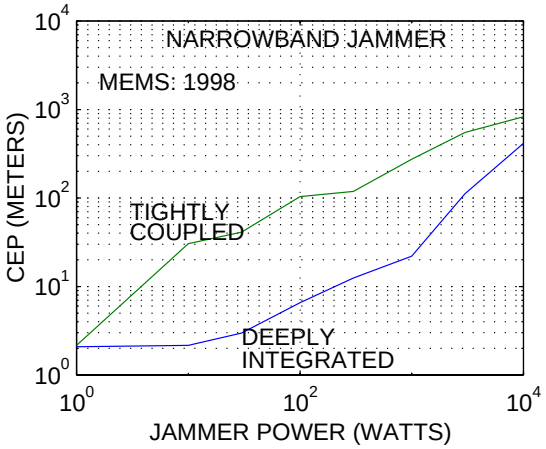


Figure 3.7: CEP vs. Jammer Power: Narrowband Jammer.

A/J improvement capability may be quantified by comparing jammer power at a constant value of CEP. The resulting improvement in A/J capability due to deep integration can be seen in Figure 3.8. For wideband jamming, improvements of at least 15 dB are seen for CEP values ranging from 6 to 120 m. For narrowband jamming, improvements of at least 15 dB are seen for CEP values ranging from 4 to 80 m. Improvement is seen to decrease as the CEP decreases below 10 m. In this case, the decrease in CEP results from a decrease in jammer power, and the tightly coupled system tends to maintain lock with higher probability as the jammer power decreases. In the limit as the jammer power approaches zero, the tightly coupled system approaches efficient operation, and both systems give comparable performance. The improvement is also seen to decrease as the CEP increases beyond 100 m. In this case, the increase in CEP results from an increase in jammer power and the tracking quality of the deeply integrated system begins to degrade. In the limit as the jammer power increases without bound, the deeply integrated system can no longer maintain lock, and both systems are operating in a free inertial mode where the CEP is determined solely by initial navigation errors and inertial sensor errors.

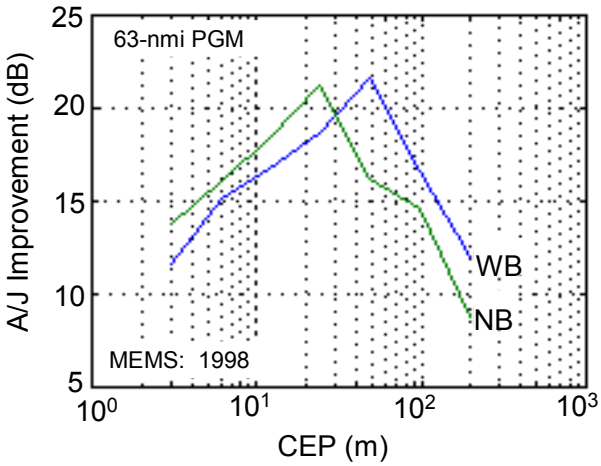


Figure 3.8: A/J Improvement due to Deep Integration.

3.3 Final Comment on Deep Integration Comparison

As shown in Reference 5, every 20 dB increase in A/J improvement in the INS/GPS system requires that the jammer increase its power by a factor of 100 to maintain the same effectiveness as a jammer. Yet the increase in jammer power makes its detection and attack much more probable. Thus, the potential benefits of deep integration are quite substantial in both comparisons reported here.

4.0 CONCLUDING REMARKS

This paper has presented several options for the integration of INS and GPS systems in order to benefit from the advantages of each system. As been shown, if the integration level between the two systems increases, the benefits also generally increase. The comparison of deeply integrated vs. closely coupled indicates that the deeply integrated approach will likely be dominant in the future.

5.0 REFERENCES

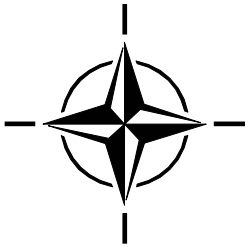
[1] Schmidt, G. and Phillips, R., *INS/GPS Integration Architectures*, Draper Laboratory Report P-4104, Cambridge, MA, February 2003. Also in NATO RTO Lecture Series 232, *Advances in Navigation Sensors and Integration Technology*, October 2003, pp. 5-1 – 5-15.

[2] Johnson, Gregory B., Lewantowicz, Zdzislaw H., "Closed Loop Operation of GPS Aided INS," *Third International Technical Meeting of the Satellite Division of the Institute of Navigation Proceedings*, The Institute of Navigation, Washington, D.C., 1990, pp. 461-470.

[3] Gustafson, D. et al., *A Deeply Integrated Adaptive GPS-Based Navigator with Extended Range Code Tracking,* Draper Laboratory Report P-3791, Cambridge, MA, January 2000.

[4] Gustafson, D. et al., *A High Antijam GPS-Based Navigator*, Draper Laboratory Report P-3776, Cambridge, MA, January 2000.

[5] Schmidt, G., *INS/GPS Technology Trends*, Draper Laboratory Report P-4036, Cambridge, MA, October 2002. Also in NATO RTO Lecture Series 232, *Advances in Navigation Sensors and Integration Technology*, October 2003, pp. 1-1 – 1-16.



Inertial MEMS System Applications

N. Barbour, R. Anderson, J. Connelly, D. Hanson,
A. Kourepenis, J. Sitomer, P. Ward
The Charles Stark Draper Laboratory
555 Technology Square
Cambridge, MA 02139-3563
UNITED STATES

email: nbarbour@draper.com

ABSTRACT

The performance of MEMS inertial technology has evolved from automotive quality to that approaching tactical-grade quality (1 deg/h, 1 mg). This evolution is a direct result of advances made in the key technology areas driven by gun-launched projectile requirements. The application of silicon MEMS inertial technology to competent munitions efforts began in the early 1990s. Initially, gun hardness was demonstrated at the sensor level, although the bias-and-scale factor of these gyros and accelerometers was mostly suitable for automotive or commercial use. Subsequently, development programs were initiated to develop gun-hard inertial systems with greatly improved sensor performance, and with a goal of low production cost.

This paper discusses the evolution of low-cost MEMS inertial system technology development for guided projectile INS/GPS systems and high performance IMUs. The evolution in sensors and packaging to realize performance improvement and system size reduction are presented. Recent data from the culmination of a three-year effort to develop an 8 cu in IMU are summarized, and represent the highest performance to date for an all-silicon IMU. Further investments in gun-hard Silicon MEMS systems will ultimately realize IMUs that are smaller (less than 2 in³ (33 cc), higher performing (1 deg/h and less than 1 mg), and lower in cost (less than $1200 per IMU and $1500 per INS/GPS) than is achievable in any competing technology.

1.0 INTRODUCTION

The performance levels of MEMS inertial technology is approaching tactical-grade quality (1 deg/h, 1 mg). This evolution is a direct result of advances made in the key technology areas driven by gun-launched projectile requirements. These applications have a unique combination of requirements including, performance over temperature, high-g launch survivability, fast initialization and startup, small size, and relatively low overall system cost. The application of silicon MEMS inertial technology to competent munitions efforts began in the early 1990s. Initially, gun hardness was demonstrated at the sensor level, although the bias-and-scale factor of these gyros and accelerometers was mostly suitable for automotive or commercial use. Subsequently, development programs were initiated to develop gun-hard inertial systems with greatly improved sensor performance, and with a goal of low production cost. This paper discusses the evolution of low-cost MEMS inertial systems through the Extended Range Guided Munition (ERGM) Demonstration, the Competent Munition Advanced Technology Demonstration (CMATD), and the DARPA Micromechanical Inertial Measurement Unit (MMIMU) programs. ERGM Demonstration and CMATD involved guided projectile tests of MEMS INS/GPS systems, whereas MMIMU concentrated on the development of a high-performance MEMS IMU. Other key technology developments in MEMS sensors and

packaging are also described. The culmination of much of the technology evolution will be in the recently started Common Guidance IMU (CGIMU) program, which has the goal of being incorporated across multiple projectile platforms. Figure 1 provides a top-level description of the technology roadmap for the ERGM, CMATD, MMIMU, and CGIMU systems.

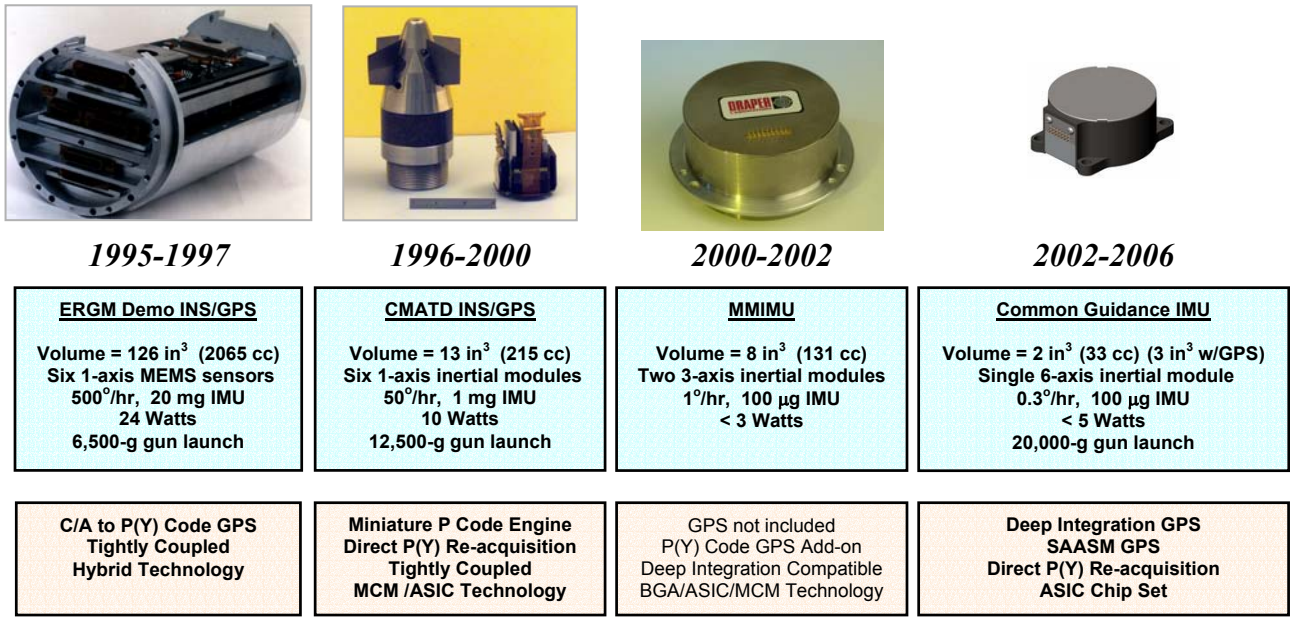


Figure 1: System Technology Roadmap.

2.0 ERGM DEMONSTRATION, CMATD, MMIMU

2.1 ERGM Demonstration INS/GPS

In March 1995, the Naval Surface Fire Support branch initiated a proof-of-concept demonstration for the Extended-Range Guided Munition (ERGM). The ERGM Demonstration program was the first successful demonstration of a gun-launched MEMS-based INS/GPS system. The system consisted of a 126 in^3 (2065 cc) avionics package containing a 6-degree-of-freedom MEMS inertial system, a Rockwell-Collins C/A-to-P(Y) code reacquisition GPS receiver with L1 tracking only, a TMS320C30 flight processor and power conversion and regulation electronics, which were sectionally mounted into a Deadeye Projectile.

The relatively generous volume of 126 in^3 (2065 cc) allowed conservative, rugged packaging technologies to be used to meet the required survivability goals. Five PWBs were hard-mounted to rigid aluminum frames and bolted into a cylindrical housing with end plates that served as the primary load bearing structure. The sensors and their discrete electronics were packaged using thin-film hybrid MCM-C technology and mounted in bulky hermetic metal housings structurally bonded to standard PCBs. The ERGM Demonstration sensor electronics packaging appears in Figure 2.

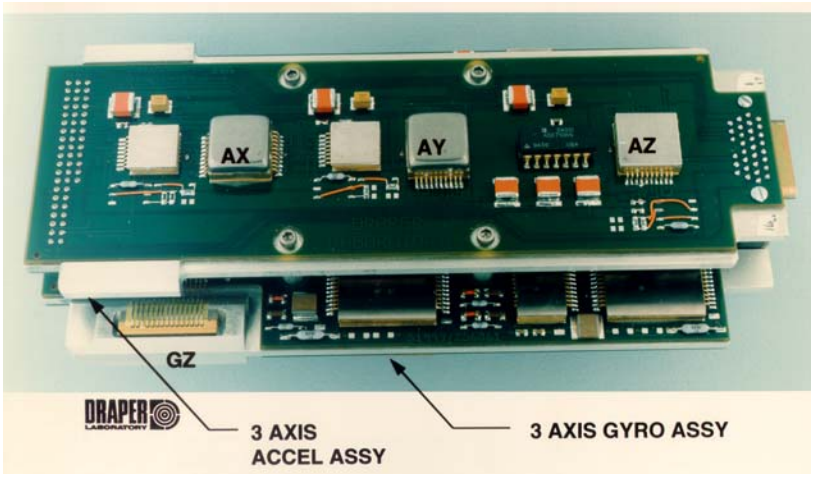


Figure 2: ERGM Demonstration Sensor Electronics Packaging.

A photo of the first of three (November 1996 and two in April 1997) successful ERGM Demonstration test flights is shown in Figure 3. This effort first demonstrated successful reacquisition of GPS after gun launch and proved the survivability and ability of MEMS inertial components to operate after launch and accurately measure body rates and accelerations. The MEMS-based system was composed of repackaged automotive-grade inertial components (Draper Laboratory TFG gyros and pendulous accelerometers with uncompensated performance of 1,000 deg/hr and 50 mg) and was able to perform down-determination successfully and provide inputs for a full navigation solution.



Figure 3: ERGM Demonstration Flight Test.

2.2 CMATD INS/GPS

From March 1996 through February 2000, under funding from the Office of Naval Research, a series of three flight tests for the Competent Munitions Advanced Technology Demonstration (CMATD) Program was completed. The objective was to demonstrate MEMS-based guidance, navigation, and control (GN&C) within the fuze section of unguided artillery rounds. Figure 4 is a photo of the CMATD 5-inch (127 mm) projectile in-flight, 20 ms after the 6,500-g gun launch. The system GN&C is 13 in^3 (215 cc) total, with 8 in^3 (131 cc) for the G&N electronics. Although the MEMS gyros and accelerometers were similar to ERGM Demonstration, the CMATD sensor electronics were the first to be ASIC-based. This contributed to an order of magnitude improvement over ERGM Demonstration performance.

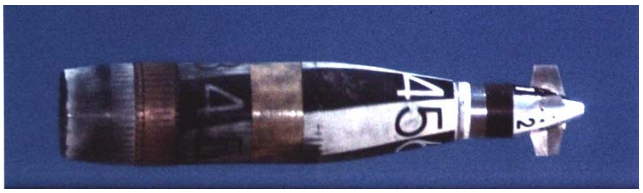


Figure 4: CMATD Projectile In Flight.

The volume constraint of 8 in^3 (131 cc) for the electronics assembly was very aggressive, and is shown in Figure 5. This system consists of a flight computer module, three orthogonal accelerometer modules, three orthogonal gyroscope modules, a two-card GPS receiver, a TCXO clock board, and a voltage regulator card. Each of these assemblies is molded in epoxy and secured in a cavity of the projectile housing by wax and glass bead potting material. A backplane and flex cables provide electrical interconnection between modules and external interfaces for system initialization. All modules are constructed using MCM-L technology, where unencapsulated silicon chips are attached to multilayer laminated circuit boards. Chip resistors, capacitors, and bare integrated circuit die are attached to the circuit board using conductive epoxy. A combination of aluminum wire bonds and conductive epoxy are used for electrical connections. This module assembly process does not preclude the use of prepackaged integrated circuits, but bare dies are used to attain the highest density circuit construction. The modules are over-molded with epoxy to provide mechanical and environmental protection and assist with thermal management. Modules fabricated in this manner have survived centrifuge tests in excess of 30,000 g and more than 400 thermal shocks from -55°C to +125°C. The modules are integrated into the G&N electronics by soldering pins into a backplane.

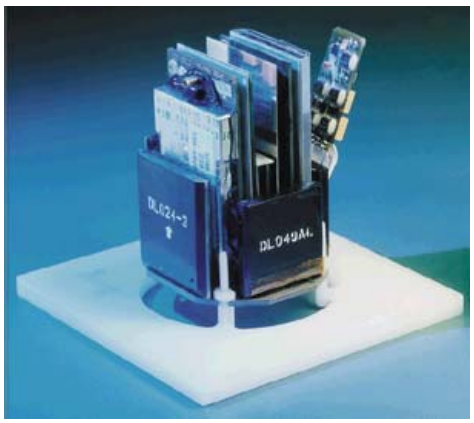


Figure 5: CMATD Electronics Assembly.

The CMATD Program culminated in flight tests of three projectiles at Yuma Proving Ground on August 3, 1999, August 5, 1999, and February 2, 2000. All projectiles were launched at a setback acceleration of approximately 6500 g with initial velocities of approximately 2200 ft/s (670 m/s).

The initial flight tests demonstrated survivability of the overall projectile design and subsystem functionality and performance. From the telemetry data acquired from the first two flights, all six MEMS instruments survived the gun launch and operated as expected and provided accurate in-flight measurements. The lessons learned in these test flights regarding the control actuation system (CAS), roll control software, and launch signal subsystems were modified for the third projectile. Test Flight 3 was conducted February 2, 2000, and the GN&C system survived gun launch and all systems operated. GPS was reacquired successfully at 31 seconds after launch and the closed-loop guidance, navigation, and control executed as designed.

2.3 MMIMU

The Special Projects Office of the Defense Advanced Research Projects Agency (DARPA) and the Air Force Research Laboratory (AFRL) sponsored Draper Laboratory in 2000 to develop and demonstrate the world's highest performance MEMS IMU (DARPA MMIMU). The performance requirement is a 10 deg/h, 500 µg IMU with a performance goal of 1 deg/h, 100-µg, and with a unit production cost goal of $1200. Designed as a low-cost, smaller, low power alternative to Honeywell's ring laser gyro-based tactical-grade HG1700 IMU, the MMIMU is 2.7 inches (68.5 mm) in diameter and 1.4 inches (35.5 mm) high (8 in^3) with a weight of 260 grams. The IMU is designed to perform over a temperature range of -40 to +85°C and consume less than 3 W.

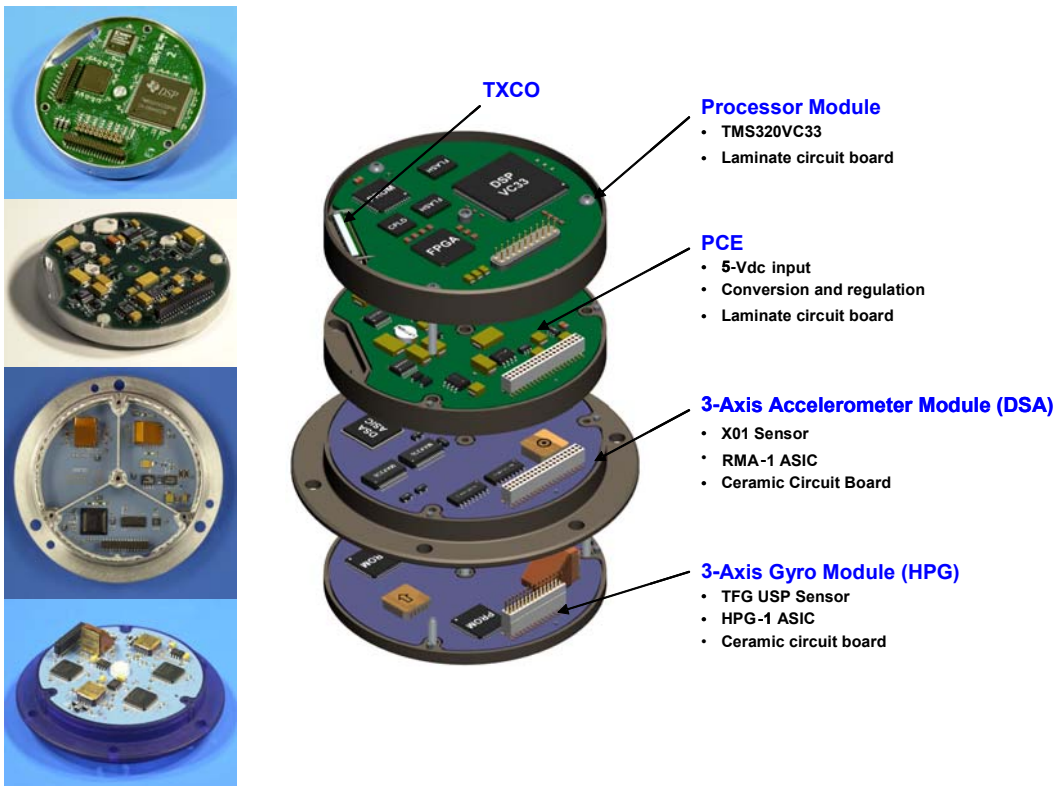


Figure 6: MMIMU Assembly.

Development experience and the need to design for ease of manufacture and low cost drove the MMIMU designs to much simpler implementations. The MMIMU assembly shown in Figure 6 features a set of four plug-in modules with screw attachments. From top to bottom are the IMU processor, power conversion electronics (PCE), accelerometer, and gyro modules. Each module consists of a PCB mounted to a Kovar frame, and alignment pins are used to guide module-to-module assembly and connector mating. Top and bottom seam-welded covers provide a hermetically-sealed system.

To meet the volume constraints, a novel planar stacked disk approach was developed for system packaging. Inertial sensors are hermetically sealed in an leadless ceramic chip carrier (LCCC). A separate 3-axis accelerometer and 3-axis gyroscope instrument module are configured with ASIC electronics, further improved to reduce the number of off-chip components. The two 3-axis inertial instrument modules contain the latest MEMS TFG and pendulous accelerometer sensor designs. Sensors are hermetically sealed in 20-pin LCCC packages and are mounted in an orthogonal configuration on each low-temperature co-fired ceramic (LTCC) circuit board. Ceramic mounting blocks are employed for the orthogonal set, and a separate mixed-signal CMOS ASIC in a chip-scale package operates each sensor.

ASIC electronics implemented in CMOS processes provide excellent performance at low power and cost, while enabling the small size objectives to be met. Much of the gains in performance experienced in TFG development are directly attributable to the ASIC electronics. The MMIMU gyro ASIC, the High-Performance Gyro digital ASIC (HPG-1), was developed under the DARPA MMIMU Program. This third-generation ASIC uses a high-speed Σ–Δ converter to acquire the gyro rate information directly out of the preamplifier. All sense axis processing is performed digitally, eliminating errors associated with drift in the baseband electronics while achieving dynamic ranges in excess of 140 dB. The accelerometer electronics form a differential capacitive measurement system consisting of a carrier signal generator and demodulator circuitry providing a DC output proportional to acceleration. During closed-loop operation, control compensation and rebalance drive circuitry are added. An existing second-generation analog ASIC (RMA-1) was used for the accelerometer. The ASICs were packaged in custom ball grid array packages.

Table 1: MMIMU Sensor Performance

Parameter		Gyros		Accelerometers	
		Goal	Actual	Goal	Actual
Bias Turn-on Repeatability	*deg/h or mg*	1 (1σ)	3 (1σ) (1)	0.5	2 (1σ) (1)
Bias In-run Stability	*deg/h or mg*	1 (1σ)	5 (1σ) (2)	0.1 (1σ)	1 (1σ) (2)
Bias Drift	*deg/h or mg*		5 (1σ) (3)		2 (1σ) (3)
Scale Factor Turn-on Repeatability	*ppm*	140 (1σ)	70 (1σ) (1)	210	125 (1σ) (1)
Scale Factor In-run Stability	*ppm*	140 (1σ)	100 (1σ) (2)	210	600 (1σ) (2)
Axis Misalignment	*mrad*	0.5	1	0.5	1
Input Axis Repeatability	*mrad*	0.1	0.2	0.1	0.2
Maximum Input	*deg/s or g*	1,000	1,000 (4)	50	45 (4)
Bandwidth	*Hz*	150	150 (4)	100	100 (4)
Random Walk	*deg/√h or m/s/√h*	0.030	0.050	0.035	0.02

Notes: (1) Turn-on to turn-on over 0°C to +70°C, power-down, and mount/dismount, 14 days
(2) Post-compensation over 0°C to +70°C
(3) RSS of turn-on and in-run performance
(4) Typical; other ranges available

Electronic components are surface mounted with solder and conformal coated with no module or system-level potting. Analysis has shown that combinations of die attach adhesive and a rigid structural frame are adequate to support the PCB module stack under loads applied during launch. Vibration isolation is an integral part of the mounting plate and can be customized for specific environments by the end user.

Build of two MMIMUs was started, with one completed and tested by August 2002. Table 1 presents a summary of the MMIMU goals and the actual IMU test data.

These results represent the highest published performance data attained to date on an all-Silicon MEMS IMU. The DARPA MMIMU Program was the culmination of three years of focused development on advancing the performance of MEMS gyroscopes. This effort leveraged 10 years of development and over $100M of Draper IR&D and government investments in the development of MEMS inertial technology.

3.0 OTHER KEY TECHNOLOGY DEVELOPMENTS

Performance for gun-hard munitions must be maintained through all environments, including high-g launch shock in excess of 20,000 g, a wide temperature range of -54°C to +125°C, and also over a 20-year duration, a time period typically identified for fielded systems. System deployment must be achieved with requisite reliability and without maintenance. Achieving the requisite inertial performance across the combination of environments are the principal challenges facing MEMS technology. This section describes some of the key technology developments for low-cost, gun-hard systems. Much of this work was performed under Draper Laboratory internal funding, and DARPA/US Army funded Manufacturing Low-Cost MEMS Inertial Sensors and High-g IMU-on-a-Chip contracts.

3.1 Sensors

The TFG is a proven design for high-g applications and has undergone many design iterations and incorporated many performance-enhancing features to ease fabrication and increase performance. Performance data indicate that the TFG currently performs at levels in the 10 to 50 deg/h range (3σ) over temperature ranges of -40°C to 85°C for many months time and shock inputs of up to 12,000 g. The companion accelerometer sensor is a pendulous mass displacement device manufactured using a similar dissolved wafer SOI process. An unbalanced proof mass plate is suspended by torsional spring flexures in a see-saw type configuration. Proof mass and flexure design variations yield devices with full-scale ranges from 1 to 100,000 g.

Trades and analyses conducted under the DARPA MMIMU program indicate that the optimal gyro performance is achieved at a thickness of between 50 and 100 μm. Continued evolution of advanced processes to build thicker, more 3-dimensional parts that are less susceptible to fabrication tolerances is critical to the performance and cost targets.

Major advances in sensor design and fabrication included development of in-plane accelerometers (IPAX), out-of-plane gyroscopes (OPG), and in-plane gyroscopes with an upper sense plate (USP) pick-off. The USP design is required to provide a higher signal-to-noise ratio and improve performance during vibration inputs. IPAX and OPG sensors allow planar mounting of sensors to further minimize overall system packaging volume. Working devices of two TFGs and one OPG on one chip, and two IPAXs and one out-of-plane pendulum accelerometer on another single chip have been demonstrated under DARPA/US Army AMCOM funding. These are necessary for IMUs smaller than 2 cu. in. (33 cc), and further development is required to perfect these chips.

3.2 IMU System Architecture

The evolution of ASIC electronics is critical to furthering the performance and miniaturization of MEMS systems. Varying mission needs are readily accommodated by versatile electronic configurations adapted for specific requirements. Figure 7 depicts the IMU system architecture evolution from ERGM Demonstration through MMIMU. Each stage represents an order of magnitude improvement in performance. Continued development of digital ASIC electronics with hard-wire signal processing is required to realize the cost, performance, and size objectives for an all-digital IMU architecture.

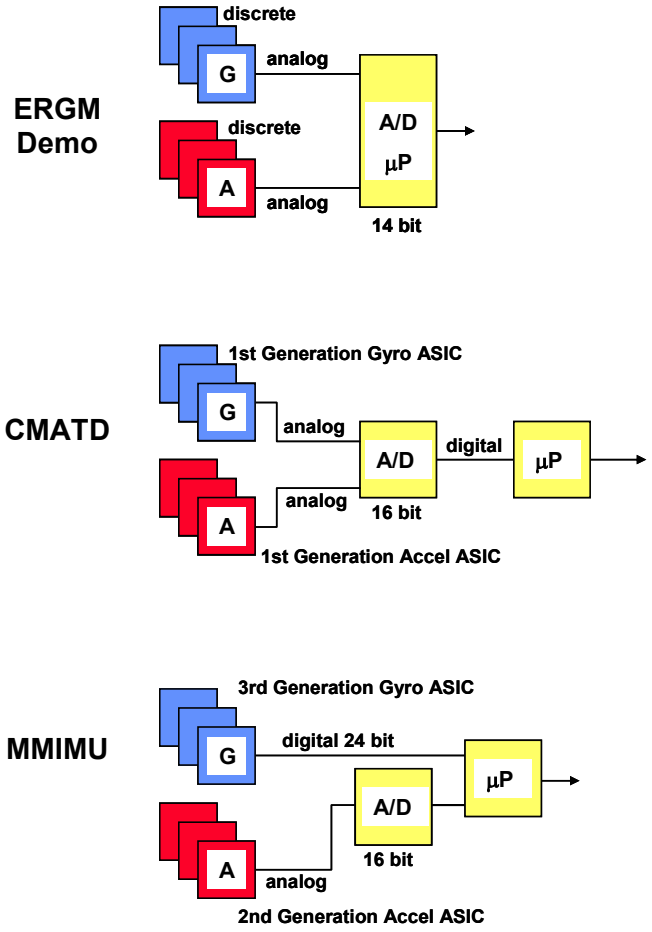


Figure 7: IMU System Architecture Evolution.

3.3 GPS Receiver Technology

Although this paper deals primarily with MEMS development, the importance of GPS in realizing performance and size needs to be mentioned. GPS technology is also required to continually evolve in terms of miniaturization, performance, and cost. Primary GPS requirements for competent munition applications include low power, small volume, high-g survivability and fast reacquisition of GPS after barrel exit. The need for rapid reacquisition imposes the need to precisely maintain the GPS clock frequency reference across the shock event.

Maintaining GPS lock against both intentional and non-intentional jamming is a critical requirement growing in importance. Because of the inherent accuracy in weapon systems employing GPS, much work is being performed in developing methods of denying GPS availability. Various techniques are employed to boost the resistance of GPS to these jamming technologies. In addition to antenna noise cancellation, hardware filters, enhanced signal processing, body shading, and antenna null techniques currently employed, methods for deeply integrating the INS/GPS systems are also under development. These deep integration algorithms employ unique filters to optimally blend the inertial and GPS information and control the code and carrier tracking performance of the receiver. By narrowing the tracking bandwidths during high jamming, additional immunity and loss of lock performance is obtained. Deep integration techniques are most poised to take advantage of the low-cost inertial and GPS systems and become a generic capability within the INS/GPS technology.

3.4 Sensor and System Packaging

High-g requirements presented significant packaging challenges to minimize the size and cost of a product expected to last 20 years in an uncontrolled environment. Typical requirements include a 20,000-g setback acceleration, angular rates up to 250 revolutions per second, and a 5000-g set-forward acceleration upon exit from the gun barrel. Experience to date suggests electronic assemblies survive gun launch provided they are properly mounted. Shock mounts are typically employed for inertial components to attenuate and dampen the high-g launch loads and in-flight vibration inputs.

Micromechanical inertial instruments were initially automotive-based designs repackaged for high-g applications. ERGM Demonstration packaged these automotive MEMS sensors and ASICs in standard thick-film hybrid hermetic packages mounted to multilayer epoxy glass laminate printed circuit boards (PCBs). CMATD combined higher performing sensors, second-generation ASIC electronics, and multilayer multichip module-laminate (MCM-L) PCBs. Current generation instruments use more advanced ASIC electronics that eliminate virtually all off-ASIC components.

Future IMUs for gun-launched projectile applications require decreasing the volume of the MMIMU by a factor of 4. The inertial instrument modules dominate the current size of the MMIMU design. To minimize development time and cost, commercial field programmable gate arrays (FPGAs) were used for many digital functions. Future designs package improved ASICs with configurable gate arrays (CGAs) to replace FPGAs, and passive conditioning electronics into a custom ball grid array (BGA) package. Using CGAs, the current MMIMU board diameter is reduced from 2.6 inches (66 mm) to 1.8 inches (46 mm), yielding a 50% volume reduction.

Three-axis measurements are achieved by rotating sensor packages on ceramic mounting blocks. Further size reductions are achieved using off- axis sensors for orthogonality. Inertial input axes are typically fixed by the design and mounting of the sensor in the three-axis instrument module. The pendulous accelerometer sensor measures acceleration normal to the module circuit board, while the TFG measures rotations in the plane of the circuit board. By using the new OPG and IPAX sensor devices, ceramic mounting blocks are eliminated and the heights of individual modules are greatly reduced. Utilizing a combination of these new sensor technologies and the aforementioned ASIC electronic advances with CGA devices custom packaged in a BGA format enables the realization of a complete 6-axis inertial instrument module, thus yielding an additional 50% volume reduction. Figure 8 illustrates the size reduction advantages of using these latest packaging techniques.

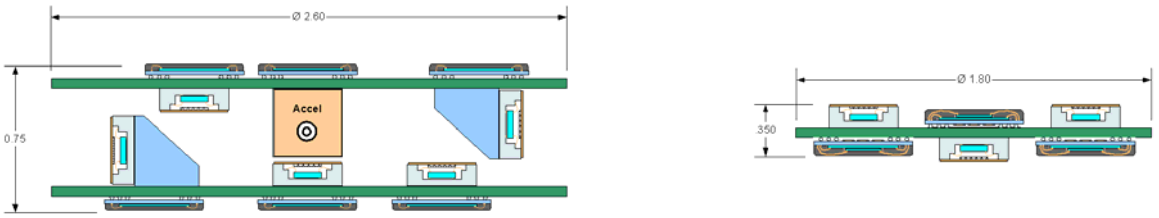


Figure 8: MMIMU 3-Axis Sensor Modules vs. later OPG and IPAX 6-Axis Sensor Module.

4.0 CGIMU

The goal of the Army's Common Guidance IMU program is to develop a new system that extends the capabilities of the previous systems further yet in terms of highest performance with high launch loads, anti-jam GPS, decreased volume, and low production cost ($1200 per IMU and $1500 per INS/GPS in high volume). Honeywell, in partnership with Draper Laboratory, was funded in 2001 to develop a common system for use in the majority of the Army's, Navy's, and Air Force's tactical weapons. Significant development effort is planned within the scope of this program to further increase sensor performance while reducing packaging volume and overall system cost. Honeywell's program draws significant leverage from previous developments. The MMIMU technology is the baseline for Phase 1 of the CGIMU. The final result of this program is expected to provide a producible production-ready qualified system for guided tactical weapons. Table 2 outlines the three phases of the CGIMU program.

Table 2: Common Guidance IMU Program

Parameter	IMU Volume	Gyro Performance	Accelerometer Performance	Completion
Phase 1	8 cu. in. (131 cc)	200°/hr (3σ)	9 mg (3σ)	April 2003
Phase 2	4 cu. in. (66 cc)	20°/hr (3σ)	4 mg (3σ)	October 2004
Phase 3	2 cu. in. (33 cc)	1°/hr (3σ)	0.3 mg (3σ)	October 2006

5.0 THE FUTURE

Over the next three to five years the applicability of MEMS for high g applications will be conclusively demonstrated. From five to ten years onward, the insertion of high volume production MEMS IMUs and INS/GPS systems into a wide range of tactical systems is expected to occur at an ever-increasing pace. During this time the opportunity for further MEMS technology improvement will still exist. The vision for far future inertial MEMS reflects a radical departure from the demonstration systems described in this paper. Wafer-scale integration of high-performance planar array sensors, with multi-channel digital ASICs and multi-axis on-chip sensors, will create complete systems on a chip, offering a further order of magnitude reduction in volume. Using high-volume foundries, these tactical-grade instruments will thereafter be reduced to commodity items and installed as chip sets in higher-level systems. Future INS/GPS system designers will be able to select inertial and GPS chip sets with desired performance attributes out of catalogs in the same manner that an analog circuit designer selects operational amplifiers today.

In addition to the needs described for competent munitions, the prevailing thought is that commercial applications will evolve to take advantage of the higher performance afforded by these technologies. Self-locating cell phones, intelligent vehicle highway systems, personal navigation, and autonomous control are all applications poised to integrate these technologies and exploit its utility. Analogous to the proliferation of GPS into common life, once these technologies are available, the engineers and designers closest to the problems will find techniques to employ singular or integrated aspects of these technologies to address the needs.

6.0 ACKNOWLEDGEMENTS

The authors gratefully acknowledge continued support from Draper Laboratory and the many dedicated engineers, scientists, and technicians who contributed to this development. We also wish to recognize the following government organizations for their contractual support: ERGM Demonstration – NAVSEA PMS529 under contract N00030-94-G-0060-EK/4; CMATD – Office of Naval Research under contract N00014-96-C-0041; Manufacturing Low-Cost MEMS Inertial – DARPA/US Army under contract DABT63-95-C0080; High-g IMU on a Chip - DARPA/US Army AMCOM under contract DAAH01-99-C-R229; and MMIMU - DARPA/Air Force Research Laboratory under contract F33615-98-C-1201. Please note that the content of the information herein does not necessarily reflect the position or the policy of the government and no official endorsement should be inferred. Portions of this paper have previously been published in the Proceedings of the Institute of Navigation GPS 2001 Conference, Salt Lake City, UT, 11-14 September 2001.

7.0 BIBLIOGRAPHY

Gustafson, D., R. Hopkins; N. Barbour and J. Dowdle, “A Micromechanical INS/GPS System for Guided Projectiles,” ION 51st Annual Meeting, Colorado Springs, CO, June 5-7, 1995.

Dowdle, J. and K. Flueckiger, “An Integrated GPS/Micromechanical IMU for Navy 5” Projectiles,” The Institute of Navigation Conference, Cambridge, MA, June 18-20, 1996.

Connelly, J., and G. Brand, “Advances in Micromechanical Systems for Guidance, Navigation, and Control,” AIAA Guidance, Navigation and Control Conference, New Orleans, LA, 11-13 August 1997.

Barbour, N., E. Brown, J. Connelly, J. Dowdle (Draper), and G. Brand, J. Nelson, J. O’Bannon (Boeing), “Micromachined Inertial Sensors for Vehicles,” Intelligent Transportation Systems Conference, Boston, MA, November 1997.

Gai, E., “Guiding Muntions with a Micromechanical INS/GPS System”, 4th St. Petersburg Conference on Integrated Navigation Systems, St. Petersburg, Russia, May 1998.

Kourepenis, A., J. Borenstein, J. Connelly, R. Elliot, P. Ward, M. Weinberg, “Performance of MEMS Inertial Sensors,” 24th Joint Services Data Exchange Conference, Anaheim, CA, November 16-20, 1998.

Brown, T., B. Davis, D. Hepner, J. Faust, C. Myers, C. Muller, T. Harkins, M. Holis, and B. Placzankis, “Strap-Down Microelectromechanical (MEMS) Sensors for High-G Munition Applications,” 10th Electromagnetic Launch Technology (EML) Symposium, San Francisco, CA, 25-28 April 2000. Journal: IEEE Transactions on Magnetics, Vol. 37, No. 1, Pt. 1, pp. 336-42, January 2001.

Flueckiger, K., "A High Anti-Jam MEMS-Based INS/GPS Navigator," Proceedings for the 26th Joint Services Data Exchange (JSDE) for Guidance, Navigation, and Control Symposium, October, 2000.

Anderson, R., D. Hanson, and A. Kourepenis., "Evolution of Low-Cost MEMS Inertial System Technologies," ION GPS 2001, Salt Lake City, UT, September 11-14, 2001.

Gustafson, D., J. Dowdle, and K. Flueckiger, "A High Anti-Jam GPS-Based Navigator," The Draper Technology Digest, Vol. 5, pp. 4-13, 2001.

Sitomer, J., J. Ha, A. Kourepenis and J. Connelly, "High-Performance MEMS Inertial Measurement Unit (MMIMU) for Tactical Applications," IEEE PLANS 2002, Palm Springs, CA, April 2002.

Warnasch A., and A. Killen, "Low-Cost, High G, MEMS IMU Program," IEEE PLANS 2002, Palm Springs, CA, April 2002.

Connelly, J., A. Kourepenis, and T. Marinis, "Micromechanical Sensors in Tactical GN&C Applications," AIAA Guidance, Navigation and Control Conference, Monterey, CA, August 5-8, 2002.

Characteristics and Overview of a Silicon Vibrating Structure Gyroscope

Dr J. Richard Fountain
Senior Consultant Engineer
BAE SYSTEMS
Clittaford Road
Plymouth PL6 6DE
UNITED KINGDOM

ABSTRACT

This paper provides details of the BAE SYSTEMS silicon vibrating structure gyro. Information is presented on the basic design of the silicon ring based structure and details are also provided on the gyro characteristics and performance.

1.0 INTRODUCTION

BAE SYSTEMS together with its partner Sumitomo Precision Products Company Ltd. have developed a silicon Micro-machined Electro-Mechanical System (MEMS) gyro for commercial applications.

The design takes full advantage of the techniques developed in the electronics industry and is highly suited to high volume manufacture. As a result a true low cost sensor has been introduced into the market place which will satisfy a wide range of commercial applications, particularly automotive. In addition to this, the sensing element can withstand the environments typical of many military and aerospace applications. By use of more sophisticated control algorithms the performance of the gyro will be improved and as such is already challenging the current thinking on gyro technology for military programmes.

2.0 BASIC PRINCIPLES

All vibrating gyroscopes rely on the phenomenon of the coriolis acceleration. This acceleration is experienced by a particle undergoing linear motion in a frame of reference which is rotating about an axis perpendicular to that of the linear motion. The resulting acceleration, which is directly proportional to the rate of turn, occurs in the 3rd axis which is perpendicular to the plane containing the other two axes, Figure 2.1. Thus, in a rate sensor, vibratory motion is coupled from a primary vibrating mode into a second mode, when the sensor experiences angular rate.

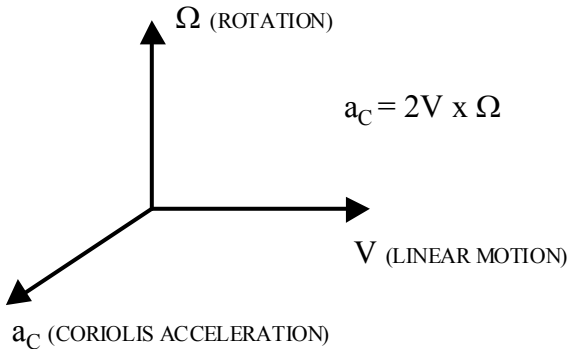


Figure 2.1: The Coriolis Acceleration Phenomenon.

There are clearly many practical implementations which can be used to produce a gyroscope (rate sensor). However, it is convenient to subdivide these into 3 groups as follows (Ref. 1), (see Figure 2.2).

i. Simple Oscillators (mass on a string, beams)

ii. Balanced Oscillators (tuning forks)

iii. Shell Resonators (wine glass, cylinder, ring)

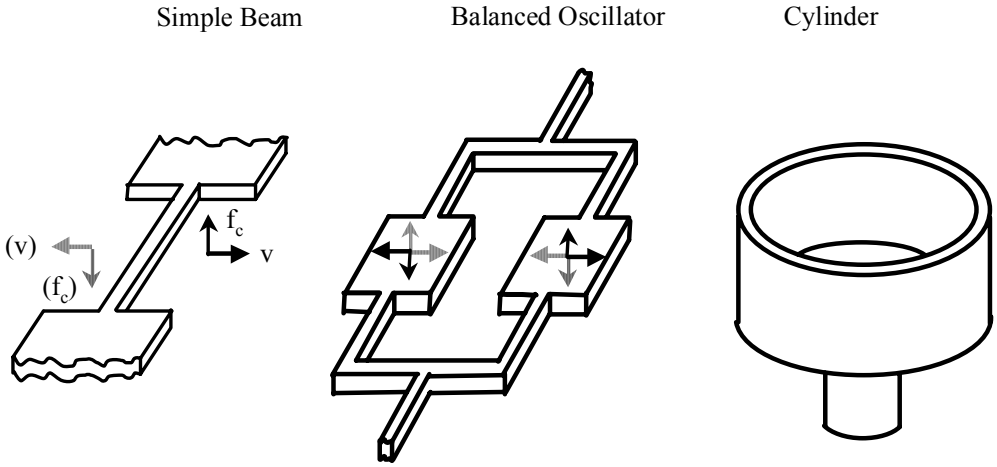


Figure 2.2: Resonator Classifications.

While many rate sensors have been produced using designs that fall into the first two categories, all vibrating gyros manufactured by BAE SYSTEMS belong to the third category. By correct design of a shell resonator it is possible to overcome problems associated with resonator mount sensitivity experienced by simple oscillators and balanced oscillators and thus improve bias performance, and greatly reduce sensitivity to shock and vibration. In fact, as will be seen from this paper, the ring design (Ref. 2) offers considerable advantages and extremely good shock and vibration characteristics have been achieved. Because the design team have evolved the shell resonator technology from the first product, VSG (piezo-ceramic cylinder), to VSG 2000 (metal ring resonator), into silicon, then all of the basic principles were well understood at an early stage. As such a rapid development programme, greatly assisted by the silicon processing expertise of Sumitomo, has been possible.

2.1 Use of Silicon

Clearly one of the major benefits of the use of silicon is that it is the route to cost reduction. By taking advantage of the wafer processing technology developed for the electronics industry a high volume, low cost and robust manufacturing process can be designed. The experiences of accelerometer manufacturers has confirmed this. However, one should not overlook the mechanical properties of silicon which can be a surprise to those unfamiliar with the material. In its crystalline state silicon has a fracture limit of 7 GPa, which is higher than the majority of steels. Coupled with this is a low density of 2330 kg/m^3, resulting in a very robust material under its own weight.

The resonator design described in this paper takes full advantage of these properties by etching the mechanical element out of the crystalline material. This ensures that the properties of the resonator are stable over life and environment. In addition to this, the planar ring structure described benefits from having all the vibration energy in one plane. As such, under angular rate, there is no coupling of vibration from one crystal plane to another, so that parameters such as frequency, modal frequency split and Q are very stable over temperature.

3.0 RESONATOR DESIGN

3.1 Sensing Element

The sensing element is shown schematically in Figure 3.1. Each resonator comprises a 6 mm silicon ring, supported by eight radially compliant spokes, which are anchored to a support frame 10 mm x 10 mm. Current carrying conductors are deposited and patterned onto the top surface only, and pads for wire bonding are located on the outer support frame. The chip is anodically bonded to a supporting glass structure which is thermally matched to the silicon.

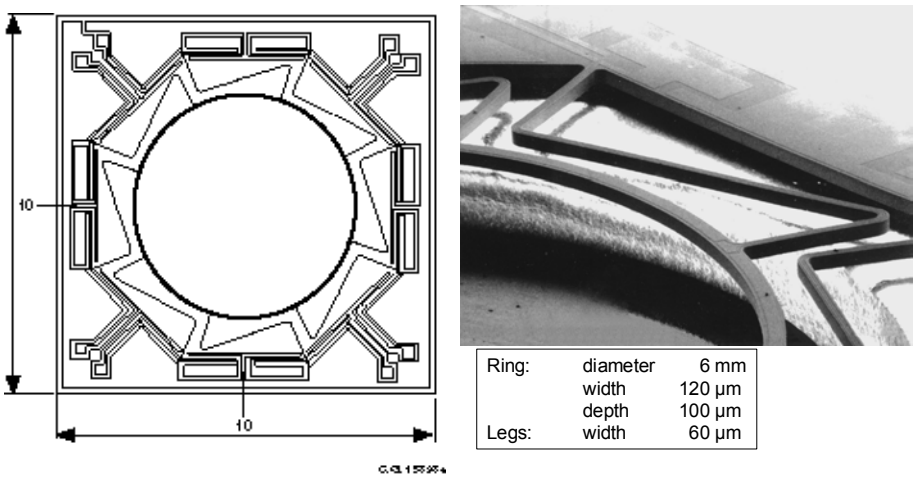


Figure 3.1: Sensing Element.

There are eight identical conducting loops which each follow the pattern, bond pad – along length of support leg – around 1/8 segment of ring – along length of next support leg – bond pad. Each leg thus contains 2 conductors, one each from adjacent loops, in addition to a 3rd conductor, which lies between them, to minimise capactitive coupling. The silicon substrate is also connected in order to provide a ground plane. The drive and pick-off mechanisms will be described in detail in the next section, but firstly some of the mechanical properties will be discussed.

The fundamental vibration mode of interest is the Cos 2θ mode which is at 14.5 kHz. This is in fact a mode pair, angularly separated by 45º. The gyro design is of the resonant type so that the frequency splitting between these complimentary modes must be minimised, typically $<f_n/2Q$ Hz. Again the crystal symmetry of silicon helps here, with no contribution from the material to frequency splitting. The greatest contribution is from manufacturing tolerances, but these are minimised by the micromachining technology used. Any additional trimming requirement is satisfied by use of a laser to remove mass from the system.

The lowest order vibration mode, which is vertical whole ring motion with respect to the mount, is at >5 kHz. As a result of this the sensor is insensitive to usually experienced vibration inputs, as will be shown in the performance characteristics. By use of finite element analysis constant DC accelerations have been modelled. With an acceleration of 10,000 g applied the maximum stress is more than an order of magnitude below the fracture limit of the material. Thus the sensing element is extremely robust against shock and vibration, without the need for any protective mounts or dampers.

3.2 Drive and Pick-Off

It will be noticed that the pattern of conductor loops described in the previous section matches exactly the requirements of a Cos 2θ mode pattern (Ref. 1). These loops together with a magnetic field, which is

perpendicular to the plane of the ring, and confined to the region of the ring, provide the drive and pick-off transducers (Ref. 3). The transducers are in pairs, 180º apart, and can be traced clockwise as, primary mode drive, secondary mode drive, primary mode pick-off and secondary mode pick-off. The magnetic field is provided by a Samarium Cobalt magnet and a magnetic circuit comprising 2 pole pieces. The entire structure is housed in a standard hermetic metal IC can package, which is shown schematically in Figure 3.2.

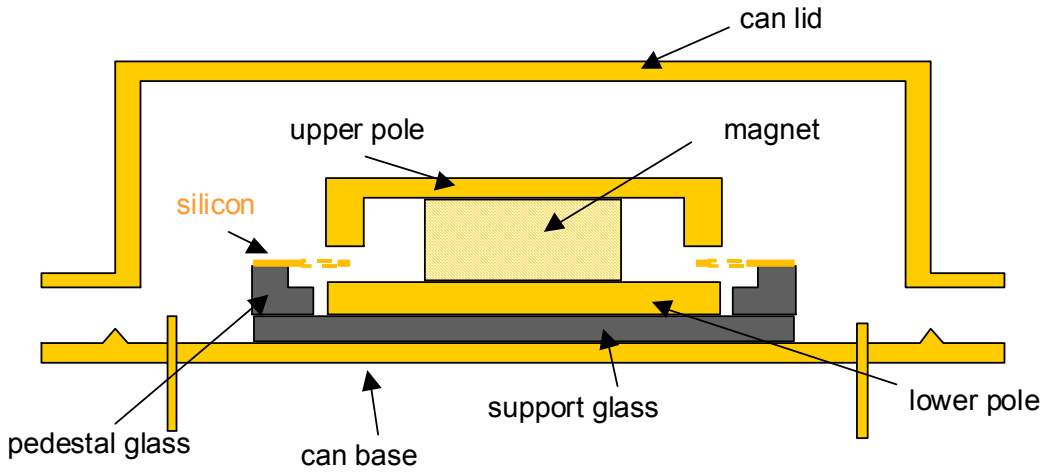


Figure 3.2: Hermetic Metal IC Can Package.

The magnetic circuit has been designed to load the magnet at its maximum energy point, and thus improve its thermal stability, and to maximise the field at the ring.

The force developed by each drive transducer with a voltage V_D applied is given by:

$$F = K_r V_D g_D$$

where:

$$K_r = 0.25 B \pi R$$

and g_D is the amps/volt gain of the current amplifier, B is the magnetic field and R is the radius of the ring.

The signal developed by a pick-off transducer, which is a velocity detector, is given by:

$$V_P = a \omega K_P$$

a is the amplitude of the vibration at an angular frequency ω and:

$$K_P = 0.25 B \pi R$$

This signal is applied to an integrating amplifier to give a signal V_{PO} proportional to amplitude.

It can be shown that the transfer function of the head on resonance is given by:

$$\frac{V_{PO}}{V_D} = \frac{g_p g_D B^2 Q \pi R}{8 h_r t_r \rho \omega}$$

where Q is the Quality factor of the resonance, h_r the width of the ring, t_r the thickness of the of ring, ρ the density of silicon and g_p is the volt/volt gain of the pick-off amp (note this is an integrator so $g_p \alpha 1/\omega$).

4.0 ELECTRONIC CONTROL

Thus far the paper has described the Silicon sensing element, which is the heart of the gyroscope. This obviously needs to be integrated with control electronics in order to produce a fully functional sensor. While it may be possible to operate a gyro in an open-loop mode, considerable performance advantages are gained by operating closed loop. Reference is made to Figure 4.1.

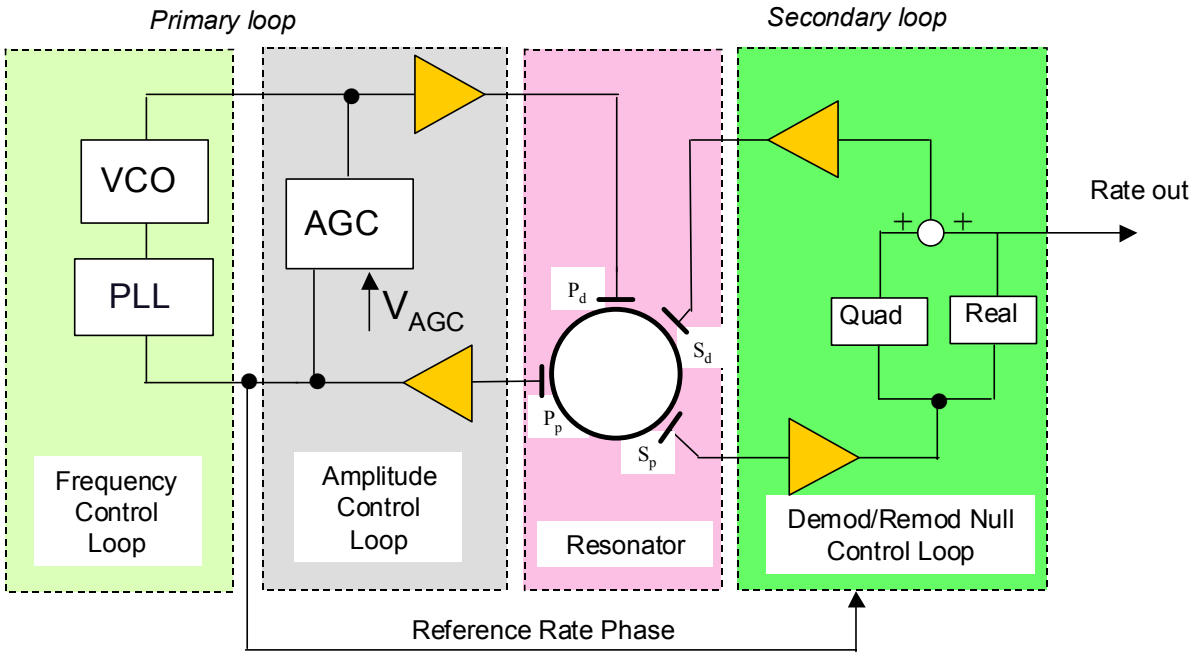


Figure 4.1: Closed Loop Control Electronics.

The primary mode is controlled by the primary loop which comprises both a VCO loop, to maintain the vibration on resonance, and an AGC loop which maintains constant amplitude of motion. Under applied rotation, energy is coupled from the primary mode to the secondary mode. It is possible to measure the amount of vibration on the secondary pick-off as a measure of rate. However, in this implementation a secondary loop is used to maintain the secondary vibration at zero, and the amount of drive required to do this is a measure of the applied rate.

By maintaining a constant modal pattern on the resonator the linearity and bias of the system is improved. The combination of the AGC loop and the secondary loop also serves to remove Q from the scale factor. A fully open loop system would have a Q^2 dependence. The secondary loop comprises two parts, a rate loop and a quadrature loop. The use of a quadrature loop to null quadrature motion significantly reduces errors due to frequency differences between the primary and secondary modes.

In order to understand the details of the closed loop electronics then a comprehensive error model is required. Such a model has been developed which includes physical errors such as frequency split, delta Q, electrode misalignment and mode misalignment to electrode pattern, together with electronic gain, phase and crosstalk errors. This model is beyond the scope of this paper.

With reference to the closed loop scheme in Figure 4.1, and the drive and pick-off terms described earlier, it is possible to examine the key error drivers to scale factor. These can be summarised as:

$$SF\alpha\frac{V_{AGC}}{g_{DS}g_pB^2}$$

Where V_{AGC} is the demand level of the AGC loop and g_{DS} is amps/volt gain of the secondary driver and g_p is again the volt/volt gain of the primary amplifier. Since the pick-off amplifier is an integrator then it would be more correct to express this as:

$$SF\alpha \frac{\omega V_{AGC}}{g_{DS} g'_p B^2}$$

Since V_{AGC} and the gain terms are purely electronic terms and ω is very stable for this silicon structure, then the dominant term in the scale factor is B^2, which is well understood and compensated thermally.

The dominant noise source in the gyro is pick-off amplifier noise V_N (V/√Hz). By including the dynamics of the system in the analysis it is possible to express this noise in terms of a rate equivalent noise figure. It can be shown that at the secondary pick-off the noise , A, is given by:

$$A = \frac{K_1 f_n^2 V_N}{g_D Q^2 B^2 V_{PD}} \qquad {}^{\circ}/_{\sqrt{Hz}}$$

Where V_{PD} is the voltage applied to the primary drive and K_1 is a term that includes the dimensions of the resonator and mode shape (Bryan factor). f_n is the resonant frequency (ω/2π).

As with all coriolis gyros gain is applied to achieve a given output bandwidth, f_{BW} Hz, so that the rate equivalent noise at the output is approximately:

$$\frac{K_1 f_n V_N}{g_D Q B^2 V_{PD}} \sqrt{\frac{4 f_{BW}^3}{3}}$$

The theory predicts that for a gyro with a 40 Hz bandwidth then an rms noise figure of 0.2 °/s is expected in the band. This is in very good agreement with that measured, as is shown in the gyro performance section. The same gyro measured over a band 0-10 Hz has a noise figure of 0.025 °/s.

5.0 SILICON PROCESSING

In order to produce a robust and reliable manufacturing process then reduction in processing steps through simplicity in design is key. As such the sensing element requires only 3 mask levels for the silicon fabrication. The processing steps are shown schematically in Figure 5.1. A 100 μm wafer has a deposited oxide layer patterned with mask level 1. A metal layer is then sputter deposited and patterned with mask level 2. Finally photo-resist is spun and patterned with mask level 3 to define the resonator structure, which is then etched with a dry deep trench etch process.

It is a considerable advantage of the deep trench etch process used that photo-resist can be used as a mask. Following etching to produce the mechanical component the photo-resist is stripped away leaving a wafer of silicon resonators. The silicon wafer is anodically bonded to a pre-cavitated glass wafer and diced to release individual sensor elements.

The design avoids the necessity for small gaps between the resonator and surrounding material and so problems with ‘stiction’ are avoided. A further advantage is that the ring resonator has all its vibration in one plane so that all the silicon processing is planar, avoiding the necessity for multi-layer processing.

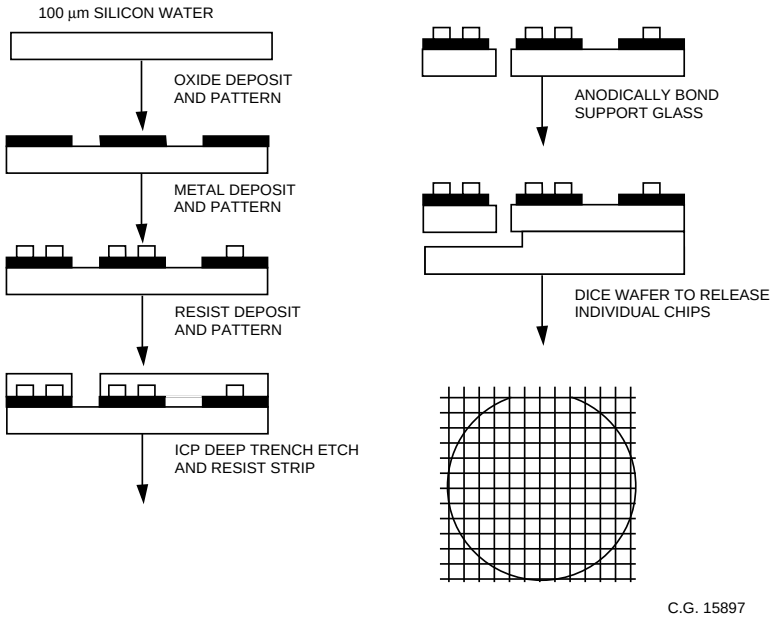


Figure 5.1: Processing Steps.

6.0 PERFORMANCE CHARACTERISTICS

A summary of key parameters is provided in Table 1. These represent typically achieved performance, but see Appendix A for measured noise and bias characteristics.

Table 1: Key Parameters

Parameter	Value	Units
Supply voltage (RRS01)	±5 to ±15	V DC
Current (discrete electronics)	<50	ma
Scale factor (rates ± 100 °/s)	20	mV/°/s
SF Temp sensitivity (-40 to +85°C)	<±1	%
Linearity (rates ± 100°/s) (of full scale)	<1	%
Bias – set	<0.5	°/s
Bias Temp sensitivity (-40 + 85°C)	<±3	°/s
In run (0-30 min) 1σ	0.05	°/s
Switch on repeatability 1σ	<0.06	°/s
Bandwidth	>45	Hz
Noise rms (0-45 Hz)	<0.5	°/s

It should be noted that this data is unmodelled and does not represent the ultimate performance of a fully compensated sensor. In particular the scale factor change with temperature at ±2% is achieved easily with all sensors using a standard passive compensation circuit. For gyros where the compensation is calculated for a particular sensor a scale factor change of <0.35% is typical. The bias performance in Table 1 is raw data. Additional compensations have been developed to considerably improve bias performance for military and aerospace versions of the sensor. In-run drift includes warm up in the figure quoted. However if a sensor is allowed to warm up and stabilise then in-run drifts of <17°/hr have been achieved. The gyro has also been used to measure earth rate.

Not quoted in the table are shock and vibration characteristics. Vibration levels of 30 g rms (0.3 g²/Hz up to 3 kHz) have been applied without degradation of noise performance or change in bias value during the vibration. Unchanged bias has also been measured through 1000 g (½ sine 1.0 ms) shocks, and units have been repeatedly subjected to survival shocks of 1.2 m drops (~ 5000 g).

7.0 CONCLUSIONS AND FURTHER WORK

This paper has described a silicon micromachined gyroscope developed in partnership between BAE SYSTEMS and Sumitomo Precision Products. The robust design is ideally suited to high volume manufacture and has already demonstrated performance that satisfies a wide range of applications. There is some strong evidence that performance can be considerably improved by the use of more complex control algorithms for use in military and aerospace applications. The detailed design described here represents the first product, but not the final story. Research is already underway to answer the problems of the future. In particular areas such as integration of electronics onto the sensing element, smaller resonators, digital control loops and development of an angle sensor are being progressed. To produce a coriolis angle sensor requires axial symmetry about the rate axis and the ring structure is ideally suited for this.

In conclusion, for a high performance to cost ratio in angular rate measurement then silicon micromachined gyros represent the future. This paper has shown that the technology is available now for exploitation in many application areas.

8.0 REFERENCES

[1] Fox, C.H.J. & Hardie, D.S.W., “Vibratory Gyroscopic Sensors”, Symposium Gyro Technology, (DGON), 1984.

[2] Varnham, M.P. et al, US Patent 5226321.

[3] Hopkin, I.D. et al, US Patent Application.

[4] “Noise Analysis in Operational Amplifier Circuits”, Texas Instruments Application Note, SLVA043A, 1999.

[5] Tehrani, M.M., “Ring Laser Gyro Data Analysis with Cluster Sampling Technique”, Proceedings of SPIE, Vol. 412, 1983.

[6] IEEE, IEEE Specification Format Guide and Test Procedure for Interferometric Single-Axis Fibre Optic Gyros, Doc No. 952-1997, Annex C, IEEE, 1997.

For simplicity References 2 and 3 are merely exemplars taken from an extensive patent coverage of this technology.

APPENDIX A – MEASURED SILICON GYRO CHARACTERISTICS

This appendix provides information on measurements and analysis of a BAE SYSTEMS silicon gyroscope.

A.1 SILICON GYRO DERIVED NOISE MODEL

The model has been derived on the basis of shaping white gaussian noise with an appropriate filter. The filter parameters are chosen to match the characteristics of the PSD (Power Spectral Density), calculated from the raw silicon gyro data (see Figure A.1). In Figure A.1, a log-log plot, the slopes are at +1 and –1, equating to 20 dB per decade.

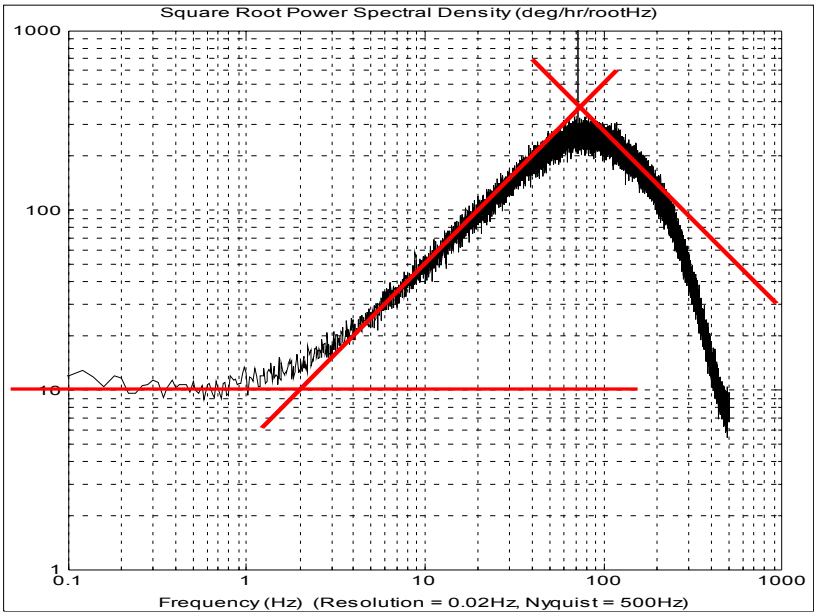


Figure A.1: PSD for 1 kHz (ISA X-Gyro) Data.

The gaussian noise is defined to be zero mean with a standard deviation of 1.0 rad/s. The gain required to match the actual gyro PSD, is included in the filter transfer function.

$$filter\ transfer\ function, F(s) = \frac{25(s+12.56)}{s^2 + 2\zeta\omega_n s + \omega_n^2} \quad (gain = 25) \qquad \text{(A.1)}$$

$$where,\ \omega_n = 2\pi f$$

$$f = 80\ Hz$$

$$then,\ \omega_n = 2\pi 80$$

$$= 502.65\ rad/s$$

$$damping\ ratio,\ \zeta = \frac{1}{\sqrt{2}} = 0.7071$$

$$giving, F(s) = \frac{25(s+12.56)}{s^2 + 710s + 252657} \qquad \text{(A.2)}$$

The s coefficient in the numerator gives a break point at $12.56/2\pi = 2$ Hz.

Although this noise model has been derived from measured data, it agrees well with mathematical analysis of the gyro electronic circuit.

A.2 FULL GYRO ERROR MODEL BLOCK DIAGRAM

The block diagram depicting the implementation of the silicon gyro rate errors (in this case, angle increments), including the shaped noise, is shown in Figure A.2.

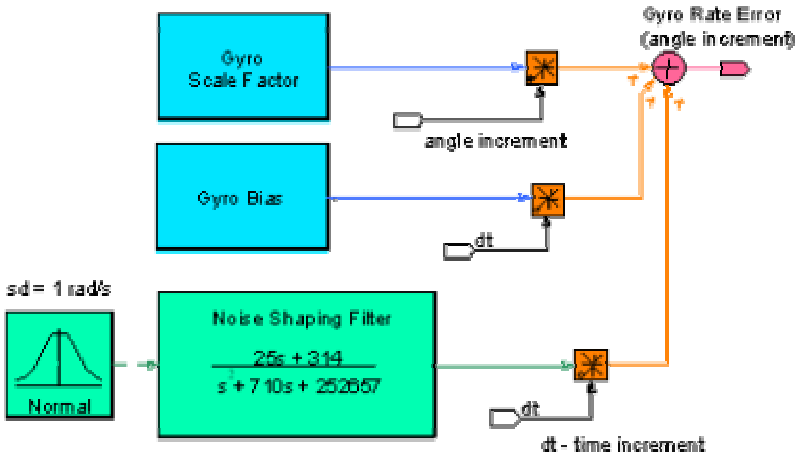


Figure A.2: Gyro Error Model Block Diagram.

The angle increment value is the true angle increment, required for calculating the scale factor error, with dt, the delta time increment.

Note that this model does not include the flicker noise, that is required to model the low frequency characteristics of the gyro (see Section A.3).

A.3 LOW FREQUENCY NOISE

At low frequency, below about 0.1 Hz, the noise characteristics of the silicon gyro become dominated by flicker noise (also known as 1/f noise and pink noise). Flicker noise is present in all active electronic devices (see Ref 4), and occurs in the gyro electronics at the output stage, prior to and including any Analogue to Digital Converter (ADC).

The gyro itself in isolation, including drive and control electronics, will have much lower flicker noise than presented below. If flicker noise is perceived to be a problem for a particular application, then careful selection of the output stage components (including the ADC, if digitisation is required) must be exercised.

If there are outside influences (such as temperature change or power supply variations, for example) acting at relatively long time constants, then these may introduce rate variations, such as a ramp, which could obscure the observation of flicker noise.

Within the control loops of the gyro, the frequency is relatively high and noise will be dominated mainly by thermal noise and shot noise (independent of temperature, related to current flow). Both thermal and shot noise are white noise processes.

Flicker noise has a PSD that is dependent on the inverse of frequency,

$$S_{flic\,\mathrm{ker}} = \frac{B^2}{f} \tag{A.3}$$

where B is the characteristic of the device (units of rate, for the gyro).

Integrating, to obtain the variance gives,

$$\sigma^2_{flic\,\mathrm{ker}} = \int_{f_l}^{f_h} \frac{B^2}{f}\,df = B^2 \ln\frac{f_h}{f_l} = B^2(\ln f_h - \ln f_l) \tag{A.4}$$

where, f_l = lowest frequency, f_h = highest frequency (f_h - f_l = system bandwidth)

and, ln, is the natural logarithm.

White noise is characterised by a flat PSD, giving,

$$S_{white} = Q^2 \tag{A.5}$$

where Q is the characteristic of the device (units of rate per root Hz, for the gyro)

Intergrating, to obtain the variance gives,

$$\sigma^2_{white} = \int_{f_l}^{f_h} Q^2\,df = Q^2(f_h - f_l) \quad or\ Q^2 \text{ x } bandwidth \tag{A.6}$$

Therefore, at low frequency, the total noise is given by the combination of flicker noise and the white noise components,

$$\sigma^2_{total} = \sigma^2_{flic\,\mathrm{ker}} + \sigma^2_{white} = B^2(\ln f_h - \ln f_l) + Q^2(f_h - f_l) \tag{A.7}$$

A.4 NOISE CHARACTERISTICS

Noise data from a BAE SYSTEMS silicon gyro is presented in Figure A.3, Allan Variance (in this case the Allan (Standard) Deviation) and Figure A.4, PSD at low frequency (see Figure A.1 for a higher frequency PSD plot).

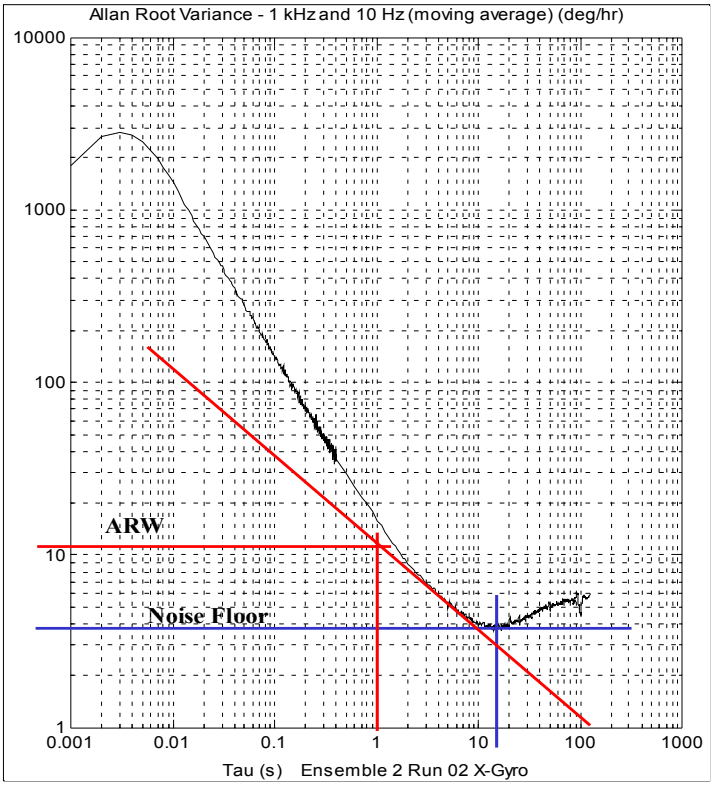


Figure A.3: Allan (Square Root) Variance.

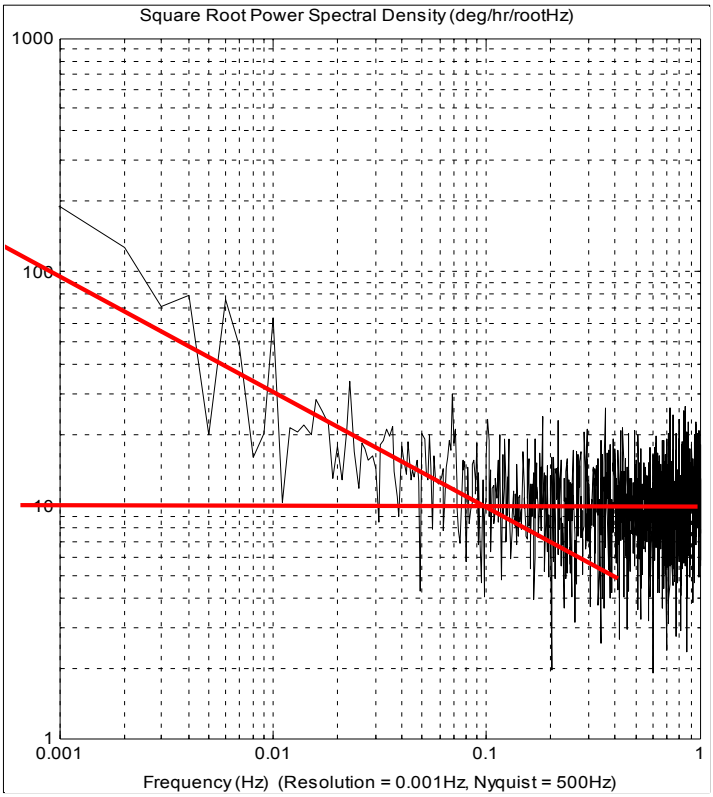


Figure A.4: PSD – Low Frequency.

The Allan Variance (Ref 5,6) and PSD provide the same information but in a different form. Note that the Allan Variance has units of time on the x-axis, with the PSD x-axis units being in Hz.

From Figure A.3 the noise floor, at just under 4 deg/hr, is reached at about a 15 s averaging period. This is the point at which longer averaging times will not reduce the noise, since the flicker noise increases as the frequency reduces (see equation (A.4), this is clearly seen in Figure A.4. The flicker noise characteristic (B in equation A.3), can be obtained from the PSD or the Allan Variance (it is sometimes referred to as Bias Instability) but when using the Allan Variance, the correct scaling must be used ($\sqrt{}$ (ln(2) 2/π) for Ref 5 or $\sqrt{}$(ln(2) 4/π) for Ref 6). The Angular Random Walk (ARW) is approximately 10/60 = 0.17 deg/$\sqrt{}$hr (see Ref 5 for the calculation).

A.5 BIAS CHARACTERISTICS

A typical BAE SYSTEMS silicon gyro bias characteristic is shown Figure A.5, with the residual bias error (the difference between the raw bias and bias fit plots in Figure A.6.

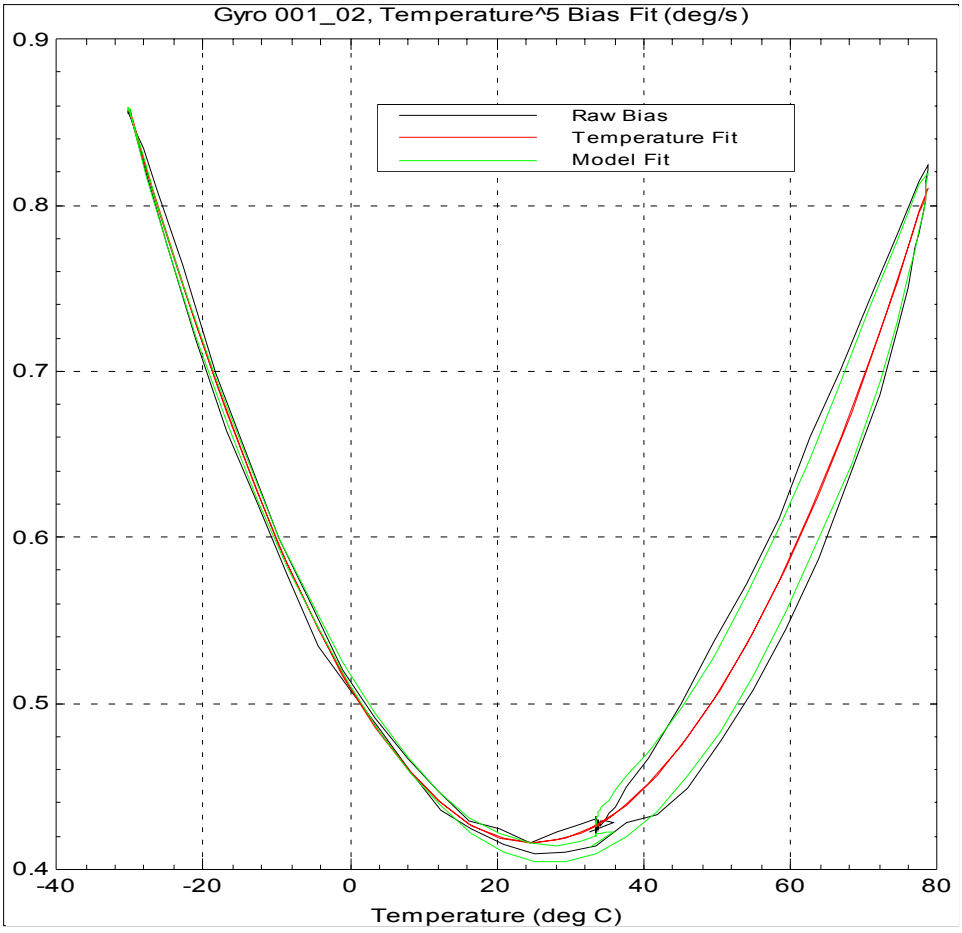


Figure A.5: Silicon Gyro Bias and Bias Fit.

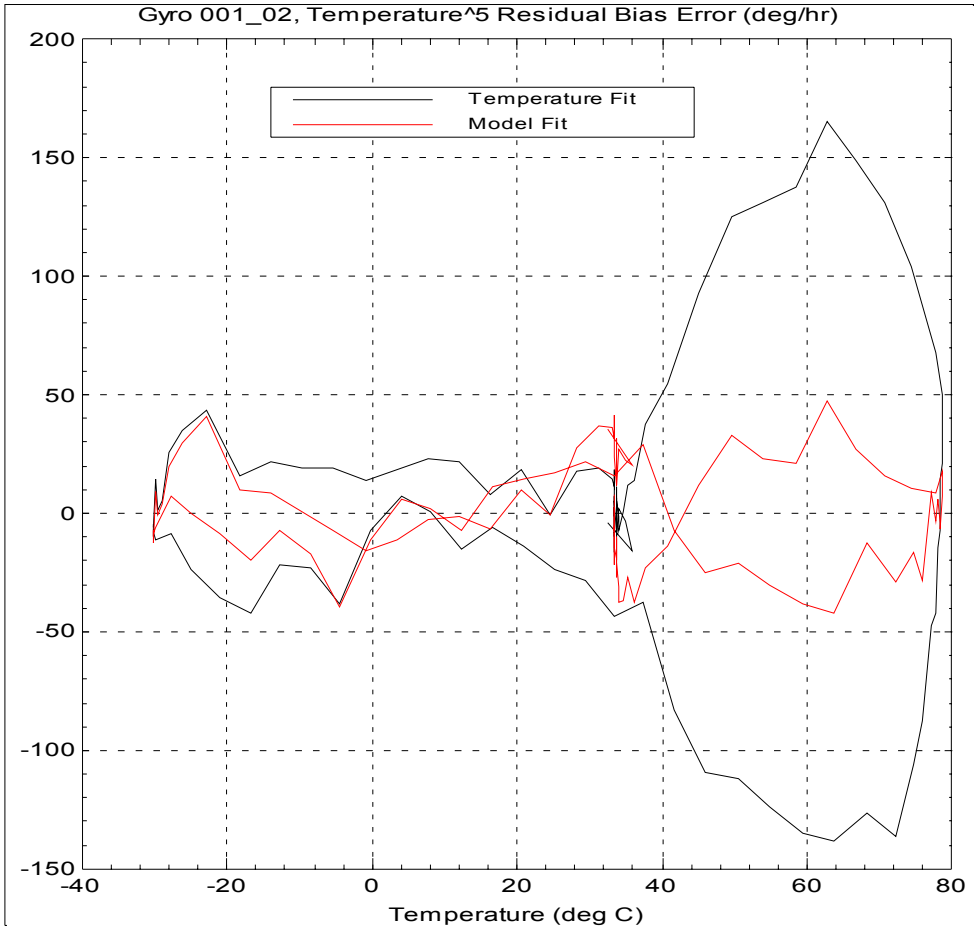


Figure A.6: Residual Bias Error.

A gyro temperature fit to order 5 has been used and because of bias hysteresis this fit has relatively large errors above about 30 deg C. The compensation has been applied to the same data as used for calibration and therefore does not indicate long term stability or ageing effects, which could typically introduce an additional 100 deg/hr,1σ, error.

What it does show is that the "Model Fit", which uses a detailed mathematical model of the gyro, provides a more accurate bias correction, especially in following the hysteresis loop.

MEMS in FRANCE
An Overview of Trends and Products for Aeronautic & Defense Applications

****

Gaëtan Menozzi
MEMSCAP
Parc des Fontaines 38 926–Crolles- France
Eric Pleska
DGA- STTC
Département Guidage et Navigation
8 Boulevard Victor - 00303 -Armées

Abstract

This paper presents an overview of the expertise of France in MEMS from R&D to products for civil and military applications and this within the European context. The paper compiles the results of programs of different military projects conducted for the development of advanced miniaturized navigation systems during the last two decades and especially synthetic information issued form the task force "Military MEMS 2001+" led by the two authors during 2001.

The paper will present the basic road map for systems, sub-systems and basic sensor components. Two main domains where France demonstrates a recognized expertise worldwide are addressed: INS Inertial Navigation Systems and ADC Air Data Computer.
In these two navigation fields, the paper presents tables of expertise and roadmaps in MEMS sensors for navigation such as accelerometers, gyrometers, pressure sensors. Examples from major defense companies and research centers are shown

1.0 Introduction

This paper as an overview of MEMS in France for military applications is issued from two sources: the programs of development at STTC-DGA and the report of the Task Force "Military MEMS in France". It seems necessary to explain how such work has been done and the expertise and involvement of the two authors in military, MEMS and navigation.

First of all the STTC at DGA (Services des stratégies Techniques et des Technologies Communes de la Délégation Générale de l'Armement) is in charge of the development of common basic components inter-army for air, sea and land. STTC has launched and funded since the 80's the development of miniaturized sensors, not yet called MEMS at that time. STTC and the industrial companies expert in this domain have elaborated strategies and roadmap that have been updated along the 90's and taken as a basis for the Task Force.

Eric Pleska is Director of Advanced Research in Navigation Systems and sub-systems at STTC at DGA. He is currently heading different programs of development in IMUs, mini IMUs and µIMUs, AHRS, stellar seeking systems.
Secondly part of the information is issued from the task force "Military MEMS 2001+" report for the CSD. The CSD, "Conseil Scientifique de Défense" (Scientific Advisory Board) acting on specific topics on demand of the French Ministry of Defense decided in 2000 to analyze the topic MEMS for military, and the task force launched, worked and reported within 10 months in 2001. **Gaëtan Menozzi** was asked to lead the task force due to his involvement in the MEMS area and his past experience in the aerospace business and Eric Pleska was part of the task force as representative of the STTC-DGA.

In the **military** field, the author has been working for a long time in sensors and µsensors/MEMS for aeronautics and defense applications within the Thales Group, (former

Thomson CSF & Sextant Avionique). During this period, he has launched and has participated in European Military Euclid project called BRAMMS involving UK, France, Italy, and Netherlands. This project was aimed at defining the needs in miniaturization for air, sea and land applications, and the capabilities of current MEMS or the need of future developments with priorities.

Gaëtan Menozzi is involved in different organizations and projects dealing with MEMS in Europe and in France, in civil and military applications. In the **civil** domain, the author is currently Chairman of NEXUS, the European network of Microsystems, and chairman of EURIMUS a 5 years strategic Eureka program. This gives a European overview of civilian expertise in MEMS products that could be used as COTS for military applications. The USCS -User-Supplier-Clubs- the core of the NEXUS activities, represents an excellent forum place for exchanging on dedicated MEMS domains. Especially the USC Aerospace and Geophysics, addresses the Road map for aeronautic and defense applications.

In conclusion to this introduction, the following sections of this paper will cover:

- "Military MEMS 2001+": The Task Force, partners involved, plans and domains.
- Roadmaps & plans for MEMS at STTC - DGA
- From R&D to components/systems: who's who in France and examples of MEMS development in progress
- Air Data & MEMS Pressure sensors: tables and roadmaps
- IMUs : accelerometers & rate Gyros: tables and roadmaps
- MEMS: the challenges and threats in design/manufacturing

2.0 "Military MEMS 2001+": the Task Force for military MEMS

This paper addresses part of the information issued from the Task Force report that are related to the two navigation domains Inertial and Air data, the following section will describe the partners of the task force, the plans and the domains covered

The main missions given to the MEMS Task Force by the CSD for the French Ministry of Defense were the following:

- The main area where MEMS demonstrate high potential with new military products issued from their application,
- Establish Road maps for the different systems domain such as navigation and radio navigation, RF communications for Radar and countermeasures, UAVs & µUAVs, biochemical, optronics.
- Deliver a status of French expertise and benchmark the European and overseas capabilities in MEMS R&D and production,
- Analyze the possible cooperation from dual applications field,
- Analyze the menaces around this new technology.

The task force was launched in early 2001 and involved the following members:

- Chairman: G. Menozzi - MEMSCAP
- Secretary: D. Luzeaux - DGA/STTC
- CSD: General M.A. Boileau and A. Migus
- Defense Systems / equipment:
  Auxitrol, MBDA, Sagem, Thales Group
- Space System / equipment:
  Astrium (Now EADS/Astrium, Alcatel Space
  & CNES (the French Space Agency part of ESA)
- Research center:
  CEA-LETI
- DGA: DGA-STTC

This team represents the main actors in the field of defense that are designers, users or suppliers/users of MEMS technology for the miniaturization of their sub-systems or systems. They are more generally equipment and systems manufacturers for military applications as well as civil aircraft. The next sketch shows the French military "food chain" in between Prime Contractors, Navigation System/Equipment manufacturers and Component/sensor manufacturers.

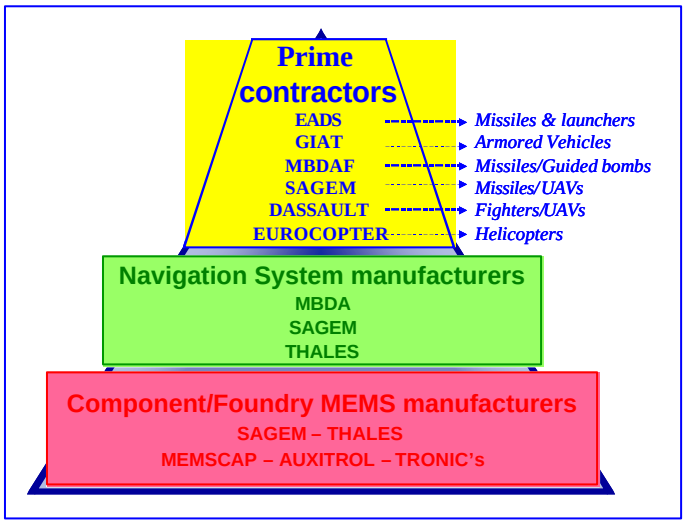


Fig. 1: the French defense industrial organization & the MEMS foundries

Prime contractors are aircraft, missiles, armored vehicles contractors and manufacturers.
Systems manufacturers are involved in design, manufacturing and qualifying navigation systems for all the different applications for defense. Component/sensors MEMS manufacturers are designing and/or manufacturing MEMS components for equipment and systems manufacturers.
As regards MEMS manufacturing, which was one of the demand for the Task Force, this topic will be addressed in a future section to highlight the different position of these companies from IDM Integrated Design Manufacturer, Fablite –mix fab, mix outsource, and fabless just subcontracting the MEMS part to external foundries.

The Task force has established the plan for the 9 months planned for this work taking into account the request from the CSD.

- 1st objective of the Task Force
  - Key application fields & Priorities
  - Review of MEMS, MOEMS, RF MEMS
  - Evolutions, impacts & Roadmap
- 2nd objective of the Task Force
  - MEMS & the challenges - The industrial challenge
  - Evolution in Europe: status of who's who (institutes/industrials)
  - Status of funding of MEMS R&D in Europe
  - The challenges and the threats: FOEs & technology acquisition and proposals

The task force established a roadmap for its work that is described in the following sketch.
Not to duplicate information's sources, it was decided to make the status of the existing equipment (0), secondly to interview the DGA about its PP30 (1) Program Plan for the 30 years defining the main strategies for air, sea, land defense, then compile information from the MEMS task force members (2), and finally to define as a synthesis, sub-systems and technologies for each strategic domain with roadmaps and specifications (2). The final report to the CSD had to give strategic guidance with recommendations.

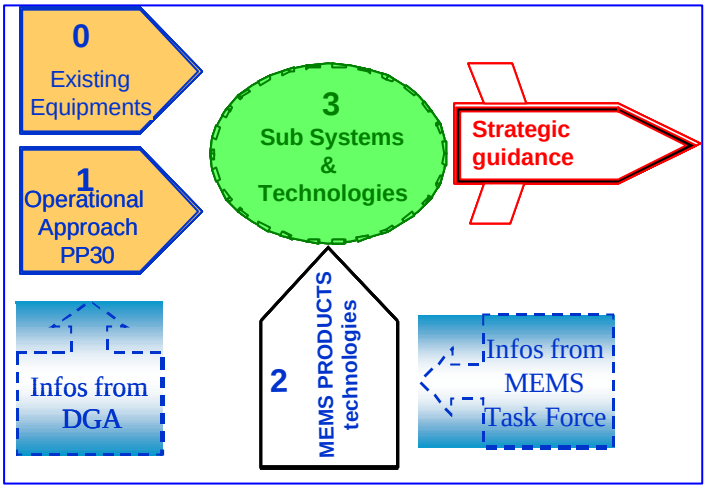


Fig. 2: Strategy roadmap of the Task Force

The Task Force decided to focus especially on the main domains air and defense that are aircraft, helicopters and missiles, in order to analyze synergies and communalities on systems, sub-systems and components. The analysis has been carried out taking into account first of all the miniaturization of existing systems thanks to the MEMS technology and secondly the emergence of new sub-systems due to the MEMS technology.

The next figures show communality of systems in civil and military aircraft, helicopters, cruise missiles and missiles. This leads to plan common basic MEMS development when specifications are quite similar.

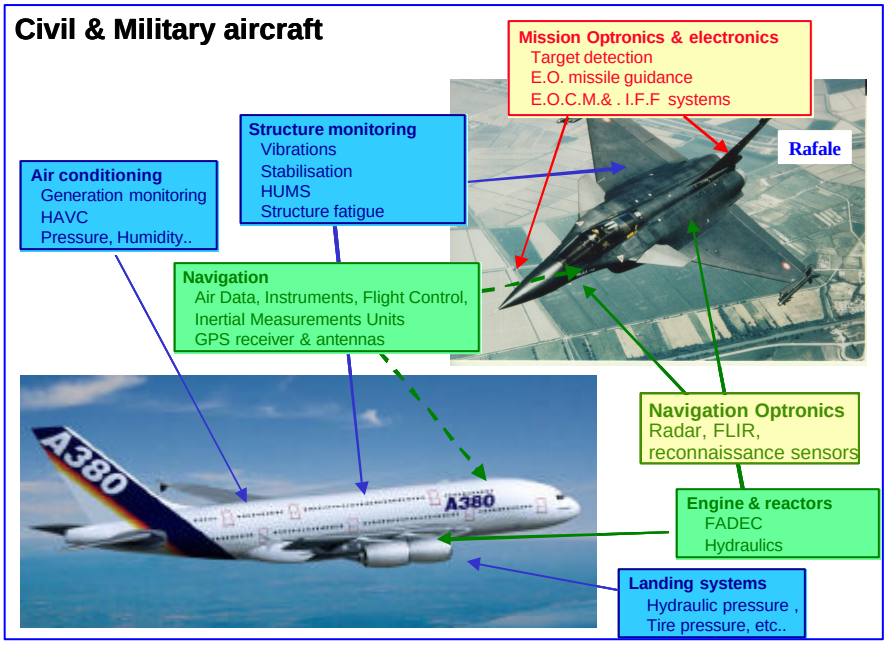


Fig. 3: Common systems on civil and military aircraft

The structure of this analysis was defined in the following sub-areas:

a) Aircraft platforms & structures including propulsion and energy generation
b) Avionics and flight control
c) Missions Optronics & electronics

d) Landing gear
e) Other systems.

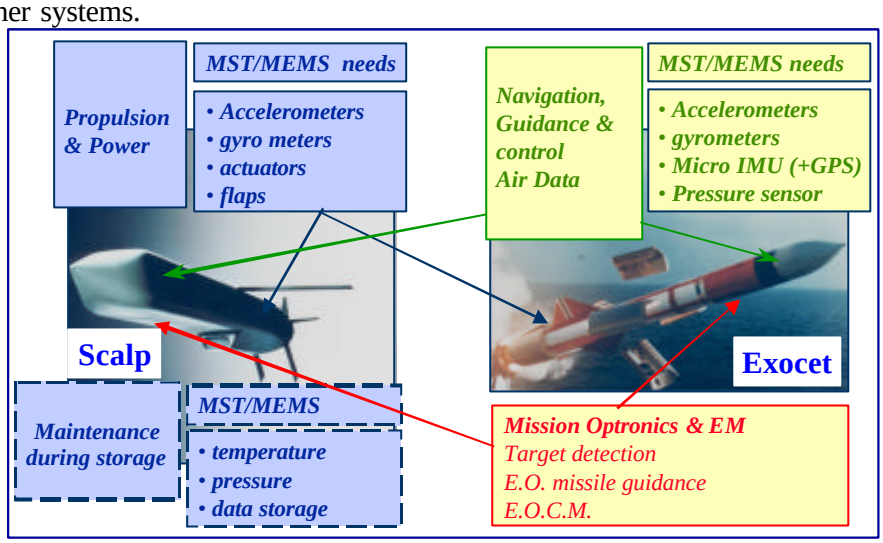


Fig. 4: Main systems and subsystems on missile applications. Left: SCALP French/UK cruise missile - Right: Exocet anti-ship missile - *(Courtesy of MBDA)*

From these two figures and the one of the helicopters, for which analog systems could be listed the main systems have been described for the part of the aircraft such as:

- Platforms and Structures,
  - Aircraft structure: HUMs and Ultra HUMS have promising new development using MEMS
  - Engines control: FADEC systems will use high temperature MEMS sensors
  - Energy distribution
- Avionics & Flight control,
  - Air Data systems
  - Navigation and Flight control
  - Man machine Interfaces
- Missions Optronics & electronics.

Table 1: future air & missiles MST/MEMS status & requirements

FUTURE AIR & MISSILES MST/MEMS REQUIREMENTS			
Systems	***Sub-systems***	***Function***	***MEMS***
Aircraft platforms & structures			
Aircraft structure	**HUMS** Mechanical diagnostics **ULTRAHUMS**	Accelerometers in array Thermal transducers Ultrasonic imaging probes	Low size & cost µaccelerometer for array network wireless MST/MEMS
Engine control	**FADEC** (Full Authority Digital Engine Control) Engine monitoring Diagnostics	Pressure sensors Temperature sensors Torque, speed, valve Tachometer, position.	High temperature SOI/SiC (400°C to 600°C) µmagnetometers: GMR, Hall µaccelerometers, GMR
Energy distribution	**APU** (Auxiliary power U.) **HCM** (Hydraulic Control monitoring) Hydraulic servo valve **ELMS** (Electrical load management)	Pressure sensors Pressure transducers Switches Switches Current measurement	High temperature SOI/SiC High pressure/high temperature Silicon/SOI pressure sensors µswitches wafer level contact array Power tags: GMR

Avionics & flight control			
Systems	***Sub-systems***	***Function***	***MEMS***
Air Data systems	**ADM** & **ADC** **PMU** & **PTMU** **MMP** (Mobile Multi function Probe) **MADCs**: (Multi function probe & Air Data Computer)	Pressure sensors Temperature sensors Pressure sensor Temperature probe Integrated probe ADC close to the structure of the aircraft	High accuracy silicon pressure sensor & µmagnetometers: GMR, Hall effect µgyro, accelerometers MEMS temperature probes Highly integrated MEMS sensors & packaging concept
Navigation	**IRS** Inertial Reference Systems (aircraft) **INS** Inertial Navigation Systems (trainer) **AHRS** Attitude & Heading Reference System (helicopter) **INS** (for missiles, cruise missiles & smart munitions)	IMU class 1 + GPS IMU class 2+ GPS IMU class 3 + GPS IMU class 3 + µGPS	µaccelerometers MEMS no MEMS gyros µaccelerometers MEMS no MEMS gyros µaccelerometers MEMS MEMS gyros in long term µaccelerometers MEMS MEMS gyros in mid term Improv. shocks & vibrations
Flight control	Stabilisation Fly by wire	Sensor network Optical interconnect	Accelerometers MEMS Rate gyrometers MEMS MOEMS
Man machine Interfaces	**ISIS** (Integrated Stand-by instruments Systems) Wafer displays **HUDs** & Helmet displays	µIMU µADM Sighting systems Position & integration	µ accelerometers, µgyro Pressure sensor µmirror displays µhallogen array µvalves MEMS

Missions Optronics & electronics			
Missions Optronics & electronics	Navigation sensors Laser Range Finder Stabilization Missile guidance **IFF** (Identification of Friends & Foe) Reconnaissance. Target detection	Cooled FPAs Focal Planar Array µIMU fast steering mirrors low cost INS/IMU navigation sensors steering active optics Active suspensions µscanning structures	µbolometers MEMS µaccelerometers MEMS MEMS gyros in long term MOEMS (See aircraft IMUs) (See aircraft IMUs) MOEMS µmachined silicon FPAs +µbolometers PZT MEMS µpositionners Active optics

This table gives the list of the main MEMS components that are presently or will be used for these applications. Some of these components are either available and/or under development for one application such as the aircraft fighter. Future developments will focus on upgrading these components for missile and smart munitions or bombs with specific improvements and evaluation tests for meeting severe environmental conditions requirements, such as temperature range, vibrations, high Gs shocks, linear acceleration….
Based on this analysis the task force decided to concentrate on systems needing priorities of miniaturization through the development of basic MEMS sensors. The following sections will address two main navigation systems that are Air Data and IMUs Inertial Measurement Units.

3.0 Roadmaps & plans for MEMS at STTC – DGA

STTC, within its Department of Navigation has built a roadmap for the development of multi purpose IMUs and µIMUs, AHRS in the defense area .
The next figure shows the military operational needs in the axis that are mission duration, needed accuracy, and dynamic range for fighters, helicopters, missiles, cruise missiles, UAVs, UCAVs, land navigation for tanks, trucks, artillery and ammunitions, shells, and smart bombs.

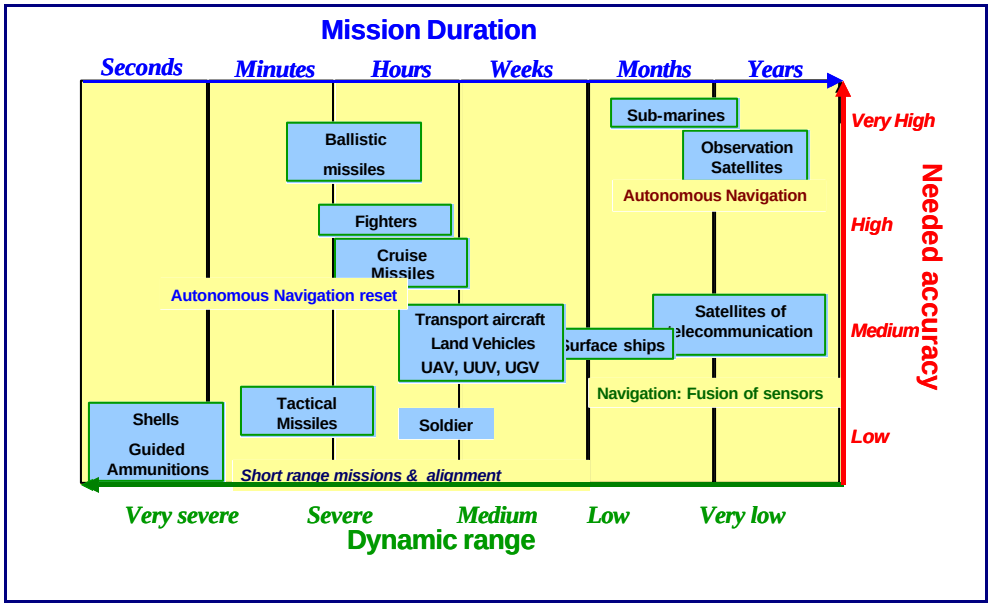


Fig. 5: Operational needs in navigation systems *(Courtesy of DGA E. Pleska)*

As an example of the continuous effort in R&D funded by DGA in the last decades the next figure 6 shows the different stages of miniaturization of 0,01°/h rate gyros since the 50's. These comprise the evolution of rate gyros measurement physical principles: from mechanical floated and tuned gyros, to optical with ring laser and fiber optical gyros, towards micro mechanisms and micro technologies with VBA and MEMS.

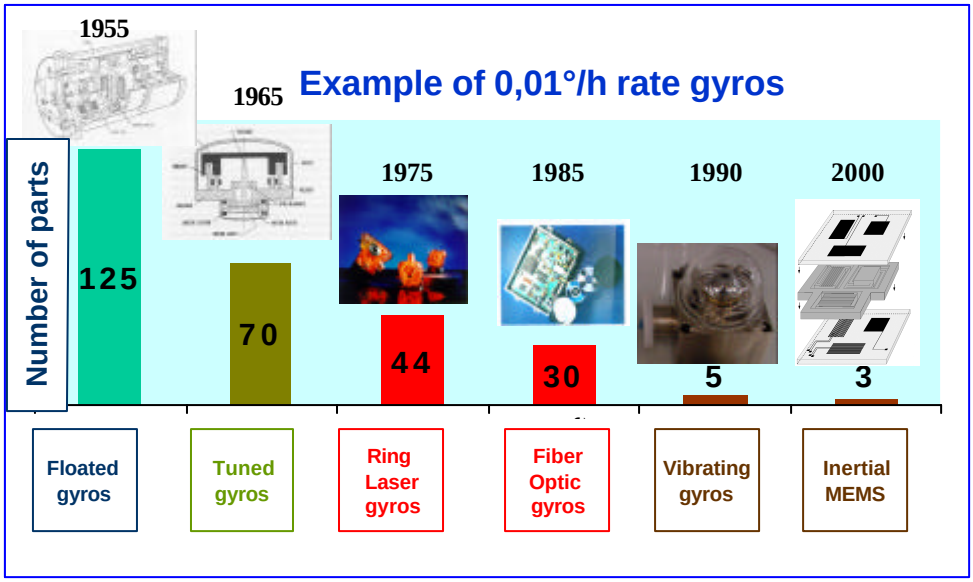


Fig.6: Rate gyros evolution- Physical principles and number of parts and micro mechanical

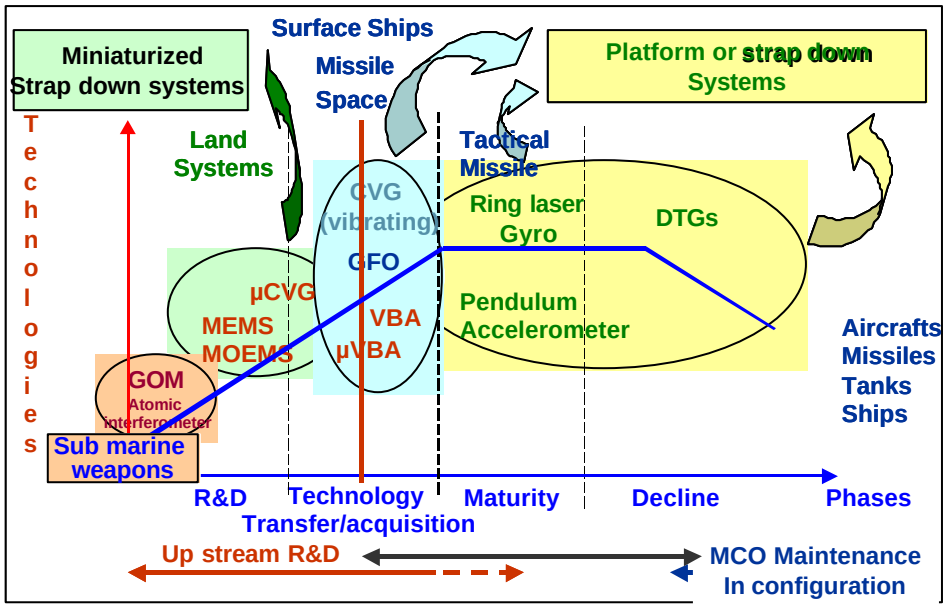


Fig. 7: Overview rate gyros in 2002: the curve of R&D/maturity/decline
(Courtesy of DGA E. Pleska)

In the sense of funding new technologies and principles for miniaturized IMUs, the Department of Navigation at STTC is leading research in

- Microsystems & micro technologies: MEMS, MOEMS, vibrating MEMS, thermo-mechanical MEMS
- Functional materials including Hardened Optical Fiber, Ceramic & active monocrystals, Nanograin metals
- Inertial sensors including : Vibrating technology, Atomic interferometry, Algorithms & signal conditioning, Kalman filtering, Particular filtering

The structure of research and development of MEMS sensors in France is based on upstream R&D at research Centers in collaboration with companies having the expertise of "sensorists" such as Thales Avionics, Sagem and Auxitrol. The next sketch shows the main partners involved in this development including the MEMS foundry companies able to insure the MEMS manufacturing

ONERA is the research center attached to DGA. Its main activities belong to inertial sensors accelerometers and gyrometers. Since the beginning of the 90's ONERA has being involved in development of high accuracy accelerometers using quartz microtechnology. The first success was the development of a VBA Vibrating Beam Accelerometer in a dual differential chip mode mounting. This know-how has bean transferred in the mid of the 90's to Sagem and Thales Avionics (former Thomson CSF/Sextant Avionique) Now this MEMS accelerometer has been introduced inside IMUS for military applications.

CEA-LETI is one of the most advanced research center in Europe for R&D on microelectronics as well as MEMS from sensors, actuators, MOEMS, RF MEMS and bi-MEMS. The aim of LETI is to develop and to transfer processes and components to industry. First comb drive accelerometer has been developed with Sextant Avionique in the mid of the 80's for military applications.

CNRS LPMO and IEF are more at the up stream R&D as academic centers. Their expertise is well established in the field of sensors and actuators in MEMS technology either silicon based or also micro-molding technique.

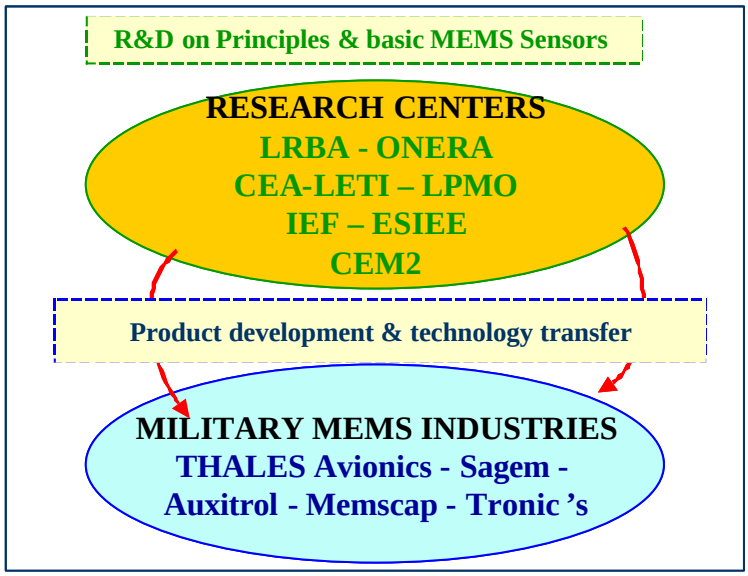
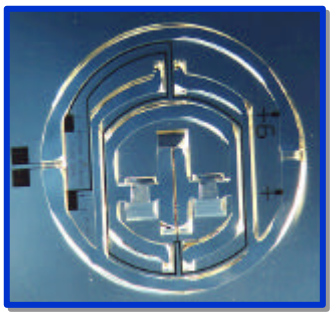
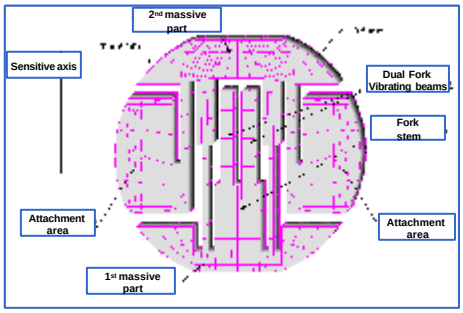


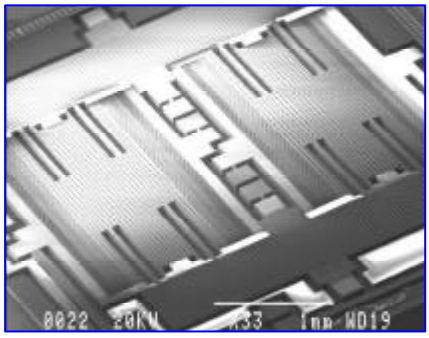
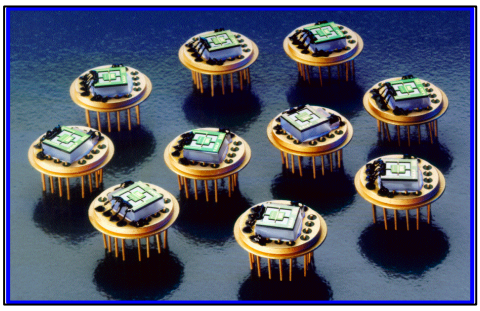
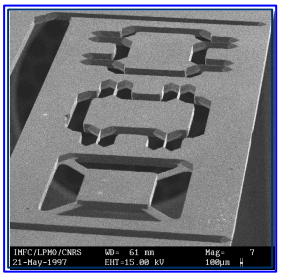
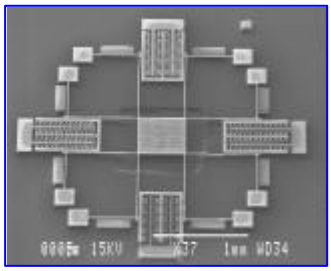
Fig. 8: Structure of the MEMS R&D in France: from Research Centers to products

Generally in France, the main developments in R&D for MEMS sensors, involve both research centres and industry, a mandatory rule of the DGA through its main R&D programs that are upstream R&D such as PEA (as Programme d'Etudes Amont) and more closer to the industrialization DMDP (Développement Multi-Programmes pour la Diminution des Prix)

Some examples of such development are given in the following table including pictures with some characteristics of principle, material, and data.

Table 2: from R&D to components: examples of developments with research centers

ONERA Quartz VBA accelerometer	**ONERA** Quartz micro gyro: in progress
	
- Development 1990-1995 - Dual chip in differential mode - Bias Stability : 120 µg in run - Bias Stability : 350 to 600 µg long term - Linearity : 10^{-4} F.S. (Modeled) - Tech. transfer to SAGEM & Thales	- Range: ± 100°/s - Bias: <0,01 °/s tbd - Volume: tbd - Tech. transfer to be done in the future

	**CEA-LETI: MEMS sensors** Silicon micro gyro: in progress - THALES Avionics Gyrosil - Process development in DRIE - High thick SOI bulk - Range: ± 100°/s - Bias <0,01 °/s (short term: 24 hours) - Bias <0,2 °/s (long term: 1 year) - Volume: MEMS sensing <1 cm^3 - Volume: <10 cm^3
	**CEA-LETI: MEMS sensors** SOI pressure sensor: 1995 –THALES Avionics P 92 piezoresistive –Sensor development –Technology transfer to the THALES Foundry
	**CNRS/LPMO** **3** axis accelerometer - Measured performance 1st-2nd– 3rd axis - Measurement range: > ±1 g - ~ ±0.8g - Resolution: 160- 40 µg/ $Hz^{1/2}$ - Resonance frequency:460 Hz - 436 Hz - Mechanical sensitivity: 1.17 –1.3 µm/g - Q factor: 9 - 8
	**CNRS/LPMO** 2 axis micro-gyrometer –Quartz technology –Development in progress –Performances: confidential
	**IEP: Institut d'Electronique Fondamentale** Micro-molded or micro-electroforming micro gyro:– 1 or 2 axis – Electro thermal servo loop control – Range: ± 100°/s to ± 10000°/s – Bias: <0,01 °/s/ to 0,1 °/s tbd – Volume: tbd – in progress

4.0 Air Data & MEMS pressure sensors: tables and Roadmaps

The typical Air Data systems consist of: **ADM** Air Data Module, PMU Pressure Measurement Unit, PTMU : Pressure Temperature Measurement Unit & ADC Air Data Computer.

MST/MEMS based silicon pressure sensors are being introduced for all new programs including retrofit and MLU Mid Life Upgrade of the aircraft.
In this domain, the key component required for primary Air Data systems are the pressure sensor. The major specifications to reach is 10^{-4} F.S. all errors included of the maximum altitude range (30 000 feet for a civil aircraft and 60 000 feet for a fighter) This range of accuracy is obtained by MEMS resonant beam principle, while piezoresistive gauges MEMS are limited to 2 to 5.10^{-4} F.S.

Thales Avionics is one of the leaders in primary Air Data systems. First applications were qualified for commercial avionics large aircraft: Airbus, Boeing and commuters Canadair – Bombardier as well as military applications in the beginning of the 2000's for Rafale fighters and Eurocopter Tiger military helicopter.

Examples of high accuracy 10^{-4} F.S. MEMS pressure sensors that are currently used in Primary Air Data systems are shown here after, in the following pictures. These MEMS pressure sensors equip both all Airbus and Boeing 777, 737-500 to 800, and Rafale fighter.

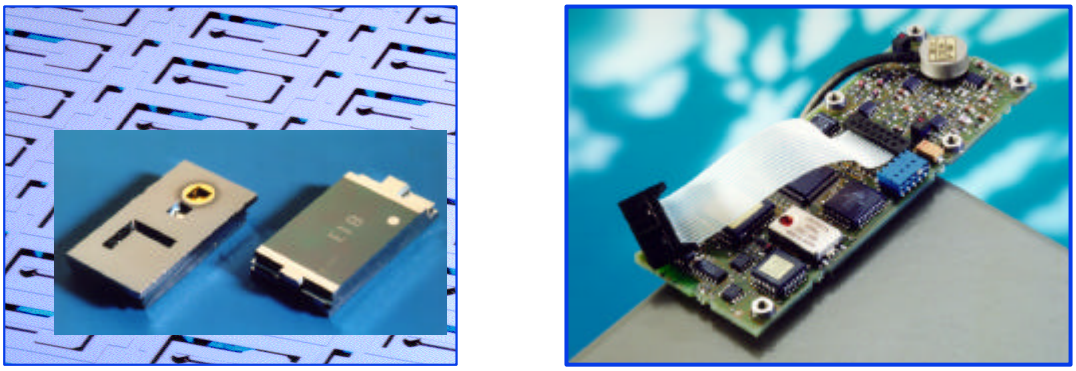


Fig. 9: resonant MEMS pressure sensor: wafer & cell & 10^{-4} FS ADM Primary Air Data Module *(Courtesy of THALES Avionics)*

Examples of mid accuracy 2 to 5 10^{-4} F.S. MEMS pressure sensors from MEMSCAP AS that are currently used in primary and secondary Air Data systems are shown in the next pictures.

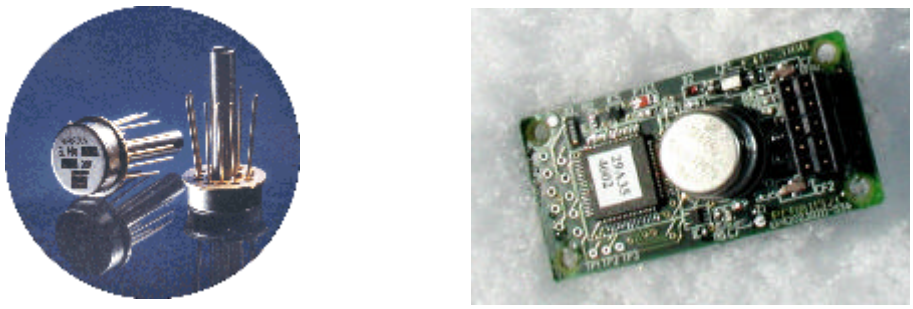


Fig. 10: left: 5.10^{-4} F.S. piezoresistive silicon MEMS pressure sensor cells. Right: 2 10^{-4} F.S. Air Data Module TP 3000 pressure sensor *(Courtesy of MEMSCAP)*

These MEMS pressure sensors equip both all-civil and military aircraft.

The following table 3 shows the status of the main pressure sensors manufacturers for aeronautics applications, including Air Class A for primary Air Data, Air Class B as secondary Air Data system. The table presents also the status of pressure sensors for Engine control with 3 classes for high temperature and high pressure as well as accuracy.

Table 3: status of the pressure sensors industry for aeronautics and defense. Evolution from electromechanical towards MEMS technology.

		Air Cl A	Air Cl B	Engine Cl A	Engine Cl B	Engine Cl B
	Performances	10^{-4} F.S. 3 bars -125°C	5.10^{-4} F.S. 3 bars -125°C	10^{-4} F.S. 60 bars-150°C	5.10^{-4} F.S.. 60bars-200°C	5.10^{-4} F.S.. 100bars-600°C
Quantity/year	**EU**/*USA*	**4000**/*7000*	**2500**/*3000*	**8000**/*12 000*	**2000**/*3000*	**2000**/*3 000*
Electro Mechanical technology	**Resonant quartz**	**Thales Avio.**				
	Vibrating cylinder	**Weston**	**Smiths**	**Weston**	.	.
MST/MEMS Micro technology	**Silicon gauges**	*Honeywell*	**Thales Avio. Memscap** *Kulite*	**Weston Lucas**		
	Silicon/capacitive		*Collins Rosemount*	*Hamilton Standard*	*Hamilton Standard.*	
	Silicon vibrating	**Thales Avio. GE/Druck**	**Thales Avio.**			
	SiC Gauges				*Honeywell*	*Kulite*
	SOI Gauges		**Thales Avio.** *Kulite*	*Kulite*		**Thales Avio.** *Kulite*
	Technology 2000			**Technology 2002-05**		

A roadmap for the future of high temperature pressure sensors has been established within the Task force and highlight the challenges for achieving 600ºC for integrated pressure sensors inside the P3 engine chambers. This demonstrates the limits of today materials for next generation of pressure sensors.

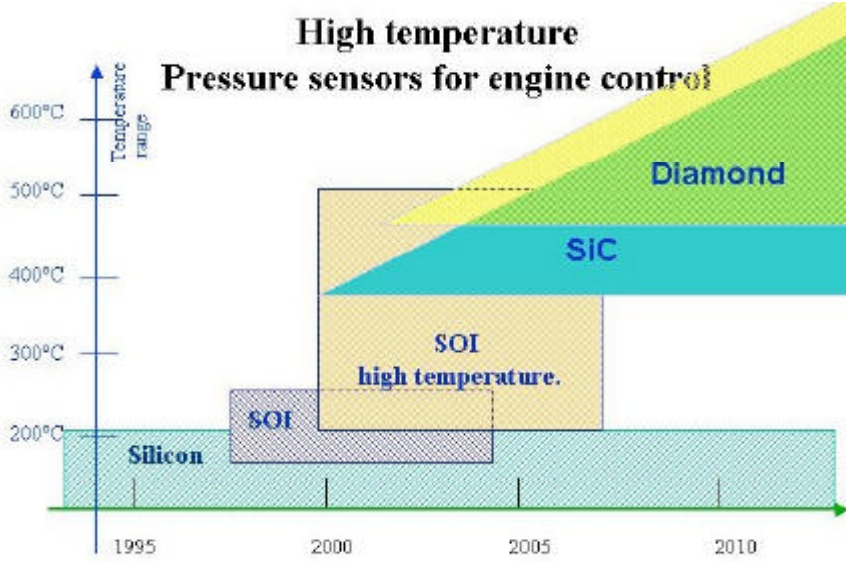


Fig. 11 Roadmap of materials for high temperature pressure sensors.

5.0 Navigation and Inertial Measurement Unit

Inertial systems, can be classified into two main subsystems:

IRS (Inertial Reference Systems) are basic systems for civil aircraft, fighters and military transports. High accuracy RLGs of 0.001 deg/hour are needed or hybridization GPS with FOGs (Fiber Optic Gyros) give the same IMU class.

To date, inertial sensor rate gyros are based on optical RLGs (Ring Laser Gyros) and accelerometers or electromechanical systems. Future systems will still require high performance gyros. High performance MST/MEMS accelerometers are, currently, being developed and will be used in future systems after improvements of performances.

AHRS (Attitude & Heading Reference Systems) are basic systems for advanced /basic trainers and military helicopters (also cruise missiles use such inertial systems). Rate gyro accuracy is 0.01 deg/hour given by RLGs or FOGs, MEMS accelerometers are being used now.

The Task Force "MEMS 2001+" defined as a priority, the analysis of the IMUs and basic components as accelerometers and rate gyros. Different roadmaps have been drafted to classify the IMUs and to focus on the needs of systems, sub-sytems components and finally to look at the specific MEMS components roadmaps.

The next sketch precise the development stages of MEMS components form the beginning of the development, the time when they can be introduced in IMUs and the evolution of the IMUs volume. This takes into account MEMS and optical gyros.

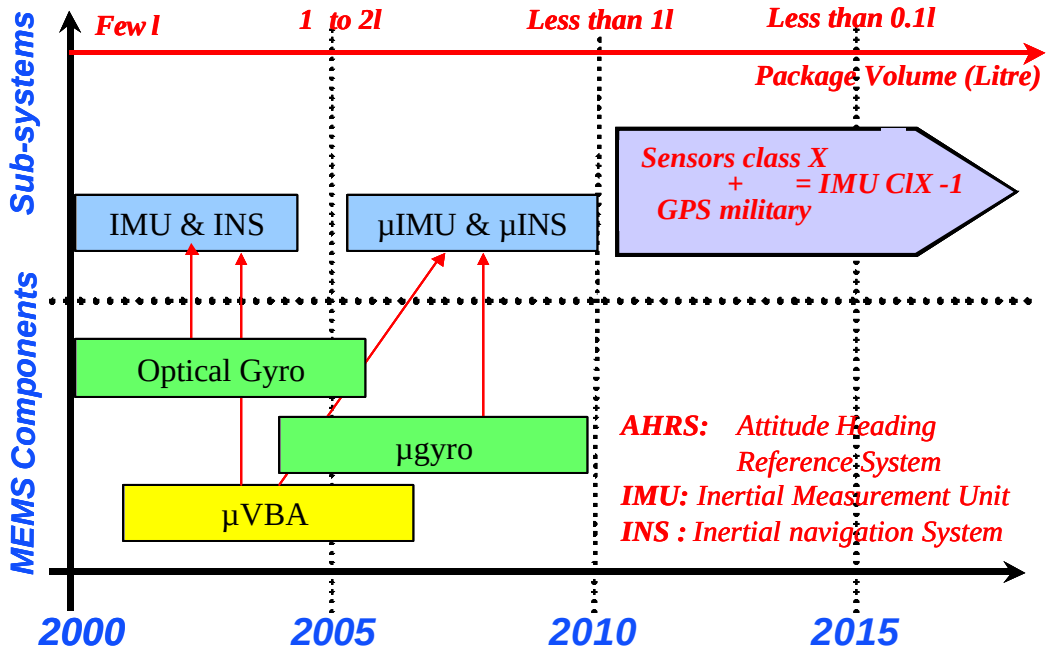


Fig. 12 Roadmap for AHRS, IMU, INS *(source Task Force MEMS 2001+)*

The definition of IMU class is illustrated in the next schematic. It gives the status and specs for IMUs class. The accuracy is based on the combination of accuracy of accelerometers – Z-axis – as well as the rate gyros performances – X-axis. It illustrates also the fact that a lower

class IMU like “class X” could be upgraded by the hybridisation with GPS even commercial class, such as sensors Class X + GPS = IMU Class X-1. This results in a domain of technologies that is accessible and could lead to fort risk of proliferation.

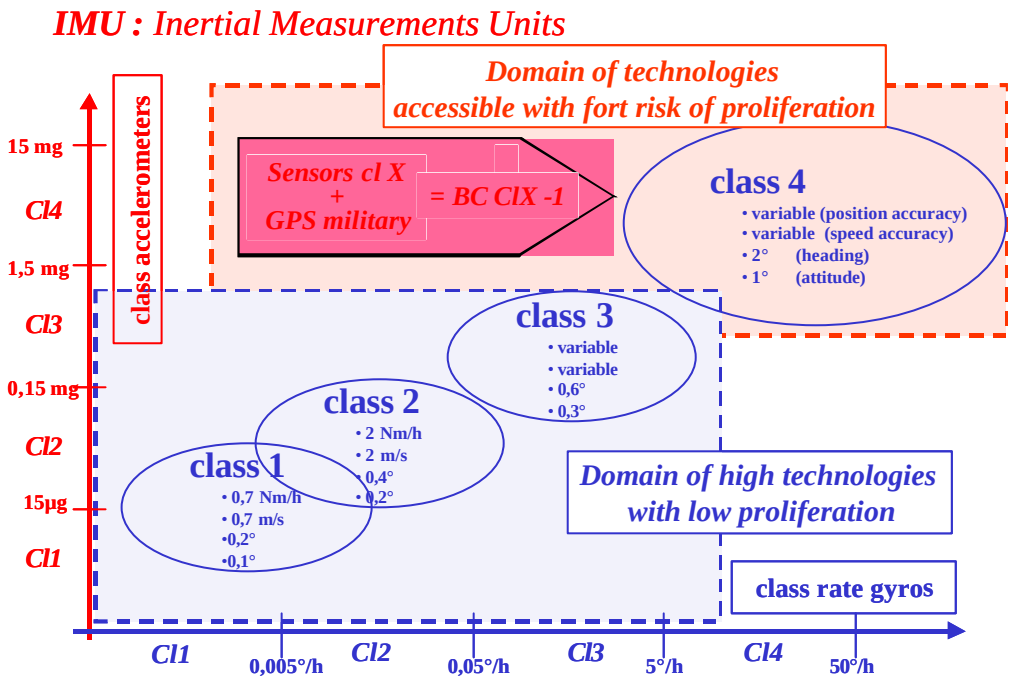


Fig. 13: IMUs class versus rate gyros class and accelerometers class

Since the early 90’s, DGA has funded different programs of R&D to develop miniaturized basic sensors such as accelerometers and now micro rate sensors. In 1997 DGA has launched a program for the development of a generic basic family of IMUs for multiple applications IMU

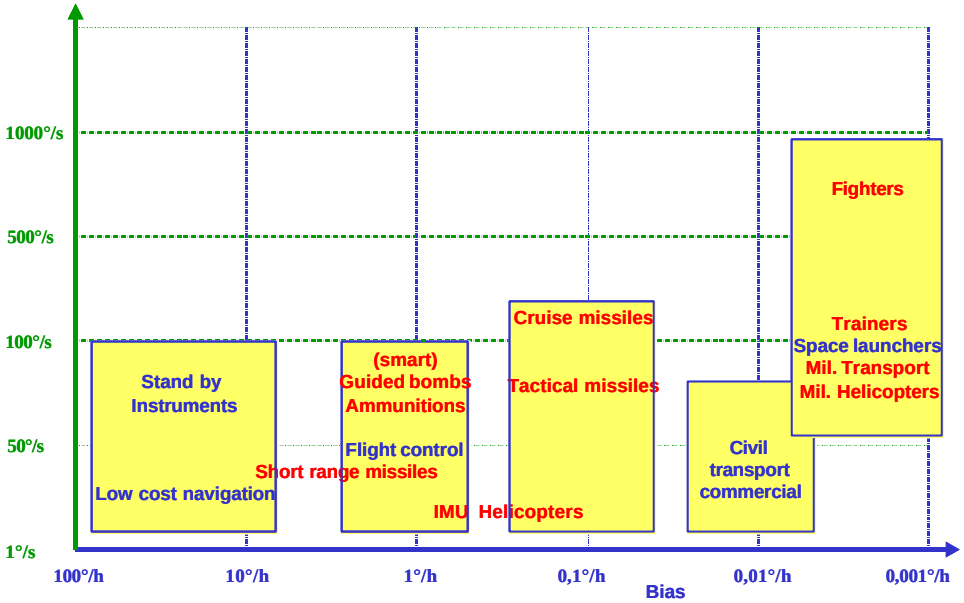


Fig. 14: rate gyros performances versus applications

sub-systems: land vehicles, AHRS, ISIS. The domains of utilization are described in these charts 13 & 14 giving the bias versus the range for gyros and the perfomances at 3 s versus the range for accelerometers.

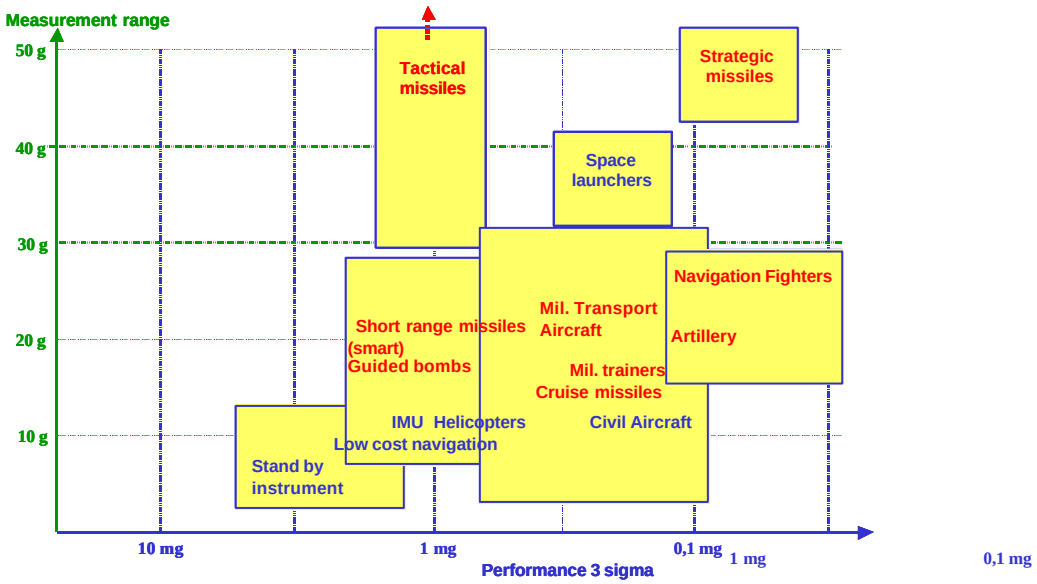


Fig. 15: accelerometers performances versus range and application domains.

The example of hybridization is shown on the upper part of the figure 12. The combination of Sensors of Class X and hybridization with GPS tends to an IMU of Class X-1. This will allow the use of less accurate accelerometers and rate gyros enabling the utilization of MST/MEMS for each sensor or combined accelero/gyro multisensors systems.

5.1 Accelerometers: roadmaps and industrial status

At this stage the task force "MEMS 2001+" decided to analyze the roadmaps of each basic component in order to know if such class or hybridization would be possible and at what timescale. The Task Force "MEMS 2001+" has reviewed and updated the previous roadmap issued from Sextant Avionique (now Thales Avionics) and used within different

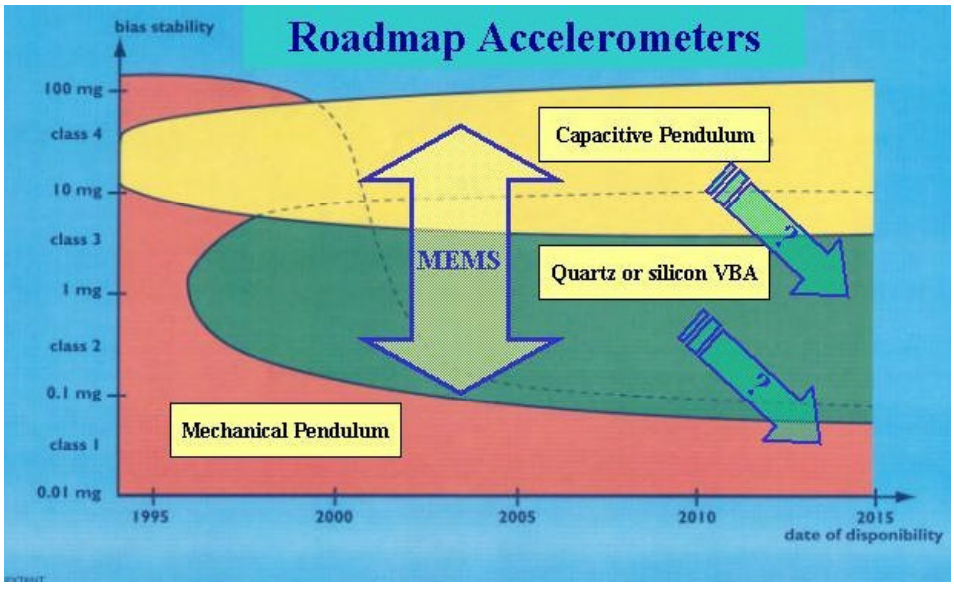


Fig. 16: roadmap accelerometers technology versus class versus time. *(Courtesy of SAGEM & THALES Avionics)*

programs and projects such as BRAMMS. The graph on figure 15 gives the roadmap for accelerometers and the table 4 the who's who of accelerometer manufacturing in this domain.

Table 4: status of the accelerometer industry for aeronautics and defense. Evolution from electromechanical towards MEMS technology.

Accelerometers in Aerospace & Defense

		CL 1	CL 2	CL 3	CL 4
	Performances	10^{-5}	10^{-4}	10^{-3}	10^{-2} 10^{-3}
Quantity/an	**EU**/*USA*	**1000**/*5000*	**3000**/*9000*	**5000**/*10 000*	**10000**/*30 000*
Electro-Mechanical Technology	**Pendulum**	**Thales Avio.** *Honeywell Geospace*	**Thales Avio.** *Honeywell*	**Thales Avio.** *Honeywell*	**Thales Avio.** *Honeywell*
	Capacitive Quartz	*Honeywell*		*Honeywell Systron Do.*	*Syston Do.*
	Quartz VBA	**Sagem**	**Sagem** *Kearfott*	*Honeywell*	*Honeywell*
Micro technology MEMS	**µVBA silicon/quartz**	**Thales Avio. Sagem** *Honeywell*	**Thales Avio.** *Honeywell Kearfott*	**Thales Avio.**	**Thales Avio.** *Honeywell*
	Silicon capacitive		*Endevco*	*A.D.*	**Sagem - Colibrys** *N.Grum.*
	Quartz capacitive			**Thales Avio.**	
	Technology 2000		**Technology 2002-05**		

5.2 Gyrometers: roadmaps and industrial status

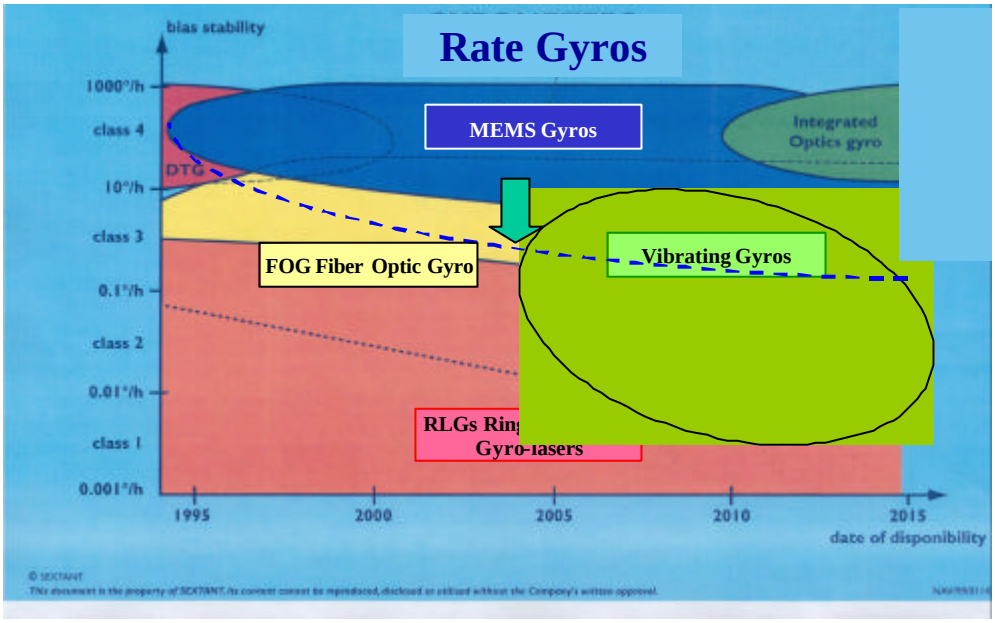


Fig. 17: roadmap rate gyros class versus technology *(Courtesy of SAGEM & THALES Avionics)*

Table 5: status of the rate gyros industry for aeronautics and defense. Evolution from electromechanical towards MEMS technology.

Rate gyros in Aerospace & Defense

		CL 1	CL 2	CL 3	CL 4
	Performances	0,001°/h	0,01°/h	0,1°/h<10°/h	> 10°/h
Quantity/an	**EU**/*USA*	**1000**/*5000*	**3000**/*9000*	**5000**/*10 000*	**10000**/*30 000*
Electro-Mechanical Technology	**RLG** Ring Laser Gyro	**Thales Avio.-Sagem-BAe** *Litton Honeywell*		**Thales Avio. Sagem** *Litton Honeywell*	←
	HRG Hemispheric Ring Gyro		*Litton (Delco)*	*Litton (Delco)*	
	FOG Fibre Optic Gyro		**Sagem-Litef** *Litton-Honeywell*		←
	Vibrating Structure			**BAe- Bosch**	*Systron Do. Condor*
Micro technology MEMS	**IOG** Integrated Optic Gyro				**Thales Avio.**
	Vibrating silicon		*Endevco*		**Bosch - BAe Thales Avio.** *Allied -Kearfott Endevco.*
	Vibrating Quartz			**Thales Avio**	
	Technology 2000		**Technology 2005**		

In MEMS accelerometers, some achievements have been done during the late 90's; such as this high accuracy accelerometer designed by the ONERA lab in France and transferred to both SAGEM and THALES Avionics companies. This MEMS accelerometer is utilized in high end IMUs and for both civil and military applications.

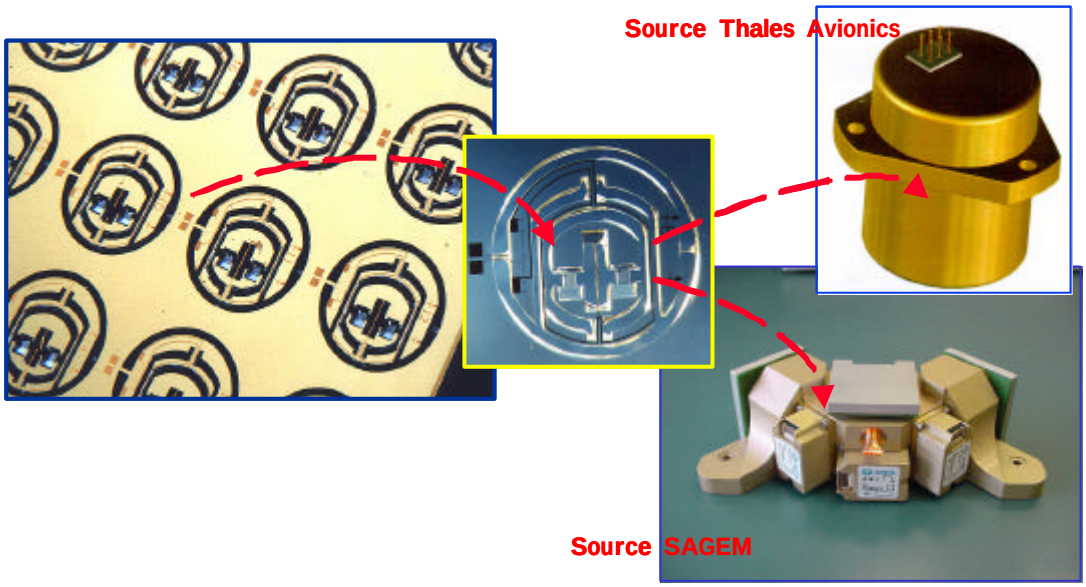


Fig. 18: Dual differential quartz resonant beam accelerometer integrated in a single component (Thales Avionics Top right) and in an IMU for military applications (Sagem bottom right)

In rate gyros, even developments are being carried out in MEMS technology, today just low accuracy rate gyros are foreseen mainly for mid performances applications, such as Integrated Stand-by Instruments and short range navigation systems for defence.

5.3 MEMS: the challenges and threats in design/manufacturing

The Task Force has addressed two main topics that are related to the challenges of mastering the different stages of MEMS: design, simulation, manufacturing:fornt end and back end, packaging, calibration and test.

The conclusions of the group were established in relation with the performances of the MEMS. Low performances MEMS allow the possibility of a COTS approach. (Components of the Shelf), MEMS with mid performances and also MEMS with high performances require different methodologies from one company to the other.

MEMS low performances: « COTS »: there is the possibility to buy & to design around components from COTS. The risk is the proliferation in military applications. The company at this level is operating as a fabless company.

MEMS mid performances: there is the possibility to conceive the design of specific component and to sub-contract the MEMS device to open foundries.
In this model the knowledge of the company is to master the sub-system level that means to master the fundamental of the technology by internal R&D in MEMS. In this case the risk of proliferation is minimized.

MEMS high performances: this is the domain of the expertise of the system manufacturer. The enterprise's strategy is to be captive in design and manufacturing: this is the IDM model, Integrated Devices Manufacturing. In this case it is difficult to sub-contract to open foundries, but the main issue is to be still able to invest in the latest generation of equipment and laboratories that means to have access to the most advanced material & process? In this case the risk of proliferation is low.

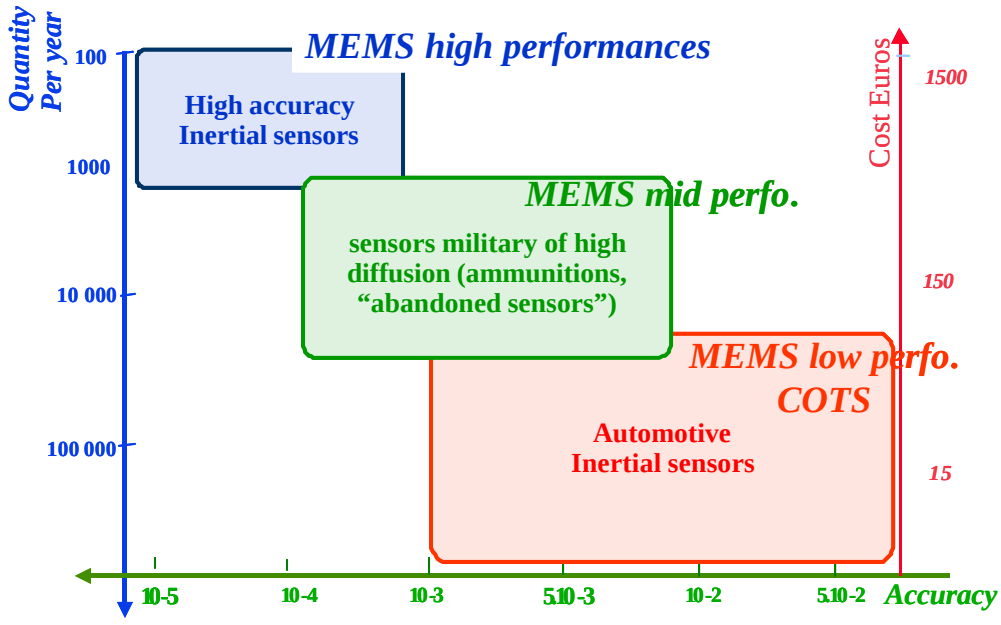


Fig. 19: inertial MEMS and dual applications/COTS

This graph of figure 19 show the case study of inertial sensors with 3 different levels of performances: low, medium and high accuracy.

6.0 Conclusions

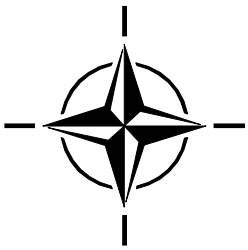
The result of the task force is manifold. It has been considered that establishing a consensus the main expert French companies in defense was very valuable for road mapping, establishing the priorities in R&D for miniaturized systems and sub-systems. Also the joint work with the DGA and the corroboration of their mid to long term plan has generated good exchanges between the members of the task Force.
Finally the status of the industrial MEMS manufacturing has been considered as a big issue for insuring the future of MEMS manufacturing in defense applications. This belong s to the strategy of the defense company but also it is linked to the existing today MEMS foundries in France. This point was also a question mark for all the companies willing to maintain a Fablilte model so minimizing the investments costs but willing still to master the noble part of the MEMS sensors

7.0 Acknowledgments

The authors would like to thank all the members of the MEMS 2001+ task Force for their contribution in the work done and especially for this NATO paper,

DGA/STTC/DTGN:	Eric PLESKA
MBDA F:	Jacky GROSSET
SAGEM SA:	Jean Michel CARON
THALES Avionics;	Charles DUSSURGEY
CEA-LETI:	Gilles DELAPIERRE
CEM2/Montpellier:	André BOYER
IEF:	Alain BOSSEBOEUF
LPMO:	Michel de la BACHELERIE
ONERA:	Pierre TOUBOUL

✧✧✧✧✧✧✧✧✧✧✧✧



Silicon IMU for Missile and Munitions Applications

Dr J. Richard Fountain
Senior Consultant Engineer
BAE SYSTEMS
Clittaford Road
Plymouth PL6 6DE
UNITED KINGDOM

ABSTRACT

This paper considers the silicon gyro based Inertial Measurement Unit (IMU) developed by BAE SYSTEMS, which is presently being tested on a number of munitions and missile programmes, with the requirement to operate under high dynamic range and high roll rate conditions. The BAE SYSTEMS silicon IMU design incorporates a rotated axes sensor set to maintain manageable rates on the sensing axes, while achieving the desired performance over the full rate range of the platform. The paper examines the construction and definition of the rotated sensor axes configuration and the approach taken to characterise and calibrate the IMU.

1.0 INTRODUCTION

A number of application areas in guided munitions, projectiles and missiles have requirements for operating at relatively high rates (typically, above 5 Hz or 1800 deg/s) in one particular axes, with a reduced rate range in the other two axes. Usually, for these type of platforms, this is coupled with a requirement for small size, low cost and high shock survivability, which steers the design towards using the latest silicon Micro-machined Electro-Mechanical Systems (MEMS) inertial sensor technology. The large number of expected units to be produced also requires that the design and manufacturing and test processes must incorporate the need for high rates of unit production.

The IMU developed by BAE SYSTEMS uses silicon gyros and accelerometers and is referred to as the Silicon Inertial Measurement Unit (SiIMU®). The BAE SYSTEMS SiIMU® design uses a rotated axes sensor set to achieve the required platform performance, while maintaining manageable rates on the sensing axes.

1.1 SiIMU® Construction

There are three sensor axes which are in the form of a right handed orthogonal set, rotated relative to the body axes. Each sensor axis has an associated set of sensors comprising a gyroscope, gyroscope temperature and an accelerometer (including temperature sensor), which sense along each of the sensor axes.

Three body axes are defined for the SiIMU® which also form a right handed orthogonal set, defined as Roll (X), Pitch (Y) and Yaw (Z).

The SiIMU® is a hermetically sealed device, with upper and lower covers welded to a mounting flange.

The electrical interface is via a pin-array header and is designed to be connected to a host system using a customer supplied mounting flexi-rigid. For operation and survivability and high g-levels, there is an option to pot the sensor cluster. The layout of the major components is shown in Figure 1.1.

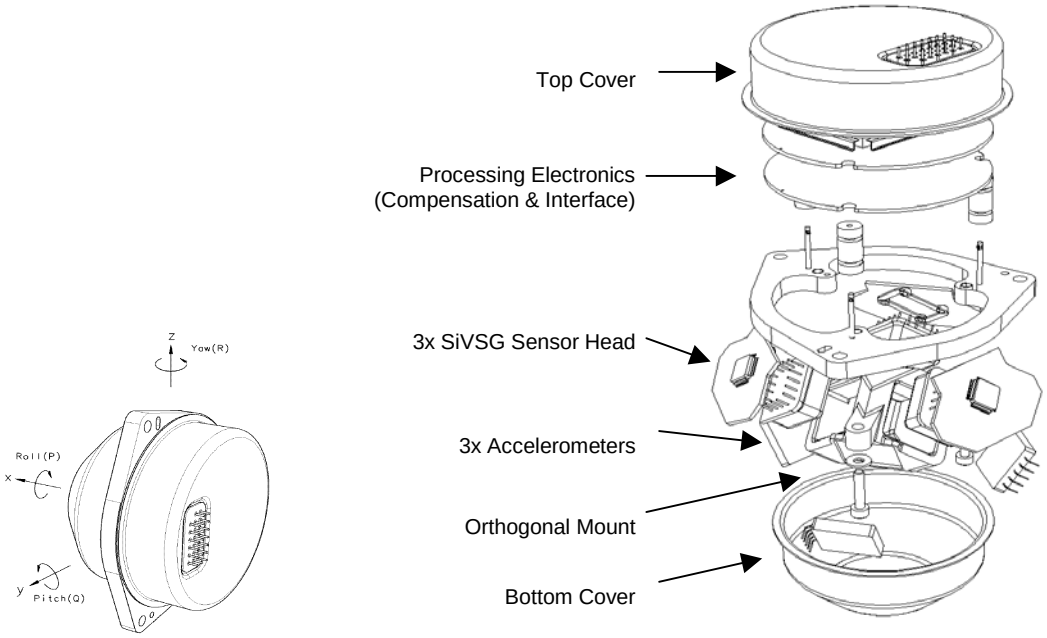


Figure 1.1: BAE SYSTEMS SiIMU® Component Layout.

1.2 SiIMU® Specification

A typical specification of the SiIMU® is given in the table below, but the performance and rate and acceleration ranges can be tailored to meet specific platform requirements.

Parameter	Rate	Acceleration
Range (nominal, for zero on other two axes) (other ranges available)	±1000 deg/s (X axis) ±720 deg/s (Y, Z axis)	±50 g ±34g
Bias Repeatability (run-to-run, etc) g Sensitivity	 200 deg/hr 1σ 7 deg/hr/g 1σ	 20 mg 1σ
Scale Factor Scale Factor Error Scale Factor Linearity Error (>110 deg/s, <-110 deg/s) ±110 deg/s	 500 ppm 1σ 500 ppm 1σ 200 deg/hr 1σ	 1000 ppm 1σ 1000 ppm 1σ
Misalignments	2 mrad 1σ	2 mrad 1σ
Noise In Band @ 1000Hz data rate Random Walk	 8 deg/s rms ARW 1 deg/√hr	 8 mg rms VRW 1 m/s/√hr
Bandwidth (-90 deg phase shift)	75 Hz	75 Hz
Start-Up Time	1 s max	1 s max
Mass	250 gm	
Electrical Supply Voltage Power Consumption	 +15V and +5V DC 5 VA	
Environment Temperature Vibration (operational) Shock	 -40 deg C to +72 deg C 18 g rms (20 Hz to 2 kHz) 100 g (11 ms, ½ sine)	

The SiIMU® is presently being tested on a number of munitions and missile programmes, which require the unit to survive very high g-levels (accelerations) and operate under high roll rate conditions.

In 2002, a BAE SYSTEMS SiIMU® successfully aided the guidance of an Extended Range Guided Munition (ERGM) round, 39 nautical miles to its designated target area at White Sands Missile Range, NM. The SiIMU® was used to establish the orientation of the projectile immediately after launch, enabling GPS satellite acquisition and provided inertial data for weapon guidance throughout the flight. The SiIMU® used in ERGM is a gun-hardened derivative of the BAE SYSTEMS generic SiIMU®, being extremely robust, having been demonstrated to survive shocks in excess of 20,000g.

BAE SYSTEMS were awarded a development contract from Saab Bofors Dynamics AB to enable the tailoring of a special-purpose Inertial Measurement Unit (IMU) for the Saab Bofors Dynamics MBT LAW anti-tank missile. The MBT LAW IMU is a derivative of the BAE SYSTEMS SiIMU®.

The SiIMU® has also been selected by Matra BAe Dynamics (MBDA) for the UK Block 2 Vertical Launch Seawolf missile programme and is due to be flight trialed in the near future.

2.0 ROTATED AXES DEFINITIONS

The inertial sensors, gyros and accelerometers, are arranged on the edges of a cube. This configuration defines an orthogonal axes set, the sensors being rotated from the vertical but the individual sensors are not skewed (a skewed arrangement has sensors that are not orthogonal). The geometry is shown in Figures 2.1a, 2.1b and 2.2 and the angle definitions are derived below.

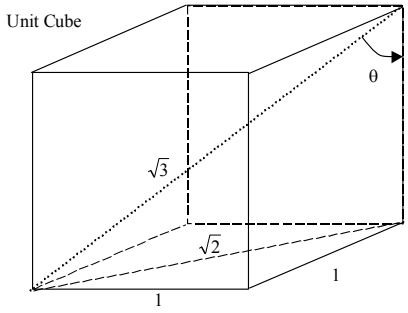


Figure 2.1a: The Unit Cube Dimensions.

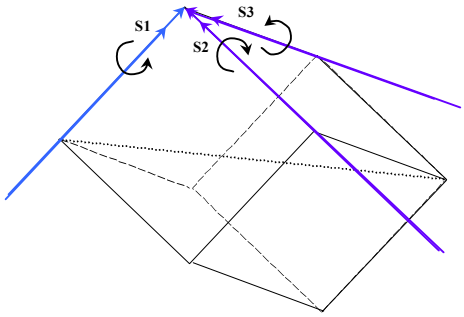


Figure 2.1b: Rotated Cube With Sensor Directions.

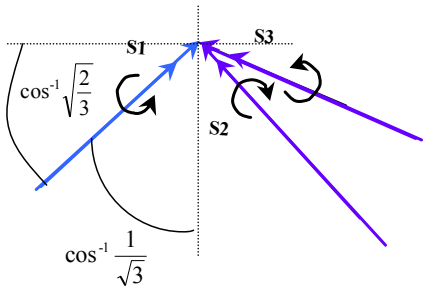


Figure 2.2: Sensors Vertical Angle.

2.1 Angles on the Rotated Cube

The sensors are skewed to the vertical by rotating about an edge, until the cross diagonal is horizontal, all sensors are then at an angle of 54.73 deg to the vertical and uniformly spaced at 120 deg in the horizontal plane.

Consider the unit cube (Figure 2.1a),

$$\text{Diagonal (face)} = \sqrt{1+1} = \sqrt{2}$$

$$\text{Cross Diagonal} = \sqrt{1+\sqrt{2}^2} = \sqrt{3}$$

$$\theta = \cos^{-1}\frac{1}{\sqrt{3}} \text{ , the angle to the vertical}$$

$$\theta = 54.7356 \text{ deg}$$

2.2 Sensor to Body Transformation – Direction Cosine Matrix

The inertial outputs from the SiIMU® are defined in the body axes, which for the rotated sensor SiIMU® do not correspond to a single sensor output. A transformation matrix is therefore required, the Direction Cosine Matrix (DCM), to convert and combine the sensor outputs into the body axes.

Defining an orthogonal body axes set X, Y, Z and corresponding orthogonal sensor axes set s1, s2, s3, as shown in Figures 2.3a and 2.3b , then the required DCM can be derived as follows.

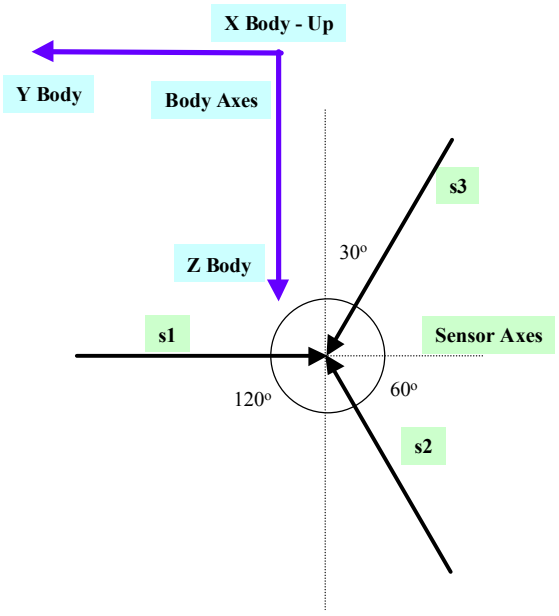


Figure 2.3a: Horizontal Sensor Configuration.

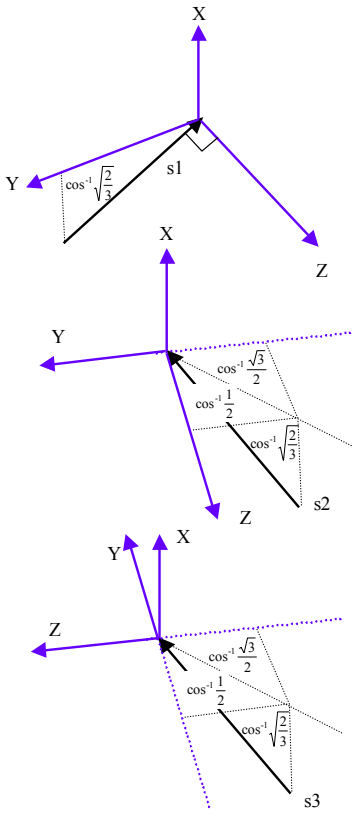


Figure 2.3b: Vertical Sensor Configuration.

Note: Sensor s1 is orthogonal to the Z axis.
Sensors s2 and s3 are at 30 deg to the Y axis in the horizontal plane.
All sensors are at $\cos^{-1}(1/\sqrt{3})$ deg to the X axis in the vertical plane.

From the diagrams in Figures 3a and 3b, the components of s1, s2 and s3 in the body axes are,

$$X_{s1} = s1\frac{1}{\sqrt{3}} \qquad X_{s2} = s2\frac{1}{\sqrt{3}} \qquad X_{s3} = s3\frac{1}{\sqrt{3}}$$
$$Y_{s1} = -s1\sqrt{\frac{2}{3}} \qquad Y_{s2} = s2\frac{1}{\sqrt{6}} \qquad Y_{s3} = s3\frac{1}{\sqrt{6}}$$
$$Z_{s1} = 0 \qquad Z_{s2} = -s2\frac{1}{\sqrt{2}} \qquad Z_{s3} = s3\frac{1}{\sqrt{2}}$$

This gives the transformation equation, sensor to body,

$$\begin{bmatrix} X \\ Y \\ Z \end{bmatrix} = \begin{bmatrix} \frac{1}{\sqrt{3}} & \frac{1}{\sqrt{3}} & \frac{1}{\sqrt{3}} \\ -\sqrt{\frac{2}{3}} & \frac{1}{\sqrt{6}} & \frac{1}{\sqrt{6}} \\ 0 & -\frac{1}{\sqrt{2}} & \frac{1}{\sqrt{2}} \end{bmatrix} \begin{bmatrix} s1 \\ s2 \\ s3 \end{bmatrix}$$

2.3 Configuration Characteristics

This rotated configuration has the following properties and characteristics.

- The X axis has the highest rate capability, which equates to √3 times the sensor rate. For example, if the gyro sensor has a full scale rate of 1500 deg/s, the X axis can measure rates up to 2598 deg/s (just over 7 Hz), for zero rate on the Y and Z axes.
- Common mode errors (for example, electronic bias) are added (weighted by √3) for the X axis, but are subtracted (eliminated) for the Y and Z axes.
- If the SiIMU® is used in an application where the same maximum rates or accelerations will occur simultaneously in all three axes, then the full scale range requirement of the sensors will be higher than for a standard (non-rotated) inertial sensor cluster.

3.0 CALIBRATION AND COMPENSATION

The raw (uncompensated) errors of the relatively low cost sensors used in the SiIMU® are such, that to achieve the required performance for missile and munitions applications, requires the calibration of the SiIMU®.

The following errors are required to be considered for the SiIMU®.

CALIBRATION

- Sensor Bias
- Sensor Scale Factor
- ‘g’ Dependency (Gyros)
- Axes Misalignment
  - Harmonisation
  - Axes Non-Orthogonality
- Account For –
- Size Effect (Accelerometers)
- Lever Arm (Accelerometers)

COMPENSATION

- Sensor Bias
- Sensor Scale Factor
- ‘g’ Dependency (Gyros)
- Axes Misalignment
  - Harmonisation
  - Axes Non-Orthogonality
- Size Effect (Accelerometers)

For the gyros, calibration over rate and temperature is required and for the accelerometers, calibration over acceleration and temperature is required.

3.1 Calibration

3.1.1 Calibration Method

The calibration data collection and coefficient calculation process is depicted in Figure 3.1.

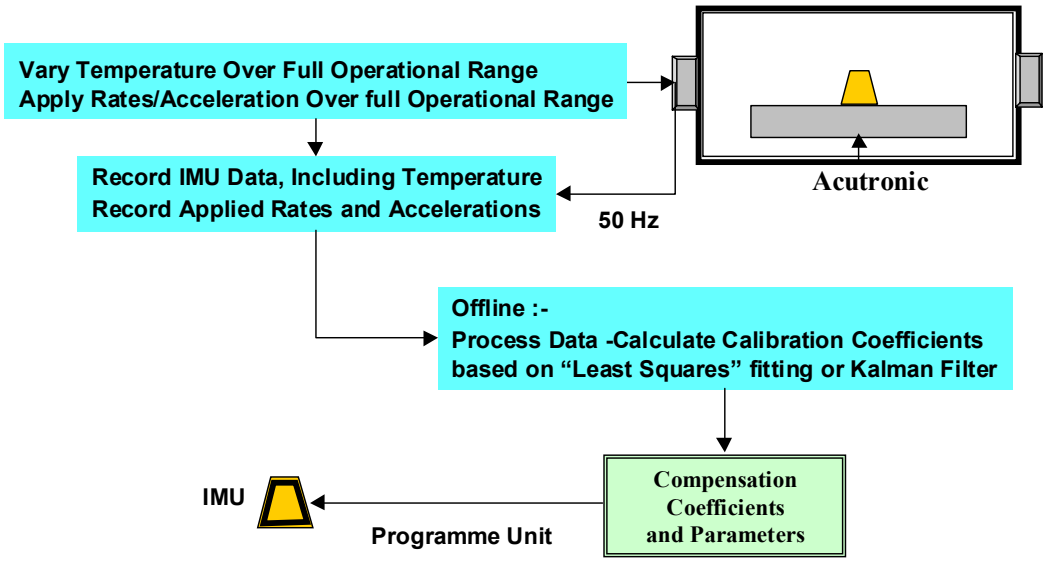


Figure 3.1: SiIMU® Calibration Method using Twin Axes Rate Table.

To fully characterise and thereby calibrate the SiIMU®, the equipment must be capable of applying maximum temperatures, accelerations and rates in at least two independent axes. One of the benefits of the skewed sensor arrangement, is that when mounted in its normal body orientation, all sensors will detect rate or acceleration by rotating or accelerating in one axis and it is therefore only necessary for one axis of the table to be capable of applying high rates or accelerations. Usually the axis around which the sensors are arranged symmetrically (the X-axis for the SiIMU®), would be aligned with the inner axis. The maximum rate requirement on the inner table will then equate to the maximum body rate and at this rate the sensors will also be subjected to the maximum rate.

A single axis rate table is not sufficient, since scale factor errors and misalignment effects need to be observable separately.

Although accelerometers can also be calibrated on a rate table (or centrifuge), up to their maximum acceleration range by applying the appropriate centripetal acceleration, the input axis must be rotated through 180 deg, to apply the opposite sign of acceleration to the sensors.

Using a twin axes rate table, the data from the SiIMU® is recorded during combined rate and temperature profiles. This data is then processed to generate the coefficients, used in compensation, for the SiIMU®.

3.1.2 Defining the SiIMU® Model

Calibration of the SiIMU® involves the calculation of the appropriate coefficients that relate to the derived model.

In general, the coefficient space can be defined by the Bivariate Taylor's series for scale factor, DCM (or misalignments) and bias as follows:

$$\dot{\theta} = \sum_{i=0}^{i=n} \sum_{j=0}^{j=m} \sum_{k=1}^{k=3} b_{ijkl} T^i \Omega_l{}^j r_k + b_l$$

$for\ l = 1,2,3$ (which defines the sensor channel)

Where: -

m,n = Maximum power in the series, for T and Ω

$\dot{\theta}$ = Measured Rate

T^i = Temperature

r_k = Input Rate (the programmed table rate)

$\Omega_l{}^j$ = Ideal output rate (in fact, only the measured rate is available)

b_{ijkl} = Calibration coefficients to be determined

b_l = Bias component

The bias component will itself have a number of coefficients and are usually calculated separately using static data.

A similar equation can be defined for the accelerometers.

For example, a typical model could include,

$$bias = b_1 + b_2 T + b_3 T^2 + b_4 T^3$$

$$rate_1 = b_{0011} r_1 + b_{1011} T r_1 + b_{0111} \Omega_1 r_1 + b_{1111} T \Omega_1 r_1 + b_{2111} T^2 \Omega_1 r_1 + b_{0121} \Omega_2 r_1 + b_{0131} \Omega_3 r_1$$

The last two terms in the above rate equation are misalignments, which may also require temperature dependant coefficients. The specific terms to include in the model can only be defined with detailed knowledge of the characteristics of the system.

Once the model has been defined the rate and temperature profiles must be considered to ensure observability of all the coefficients. Since the system is time varying due to variable rate, acceleration and temperature, the Stochastic Observability test applies, which is defined as follows (see [Gelb (1974), pp131]; [Maybeck (1979), p243]).

A sampled data system is said to be stochastically observable if the following condition is true,

$$0 < \sum_{i=k-N}^{k} \Phi^T(i,k) H^T(i) R^{-1}(i) H(i) \Phi(i,k) \leq \infty \quad \text{for } N > 0$$

For the case where R is a scalar and $\Phi = I$, H is a vector and this simplifies to : -

$$0 < \frac{1}{R} \sum_{i=k-N}^{k} H^T(i) H(i) \leq \infty \quad \text{for } N > 0$$

In the above equations, the variables relate to Kalman filter matrices and vectors (see Appendix A). The H matrix, known as the measurement matrix, consists of the model equations, calculated at each specific time point. Observability and thereby the ability to correctly identify the model coefficients, is only possible due to the fact that the H matrix is time varying (due to changes in temperature and rate).

3.1.3 Calculating the Calibration Coefficients

With the model defined and appropriate data from the SiIMU® collected during a calibration run (see section 3.1.1), the calculation of the coefficients is relatively straight forward. The standard method would be to solve the following equation.

$Ax = b$

where, A, is a matrix containing all the model parameters over the calibration period, each row being calculated at each test point, and is of dimension; number - of - test - points by number - of - coefficients (row, col).

x, is a vector of the (unknown) coefficients,

b, is the measured SiIMU output, rate or acceleration, at each test point.

The solution is,

$x = A^{-1}b$, where A^{-1} will in general be the Pseudo Inverse (A is normally a rectangular matrix and must have rank = number of coefficients, for a unique solution to exist)

An alternative to solving the above equation, is to use a Kalman filter, with the states the unknown coefficients and the model parameters forming the measurement matrix. This approach is especially recommended when the calibration method and profiles are being developed, since it provides a greater insight into how the estimation of the coefficients are converging as each test point is included. Refer to Appendix A, for a more detailed description of this approach.

3.1.4 Misalignments and Scale Factors – Specific Considerations

In higher accuracy inertial systems, it is usually the case that misalignment errors can be considered not to be significant when scale factor coefficients are being calculated (rates or accelerations applied on axis). However, this assumption cannot normally be made with lower accuracy systems, where the requirement to reduce manufacturing and components costs, can result in a wide tolerance on the mechanical accuracy of locating the sensors within the IMU cluster.

With this type of build, the sensor axes non-orthogonality errors can be relatively large (say, up to 2 deg) and the misalignment and scale factor errors cannot be easily differentiated.

The standard scale factor and misalignment equation (given below for the gyro), is no longer valid and should be replaced by a combined misalignment and scale factor (non-orthogonal) matrix.

$$\begin{bmatrix}\dot{\theta}_1\\ \dot{\theta}_2\\ \dot{\theta}_3\end{bmatrix} = \begin{bmatrix}sf_1 & 0 & 0\\ 0 & sf_2 & 0\\ 0 & 0 & sf_3\end{bmatrix}\begin{bmatrix}p\\ q\\ r\end{bmatrix} + \begin{bmatrix}0 & m_{11} & m_{12}\\ m_{21} & 0 & m_{23}\\ m_{31} & m_{32} & 0\end{bmatrix}\begin{bmatrix}p\\ q\\ r\end{bmatrix} = \begin{bmatrix}sf_1 & m_{11} & m_{12}\\ m_{21} & sf_2 & m_{23}\\ m_{31} & m_{32} & sf_3\end{bmatrix}\begin{bmatrix}p\\ q\\ r\end{bmatrix}$$

where, sf_1, sf_2, sf_3 are the scale factors

m_{11}, m_{12}, etc, are the axes misalignments

$\dot{\theta}_1, \dot{\theta}_2, \dot{\theta}_3$ are the rates in the actual gyro axes

p,q,r are the true inertial rates

The non-orthogonal matrix is given by,

$$\begin{bmatrix}\dot{\theta}_1\\ \dot{\theta}_2\\ \dot{\theta}_3\end{bmatrix} = \begin{bmatrix}sf_1 & 0 & 0\\ 0 & sf_2 & 0\\ 0 & 0 & sf_3\end{bmatrix}\begin{bmatrix}d_{11} & d_{12} & d_{13}\\ d_{21} & d_{22} & d_{23}\\ d_{31} & d_{32} & d_{33}\end{bmatrix}\begin{bmatrix}p\\ q\\ r\end{bmatrix} = \begin{bmatrix}sf_1 d_{11} & sf_1 d_{12} & sf_1 d_{13}\\ sf_2 d_{21} & sf_2 d_{22} & sf_2 d_{23}\\ sf_3 d_{31} & sf_3 d_{32} & sf_3 d_{33}\end{bmatrix}\begin{bmatrix}p\\ q\\ r\end{bmatrix}$$

where, d_{11}, d_{12}, etc, are the DCM coefficients which relate to the non - orthogonal axes set

In this case the scale factor and misalignments cannot be separated but can be calibrated as a combined set. In the above equation no assumptions of small angles has been made and it could therefore be used to represent the full body to sensor transformation DCM of the skewed axes IMU.

3.2 Compensation

Compensation is the process of correcting errors in the SiIMU® and runs in real time in the operational software. It must match the method used for calibration. Figure 3.2 shows the compensation process (compare this with Figure 3.1).

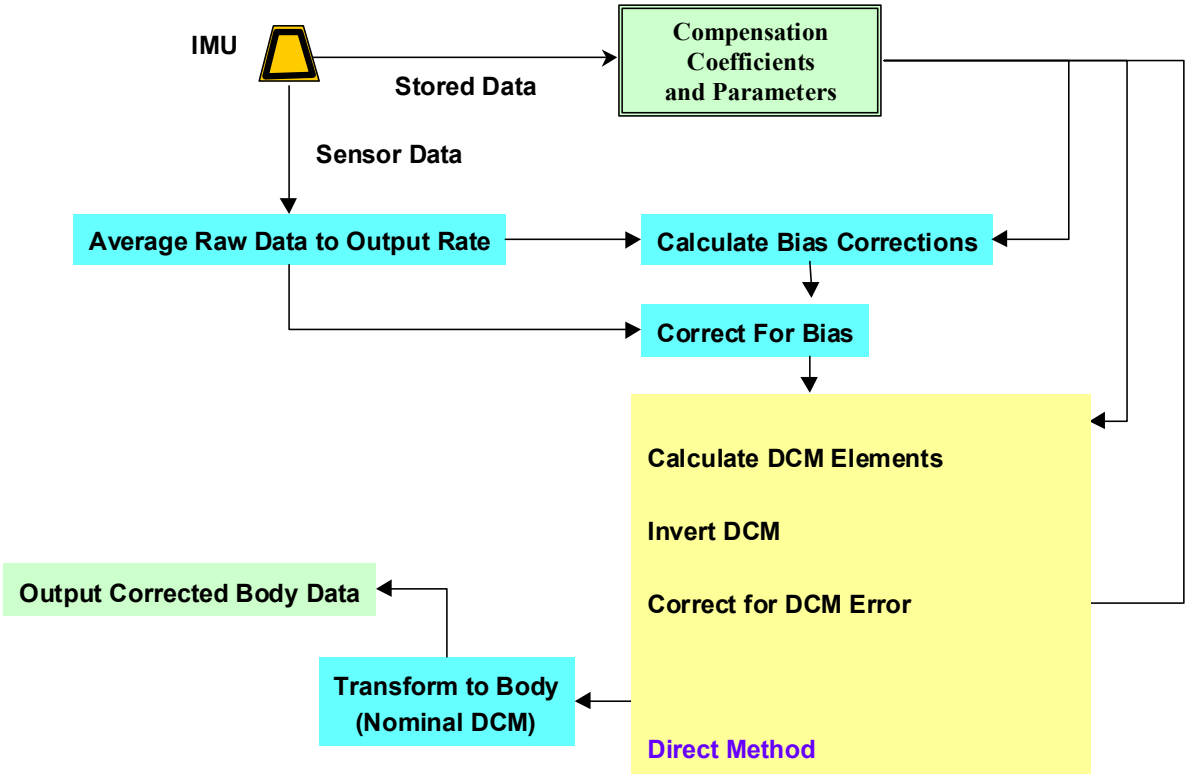


Figure 3.2: SiIMU® Real-Time Compensation Method.

In Figure 3.2, data is shown averaged down to the output rate of the SiIMU®, before being used in the compensation equations. This is important if the model includes squared or higher powers of terms, in order to minimise the noise. The DCM, which includes combined scale factor and misalignment terms, is assumed to be non-orthogonal and therefore the inverse is required (see section 3.1.4).

4.0 FUTURE SIIMU® DEVELOPMENTS

Developments are on going at BAE SYSTEMS to improve the basic performance of the sensors as well advancing the accuracy of the sensor models, which will enable performance to be enhanced through more accurate calibration.

A major system enhancement can be obtained by integrating the SiIMU® with a Global Positioning System (GPS) receiver and using the GPS velocity data to calibrate, real-time, the sensor errors. The system developed by BAE SYSTEMS that achieves this, is known as SiNAV™ (see [Powlesland, 2002]).

4.1 Integrated SiIMU® and GPS

4.1.1 Loosely-Coupled System

The loosely-coupled (using PVT data (Position, Velocity, Time)) prototype systems were based on a commercial Garmin GPS receiver and a first-generation BAE SYSTEMS SiIMU®.
The navigation performance achieved during trials is summarised by the following steady-state parameter values.

Parameter	Performance (1σ) Continuous GPS (PVT)	Performance (1σ) After 1 minute GPS Loss
Residual gyro drift	< 10º/hr	–
Residual accelerometer bias	2mg	–
Roll error	0.2º	0.26º
Pitch error	0.2º	0.26º
Heading error	1.0º	1.7º
Horizontal velocity error (RSS East / North)	0.25m/s	3m/s
Vertical velocity error	0.3m/s	1.5m/s
Horizontal position error	15m	90m
Vertical position error	20m	55m

The ground-based nature of the trials resulted in very benign platform dynamics, and in a more dynamic airborne trial, roll/pitch errors in the order of 0.1º and heading errors better than 0.2º would be achieved.

4.1.2 Closely-Coupled System

The closely-coupled system is currently under development and incorporates three significant advances when compared with its loosely-coupled predecessor:

(a) the commercial GPS receiver has been replaced by a full military specification P(Y)-code receiver for running the main application software,

(b) the COTS processing electronics has been replaced by a custom designed, embedded DSP subsystem for blending GPS and inertial data,

(c) the PVT algorithm has been replaced by a more a sophisticated ‘line-of-sight’ algorithm.

Development of the closely-coupled system is being carried out in collaboration with Rockwell Collins who are providing their NavStorm™ GPS receiver. The main system components of SiNAV™ are shown in Figure 4.1, with the unit assembly (cut-away) shown in Figure 4.2.

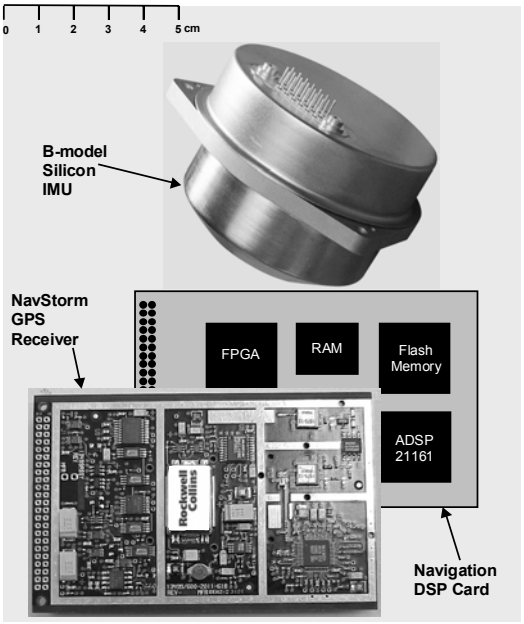


Figure 4.1– Closely-Coupled System Components.



Figure 4.2 – Unit Assembly Cut-Away.

5.0 REFERENCES

[1] Bierman, G.J., "Factorisation Methods for Discrete Sequential Estimation", Academic Press, (1977).

[2] Gelb, A. (Editor), "Applied Optimal Estimation", MIT Press, TASC, (1974).

[3] Maybeck, P.S., "Stochastic Models Estimation and Control", Vol. 1, Academic Press (1979).

[4] Zhang, Z., "Parameter Estimation Techniques: A Tutorial with Application to Conic Fitting, Image and Vision Computing", 15, pp. 59-76, Elsevier (1997).

[5] Powlesland, R.M., "SiNAV™ – Integrated MEMS/GPS Navigation System", PLANS, IEEE, (2002) et al.

APPENDIX A – OBTAINING CALIBRATION COEFFICIENTS USING THE KALMAN FILTER

A.1 KALMAN FILTER EQUATIONS

The standard discrete Kalman filter equations are as follows (see [Gelb,1974]),

$$\hat{x}_{k/k-1} = \Phi_{k-1}\hat{x}_{k-1/k-1} \quad \text{State Estimate Extrapolation} \quad (A.1)$$

$$P_{k/k-1} = \Phi_{k-1}P_{k-1/k-1}\Phi_{k-1}^T + Q_{k-1} \quad \text{Error Covariance Extrapolation} \quad (A.2)$$

$$K_k = P_{k/k-1}H_k^T\left[H_kP_{k/k-1}H_k^T + R_k\right]^{-1} \quad \text{Kalman Gain} \quad (A.3)$$

$$\hat{x}_{k/k} = \hat{x}_{k/k-1} + K_k\left[z_k - H_k\hat{x}_{k/k-1}\right] \quad \text{State Estimate Measurement Update} \quad (A.4)$$

$$P_{k/k} = \left[I - K_kH_k\right]P_{k/k-1} \quad \text{Error Covariance Measurement Update} \quad (A.5)$$

Initial Values

$$\hat{x}_0 = E\left[\hat{x}_0\right] \quad (A.6)$$

$$P_0 = E\left[(\hat{x}_0 - x_0)(\hat{x}_0 - x_0)^T\right] \quad (A.7)$$

where,

^	(circumflex) denotes the estimated state
k	subscript denotes variable at *k th* instance in time
x	state vector, dimension n
z	observation (measurement) vector, dimension m
w	white process noise vector, dimension n
v	white measurement noise vector, dimension m
Φ	state transition matrix, dimension (n x n)
P	error covariance matrix, dimension (n x n)
Q	process noise covariance matrix, dimension (n x n)
R	measurement noise covariance matrix, dimension (m x m)
H	measurement matrix, dimension (m x n)
K	Kalman gain matrix, dimension (n x m)
I	identity matrix (n x n))

For estimating calibration coefficients, the coefficients are assumed to be constant and therefore the extrapolation equations are not required ($\Phi = I$), also the measurements are normally taken individually. With these assumptions, a simplified set of Kalman filter equations can be defined, by setting *H* to *h* (vector), *K* to *k* (vector), *R* to *r* (scalar) and *z* is a scalar. This form is known as the Scalar Measurement Update Kalman filter equations.

$$i = 1$$

initialise $x_i = x_0, P_i = P_0$

$$k_i = \frac{P_i h_i}{h_i^T P_i h_i + r_i} \quad \text{Kalman Gain} \quad \text{(A.8)}$$

$$x_{i+1} = x_i + k_i[z_i - h_i^T x_i] \quad \text{State Estimate} \quad \text{(A.9)}$$

$$P_{i+1} = [I - k_i h_i^T]P_i \quad \text{State Covariance} \quad \text{(A.10)}$$

$$i = i + 1 \quad \text{(A.11)}$$

Cycle through equations (A.8) to (A.11) until all measurements have been included, the state estimate x, then holds the calibration coefficients. By saving the x and P values at each iteration, the convergence of the state estimates and covariances can be assessed as each measurement is processed.

The standard Kalman filter equations are prone to numerical instability, it is therefore highly recommended that a more robust form of the equations are used, such as the UD implementation (see [Bierman, 1977]).

A.2 EXAMPLE SET OF EQUATIONS

Assume that the gyro bias is temperature dependant but can be modelled as a polynomial to order three (cubic fit). If detailed knowledge of the initial conditions are not known, then x_0 can be set to zero and P_0 diagonals set to some large value (larger than any expected error in x_0 , see equation (A.7)) and the off diagonals set to zero (no correlation between states).

In this case the gyro bias is given by,

$$z = a + bT + cT^2 + dT^3 \quad \text{A.12}$$

where, z is the gyro bias and T is the gyro temperature.

The a, b, c, d are the coefficients to be estimated, for example, a, represents the offset (aT^0).

For this example, assume that it is known that the gyro bias will not be greater than 2 deg/s, then with x_0 set to zero, the $P_0(1,1)$ diagonal value must be set greater than 4 $(\text{deg/s})^2$ (ie, 2 deg/s x 2 deg/s). The other three P_0 diagonals can be expected to be less than $P_0(1,1)$, since these coefficients (*b, c, d*) will be less than *a* due to the multiplication by T (or powers of T), in equation (A.12). To ensure that the P_0 diagonals are not too small, it is proposed to set them to 100 $(\text{deg/s})^2$. The Kalman filter is relatively robust to P_0 being set very much higher than the actual errors, but not to being set too low.

The appropriate Kalman filter matrices and vectors are then,

$$x_0 = \begin{bmatrix} 0 \\ 0 \\ 0 \\ 0 \end{bmatrix} \quad P_0 = \begin{bmatrix} 100 & 0 & 0 & 0 \\ 0 & 100 & 0 & 0 \\ 0 & 0 & 100 & 0 \\ 0 & 0 & 0 & 100 \end{bmatrix} \quad h_i = \begin{bmatrix} 1 \\ T_i \\ T_i^2 \\ T_i^3 \end{bmatrix}$$

The Kalman gain at time i =1, is then

define,

$$k_n = \begin{bmatrix} 100 & 0 & 0 & 0 \\ 0 & 100 & 0 & 0 \\ 0 & 0 & 100 & 0 \\ 0 & 0 & 0 & 100 \end{bmatrix} \begin{bmatrix} 1 \\ T_1 \\ T_1^2 \\ T_1^3 \end{bmatrix}$$

and

$$k_d = \begin{bmatrix} 1 & T_1 & T_1^2 & T_1^3 \end{bmatrix} \begin{bmatrix} 100 & 0 & 0 & 0 \\ 0 & 100 & 0 & 0 \\ 0 & 0 & 100 & 0 \\ 0 & 0 & 0 & 100 \end{bmatrix} \begin{bmatrix} 1 \\ T_1 \\ T_1^2 \\ T_1^3 \end{bmatrix} + r_1$$

then,

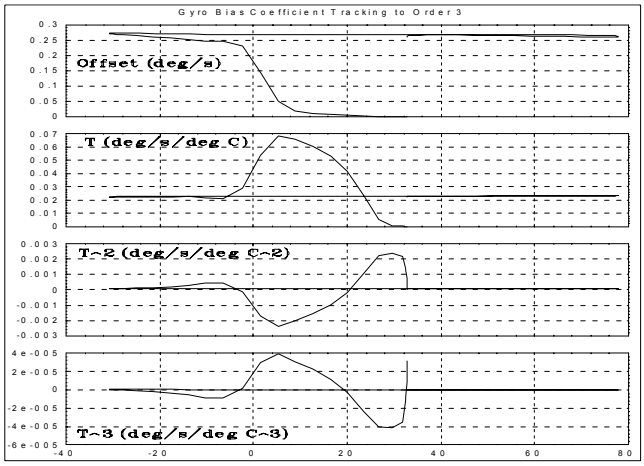
$k_1 = \dfrac{k_n}{k_d}$ the Kalman gain

Note that k_d is a scalar

k_1 is then used in equations A.9 and A.10 to calculate the first state estimate and covariance.

The measurement noise variance, r_i , is usually constant, but the advantage of the Kalman filter approach in obtaining the coefficients, is that the measurement noise can be varied to accurately model the noise on the measurement. Changes to the measurement noise can also be used to weight the measurements to, say, some particular temperature or temperatures, something which cannot be done if the solution of $Ax=b$ is used to obtain the coefficients (unless weighted least squares is used, [Zhang, 1997]).

An example set of results are given in Figures A.1a, A.1b, A.1c and A.1d, for a cubic temperature fit to gyro bias.



Figures A.1a: Kalman Filter Coefficient Tracking for Offset, T, T^2 and T^3 v Temperature (deg C).

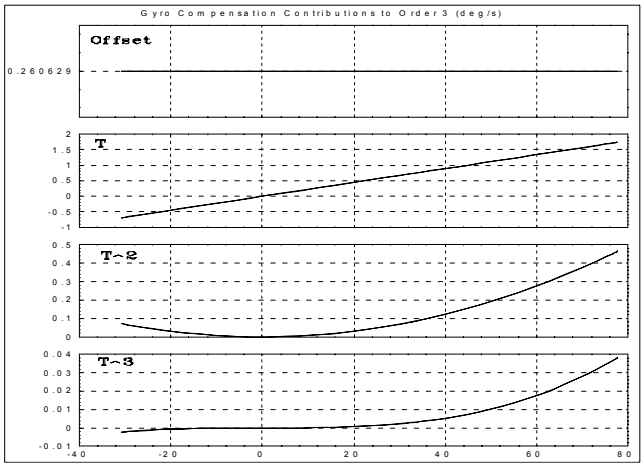


Figure A.1b: Compensation Contributions for Offset, T, T^2 and T^3 (deg/s) v Temperature (deg C).

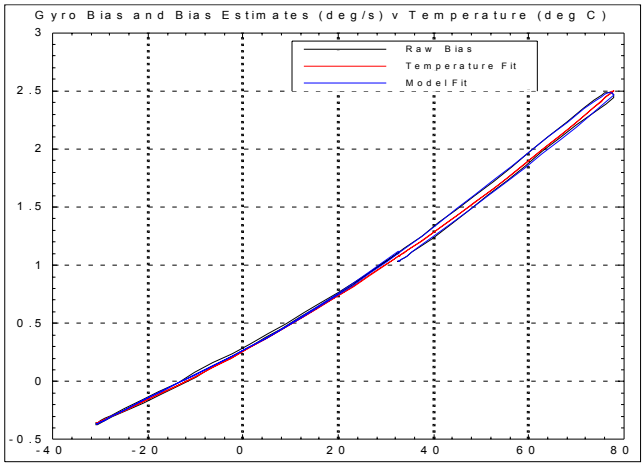


Figure A.1c: Raw Gyro Bias and Estimated Bias (deg/s) v Temperature (deg C).

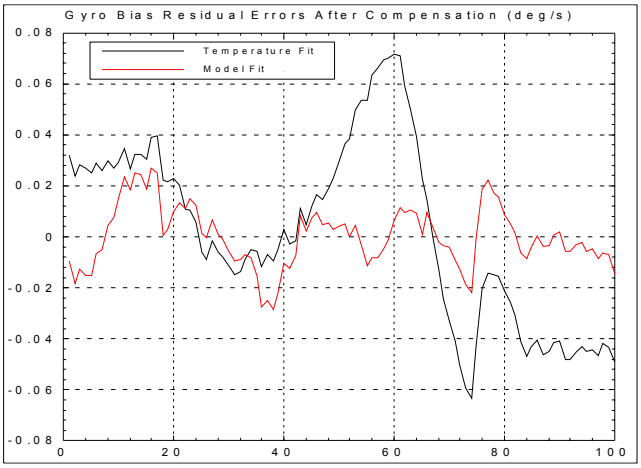
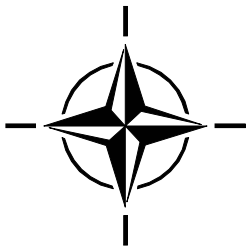


Figure A.1d: Residual Error for Temperature Fit and Gyro Model Fit (deg/s) v Temperature (deg C).

The starting temperature was just over 30 deg C and went cold first before ramping to the maximum temperature and returning to a nominal 30 deg C. As can be seen from Figure A.1a, the states (coefficients) are settling during the ramp to –30 deg C but are still being refined during the rest of the temperature profile.

Note the hysteresis in the bias (Figure A.1c), the best a temperature fit can achieve in this case is to fit a line between the hysteresis curve. The additional plot (Model Fit), in Figures A.1c and A.1d shows the improved fit to the bias using a more complex model of the gyro, which enables the hysteresis to be tracked.

The compensation contributions, shown in Figure A.1b, indicate that the T^3 term is an order of magnitude down on the T^2 contribution. This should prompt the question as to whether a lower order fit could be used.



Fiber Optic Gyro Systems and MEMS Accelerometer

Dr. Gottfried Eberhard Handrich
LITEF GmbH Freiburg
P. O. Box 774
79007 Freiburg
Germany

handrich.eberhard@litef.de

ABSTRACT

Fiber Optic Gyros (FOG) and MEMS Accelerometer are today used in inertial strapdown systems for medium accuracy and expanding into high performance strapdown navigation systems in competition with Ring Laser Gyros (RLG), whereas from the low accuracy side MEMS gyros are expanding to the medium accuracy ranges.

The FOG principle is based upon constant light velocity. This results in a phase difference of lights which are propagating through a fiber coil in clockwise (cw) or counter clockwise (ccw) directions if a rate is applied. The phase difference is proportional to the rate.

The FOG technology has been developed from an open loop design – still used in some niche markets – to closed loop design with high bandwidth and random phase modulation technique. The heart of gyro is the multifunction integrated optic chip (MIOC) which is produced in house out of $LiNbO_3$ wafers with proton exchange technique. The MIOC polarizes the light, splits the light into cw and ccw directions, modulates the light waves by electrodes and restores the Sagnac Phase and combines the cw and ccw lights. The first generation of FOG systems uses one light source splitted by a 3x3 coupler to 3 fiber coils. More than 15.000 FOGs for such triad systems have been produced and delivered. Typical applications are Attitude and Heading Reference Systems or Landnavigators which are described.

The second generation of FOG Systems use single axis FOGs with internal processor. These fiber optic rate sensors (µ-FORS) can be easily calibrated separately in high quantity and later assembled to modular systems. In the lesson the features of the µ-FORS family for bias values from 6°/h down to 0.03°/h are given. The different bias values are realised by adapting the fiber length on the coil. The other optical parts and the electronics are unchanged. One main feature for the common electronics is the tracking of the modulation frequency to the actual fiber length.

MEMS Accelerometers (MEMS Accel) are still mechanical sensors only built by micro machining technique. Most of them are small silicon pendulums which are elastically supported and the pick off is a capacity bridge. The more accurate MEMS Accels are operating in closed loop measuring the acceleration by electrostatic forces.

The technology, the mechanical sensor, the electronics is described on the example of the B-290 Triad which is a typical MEMS Accel product. Test data are presented for bias repeatability and stability and scale factor accuracy before and after temperature compensation.

1.0 BASIC FIBER OPTIC GYRO TECHNOLOGY

The evolution of the most important gyro technologies are shown over the years and the accuracies in Fig. 1.

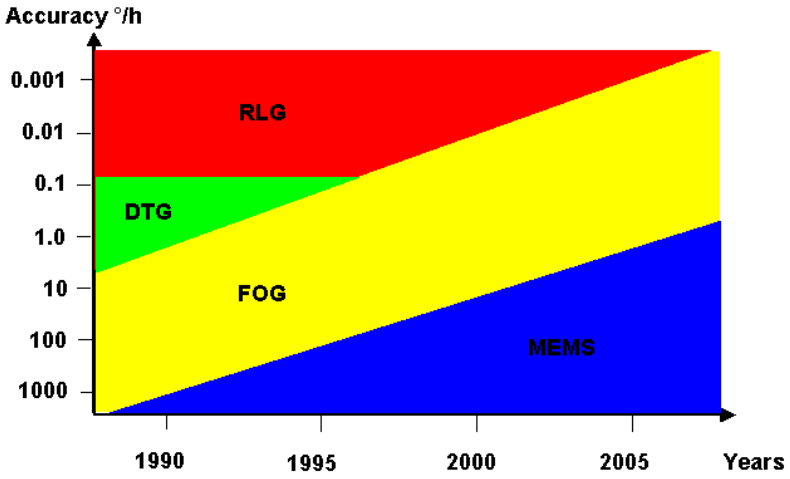


Figure 1: Evolution of Gyro Technologies.

Today the high accuracy end is still dedicated to Ring Laser Gyros. The moderate accuracy range from 0.01°/h to 30°/h is mainly covered by Fiber Optic Gyros and MEMS gyros are coming up from the low end accuracy.

If we look on Fiber Optic Gyros there exists the open and the closed loop design. The major advantage of the closed loop Fiber Optic Gyro is the high linearity of the scale factor and its insensitiveness against environment, especially against vibration.

Because of these advantages the main competition for Fiber Optic Gyros (FOG) is within the closed loop design giving room to niche applications for the open loop design. LITEF ony produces closed loop design. The bock diagram of the closed loop is shown in Fig.2. The heart of the FOG is the Multifunction Integrated Optic Chip (MIOC). The MIOC realises the polarizer, the main coupler and the modulator in one chip which is shown in Fig. 3. The MIOC production is done on $LiNbO_3$ wafers by forming proton exchanged wave guides and sputtered electrodes. 32 MIOCs are diced out of one wafer which is shown in Fig.4.

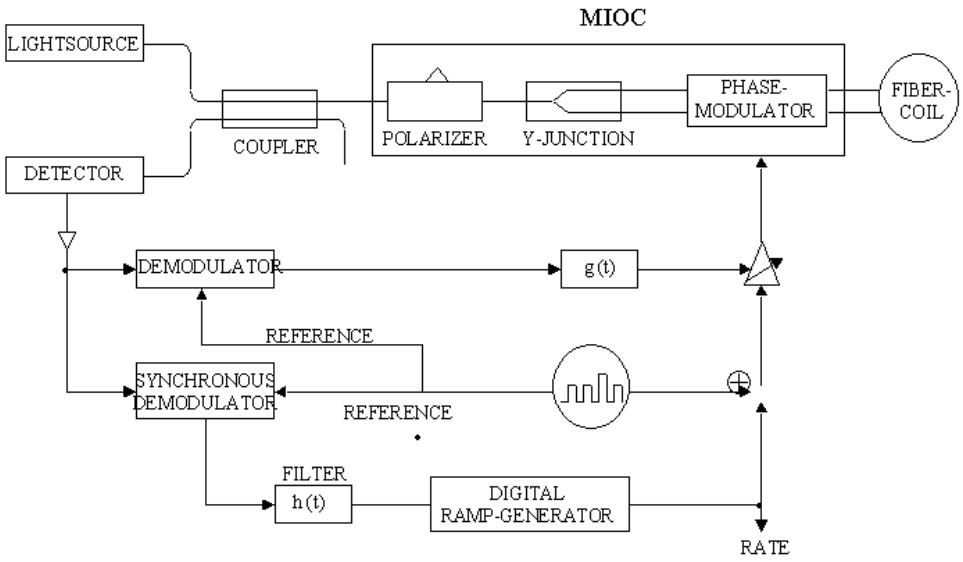
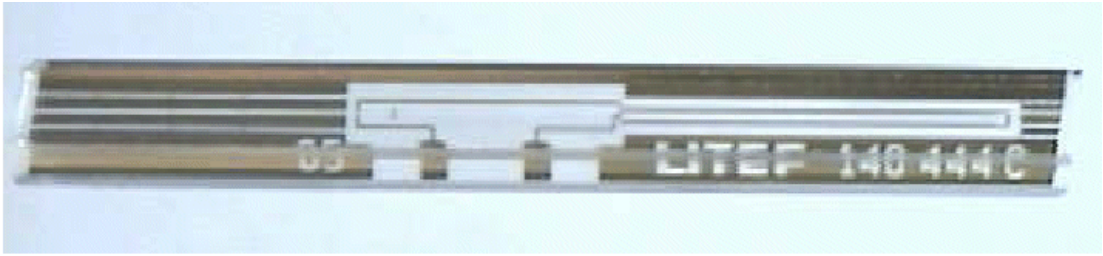


Figure 2: Block Diagram of the Closed Loop Fiber Optic Gyro.



Technical Parameter:

Light wavelength:	(840 ±30) nm
Insertion loss (Chip):	2.5 dB
Splitting ratio:	(50 : 50) ±5 %
Insertion loss (pigtailed):	3.5 dB
Polarization ratio:	65 dB
Modulation voltage:	< 3V (180° - Phase shift)

Figure 3: Multifunction Integrated Optic Chip (MIOC).

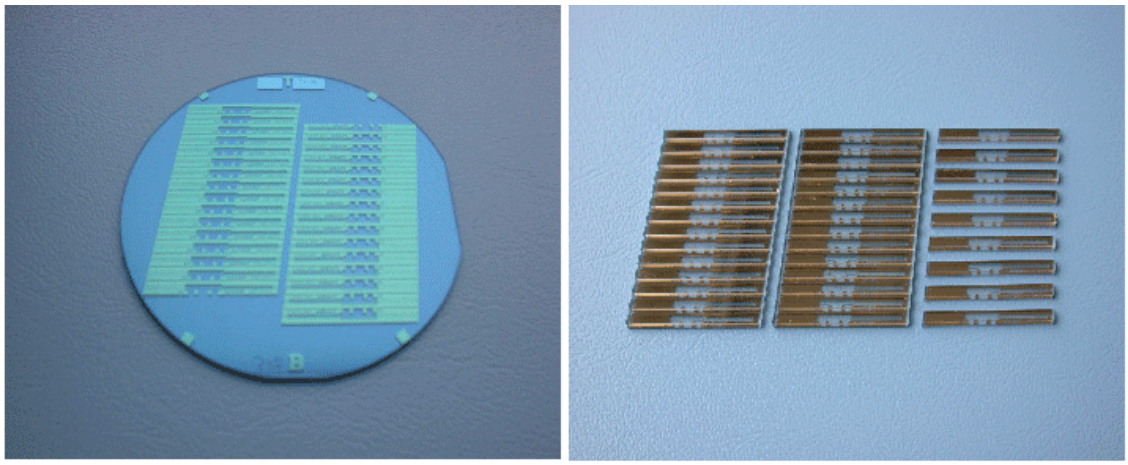


Figure 4: Lithium Niobate Technology.

The advantage of this technology is the high extinction ratio of the polarizing wave guides formed by proton exchange. The drawback of this technology is the high front end invest for an independent in house production for the MIOC and the challenge of the new technology, which requires clean rooms and equipment for lithography, proton exchange baths, annealing ovens, sputtering equipment, wafer dicing and chip polishing tools.

In the meantime LITEF produced more than 30.000 MIOCs with high yield for its Fiber Optic Gyro products.

2.0 FOG-TRIAD-SYSTEMS

In the beginning of the 1990's the SLD-lightsource package was a cost driver for Fiber Optic production. Therefore, the natural decision was to use one SLD-lightsource and distribute the light power to 3 IO-Chips and fiber coils. Such a Triad structure is shown in Fig. 5, a typical sensorblock assembly is shown in Fig. 6, which is used in an Attitude and Heating Reference System for commercial applications.

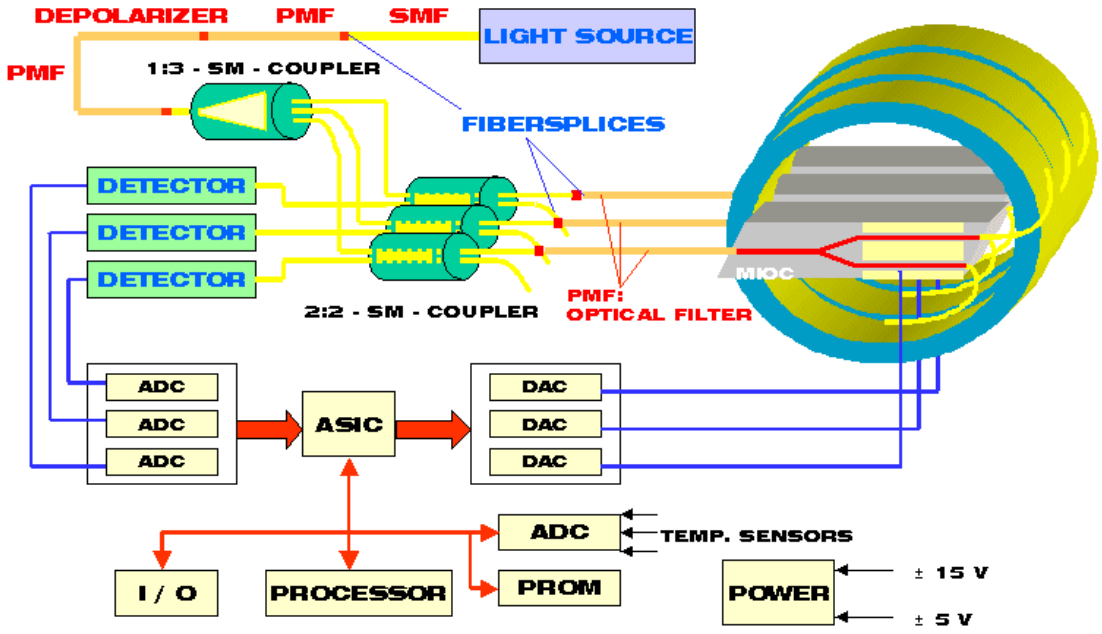


Figure 5: Fiber Optic Gyroscope – Triade Structure.

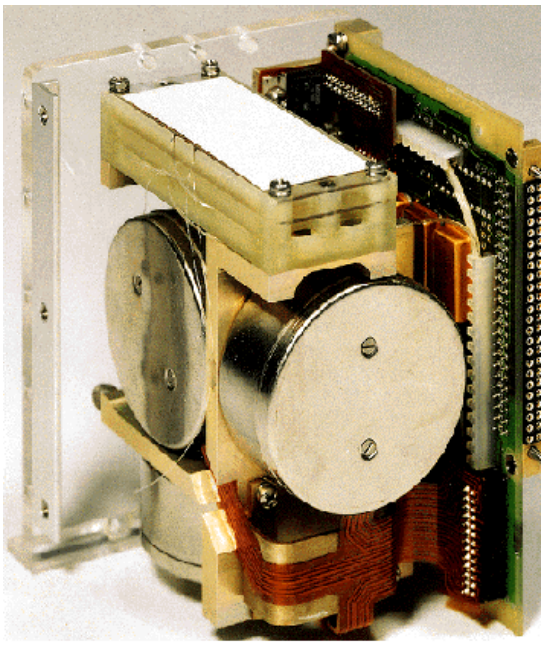


Figure 6: Sensorblock µAHRS.

In such Triad configuration LITEF developed in the past 5 different systems:

- LITEF Commercial Reference-92 (LCR-92), an Attitude Heading Reference System with bubbles as level sensor for commercial airborne applications,
- LITEF Commercial Reference-93 (LCR-93), an Attitude and Heading Reference System with integrated silicon accelerometers for commercial airborne applications,
- LITEF Transport Reference-97 (LTR-97), an Attitude and Heading Reference System with bubbles as level sensor for airline and transport application,
- LITEF Land Navigator-GX (LLN-GX), a navigator, which integrates the information of the Fiber Optic Gyros, of the bubbles, the odometer of the vehicle and of a GPS receiver to optimal navigation data,
- LITEF Land Navigator-G1 (LLN-G1), a navigator as LLN-GX, but with high accuracy Fiber Optic Gyros, with accelerometers instead of bubbles and integrated with self alignment features to north.

The accuracy span from 3°/h until 0.08°/h of those system is achieved with different coil design and fiber-length. The electronics is nearly the same.

All these systems are now in production for several years and the quantities produced have increased, e.g. between January 2000 and July 2002 more than 3.000 Triad Fiber Optic Systems have been produced. Therefore LITEF got a lot of experience in the field of Fiber Optic Gyro production yield.

If production yield is concerned the most critical production test is calibration over temperature of the system which is done on a turntable with climate chamber. Such tests are fully automatic steered by computers and four systems are calibrated simultaneously, but the test time is between 10 and 36 hours and the test equipment is expensive.

Today, the production yield in calibration of most of Fiber Optic Triad Systems is better than 90%. Besides the well known measurement for optical reciprocity and random phase modulation with its auxiliary loops the main hindrances to be removed for that yield were:

- Electronic noise at the IO-modulator which can create bias which is difficult to describe with a model. Filtering is very limited because of the required high bandwidth of 100 MHz for the modulation.
- Effects on bias by the so called “Bunny Ears” which are created by hopping over the Cosine-function of the interference patterns. Non-linearities in the detector and amplifier channel can also create bias.
- Selective optical losses in fiber and couplers which will create scale factor problems over temperature.

Because always 3 FOG axes has to be calibrated simultaneously a high performance margin for the FOGs are required to get the 90% yield in production.

3.0 MODULAR FIBER OPTIC SYSTEM DESIGN

Modular system design is a general design required for an easy assembly of a system in production. This is also realised in Fiber Optic Triad Systems. But a higher level of modularity means that each component of such a system should be testable in its function with high failure elimination, not only for an easy assembly, but also for a successful test e.g. calibration and acceptance test.

This is difficult to be achieved for Fiber Optic Gyro Triad Systems, because the total function, e.g. Bias or Scale Factor Accuracy, can only be tested with about 50% success on the component level and in calibration all parameters of all 3 axes has then to be tested simultaneously which creates high requirements for the material and processes of components and their integration.

But such a modular system design can be easily realised with single axis Fiber Optic Gyros with internal electronics and processor which compensates bias and scale factor over temperature. Than each gyro can be calibrated over temperature and afterwards assembled to systems with orthogonal or redundant skewed axes. A block diagram of such a modular system is shown in Fig. 7.

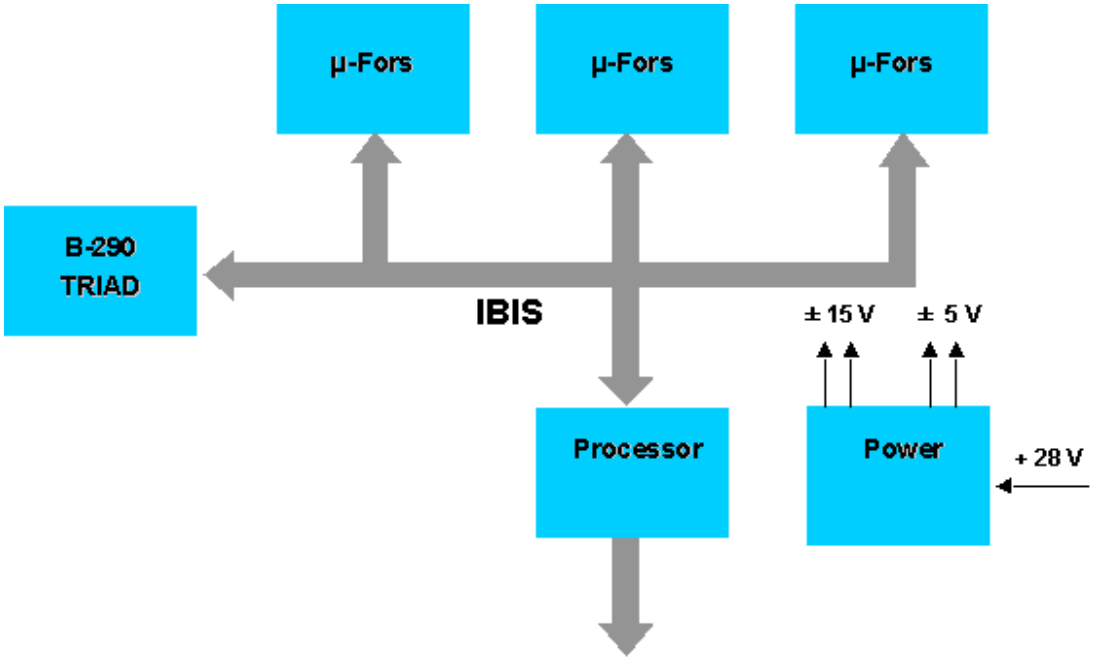


Figure 7: Modular Fog IMU Approach.

A digital synchronous bus IBIS (Intelligent Bus for Inertial Sensors) links the single axis µ-Fiber Optic Rate Sensors (µ-FORS) and the triad with silicon accelerometers (B-290 Triad) with the processor module. The data rate can be programmed between 5 Hz and 8 kHz. A power supply can be added if the required voltages (∀ 15V, ∀ 5V) are not delivered.

4.0 SINGLE AXIS µ-FORS FAMILY

µ-FORS was developed in 1995 and more than 6.000 µ-FORS have been produced and delivered. µ-FORS is a single axis Fiber Optic Rate Sensor with the necessary optics and electronics in a small housing of 76 x 55 x 20 mm^3. It requires ∀ 5V, 2W and delivers the rate data in digital format via the IBIS bus. Bias and scale factor are compensated over temperature internally by a risk processor within the digital ASIC. A lot of features can be programmed, e.g. the rate range and the output data rate.

The µ-FORS uses a SLD without peltier cooler, a binary digital MIOC with integrated DAC-function, a low cost detector and a flash ADC. The main control loop, all auxiliary loops and the risk processor are designed into a digital ASIC with 1.4 Mio transistors. The main bulk of the production quantities are dedicated to µ-FORS-36 and µ-FORS-6 the bias performance of which is shown in Fig. 8.

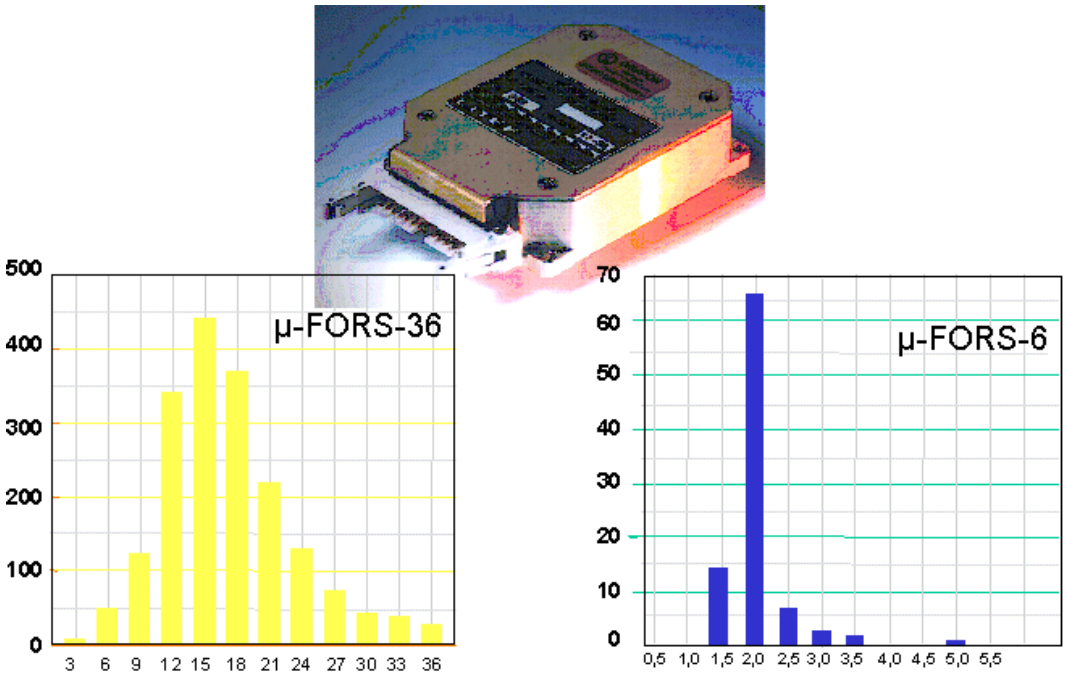


Figure 8: Bias Statistics of μ-FORS-36 and μ-FORS 6.

In the meantime, LITEF developed a μ-FORS family with the following features:

- Compact single axis rate sensors
- Temperature compensated digital output
- Rate range, resolution and data rate programmable
- Fiber coil length from 50m to 500m
- Bias residuals from 6°/h to 0.03°/h
- Scale factor from 3.000 ppm to 100 ppm
- Typical size: 76 mm x 55mm x 20mm

The major steps for the improvement of bias and scale factor to these limits was a new digital MIOC with 12 bit electrodes and a new digital ASIC with 4 Mio transistors which includes the following improvements:

- an improved hardware scale factor control
- an optical coil fiber length measurement
- modulation frequency tracking to the actual fiber length
- a bit weighing algorithm for the digital MIOC
- therefore noise and resolution reduction
- improved data path for main control loop
- ARM 7 risk processor with RAM/ROM

With the new feature – the tracking of the modulation frequency to the actual fiber length – the bias effects created by synchronous noise vanishes which is a big improvement.

The smallest µ-FORS family member is the µ-FORS-36m. The main challenge was the development of an analogue ASIC together with the multi chip module for the detector and the optimised packaging of optics and electronics in co-operation with BGT. Fig. 9 shows the inside electronics of µ-FORS-36m.

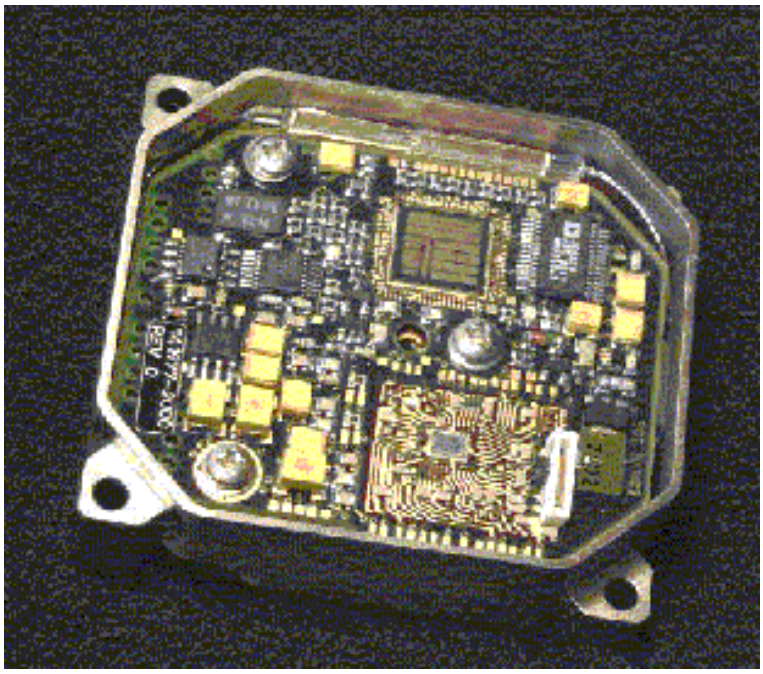


Figure 9: Fiber Optical Gyro µ-FORS-36m with Electronics in Micro-Via-Techniques.

The most accurate µ-FORS has a 500m fiber coil and a peltier stabilised SLD. This µ-FORS is shown in Fig. 10 and 11.

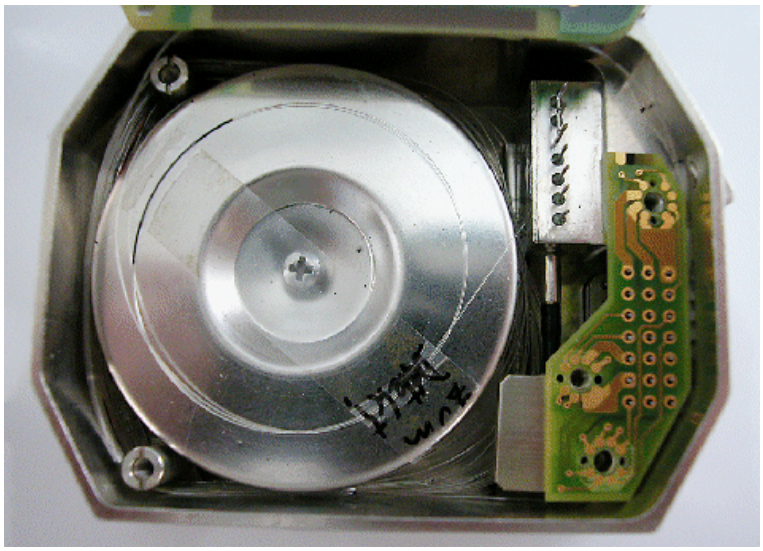


Figure 10: Optical Components of µ-FORS with 500m Fiber Coil.

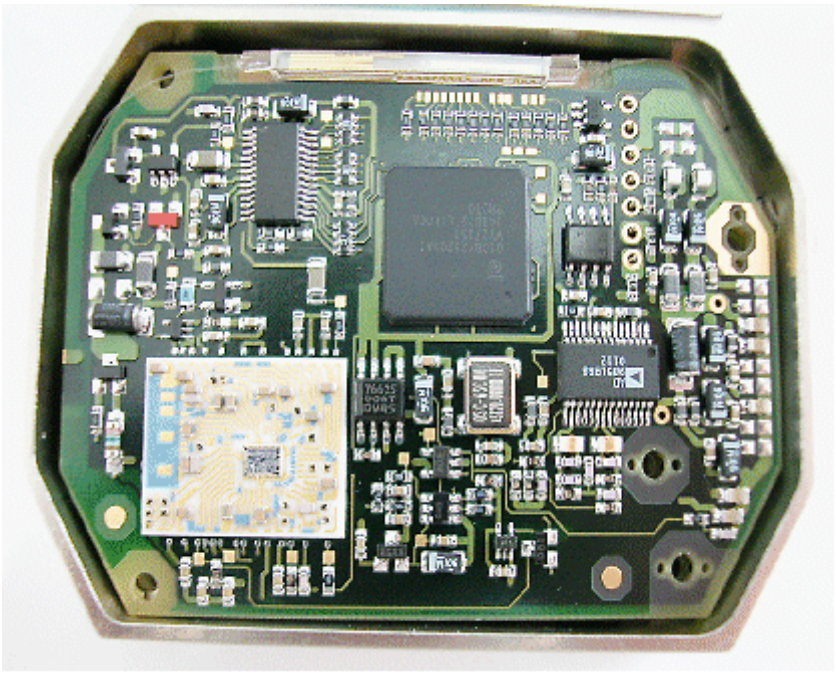


Figure 11: MIOC & Electronics Board of the µ-FORS.

In Figure 12, the measured bias values of 100 µ-FORS-36m are shown. It can be seen that all values except 3 sample are within ∀ 3°/h.

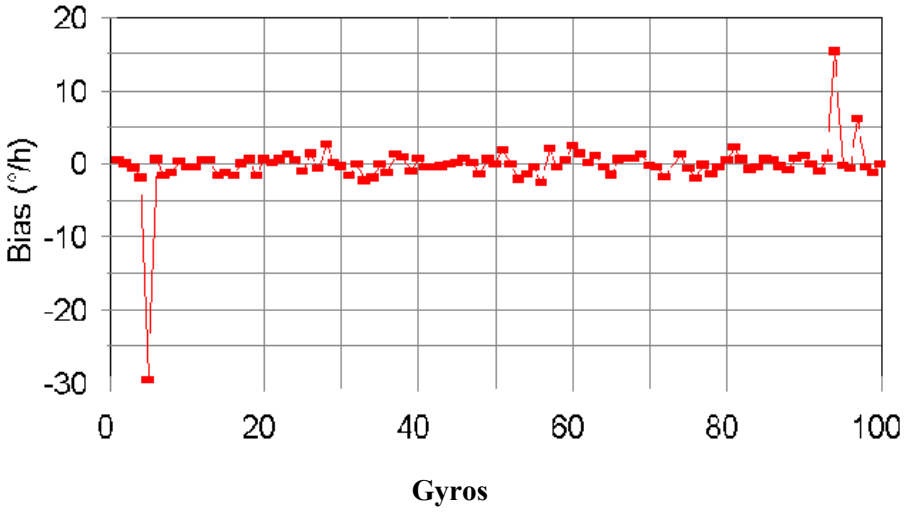


Figure 12: µ-FORS 36m at Room Temperature.

The best performance of 500m FOGs in production is shown in the bias statistics of Fig. 13; 90% of the produced gyros are below 0.04°/h bias and the typical bias (highest peak) is 0.015°/h.

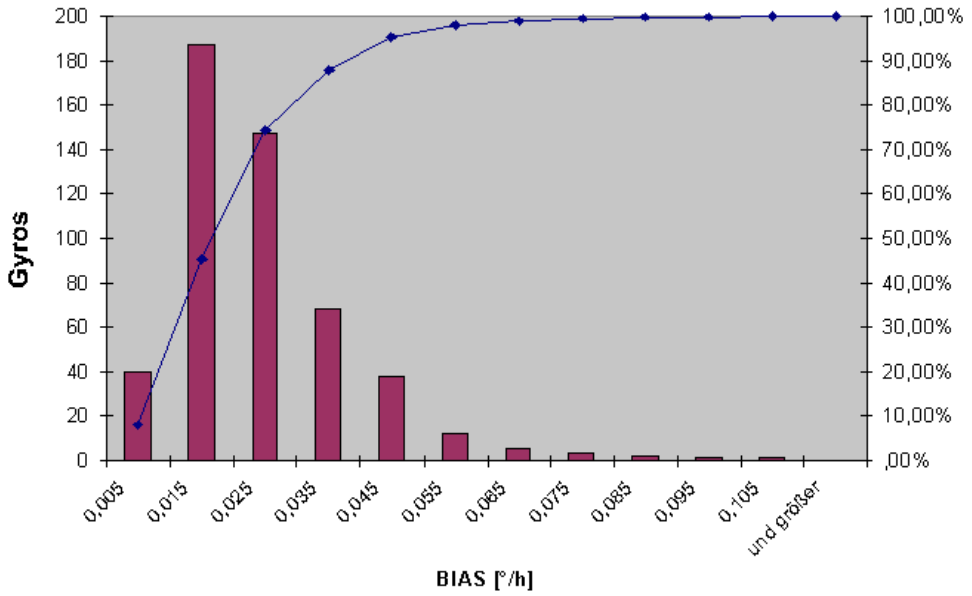


Figure 13: Bias Statistics of a 500m FOG.

5.0 MEMS ACCELEROMETER

Most of the MEMS accelerometers principles use elastically supported pendulums produced by bulk micro machining. An typical example of that type is LITEF's accelerometer B-290 the principle of which is shown in Fig. 14.

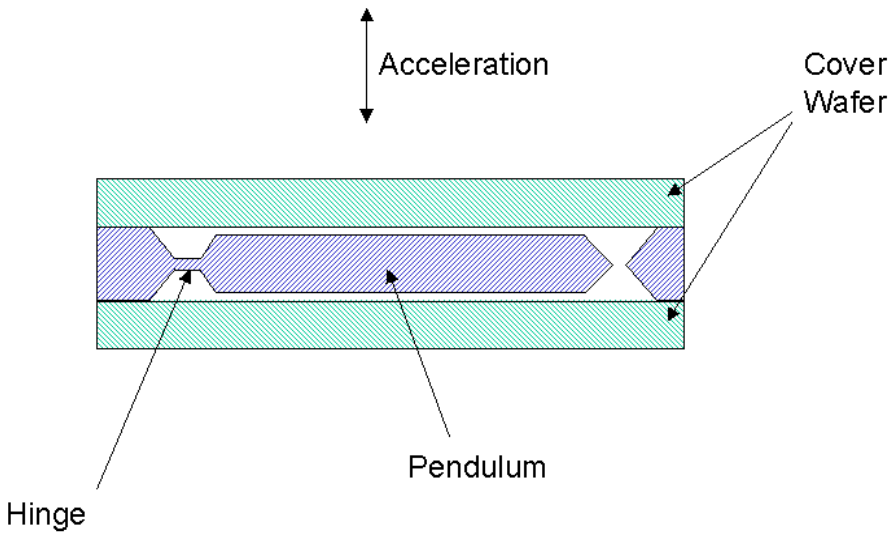


Figure 14: Principle of the Silicon Accelerometer B-290.

An acceleration is changing the position of the pendulum and the gaps between the cover wafers. The gaps are used as a capacity bridge for the pick-off and as the restoring torquer by electrostatic forces.

The total Silicon chip is shown in Fig. 15. The chip is built out of five silicon wafers by silicon direct bonding: Two shield wafers are added to avoid stray capacities.

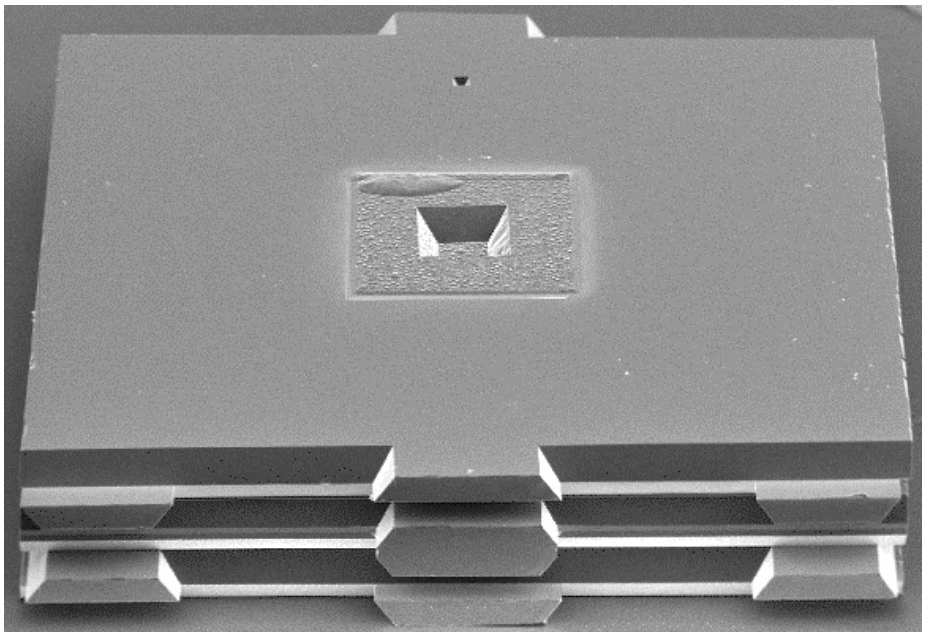


Figure 15: Silicon Accelerometer Chip for B-290.

If the chip is opened you can see the pendulum with the hinges and the electrode with shielding frame on the other side in Fig. 16. The production process of the chip is a real batch process on 5 wafers for 140 chips which are bonded together at the end of process and then cut into 140 accelerometer chips. The pendulum wafer is shown in Fig. 17.

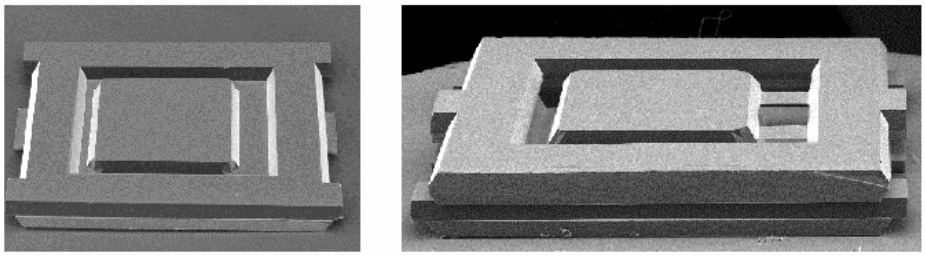


Figure 16: Open Accelerometer Chip for B-290.

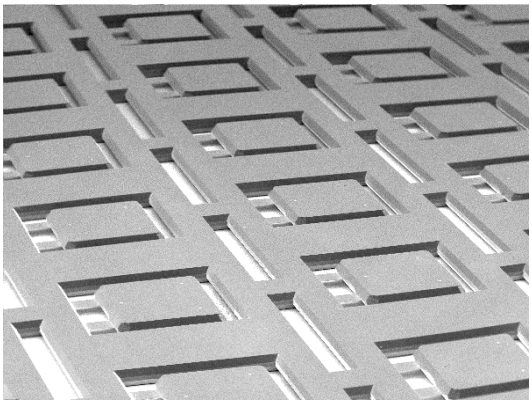


Figure 17: Pendulum Wafer for B-290.

The sensor electronics switches the voltage at the capacitor bridge and senses the for differences in the capacitor bridge by a charge amplifier and an A/D-converter. A signal processor performs the linearization and steers the restoring by electrostatic forces. The digital acceleration output of the processor is compensated in bias and scale factor over temperature. The electronics for a sensor is packaged on two small hybrids, 3 sensors and 3 electronics are packaged in a triad as shown in Fig. 18.

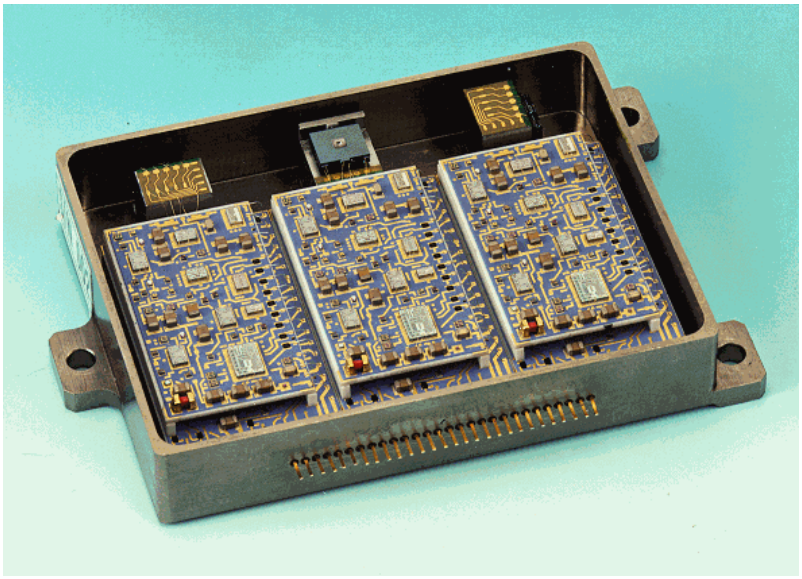


Figure 18: Open B-290 Accelerometer Triad.

In a cost reduction program a mixed signal ASIC was developed for the charge amplifier, different voltage controls and the A/D-converter used for each sensor. Only one signal processor is used for three sensors which dropped cost and power of the B-290 Triad. The new B.290 Triad is shown in Fig. 19.

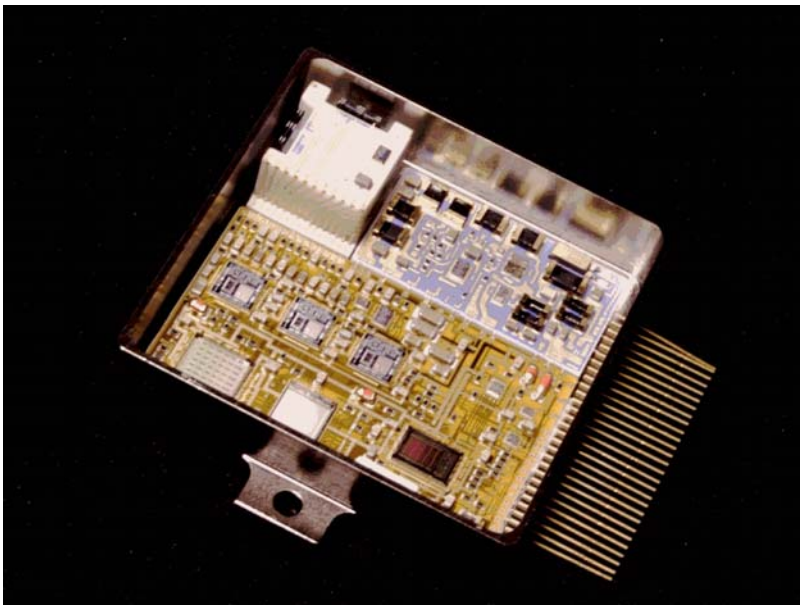


Figure 19: New Design of the B-290 Accelerometer Triad.

Each B-.290 Triad is calibrated over temperature and scale factor and bias is compensated inside by the signal processor. Typical scale factor and bias repeatability over temperature are shown in Fig. 20 and Fig. 21.

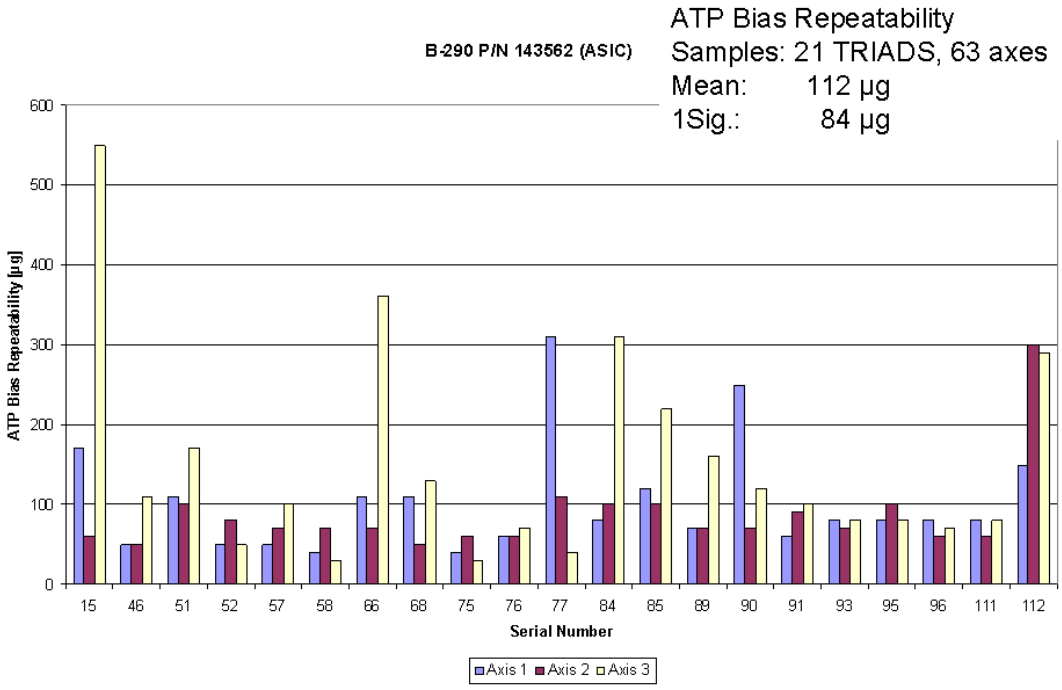


Figure 20: Example for a Modular Measurement Unit.

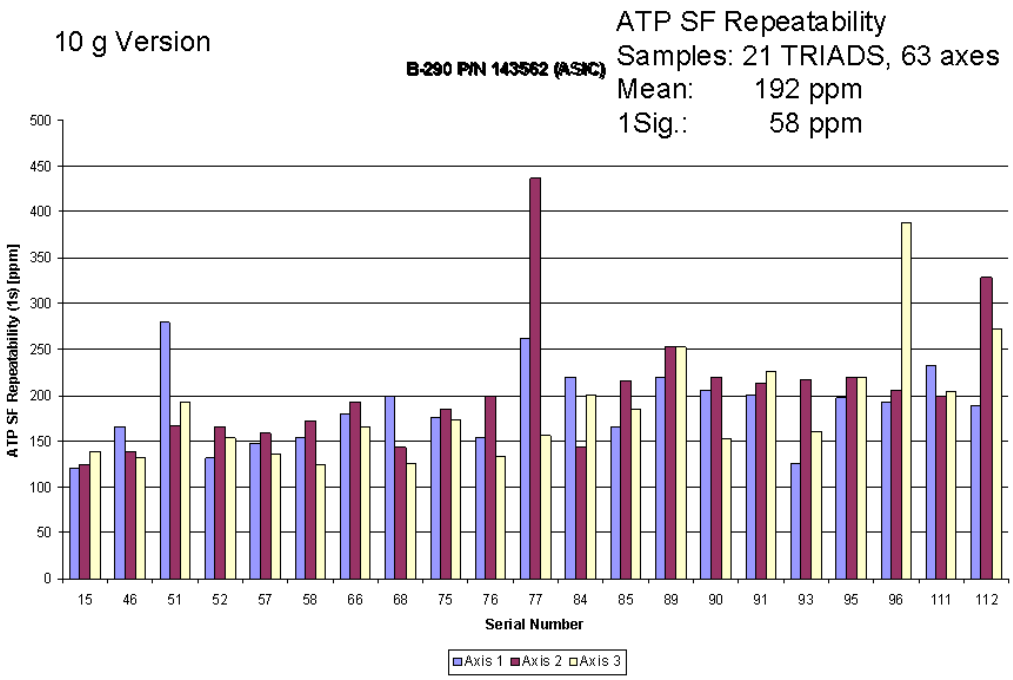


Figure 21: Bias Repeatability over Temperature.

6.0 INERTIAL MEASUREMENT UNIT

Three µ-FORS and one B-290 Triad are the inertial sensors for an orthogonal Inertial Measurement Unit, only the processor and perhaps a separate power supply has to be added according to the block diagram of Fig. 7. Due to separation into single axis Fiber Optic Gyros it is easy to fit the packaging to different geometry requirements. The IMU packaging can be done by LITEF, but also by customer by buying a sensor package.

As an example in Fig. 18 a packaged IMU is shown with integrated IMU processor and power supply. The size is 13 x 11 x 7,5 cm^3, the weight is 1,1 kg.

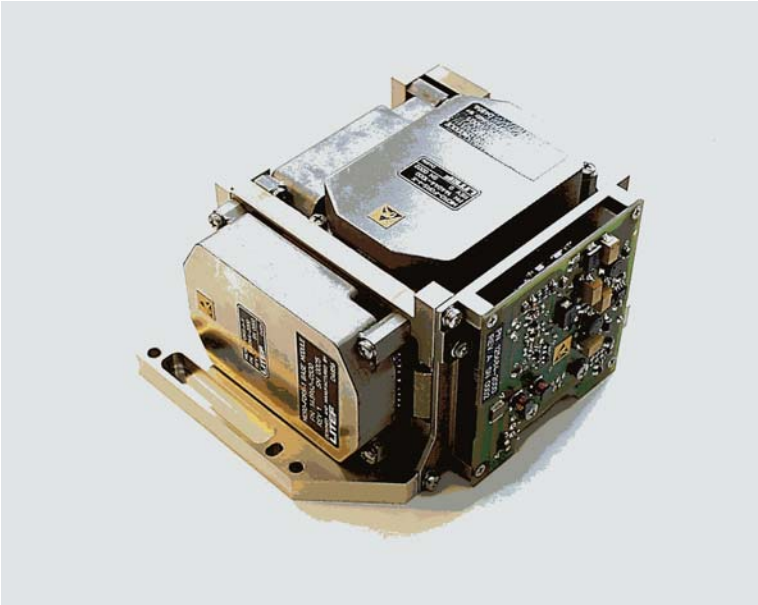


Figure 22: Example for a Modular Measurement Unit.

REPORT DOCUMENTATION PAGE

1. Recipient's Reference	2. Originator's References	3. Further Reference	4. Security Classification of Document
	RTO-EN-SET-064 AC/323(SET-064)TP/43	ISBN 92-837-1114-9	UNCLASSIFIED/ UNLIMITED

5. Originator

Research and Technology Organisation
North Atlantic Treaty Organisation
BP 25, F-92201 Neuilly-sur-Seine Cedex, France

6. Title

Advances in Navigation Sensors and Integration Technology

7. Presented at/Sponsored by

The Sensors and Electronics Technology Panel (SET) in support of a Lecture Series presented on 20-21 October 2003 in London, UK; 23-24 October 2003 in Ankara, Turkey; and 27-28 October 2003 in Paris, France.

8. Author(s)/Editor(s)	9. Date
Multiple	February 2004
10. Author's/Editor's Address	**11. Pages**
Multiple	228

12. Distribution Statement

There are no restrictions on the distribution of this document. Information about the availability of this and other RTO unclassified publications is given on the back cover.

13. Keywords/Descriptors

Accelerometers
Accuracy
Air navigation
Algorithms
Fiber optic gyroscopes
Fiber optics
Global positioning system
Guidance
Gyroscopes
IMU (Inertial Measurement Units)
Inertial navigation
Integrated systems
MEMS (Micro-Electro-Mechanical System)
Microelectronics
Mission profiles
Navigational aids
Performance evaluation
Precision guided munitions
Strapped down systems

14. Abstract

This Lecture Series presented the current state-of-the-art in navigation sensors and integration technology through the improved use of advanced low-cost navigation sensor technologies. The following topics were covered:

- Future of interial sensors/integrated systems
- Advances in gyro technology
- Strapdown system computational elements
- Strapdown system performance analysis
- System integration principles
- Innovative MEMS navigation applications
- Advanced Sensor applications
- Highly integrated systems



NORTH ATLANTIC TREATY ORGANISATION

RESEARCH AND TECHNOLOGY ORGANISATION

BP 25
F-92201 NEUILLY-SUR-SEINE CEDEX • FRANCE
Télécopie 0(1)55.61.22.99 • E-mail mailbox@rta.nato.int

DIFFUSION DES PUBLICATIONS
RTO NON CLASSIFIEES

Les publications de l'AGARD et de la RTO peuvent parfois être obtenues auprès des centres nationaux de distribution indiqués ci-dessous. Si vous souhaitez recevoir toutes les publications de la RTO, ou simplement celles qui concernent certains Panels, vous pouvez demander d'être inclus soit à titre personnel, soit au nom de votre organisation, sur la liste d'envoi.

Les publications de la RTO et de l'AGARD sont également en vente auprès des agences de vente indiquées ci-dessous.

Les demandes de documents RTO ou AGARD doivent comporter la dénomination « RTO » ou « AGARD » selon le cas, suivi du numéro de série. Des informations analogues, telles que le titre est la date de publication sont souhaitables.

Si vous souhaitez recevoir une notification électronique de la disponibilité des rapports de la RTO au fur et à mesure de leur publication, vous pouvez consulter notre site Web (www.rta.nato.int) et vous abonner à ce service.

CENTRES DE DIFFUSION NATIONAUX

ALLEMAGNE
Streitkräfteamt / Abteilung III
Fachinformationszentrum der
Bundeswehr (FIZBw)
Friedrich-Ebert-Allee 34, D-53113 Bonn

BELGIQUE
Etat-Major de la Défense
Département d'Etat-Major Stratégie
ACOS-STRAT – Coord. RTO
Quartier Reine Elisabeth
Rue d'Evère, B-1140 Bruxelles

CANADA
DSIGRD2
Bibliothécaire des ressources du savoir
R et D pour la défense Canada
Ministère de la Défense nationale
305, rue Rideau, 9e étage
Ottawa, Ontario K1A 0K2

DANEMARK
Danish Defence Research Establishment
Ryvangs Allé 1, P.O. Box 2715
DK-2100 Copenhagen Ø

ESPAGNE
SDG TECEN / DGAM
C/ Arturo Soria 289
Madrid 28033

ETATS-UNIS
NASA Center for AeroSpace
Information (CASI)
Parkway Center, 7121 Standard Drive
Hanover, MD 21076-1320

FRANCE
O.N.E.R.A. (ISP)
29, Avenue de la Division Leclerc
BP 72, 92322 Châtillon Cedex

GRECE (Correspondant)
Defence Industry & Research
General Directorate, Research Directorate
Fakinos Base Camp, S.T.G. 1020
Holargos, Athens

HONGRIE
Department for Scientific Analysis
Institute of Military Technology
Ministry of Defence
H-1525 Budapest P O Box 26

ISLANDE
Director of Aviation
c/o Flugrad
Reykjavik

ITALIE
Centro di Documentazione
Tecnico-Scientifica della Difesa
Via XX Settembre 123
00187 Roma

LUXEMBOURG
Voir Belgique

NORVEGE
Norwegian Defence Research Establishment
Attn: Biblioteket
P.O. Box 25, NO-2007 Kjeller

PAYS-BAS
Royal Netherlands Military
Academy Library
P.O. Box 90.002
4800 PA Breda

POLOGNE
Armament Policy Department
218 Niepodleglosci Av.
00-911 Warsaw

PORTUGAL
Estado Maior da Força Aérea
SDFA – Centro de Documentação
Alfragide
P-2720 Amadora

REPUBLIQUE TCHEQUE
DIC Czech Republic-NATO RTO
VTÚL a PVO Praha
Mladoboleslavská ul.
Praha 9, 197 06
Česká republika

ROYAUME-UNI
Dstl Knowledge Services
Information Centre, Building 247
Dstl Porton Down
Salisbury
Wiltshire SP4 0JQ

TURQUIE
Milli Savunma Bakanlığı (MSB)
ARGE ve Teknoloji Dairesi Başkanlığı
06650 Bakanliklar – Ankara

AGENCES DE VENTE

NASA Center for AeroSpace Information (CASI)
Parkway Center, 7121 Standard Drive
Hanover, MD 21076-1320
ETATS-UNIS

The British Library Document Supply Centre
Boston Spa, Wetherby
West Yorkshire LS23 7BQ
ROYAUME-UNI

Canada Institute for Scientific and Technical Information (CISTI)
National Research Council
Acquisitions, Montreal Road, Building M-55
Ottawa K1A 0S2, CANADA

Les demandes de documents RTO ou AGARD doivent comporter la dénomination « RTO » ou « AGARD » selon le cas, suivie du numéro de série (par exemple AGARD-AG-315). Des informations analogues, telles que le titre et la date de publication sont souhaitables. Des références bibliographiques complètes ainsi que des résumés des publications RTO et AGARD figurent dans les journaux suivants :

Scientific and Technical Aerospace Reports (STAR)
STAR peut être consulté en ligne au localisateur de ressources uniformes (URL) suivant:
http://www.sti.nasa.gov/Pubs/star/Star.html
STAR est édité par CASI dans le cadre du programme NASA d'information scientifique et technique (STI)
STI Program Office, MS 157A
NASA Langley Research Center
Hampton, Virginia 23681-0001
ETATS-UNIS

Government Reports Announcements & Index (GRA&I)
publié par le National Technical Information Service
Springfield
Virginia 2216
ETATS-UNIS
(accessible également en mode interactif dans la base de données bibliographiques en ligne du NTIS, et sur CD-ROM)

NORTH ATLANTIC TREATY ORGANISATION

RESEARCH AND TECHNOLOGY ORGANISATION

BP 25
F-92201 NEUILLY-SUR-SEINE CEDEX • FRANCE
Télécopie 0(1)55.61.22.99 • E-mail mailbox@rta.nato.int

DISTRIBUTION OF UNCLASSIFIED RTO PUBLICATIONS

AGARD & RTO publications are sometimes available from the National Distribution Centres listed below. If you wish to receive all RTO reports, or just those relating to one or more specific RTO Panels, they may be willing to include you (or your Organisation) in their distribution.

RTO and AGARD reports may also be purchased from the Sales Agencies listed below.

Requests for RTO or AGARD documents should include the word 'RTO' or 'AGARD', as appropriate, followed by the serial number. Collateral information such as title and publication date is desirable.

If you wish to receive electronic notification of RTO reports as they are published, please visit our website (www.rta.nato.int) from where you can register for this service.

NATIONAL DISTRIBUTION CENTRES

BELGIUM
Etat-Major de la Défense
Département d'Etat-Major Stratégie
ACOS-STRAT – Coord. RTO
Quartier Reine Elisabeth
Rue d'Evère
B-1140 Bruxelles

CANADA
DRDKIM2
Knowledge Resources Librarian
Defence R&D Canada
Department of National Defence
305 Rideau Street
9th Floor
Ottawa, Ontario K1A 0K2

CZECH REPUBLIC
DIC Czech Republic-NATO RTO
VTÚL a PVO Praha
Mladoboleslavská ul.
Praha 9, 197 06
Česká republika

DENMARK
Danish Defence Research Establishment
Ryvangs Allé 1
P.O. Box 2715
DK-2100 Copenhagen Ø

FRANCE
O.N.E.R.A. (ISP)
29, Avenue de la Division Leclerc
BP 72
92322 Châtillon Cedex

GERMANY
Streitkräfteamt / Abteilung III
Fachinformationszentrum der Bundeswehr (FIZBw)
Friedrich-Ebert-Allee 34
D-53113 Bonn

GREECE (Point of Contact)
Defence Industry & Research General Directorate, Research Directorate
Fakinos Base Camp, S.T.G. 1020
Holargos, Athens

HUNGARY
Department for Scientific Analysis
Institute of Military Technology
Ministry of Defence
H-1525 Budapest P O Box 26

ICELAND
Director of Aviation
c/o Flugrad, Reykjavik

ITALY
Centro di Documentazione Tecnico-Scientifica della Difesa
Via XX Settembre 123
00187 Roma

LUXEMBOURG
See Belgium

NETHERLANDS
Royal Netherlands Military Academy Library
P.O. Box 90.002
4800 PA Breda

NORWAY
Norwegian Defence Research Establishment
Attn: Biblioteket
P.O. Box 25, NO-2007 Kjeller

POLAND
Armament Policy Department
218 Niepodleglosci Av.
00-911 Warsaw

PORTUGAL
Estado Maior da Força Aérea
SDFA – Centro de Documentação
Alfragide, P-2720 Amadora

SPAIN
SDG TECEN / DGAM
C/ Arturo Soria 289
Madrid 28033

TURKEY
Milli Savunma Bakanlığı (MSB)
ARGE ve Teknoloji Dairesi Başkanlığı
06650 Bakanliklar – Ankara

UNITED KINGDOM
Dstl Knowledge Services
Information Centre, Building 247
Dstl Porton Down
Salisbury, Wiltshire SP4 0JQ

UNITED STATES
NASA Center for AeroSpace Information (CASI)
Parkway Center, 7121 Standard Drive
Hanover, MD 21076-1320

SALES AGENCIES

NASA Center for AeroSpace Information (CASI)
Parkway Center
7121 Standard Drive
Hanover, MD 21076-1320
UNITED STATES

The British Library Document Supply Centre
Boston Spa, Wetherby
West Yorkshire LS23 7BQ
UNITED KINGDOM

Canada Institute for Scientific and Technical Information (CISTI)
National Research Council
Acquisitions
Montreal Road, Building M-55
Ottawa K1A 0S2, CANADA

Requests for RTO or AGARD documents should include the word 'RTO' or 'AGARD', as appropriate, followed by the serial number (for example AGARD-AG-315). Collateral information such as title and publication date is desirable. Full bibliographical references and abstracts of RTO and AGARD publications are given in the following journals:

Scientific and Technical Aerospace Reports (STAR)
STAR is available on-line at the following uniform resource locator:
http://www.sti.nasa.gov/Pubs/star/Star.html
STAR is published by CASI for the NASA Scientific and Technical Information (STI) Program
STI Program Office, MS 157A
NASA Langley Research Center
Hampton, Virginia 23681-0001
UNITED STATES

Government Reports Announcements & Index (GRA&I)
published by the National Technical Information Service
Springfield
Virginia 2216
UNITED STATES
(also available online in the NTIS Bibliographic Database or on CD-ROM)

ISBN 92-837-1114-9